Molecular Mechanisms of
Mitotic Checkpoint Complex Assembly onto Kinetochores

Elyse S. Fischer

University of Cambridge, Churchill College
and
MRC Laboratory of Molecular Biology

This dissertation is submitted for the degree of Doctor of Philosophy
September 2021

Declaration

I declare that this dissertation is the result of my own work, carried out at the MRC Laboratory of Molecular Biology, and includes nothing that is the outcome of work done in collaboration except as specified explicitly in the text.

It is not substantially the same as any work that I have, or is being, submitted for any degree or qualification except as declared in the Preface and specified in the text.

Furthermore, it does not exceed the prescribed word limit of 60,000 words.

Thesis Summary

Molecular Mechanisms of Mitotic Checkpoint Complex Assembly onto Kinetochores

Elyse S. Fischer

During metaphase, in response to improper kinetochore-microtubule attachments, the spindle assembly checkpoint (SAC), activates the mitotic checkpoint complex (MCC), to inhibit the E3 ubiquitin ligase, the anaphase-promoting complex/cyclosome (APC/C). Inhibition of the APC/C then delays premature chromosome segregation by preventing APC/C-mediated degradation of two key cell cycle regulators, cyclin B and securin. The MCC is composed of BubR1, Cdc20 and Mad2, and while their assembly is an intrinsically very slow process, in cells it is catalytically activated. Recent work points towards hierarchical recruitments of SAC proteins onto the outer kinetochore by means of a Mps1-dependent phosphorylation cascade, which creates a catalytic platform for MCC assembly.

This thesis investigates several mechanisms of catalytic MCC assembly in humans using a combination of biochemical assays and structural biology. Chapter 3 uses X-ray crystallography and NMR spectroscopy to explore the structure and function of the Bub1-Mad1 complex, including how sequential phosphorylation of the Bub1 CD1 domain by Cdk1 and Mps1 promotes kinetochore targeting of the Mad1:C-Mad2 complex. Chapter 4 investigates how Mad1 C-terminal phosphorylation by Mps1 promotes juxtaposition of SAC proteins for MCC assembly. This includes using NMR to gain detailed structural insights into how phosphorylation of Mad1 promotes its interaction with both the N-terminus of Cdc20, as well as a region within Bub1 just C-terminal to its CD1 domain. Chapter 5 investigates the structure of the Mad1:C-Mad2:O-Mad2 complex by cryo-EM and reveals a mechanism of $Mad1^{CTD}$ fold-over which has import implications for MCC assembly. Chapter 6 sets the premise for ongoing work on the molecular mechanisms of Mad2 conversion from the open to closed state by NMR.

Acknowledgements

First and foremost, I would like to thank my supervisor David Barford for his day-to-day enthusiasm, curiosity, and support of my projects. David not only provided excellent advice, guidance, and insightful discussions, but his mentorship has been instrumental in helping me find confidence in my scientific and professional capabilities. I am grateful to all past and current members of the Barford lab for providing an ambitious, and competitive work environment, but one that is incredibly supportive and enjoyable. A special thanks to Kaige Yan and Andreas Boland for their cryo-EM training. Jing Yang and Ziguo Zhang for taking care of the entire lab. Kyle Muir, Stan Yatskevich, and Claudio Alfieri for providing the perfect mix of intellectually stimulating conversations and morale-boosting daily banter.

Thank you to all of the core facilities of the LMB, and in particular, Stephen McLaughlin for biophysical experiments, Sarah Maslen for mass spectrometry, Jianguo Shi for insect cell cultures, Dom Bellini for crystallography advice, Jake Grimmett and Toby Darling for scientific computing, and all members of the EM facility. I am indebted to Conny Yu and Stefan Freund of the LMB NMR facility, whose hard work went above and beyond our expectations, and who were patient teachers as I took my first steps in learning NMR. I am additionally grateful to Gates Cambridge, the University of Cambridge, Churchill College, as well as Albert Heck and Johannes Hevler for cross-linking mass spectrometry, and to my two thesis examiners Kelly Nguyen and Kevin Hardwick.

I am also enormously thankful to my family and friends for their endless support and encouragement. To Tricia and Philip Cohen who were not only phenomenal scientific mentors but also took me in and treated me as family when I first moved to the UK over 9 years ago. My utmost gratitude and love goes to my grandfather Eddy Fischer, who gave me my love for science, research, and discovery: Thank you for always having confidence in me, for supporting my career as a biochemist even before I knew I'd become one, and for teaching me to be ambitious but, also, to always treat research as a passion and not a job. I wish you could have been here to see me become Dr. E. Fischer at 27 years of age, just as you became Dr. E. Fischer at 27, but your inspiration, memory, and genes will continue to sustain me for the rest of my life. Lastly, I am immensely grateful to everyone already mentioned and so many more for making it possible to complete this work during the COVID-19 pandemic!

List of Publications

This dissertation contains results that have been published in a peer-reviewed journal.

Fischer, E.S., Yu, C.W.H., Bellini, D., McLaughlin, S.H., Orr, C.M., Wagner, A., Freund, S.M.V., Barford, D. (2021). Molecular mechanism of Mad1 kinetochore targeting by phosphorylated Bub1. Embo Rep 22: e52242. doi: /10.15252/embr.202052242

Table of Contents

List of Figures and Tables

Table of Abbreviations and Symbols

ABBREVIATION	FULL TEXT
3C	Human rhinovirus protease
Å	Angstrom
ADP	Adenosine diphosphate
APC/C	Anaphase promoting complex/cyclosome
ATP	Adenosine triphosphate
AUC	Analytical ultracentrifugation
bp	Base pair
BSA	Bovine serum albumin
BUB1/3	Budding uninhibited by benzimidazoles 1/3
BUBR1	BUB1-related kinase
CCAN	Centromere-associate network
CCD	Charged-coupled device
CD	Circular dichroism
CD1	Conserved domain 1
CDC20	Cell division cycle protein 20
CDH1	Cdc20 homolog 1
CDK1/2	Cyclin-dependent kinase 1/2
CENP	Centromere protein
CKS	Cyclin-dependent kinase regulatory subunit
Cryo-EM	Cryo-electron microscopy
CSP	Chemical shift perturbation
CTD	C-terminal domain
CTF	Contrast transfer function
D-Box	Destruction box
DLS	Dynamic light scattering
DMSO	Dimethyl-sulfoxide
DNA	Deoxyribonucleic acid
dNTP	Deoxy-ribonucleoside triphosphate
DTT	Dithiothreitol
e-	Electron
E1	Ubiquitin-activating enzyme
E2	Ubiquitin-conjugation enzyme
E3	Ubiquitin ligase
EC	Error correction
ECL	Enhanced chemiluminescence
EDTA	Ethylenediaminetetraacetic acid
FEG	Field emission gun
FRET	Fluorescence resonance energy transfer
FSC	Fourier shell correlation
GLEBS	Gle2-binding sequence
GST	Glutathione S-transferase
HEPES	4-(2-hydroxyethyl)-1-piperazineethanesulfonic acid)
His6	Hexa-histidine
HORMA	Hop1p, Rev7p and Mad2
HRP	Horseradish peroxidase
hrs	Hours
HSQC	Heteronuclear single quantum coherence
IPTG	Isopropyl Beta-D-1-thiogalactopruanoside

IR TAIL	Ile-Arg Tail
ITC	Isothermal calorimetry
Kb	Kilobase pairs
KD	Kinase domain
K_D	Dissociation constant
kDa	Kilodaltons
KNL1	Kinetochore scaffold 1
LB	Luria broth
MAD1/2	Mitotic arrest deficient-like 1/2
MBP	Maltose binding protein
MCC	Mitotic checkpoint complex
MES	2-(N-morpholino)ethanesulfonic acid
MIM	Mad2 interacting motif
MPS1	Monopolar spindle 1
Ni-NTA	Nickel nitrilotriacetic acid
NMR	Nuclear magnetic resonance
NOE	Nuclear overhauser effects
NTD	N-terminal domain
OD	Optical density
ORF	Open reading frame
PAGE	Polyacrylamide gel electrophoresis
PBS	Phosphate buffer saline
PCR	Polymerase chain reaction
PDB	Protein data bank
PEG	Polyethylene glycol
PLK1	Polo-like kinase 1
PMSF	Phenylmethane sulfonyl fluoride
PP1	Protein phosphatase 1
PP2A	Protein phosphatase 2A
RING	Really interesting new gene
RLK	Arginine-leucine-lysine
Rpm	Revolutions per minute
RQ	Resource Q anion exchange chromatography
RS	Resource S cation exchange chromatography
RT	Room temperature
RWD	Ring-WD40-Dead
RZZ	Rod1-Zwilch-Zw10
SAC	Spindle assembly checkpoint
SDS	Sodium dodecyl sulphate
SEC	Size-exclusion chromatography
SEC-MALS	SEC-coupled multi-angle light scattering
SGD	Stochastic gradient descent-based algorithm
SNR	Signal-to-noise ratio
SUMO	Small ubiquitin-like modifier
SE	Sedimentation equilibrium
SV	Sedimentation velocity
TCEP	Tris(2-carboxyethyl)phosphine
TEM	Transmission electron microscope
TEV	Tobacco etch virus
TPR	Tetratricopeptide repeat
Ub	Ubiquitin
USER	Uracil-specific excision reagent
VPP	Volta phase plate
w/v	Weight/volume
WB	Western blot

WD40	Tryptophan-aspartic acid 40
WT	Wild type

The following table summarizes abbreviations used for key protein complexes

ABBREVIATION	FULL TEXT
APC^{CDC20}	APC with co-activator Cdc20
APC^{MCC}	APC^{Cdc20} bound to MCC
$Cdc20^{APC/C}$	Cdc20 molecule of APC/C
$Cdc20^{MCC}$	Cdc20 molecule of MCC
$Mad1^{CTD}$	C-terminal domain of Mad1
Mad1:C-Mad2	Mad1 dimer bound to two Mad2 molecules
Mad1:C-Mad2:O-Mad2	Mad1 dimer bound to two O-Mad2:C-Mad2 dimers
C-Mad2	Mad2 in the closed confirmation
O-Mad2	Mad2 in the open confirmation
$Cdc20^{NTD}$	N-terminal domain of Cdc20

All genes and proteins are human in this study unless otherwise specified. Human genes are denoted as uppercase (e.g. MAD2), human protein products of these genes are designated by sentence case (e.g. Mad2)

Chapter One
Introduction

1.1 The Cell Cycle

Cell division, a process by which cells duplicate themselves, along with their DNA, is the most fundamental process of life. In unicellular organisms, cell division creates two novel organisms from one parent. In multicellular organisms, cell division has several roles, including developmental growth, adult tissue homeostasis, and replacing damaged or dead cells. Mitotic cell division gives rise to two genetically identical daughter cells whereas meiotic cell division creates germ-line cells with half the genetic material through two subsequent cell division events.

Phases of the Cell Cycle
Reviewed in: Harashima *et al*, 2013; Schafer, 1998.

Interphase
A typical eukaryotic cell cycle is composed of two major phases, interphase, and mitosis. Interphase commences with a G1 (Gap 1) phase, where cells prepare for cell division by synthesizing proteins necessary for DNA replication and packaging, and organelles are duplicated. This causes a noticeable increase in cellular mass which is a defining feature of G1. Cells then wait in a non-growth resting phase called G0 (Gap 0) until specific signals trigger a S (Synthesis) phase where nuclear DNA is replicated. This stage is also marked by cohesion forming a ring around sister chromatids preventing premature separation (Uhlmann & Nasmyth, 1998). Final preparations for mitosis (M) occur in an additional proliferation phase called G2 (Gap 2).

Mitosis
Mitosis is the phase of the cell cycle in which sister chromatids are equally segregated into two newly created daughter cells. It is composed of 5 stages: prophase, prometaphase, metaphase, anaphase, and telophase (Fig 1.0).

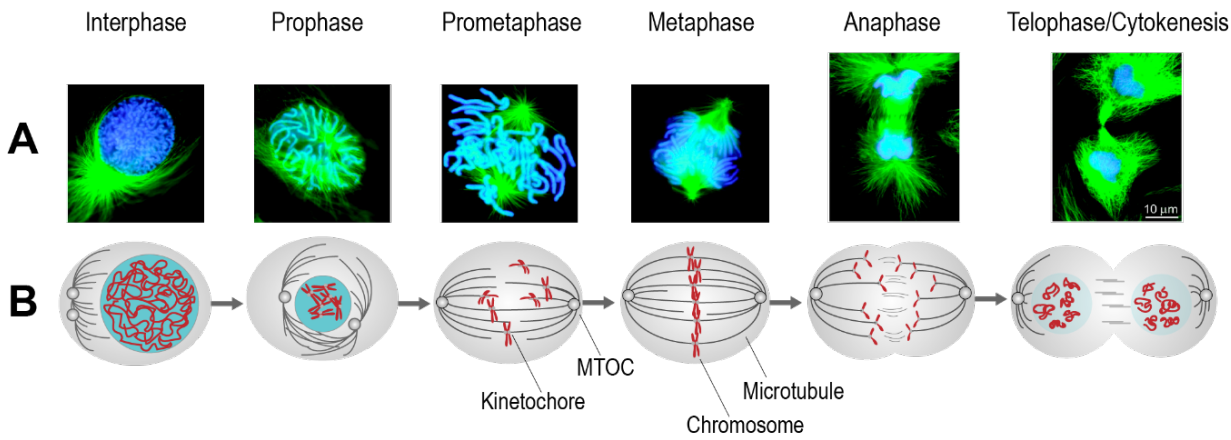

Figure 1.0: Phases of Mitosis. (A) *Fluorescence micrographs of mitosis in fixed newt lung cells. Microtubules are stained in green, and chromosomes are stained in blue (Khodjakov & Rieder, 2006).* ***(B)*** *A schematic of mitosis adapted from, Sivakumar & Gorbsky, 2015.*

In **prophase**, the duplicated DNA is condensed into tightly packed chromosomes. Microtubule organising centres (MTOC), known as centrosomes in metazoans and spindle pole bodies (SPBs) in yeast, begin to form arrays of lengthening microtubules (Reviewed in, Kilmartin, 2014). During **prometaphase** the plus-ends of microtubules capture chromosomes through kinetochore attachment. In **metaphase**, chromosomes are bio-oriented and aligned at the metaphase plate (spindle equator). Degradation of securin and cyclin B by the anaphase promoting complex/cyclosome (APC/C) then triggers **anaphase** where sister chromatids are pulled to opposite centrosomes. Securin degradation releases separase which results in cleavage of the cohesin ring and chromatid separation (Waizenegger *et al*, 2002; Hagting *et al*, 2002), while cyclin B breakdown causes Cdk1 inactivation and mitotic exit (Clute & Pines, 1999). In **telophase,** nuclei arrange around the two segregated chromatids and the actomyosin band forms, creating a contractile ring between the two daughter cells (McCully & Robinow, 1971; Bi *et al*, 1998). Finally, in the last step, **cytokinesis**, the septum degrades, and two separate daughter cells emerge.

Cell Cycle Checkpoints

Reviewed in: Hartwell & Weinert, 1989; Murray, 1992; Elledge, 1996.

The term cell cycle checkpoint was coined in 1989 when it was suggested that the cell cycle is linear with initiation of the next phase only occurring after certain criteria are satisfied (Hartwell & Weinert, 1989). Checkpoint surveillance is crucial for identifying errors and creating feedback loops which allows maintenance of genome stability across generations.

Key events include monitoring DNA replication fidelity, kinetochore-microtubule attachment, and cell size. Checkpoints usually function to delay cell cycle progression until errors can be corrected, including repairing damage or delaying progression when steps lag. If errors cannot be corrected, checkpoints can act to promote cell apoptosis (Sorger *et al*, 1997). Ultimately, correcting errors or triggering apoptosis is paramount in preventing genome instability which leads to many diseases including birth defects, cancer, and degenerative disorders (Holland & Cleveland, 2012; Santaguida & Amon, 2015). Entry and exit through critical points of the cell cycle is largely controlled by activation, inactivation, or ubiquitin-mediated proteolysis of key cell cycle regulators. For example, cyclin B, whose activation is required for entry into mitosis but whose destruction is required for mitotic exit (reviewed in Serpico & Grieco, 2020). There are two key E3 ubiquitin ligases responsible for cell cycle proteolytic events. The APC/C which will be discussed later and the Skp1-Cdc53/Cul1-F-box protein (SCF) complex (Chang *et al*, 1996; Patton *et al*, 1998; Willems *et al*, 2004).

Cyclin-dependent Kinases

Reviewed in: Satyanarayana & Kaldis, 2009; Lim & Kaldis, 2013.

Cell cycle progression, specifically the G1/S and G2/M transition, as well as each step of mitosis, is principally regulated by activation and inactivation of cyclin-dependent kinases (CDKs). Consequently, most cell cycle research focuses on how cells regulate CDK function to control cell cycle progression. CDKs are a highly conserved group of serine-threonine kinases whose activity is dependent on their associated cyclin subunits (reviewed in Hochegger *et al*, 2008; Harashima *et al*, 2013). CDK-cyclin complexes are also able to finely regulate the cell cycle by phosphorylating different sets of cell cycle effector proteins. Furthermore, CDK-cyclin complexes themselves are also regulated by inactivating and activating phosphorylation's as well as spatial and temporal regulation and association with other cofactors.

One of the most important regulators of cell cycle progression is the Cdk1-cyclin B complex, whose activation is responsible for triggering mitotic entry (reviewed Lindqvist *et al*, 2009). Prior to mitosis, Cdk1 is inactivated by Myt1 and Wee1 phosphorylation of Cdk1 during S and G phases. Activation is achieved by removal of inhibitory phosphorylation's of Cdk1 at

Thr14 and Tyr15 by the phosphatase Cdc25 (Atherton-Fessler *et al*, 1993; Deibler & Kirschner, 2010). Interestingly, initial Cdk1 activation creates a positive-feedback loop for its activation, as active Cdk1 introduces inactivating phosphorylation's on Myt1 and Wee1 and enhances Cdc25 activity by phosphorylation (Domingo-Sananes *et al*, 2011; Perry & Kornbluth, 2007). Cdk1 also creates a negative-feedback loop for itself by activating the E3 ubiquitin ligase APC/C in association with its coactivator Cdc20, which then ubiquitinates cyclin B for proteasomal degradation. Ultimately, cyclin B degradation which is required for the kinase activity of the Cdk1-cyclin B complex, inactivates the Cdk1 kinase and allows subsequent exit from mitosis (King *et al*, 1995; Hershko, 1999).

1.2 The APC/C

Reviewed in: Alfieri *et al*, 2017; Pines, 2011; Watson *et al*, 2019.

In the early 90s, the anaphase promoting complex or cyclosome (APC/C) was identified as the critical controller of the metaphase-to-anaphase transition (King *et al*, 1995; Sudakin *et al*, 2001). The APC/C is a cullin-RING E3 ubiquitin ligase that polyubiquitinates key substrates to control progression through mitosis and into S phase (Fig 1.1). The core of the APC/C is a 1.2 MDa complex composed of 14 distinct proteins and 19 subunits (Chang & Barford, 2014). The Barford group was the first to solve the complete atomic structure of the APC/C using cryo-electron microscopy (Chang *et al*, 2015). E3 ligases are responsible for the capture and presentation of substrates to E2 ubiquitin-conjugation enzymes which then either mono- or poly-ubiquitinate their substrates signalling them for proteasomal degradation (reviewed in Zheng & Shabek, 2017). The two-best known E2 enzymes are UbcH5 and UbcH10.

The APC/C complex is stable throughout the entire cell cycle however its activity is heavily regulated during mitosis by phosphorylation. Temporal regulation of APC/C activity is mediated by two structurally related co-activators Cdc20 and Cdh1 (reviewed in Yu, 2007; Pesin & Orr-Weaver, 2008; Alfieri *et al*, 2017; Watson *et al*, 2019) (Fig 1.1). Cdc20 and Cdh1 assist the APC/C in substrate recognition, using their WD40 domains to specifically identify KEN boxes, Destruction boxes (D-box), and/or ABBA motifs on substrates (the ABBA motif is only recognised by Cdc20 and *S. cerevisiae* Cdh1) (Clute & Pines, 1999; Pfleger *et al*, 2001; DiFiore *et al*, 2015). The metaphase-to-anaphase transition is mediated by APC/C bound to Cdc20 (APC/C^{Cdc20}). Activation of APC/C^{Cdc20} results in cyclin B (and

therefore Cdk1) and securin degradation. Interestingly APC/C^{Cdc20} activity requires Cdk1-dependent phosphorylation so a negative-feedback loop exists for Cdk1 (Shteinberg *et al*, 1999; Zhang *et al*, 2016b; Fujimitsu *et al*, 2016; Qiao *et al*, 2016). APC/C^{Cdh1} is then activated as Cdk1 is degraded and helps the APC/C to promote mitotic exit through ubiquitinating key substrates including Aurora A/B, Cdc20, and Plk1. Thus, another feedback mechanism occurs by which APC/C^{Cdc20} activates APC/C^{Cdh1} which inactivates Cdc20 activity. APC/C^{Cdh1} further acts throughout G1 phase to promote entry into S phase after which it is inactivated by Cdh1 phosphorylation as well as through the APC/C inhibitor Emi1.

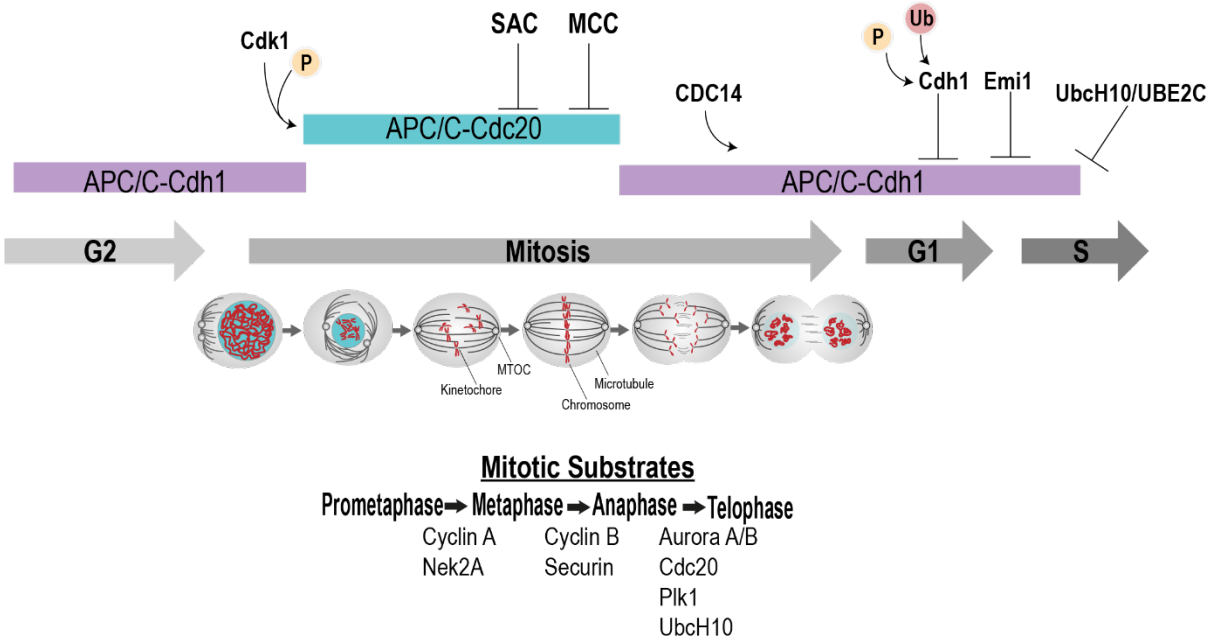

Figure 1.1: The APC/C controls cell cycle progression. *A schematic representation of the cell cycle with key activating and inhibitory steps of APC/C^{Cdh1} and APC/C^{Cdc20}. APC/C ubiquitin-dependent degradation of key mitotic substrates are outlined. Regulation of cell cycle progression by the APC/C occurs primarily through temporal regulation of Cdh1 and Cdc20 activity. APC/C^{Cdc20} is activated during the G2 to M transition by Cdk1-cyclin B phosphorylation and it ubiquitinates cyclin A and Nek2A. During metaphase, APC/C^{Cdc20} is inhibited by the SAC and directly by MCC binding to prevent premature anaphase onset. After reactivation of APC/C^{Cdc20} initiation into anaphase occurs upon cyclin B and securin degradation. Cdh1 is then dephosphorylated by CDC14 which activates APC/C^{Cdh1}. Progression into telophase and exit from mitosis requires APC/C^{Cdh1} ubiquitination of key mitotic substrates including Aurora kinases, Cdc20 and Plk1. APC/C^{Cdh1} is eventually inactivated by Emi1, Cdh1 degradation and Cdk2-cyclin A phosphorylation as well as degradation of its E2 enzymes UbcH10 and UBE2C. Diagram adapted from Zhou et al, 2016.*

1.3 Phosphorylation as a Key Regulatory Mechanism

Reviewed in: Ubersax & Ferrell, 2007; Cohen, 2002

Protein phosphorylation and dephosphorylation is responsible for regulating nearly every aspect of cellular life, including altering the function of proteins in nearly every conceivable

way. For example, phosphorylation can activate or inactive protein activity, alter protein localisation or stability, mark a protein for degradation, and many diseases are the result of abnormal phosphorylation (Fig 1.2).

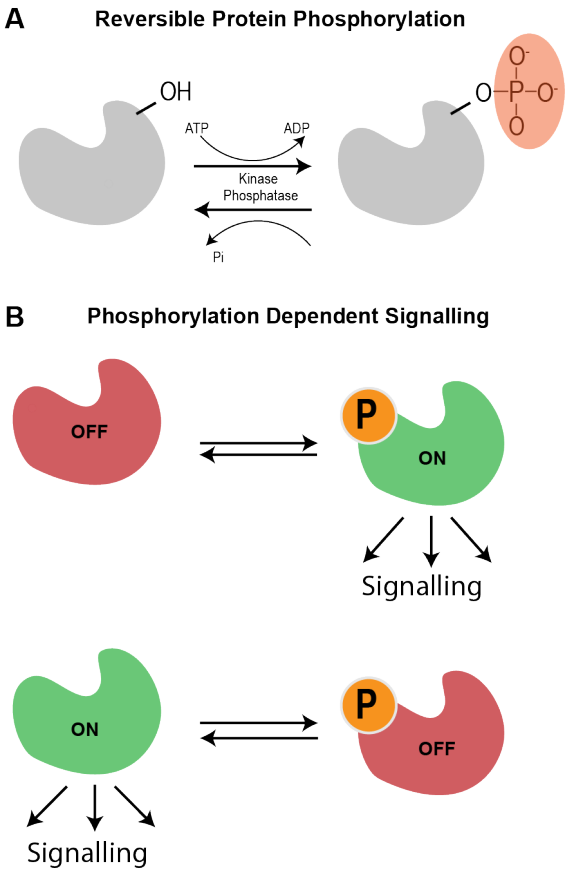

Figure 1.2: Reversible Protein Phosphorylation. (A) *Protein kinases phosphorylate substrates at serine, threonine and tyrosine side chains, a reaction which is ATP dependent. Phosphatases reverse protein phosphorylation and hydrolyse the phosphatase group.* ***(B)*** *Phosphorylation can either active or inactive protein function, often by promoting confirmational changes, or altering binding pockets, and protein-protein interactions.*

Kinases are the enzymes responsible for transferring the terminal (γ) phosphate from ATP to the hydroxyl moiety on the polar 'R' group of the respective amino acid, with nearly all eukaryotic phosphorylation happening on serine, threonine, or tyrosine residues. The addition of the phosphate group importantly changes a small polar group to a negatively-charged group which can drastically alter a proteins structure, including initiating both local and distal confirmational change, and/or regulating how the protein interacts with itself and other proteins, in addition to altering a protein's enzymatic activity. Crucial to the ubiquitous nature of protein phosphorylation is that it is readily reversible as enzymes known as phosphatases can remove the phosphate group via hydrolysis of the phosphoric acid

monoester. Ultimately, this reversibility allows phosphorylation to function as a molecular switch, which can act not only as a signal but also as a signal transducer and amplitude modifier.

1.4 The SAC and EC pathways

The two major cell cycle control mechanisms in mitosis which control the metaphase-to-anaphase transition are the spindle assembly checkpoint (SAC) and the error correction (EC) pathway (Reviewed in Nezi & Musacchio, 2009). Laser ablation studies were used to correlate anaphase onset with complete spindle microtubule capture (Rieder *et al*, 1994). Ablating an unattached kinetochore would initiate anaphase onset even if the chromosome with a destroyed kinetochore was not attached to the spindle. The focus of this thesis will be on the SAC and the regulation and assembly of its effector the mitotic checkpoint complex (MCC). Although the two pathways are separable in their downstream components and functions, they are still heavily interconnected and interdependent in an exceptionally elaborate feedback control mechanism. Notably, the EC pathway must be satisfied before the SAC can be inactivated. Both pathways are mediated through a large macromolecular assembly on centromeres called the kinetochore. Kinetochores act as the attachment point and sensor for microtubule binding (reviewed in Musacchio & Desai, 2017). Unattached or tensionless kinetochores are the base of EC and SAC signalling and importantly the outer layer of the kinetochore is the site of SAC assembly and MCC formation. Ultimately, SAC and EC mediated protection from segregation errors is key to maintaining genome stability across generations.

The EC Pathway

Error correction allows kinetochores to selectively stabilize bioriented chromosome attachments and destabilize erroneous attachments (reviewed in Nezi & Musacchio, 2009). The outer layer of the kinetochore, known as the KMN network, is thought to be responsible for creating load-bearing attachments which can then respond to tension (Cheeseman *et al*, 2006). The lack of tension, associated with lack of biorientation, as in the case of syntelic and merotelic attachments, is thought to be the mechanism by which the EC pathway senses errors. Crucial to error correction is the ability of cells to respond quickly to incorrect attachments and destabilise them, a process which is under the surveillance and control of the Aurora B kinase (Biggins & Murray, 2001; Tanaka *et al*, 2002; Ditchfield *et al*, 2003; Kallio *et al*, 2002; Krenn & Musacchio, 2015). Aurora B inhibition through small-molecule

inhibitors causes stabilisation of incorrect attachments (Hauf *et al*, 2003). Aurora B is a member of the Aurora family of serine/threonine kinases and is the catalytic subunit of the chromosome passenger complex (CPC) (Vader *et al*, 2006; Honda *et al*, 2003; Gassmann *et al*, 2004). In both yeast and humans, it has been demonstrated that phosphorylation of Ndc80 by Aurora B leads to destabilized microtubule binding and a Ndc80 phosphorylation mutant displays severe chromosome segregation defects (DeLuca *et al*, 2006; Wei *et al*, 2007; Guimaraes *et al*, 2008; Cheeseman *et al*, 2002). Besides its key role in the EC pathway, Aurora B is also important for early steps in the SAC pathway. The monopolar spindle 1 (Mps1) kinase, which is arguably the master regulator of SAC signalling, also contributes to EC, however the exact mechanisms remain elusive. Recently the Biggins lab has reported that kinetochore-bound Mps1 phosphorylates Ndc80 to weaken its interaction with microtubules, complementing the well-known activity of Aurora B (Sarangapani *et al*, 2021).

The SAC Pathway

While the EC pathway is more of a 'local' signal, the SAC is a 'global' signal for controlling mitotic exit. The SAC also monitors chromosome attachment to spindle microtubules, but its role is to create a 'wait-anaphase signal' and prevent premature chromatid separation until errors have been corrected. The SAC is now widely thought to be a 'rheostat', having a graded response to the severity of kinetochore-microtubule attachment defects (Maiato *et al*, 2004; Dick & Gerlich, 2013; Collins *et al*, 2003). Like the EC pathway, the SAC is regulated by the kinetochore. The kinetochore senses lack of bio-orientation, mainly through Mps1 kinase localisation to Ndc80 when it is not microtubule-bound. Mps1 then creates a phosphorylation cascade onto the outer kinetochore which generates the 'wait-anaphase signal' by means of the mitotic checkpoint complex (MCC) the SAC effector (reviewed in Kops & Shah, 2012). The MCC binds and inhibits APC/C^{Cdc20} and thereby prevents Cdc20 recognition and ubiquitin-mediated degradation of cyclin B and securin and therefore entry into anaphase. Activation of the SAC is the focus of this thesis and therefore will be discussed in further detail below.

A Tension or Attachment Sensor?

The SAC is persistent until correct bio-orientation of sister chromatids is achieved. It is generally agreed that bi-orientation requires two key events. Correct bi-polar attachment and proper tension. As previously mentioned, attachment sensing was first identified using laser ablation studies (Rieder *et al*, 1995). In the same year tension sensing was suggested as an

alternative mechanism (Li & Nicklas, 1995). Microtubule tension typically refers to the force generated at kinetochores when cohesion between sister chromatid pairs opposes the pulling force of bipolar mitotic spindles. This mechanism is thought to be sensed by Aurora B and the EC pathway (Pinsky & Biggins, 2005). An overview of the different types of attachment and tension errors is outlined in Fig 1.3.

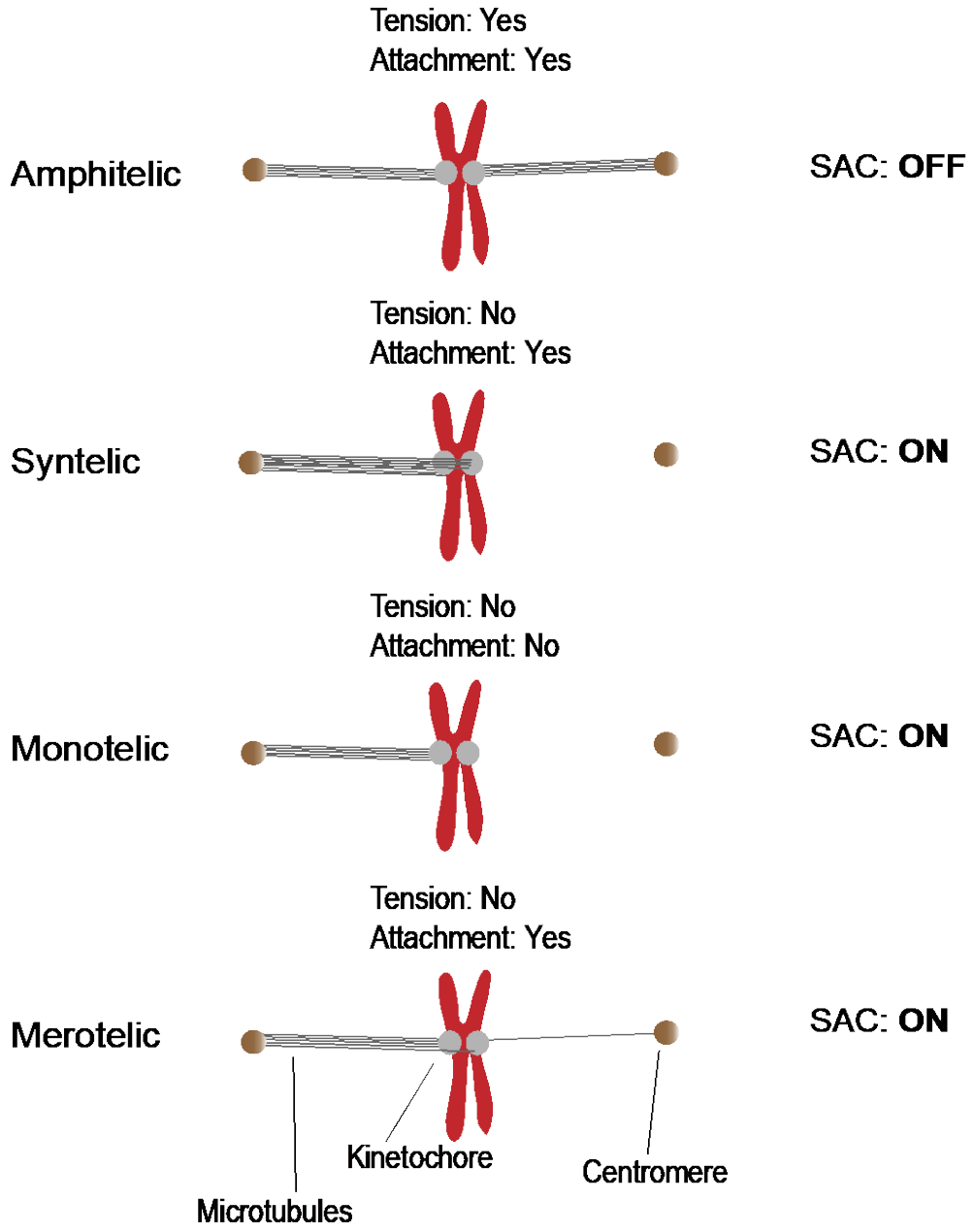

***Figure 1.3: Types of Kinetochore-Microtubule Attachments during Metaphase**. **Amphitelic**: Correct biorientation of sister chromatid. **Monotelic**: Only one sister chromatid is connected to a centromere. **Syntelic**: Both sister kinetochores are attached to a single centromere. **Merotelic**: One or both sister kinetochores are connected to both centromeres instead of one. Both correct tension and attachment are required to satisfy the checkpoint. In the case of syntelic and merotelic attachments, although kinetochores are fully-attached, incorrect tension signals the SAC to stay activated.*

Tension sensing during chromatid separation was first introduced in studies done on grasshopper spermatocytes. Artificial tension was applied to an unattached chromosome resulting in cell cycle progression despite defects in attachment still being present (Nicklas & Koch, 1969). A series of other experiments have provided compelling evidence for the tension model (Li & Nicklas, 1995; Jang *et al*, 1995; Stern & Murray, 2001). The tension model suggests that Aurora B activity is spatially regulated by tension. When there is lack of tension, Aurora B is able to reach its outer kinetochore substrates, including Knl1, Dsn1 and Ndc80. Phosphorylation of these substrates subsequently destabilizes microtubule binding and triggers SAC activation (Welburn *et al*, 2010; Ciferri *et al*, 2008; Cheeseman *et al*, 2006; DeLuca *et al*, 2006).

Important to this mechanism of SAC activation is the N-terminal RVSF motif on Knl1. Normally PP1 binds to this motif and dephosphorylates key downstream substrates required for SAC activation (Liu *et al*, 2010). However, when Aurora B is positioned close enough, it phosphorylates the RSVF motif, displacing PP1 and opposing PP1 silencing of the SAC. Repositioning of Aurora B close to Knl1 also allows Aurora B mediated phosphorylation of the N-terminal tail of Ndc80. This has been shown to enhance Mps1 binding to Ndc80 which is required for SAC activation (Zhu *et al*, 2013).

Sensing a lack of microtubule-kinetochore attachment by the SAC and EC pathways is widely accepted. However, an unattached kinetochore with a monotelic attachment is also lacking tension. Therefore, unattachment and tension can occur simultaneously making it difficult to distinguish how the SAC senses errors. Furthermore, understanding how tensionless kinetochores are sensed in syntelic and merotelic attachments is still today a highly debated topic (London & Biggins, 2014a; Nezi & Musacchio, 2009; Khodjakov & Pines, 2010; Maresca & Salmon, 2010). Specifically, the direct result of tension sensing is unclear. Microtubules which are under reduced tension due to incorrect attachments are destabilized by the EC pathway which results in a tensionless and unattached kinetochore state. It is debated whether the kinetochore then activates the SAC, i) directly by allowing the SAC phosphorylation cascade, ii) indirectly by producing an unattached kinetochore or iii) delaying anaphase onset via an independent pathway (Proudfoot *et al*, 2019). The timing of these events remains especially elusive.

1.5 Kinetochore Assembly and Function

Kinetochores are the macromolecular machines which exist at the centromere of sister chromatids. Kinetochores consists of over 80 proteins which create the interface between microtubules and chromosomes (Musacchio & Desai, 2017) (Fig 1.4). Kinetochores are also the signalling hub required to create communication between the state of microtubule attachment and SAC activity (reviewed in Foley & Kapoor, 2013). In mammalian cells, approximately 30 spindle attachments are thought to occur for each kinetochore. This is in contrast to fission yeast which makes 2-4 attachments and budding yeast where only one attachment occurs (Biggins, 2013; Pidoux & Allshire, 2004). This simplicity makes budding yeast the organism of choice for many kinetochore studies.

The Inner Layer

In vertebrates, kinetochore assembly first requires formation of the inner layer after which the outer layer assembles (reviewed in Amor *et al*, 2004; Perpelescu & Fukagawa, 2011) (Fig 1.4). The inner layer of the kinetochore associates with a unique genetic locus on the chromosome named the centromere where there is enrichment of the histone H3 variant Cenp-A (Palmer *et al*, 1987). Centromeres can be millions of base pairs long in metazoans (reviewed in Fukagawa & Earnshaw, 2014). This inner layer, also known as the constitutive centromere-associated network (CCAN) associated with CENP-A, is composed of at least 16 subunits, and is the basis for outer layer assembly (Fig 1.4). The structure of CCAN in complex with the CENP-A nucleosome was recently solved (Yan *et al*, 2019).

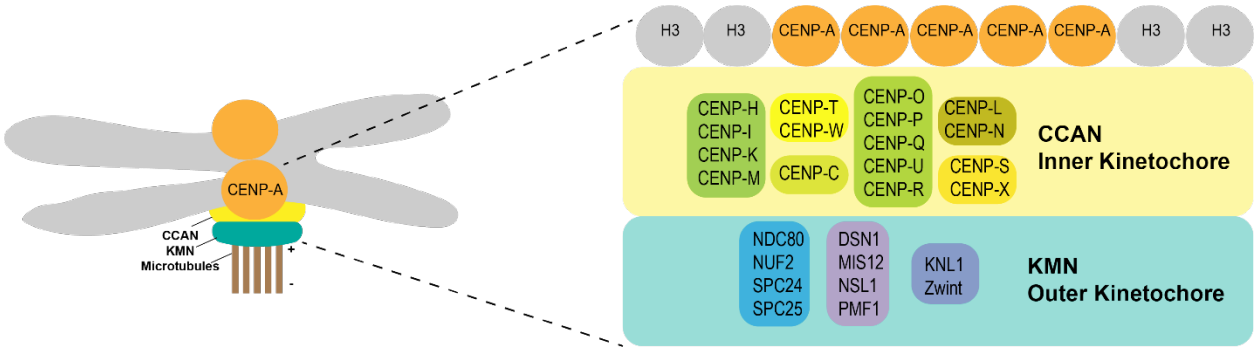

Figure 1.4: Schematic summary of the inner and outer layer of human kinetochores. *The composition of the inner and outer layer is outlined. Conserved complexes are grouped by colour. In humans, participation of several Cenp-A nucleosomes at kinetochores occurs as compared to budding yeast where only one Cse4 nucleosome participates. The outer kinetochore is the basis for attachment to plus-end microtubules which is required for sister-chromatid biorientation and separation.*

The Outer Layer

The outer layer of the kinetochore, is a 10-subunit assembly, comprised of three conserved subcomplexes known as the **K**NL1 (Spc105/Blinkin) complex (Knl1-C), the **M**is12 (Mtw1) complex (Mis12-C), and the **N**dc80 (Hec1) complex (Ndc80-C), and has been termed the KMN network (Fig 1.4). The KMN network binds to the inner layer through contacts with both Cenp-T and Cenp-C. Cenp-T binds to Ndc80C and Mis12C upon Cdk1 phosphorylation (Gascoigne & Cheeseman, 2013; Nishino *et al*, 2013; Rago *et al*, 2015). While Dsn1 phosphorylation by Aurora B stimulates the Cenp-C and Mis12-C interaction (Dimitrova *et al*, 2016; Petrovic *et al*, 2016; Kim & Yu, 2015). The KMN is also responsible for kinetochore-microtubule attachments by making several contacts with microtubules (Cheeseman *et al*, 2006). It has been suggested that the binding of a single microtubule requires as many as 20 KMN complexes. The KMN network is therefore the bridge which connects centromeres to microtubules and is responsible for proper microtubule binding and stabilisation. A partial, low resolution EM structure of the KMN core complex has been solved (Petrovic *et al*, 2014b), as well as several partial structure of Ndc80-C components (Ciferri *et al*, 2008; Valverde *et al*, 2016). However, because the KMN complex is highly elongated and flexible a full-length structure has yet to be determined.

Mis12-C

Mis12-C is composed of Dsn1/Mis13, Mis12/Mtw1, Nnf1 and Nsl1/Mis14, and is responsible for tethering the inner and outer kinetochore through interaction with the N-terminus of Cenp-C (Screpanti *et al*, 2011; Przewloka *et al*, 2011) and CENP-U in *S. cerevisiae*. Mis12 then recruits Ndc80-C and Knl1-C (Hornung *et al*, 2011; Kline *et al*, 2006; Maskell *et al*, 2010; Petrovic *et al*, 2010; Wan *et al*, 2009).

Ndc80-C

Ndc80-C components include Ndc80/Hec1, Nuf2, Spc25, Spc24. Ndc80 and is composed of a highly elongated coiled-coil of approximately 55 nm in length (reviewed in Ciferri *et al*, 2007). Ndc80-C contains two globular regions at either end. On one end, the N-terminal domains of Ndc80 and Nuf2 form calponin homology (CH) domains which bind to microtubules (Ciferri *et al*, 2008; Wei *et al*, 2007; Gimona *et al*, 2002; Slep & Vale, 2007). The N-terminus also contains a positively charged unstructured tail which is thought to enhance microtubule binding (Wei *et al*, 2007; Ciferri *et al*, 2008; Guimaraes *et al*, 2008). Importantly, it is this unstructured region of Ndc80 which is phosphorylated by Aurora B in early mitosis to promote error correction through destabilisation of incorrect microtubule-

kinetochore attachments (DeLuca *et al*, 2006; Biggins & Murray, 2001; Tanaka *et al*, 2002; Pinsky *et al*, 2006). On the other end of Ndc80-C lies the Spc24 and Spc25 heterodimer, each possessing an RWD domain that mediates kinetochore targeting (Dimitrova *et al*, 2016; Cheeseman *et al*, 2006; Ciferri *et al*, 2008). The Spc24 and Spc25 heterodimer also form additional contacts to the inner kinetochore layer through Cenp-T (Nishino *et al*, 2013; Huisin'T Veld *et al*, 2016).

Knl1-C

Reviewed in: Caldas & DeLuca, 2014.

The Knl1 complex is composed of Knl1 with Zwint bound at its C-terminus. A crystal structure of a C-terminal truncation of Knl1 shows a tandem repeat of two RWD domains connected by a 32 amino acid helix where Zwint binds (Petrovic *et al*, 2014b). Secondary structure predication suggests this is the only globular domain of the entire 265 kDa protein. Knl1-C mediated by Zwint contacts Mis12-C subunit Nsl1 for kinetochore targeting (Varma *et al*, 2013). Apart from helping to bridge the interaction between microtubules and kinetochores, the Knl1-C is crucially the base for assembly of SAC components which trigger formation of the mitotic checkpoint complex (Kiyomitsu *et al*, 2007; London *et al*, 2012; Primorac *et al*, 2013; Yamagishi *et al*, 2012; Rosenberg *et al*, 2011; Shepperd *et al*, 2012). MCC assembly is controlled by Ndc80-bound Mps1 which creates a catalytic phosphorylation cascade which assembles the MCC on to Knl1. Knl1-C is also implicated in microtubule binding at its N-terminus, to a charged patch (^{16}ERPVRRRH^{23}) just N-terminal to the SILK PP1 binding motif, although the specific role of this KNL1:MT interaction as compared to Ndc80-C:MT interaction is unknown (Espeut *et al*, 2012). As previously mentioned, PP1 also binds to the N-terminus of KNL1, specifically KNL1 has three PP1-specific interaction motifs, the ^{25}SILK^{28}, ^{58}RVSF^{61} and ^{68}FQ^{69} motifs (Choy et al., 2014). It has been shown that MTs and PP1 bind in a mutually exclusive manner in human cells, as the MT binding site overlaps with the SILK PP1 binding site. PP1 has a much higher affinity for KNL1 than MTs, and therefore displacement of MT binding during PP1 signalling is thought to be an additional sensor for microtubule-kinetochore attachment and initiation of SAC silencing (Bajaj *et al*, 2018; Welburn *et al*, 2010; Rosenberg *et al*, 2011).

1.6 The Mitotic Checkpoint Complex (MCC)

Reviewed in Liu & Zhang, 2016; Dou *et al*, 2019; Lara-Gonzalez *et al*, 2021b.

The MCC is the effector of the SAC which inhibits APC/C^{Cdc20} until correct kinetochore-microtubule attachments have occurred. Once proper bio-orientation is achieved, the production of MCC ceases and existing MCC is disassembled resulting in reactivation of APC/C^{Cdc20} and progression into anaphase.

Molecular Architecture of the MCC

The MCC was first purified as a complex in 2001, from Hela cell lysates and found to be composed of BubR1, Bub3, Cdc20 and Mad2 (Sudakin *et al*, 2001) (Fig 1.5). Figure 1.6 includes a schematic diagram of each MCC component and their respective domains. Their discovery was made by fractionating mitotic cell lysates in search of APC/C inhibitors. Around the same time other groups also confirmed the importance of these proteins in APC/C inhibition and anaphase entry (He *et al*, 1997; Fang *et al*, 1998; Hardwick *et al*, 2000; Li *et al*, 1997). All four components are highly conserved, although BubR1 in vertebrates arose out of several genome duplication events and whether Bub3 is required for proper MCC assembly and function is debated (Suijkerbuijk *et al*, 2012; Vleugel *et al*, 2012). In fact, fission yeast MCC does not seem to contain Bub3 (Sczaniecka *et al*, 2008). It is important to note that Cdc20 in the MCC (Cdc20^{MCC}) is a separate Cdc20 molecule from the co-activator Cdc20 of APC/C^{Cdc20} (Cdc20$^{APC/C}$) (Izawa & Pines, 2015). Several structures of the MCC alone or in complex with APC/C^{Cdc20} exist and have been fundamental to our understanding of how MCC inhibits the APC/C (Alfieri *et al*, 2016; Chao *et al*, 2012; Yamaguchi *et al*, 2016) (Fig 1.5).

Bub-related kinase 1 (BubR1) is the largest protein in the MCC and has numerous domains important for MCC assembly and inhibition (Fig 1.6). A complex combination of biochemical studies and structural analyses were required to determine how each motif contributes to MCC function. BubR1 binds Mad2 through an N-terminal tetratricopeptide repeating (TPR) domain. The KEN1, TPR, ABBA (A2), and D-box (D2) motifs interact with Cdc20^{MCC}. A second set of KEN and Abba motifs (KEN2 and A1) as well as a D-box (D1) interact with Cdc20$^{APC/C}$ (Alfieri *et al*, 2016) (Fig 1.6). This BubR1 interaction with APC/C bound Cdc20 forms the basis by which the MCC blocks APC/C^{Cdc20} activity through pseudo-substrate recognition. BubR1 also contains a pseudo-kinase domain at its C-terminus. Bub3, bound to the GLEBS motif of BubR1, is made up of seven WD40 repeats that form a β-propeller arrangement, however Bub3 is never seen in structures of the MCC suggesting it is flexibly tethered to BubR1 (Larsen & Harrison, 2004; Larsen *et al*, 2007). The MCC also

inhibits the catalytic activity of the APC/C by blocking UbcH10 binding to the catalytic module (Alfieri *et al*, 2016).

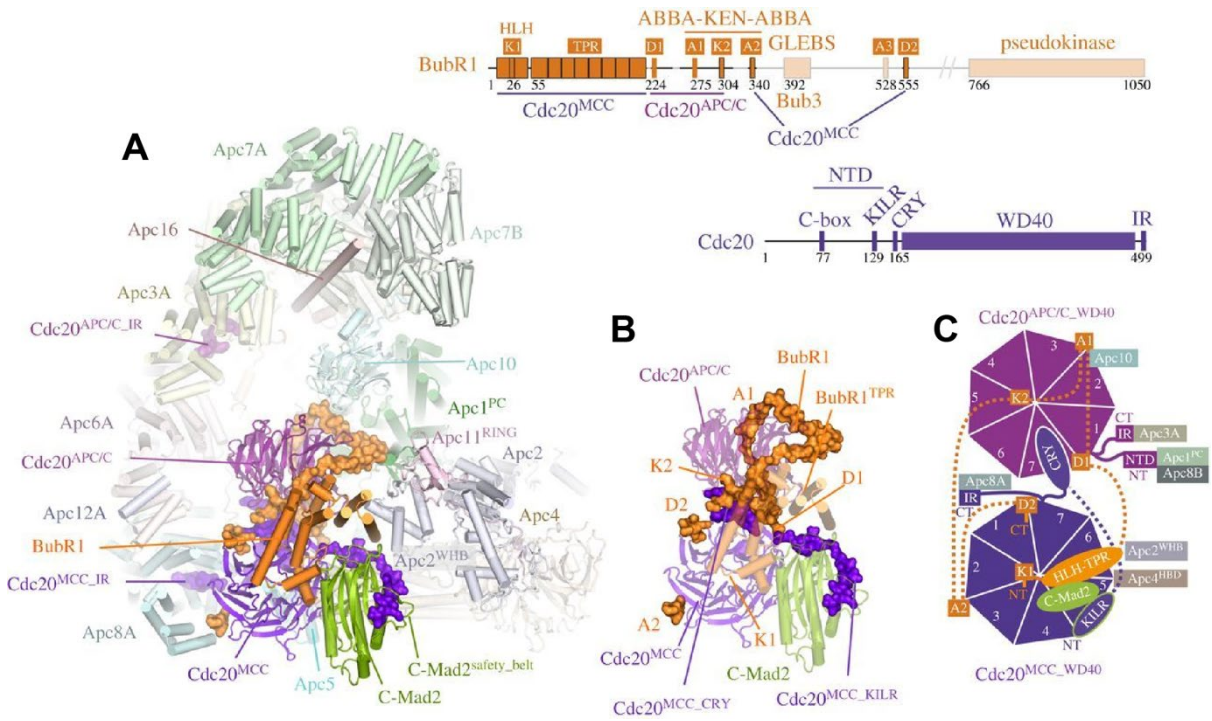

Figure 1.5: The APC/C^{MCC} Interaction. (A) *A cryo-EM reconstruction of APC/C^{MCC}. PDB 5LCW, from Alfieri et al, 2016.* ***(B)*** *Model of MCC with the extensive interactions between Cdc20^{MCC} and BubR1 highlighted.* ***(C)*** *Outlines the multifaceted interactions formed between the two Cdc20 molecules and their interactions with the APC/C and BuBR1. At the top, a schematic representation of BubR1 and Cdc20 domains is highlighted. This figure was taken with permission from Alfieri et al, 2017.*

Like Bub3, **Cdc20** contains a WD40 7-beta propeller domain which binds to KEN-boxes, D-boxes, and ABBA motifs in distinct positions on its β-propeller (Tian *et al*, 2012; Chao *et al*, 2012) (Fig 1.5 & Fig 1.6). N-terminal to the WD40 domain, Cdc20 includes a KILR/MIM motif which contributes to APC/C binding through binding to Apc8 and while part of the MCC selectively binds to C-Mad2 (Luo *et al*, 2002; Izawa & Pines, 2012) (Fig 1.5 & Fig 1.6). Cdc20 also comprises a central KEN box and CRY box which facilitates its own degradation by APC/C^{CDH1} to allow exit from mitosis into G1 and S phases (Pfleger *et al*, 2001; Reis *et al*, 2006) (Fig 1.6).

Mad2 is a HORMA domain containing protein which adopts both an inactive open (O-Mad2) and active closed (C-Mad2) confirmation. Conversion of Mad2 from the open-to-closed state is required for entrapment of the MIM of Cdc20 motif. This process is the rate-limiting step of MCC assembly and will be discussed thoroughly later on. When Mad2 is in the closed

confirmation, it rapidly binds Cdc20, after which both Mad2 and Cdc20 have high affinity for BubR1 and the MCC forms spontaneously.

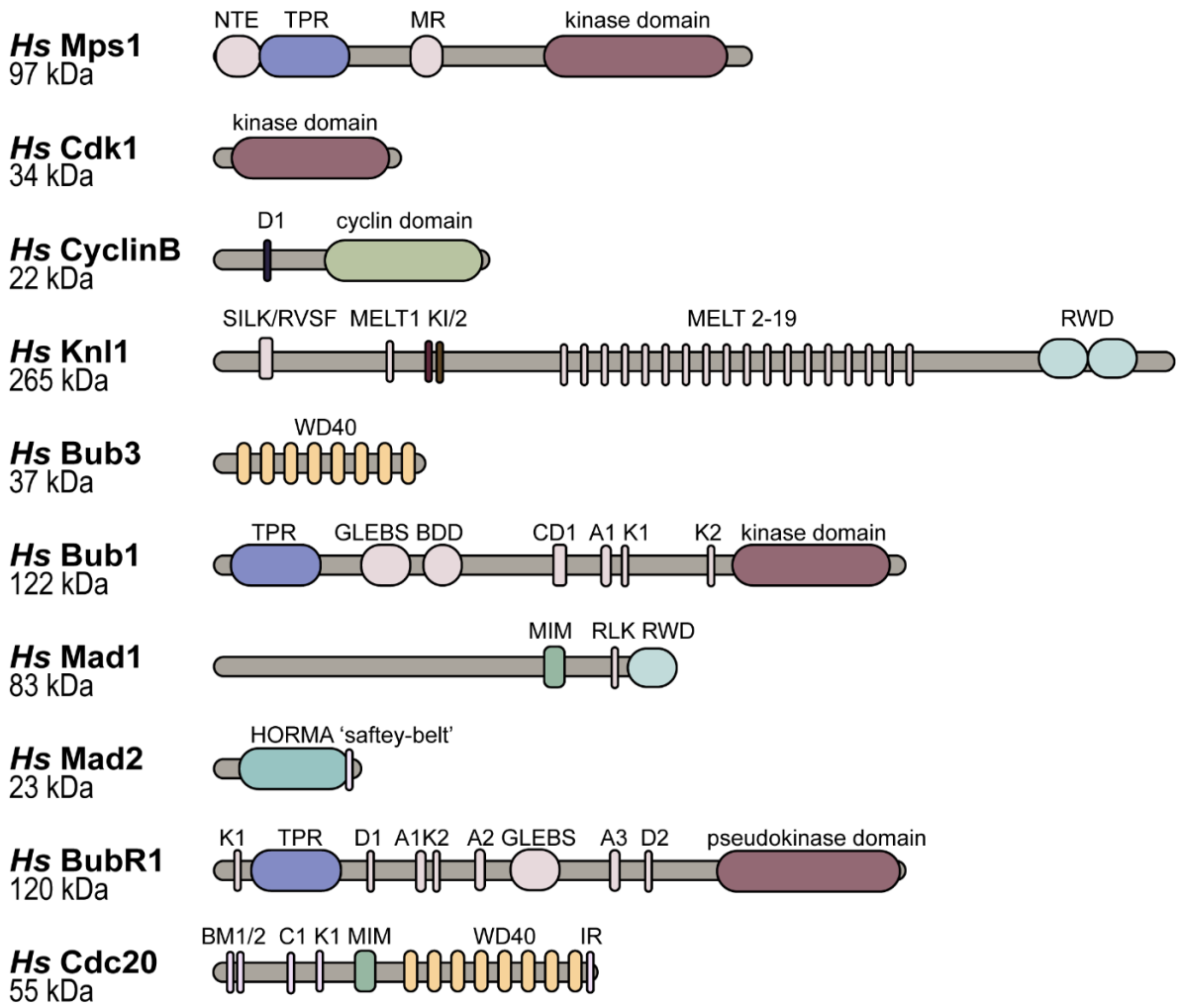

Figure 1.6: Domains of SAC proteins. *Schematic diagram of components of the MCC and proteins required for MCC assembly onto the outer kinetochore are shown. Important domains in SAC signalling are outlined in coloured ovals.*

MCC Inhibition of APC/C

The critical function of the MCC is to prevent ubiquitination of cyclin B and securin by APC/C^{Cdc20}. Cdc20 bound to APC/C is the target of the MCC (Hwang *et al*, 1998; He *et al*, 1997). The MCC targets Cdc20 by directly binding to the APC/C and blocking the substrate recognition site of the Cdc20 co-activator molecule and thereby preventing APC/C substrate ubiquitination (Herzog *et al*, 2009; Alfieri *et al*, 2016; Yamaguchi *et al*, 2016; Izawa & Pines, 2015) (Fig 1.5). As previously mentioned, BubR1 has a N-terminal KEN box motif that is normally recognized by APC/C^{Cdc20} as a degron. However, BubR1 uses this degron to act as a pseudo-substrate inhibitor, blocking APC/C^{Cdc20} from recognising other substrates (Lara-

Gonzalez *et al*, 2011; Chao *et al*, 2012; Tang *et al*, 2001; Burton & Solomon, 2007; Sczaniecka *et al*, 2008; Han *et al*, 2013). Key to the ability of BubR1 to do this, is Mad2, which helps to position the KEN-box of BubR1 to bind APC/C^{Cdc20}. Furthermore, Apc10 usually contributes to Cdc20 substrate recognition and the structure of APC/C$^{Cdc20:MCC}$ shows that Apc10 gets displaced away from the substrate-recognition site upon MCC binding (Alfieri *et al*, 2016) (Fig 1.5).

1.7 Activation of the MCC

The SAC is a highly regulated signal transduction cascade under the surveillance and function of several kinases, including Aurora B, Cdk1, and Mps1, as well as the phosphatases, PP1 and PP2A (Saurin, 2018). The activation and action of these enzymes, in particular Mps1 which is at the apex of SAC signalling, is responsible for triggering MCC assembly onto the outer kinetochore. This requires a remarkably complex network of interactions which control kinase and phosphatase localization and activity states to finely tune the signalling cascade.

Mps1 is the master regulator of MCC assembly onto kinetochores. Mps1 is required for checkpoint activity and kinetochore localization of almost all proteins involved in MCC formation (Weiss & Winey, 1996; Abrieu *et al*, 2001; Tighe *et al*, 2008; Nijenhuis *et al*, 2013; Zhu *et al*, 2013; Zich *et al*, 2012; Hardwick *et al*, 1996). Over expression of Mps1 can activate the checkpoint even in the presence of intact kinetochore-microtubule attachments. This occurs through hyperphosphorylation of Bub1 and Mad1 (Hardwick *et al*, 1996). Additionally, Mps1 persistence at the kinetochore, such as through KMN tethering, delays anaphase onset and can induce cell death (Jelluma *et al*, 2010). Furthermore, inhibiting Mps1 by adding reversine, a selective inhibitor of Mps1 kinase activity, impedes localisation of all downstream checkpoint proteins and creates a defective checkpoint (Maciejowski *et al*, 2010; Sliedrecht *et al*, 2010; Vigneron *et al*, 2004).

Localisation of Mps1

Ndc80 is believed to be the direct receptor of Mps1 at kinetochores (Stucke *et al*, 2004; Martin-Lluesma *et al*, 2002). Importantly, Mps1 localisation is thought to be a sensor for microtubule attachment as Mps1 can only interact with Ndc80 when it is not bound to microtubules through a mutually exclusive binding site (Ji *et al*, 2015; Hiruma *et al*, 2015). This suggests that in parallel to the EC pathway, the SAC signalling pathway also senses the

state of microtubule-kinetochore attachments. Although Ndc80 is believed to be directly responsible for Mps1 localisation, the precise mechanisms by which Mps1 is localised upon SAC initiation is still debated. Mps1 contains a N-terminal extension (NTE) which is responsible for kinetochore targeting by binding to the N-terminal Ndc80 CH domain (Ji *et al*, 2015). Inhibition of Aurora B also prevents Mps1 recruitment, while tethering Mps1 bypasses the SAC assembly requirement for Aurora B (Saurin *et al*, 2011). One suggested model for how Aurora B might be responsible for Mps1 kinetochore targeting is by phosphorylating the Ndc80 CH domain which then enhances Mps1 binding (Zhu *et al*, 2013). Another possibility is that Aurora B phosphorylates the Mps1 NTE to relieve autoinhibition (Nijenhuis *et al*, 2013; Combes *et al*, 2018; Lee *et al*, 2012).

1.8 Mps1 Phosphorylation-dependent MCC Assembly

Proper kinetochore localisation of Mps1 triggers assembly of all other pre-MCC components and ultimately catalyses MCC formation. How kinetochores and specifically Mps1 kinase activity recruits checkpoint proteins and how phosphorylation of each protein contributes to localisation and stimulation of downstream components is a major question in understanding mechanisms of SAC regulation. Cellular levels of MCC are finely-tuned through a balance of assembly and disassembly of the MCC (Kulukian *et al*, 2009). MCC assembly is a thermodynamically favourable reaction, but it has an extremely low rate of spontaneous formation (Faesen *et al*, 2017). MCC is known to form within minutes in the cell, a process which is dramatically accelerated by unattached kinetochores (Dick & Gerlich, 2013; Clute & Pines, 1999; Hagting *et al*, 2002). Therefore, how MCC formation is catalysed is also a question of major importance.

Key to this is the hierarchical recruitment of SAC proteins onto the outer kinetochore, which then creates a catalytic platform for MCC formation. The rate-limiting step of MCC formation is believed to be the conversion of Mad2 from an inactive open state into an active closed state which requires the Mad1:C-Mad2 platform (Luo *et al*, 2004; Simonetta *et al*, 2009; Faesen *et al*, 2017). Apart from C-Mad2 production, the spatial proximity of MCC subunits, guided by protein-protein interactions, is required for efficient assembly. The next section will discuss the mechanisms by which Mps1 phosphorylation localises, catalytically activates, and repositions pre-MCC and MCC components in a highly effective and stepwise manner.

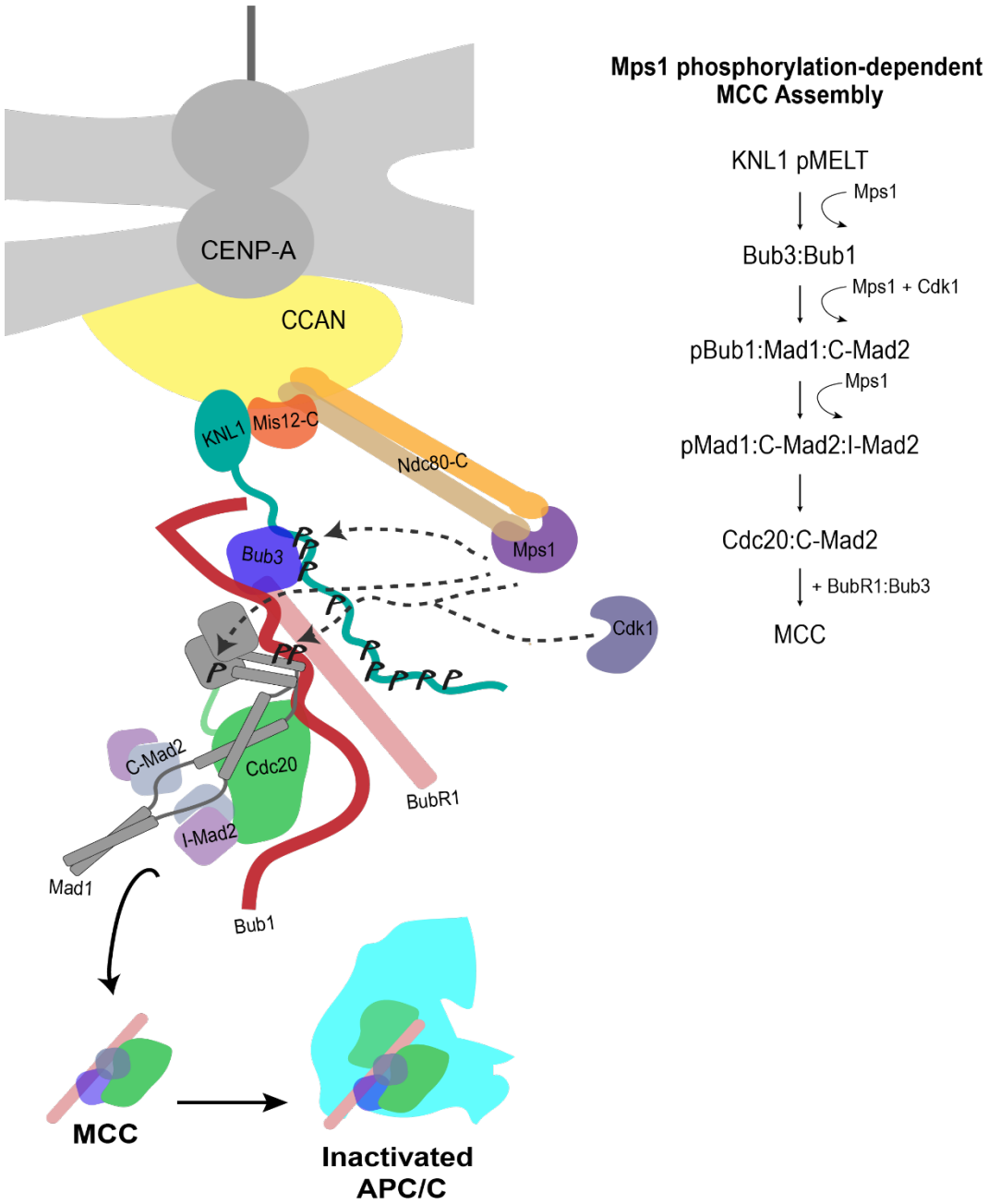

Figure 1.7: Stepwise assembly of the MCC. *On the left is a schematic model of MCC assembly onto the outer kinetochore. On the right is an outline of the essential steps in MCC assembly. Mps1 phosphorylates the outer kinetochore protein Knl1, which recruits Bub3 bound to Bub1. Mps1 and Cdk1 then phosphorylate Bub1, targeting Mad1:C-Mad2. Mps1 also phosphorylates the C-terminal head domain of Mad1 to promote an interaction with Cdc20. Cytosolic O-Mad2 is targeted to the Mad1:C-Mad2 complex, by self-dimerization, forming a Mad1:C-Mad2:I-Mad2 complex, where I-Mad2 stands for an intermediate Mad2 state. I-Mad2 then converts to C-Mad2 and which rapidly binds Cdc20 and BubR1 to form the MCC.*

Steps of MCC Assembly

Refer to Fig 1.7 for a schematic outline of MCC assembly onto kinetochores. Mps1 bound to Ndc80 is able to phosphorylate several MELT (methionine-glutamate-leucine-threonine) motifs on Knl1 (London *et al*, 2012; Bollen, 2014; Yamagishi *et al*, 2012). These

phosphorylated MELTs (MELpTs) then form the base of MCC assembly by recruiting Bub3 which is already bound to Bub1 and BubR1 (Petrovic *et al*, 2014b; Primorac *et al*, 2013; Zhang *et al*, 2014; Vleugel *et al*, 2013; Shepperd *et al*, 2012; Kiyomitsu *et al*, 2007). It is important to note that how BubR1 is targeted to kinetochores is debated, as it has been shown that BubR1 is also recruited through dimerization with Bub1, a topic which will be discussed later (Overlack *et al*, 2015).

Mps1 then phosphorylates the conserved domain 1 (CD1) of Bub1 at Thr461, after being primed by Cdk1 phosphorylation at Ser459 (Kim *et al*, 2012; London & Biggins, 2014a; Ji *et al*, 2017; Zhang *et al*, 2017). Doubly phosphorylated Bub1 then recruits the tetrameric Mad1:C-Mad2 complex through interaction with the Mad1 RLK motif. Mad1:C-Mad2 subsequently acts as the platform for conversion of cytosolic open-Mad2 into closed-Mad2 through self-dimerization and a template conversion mechanism (De Antoni *et al*, 2005; Mapelli *et al*, 2007; Sironi *et al*, 2002). Bub1 and/or BubR1 then recruit Cdc20, and the Bub1 kinase modifies Cdc20 by phosphorylation (DiFiore *et al*, 2015; Diaz-Martinez *et al*, 2015; Luo *et al*, 2004; Jia *et al*, 2016; Lischetti *et al*, 2014). The exact recruitment pathway of Cdc20 is also debated as Bub1 and BubR1 both contain multiple different Cdc20 binding motifs, several of which are required for checkpoint signalling. However, because Bub1 modifies Cdc20 and the Cdc20:C-Mad2 complex is first required for binding of both to BubR1, it seems more likely that Bub1 first targets and positions Cdc20 close to Mad1:C-Mad2 for binding to the newly converted C-Mad2 which then binds BubR1.

Interestingly, two recent studies have also shown a direct interaction of $Mad1^{CTD}$ with the N-terminal tail of Cdc20 which is dependent on Mps1 phosphorylation of the Mad1 C-terminus (Ji *et al*, 2017; Piano *et al*, 2021). This bipartite anchorage might optimally position the MIM of Cdc20 to O-Mad2 bound to Mad1:C-Mad2 promoting the Cdc20:C-Mad2 interaction. Finally, in the last step of MCC assembly, C-Mad2 is passed onto Cdc20 to form the Cdc20:C-Mad2 complex which has high affinity for the BubR1:Bub3 complex. This soluble MCC complex then targets and inhibits APC/C^{Cdc20}.

1.9 Knl1 MELT Motifs

As previously mentioned, Knl1 is phosphorylated by Mps1 at its conserved MELT motifs ([M/I/L/V]-[E/D]-[M/I/L/V]-pT) which then act as a recruitment platform for Bub3:Bub1 and possibly BubR1:Bub3 (London *et al*, 2012; Yamagishi *et al*, 2012; Shepperd *et al*, 2012) (Fig

1.8). Subsequently, MELT phosphorylation mutants at threonine position 4, create a defective checkpoint. Binding occurs through the methionine and phosphorylated threonine of the MELpT sequence which dock onto the hydrophobic and basic patches of Bub3 respectively (Primorac *et al*, 2013). Interestingly the number of MELT copy numbers within Knl1 across organisms varies substantially, suggesting that Knl1 is a rapidly evolving protein (Tromer *et al*, 2015; Vleugel *et al*, 2013, 2012). Human Knl1 has 19 MELT-like motifs as compared to *S. pombe* (Spc7) which has 8, and *S. cerevisiae* (Spc105) which only has 5. Not all MELT motifs have the same activity towards Bub3 recruitment (Vleugel *et al*, 2015). In humans it is suspected that 6-7 MELTs bind Bub3 during a fully active SAC (Nijenhuis *et al*, 2013) (Fig 1.8A).

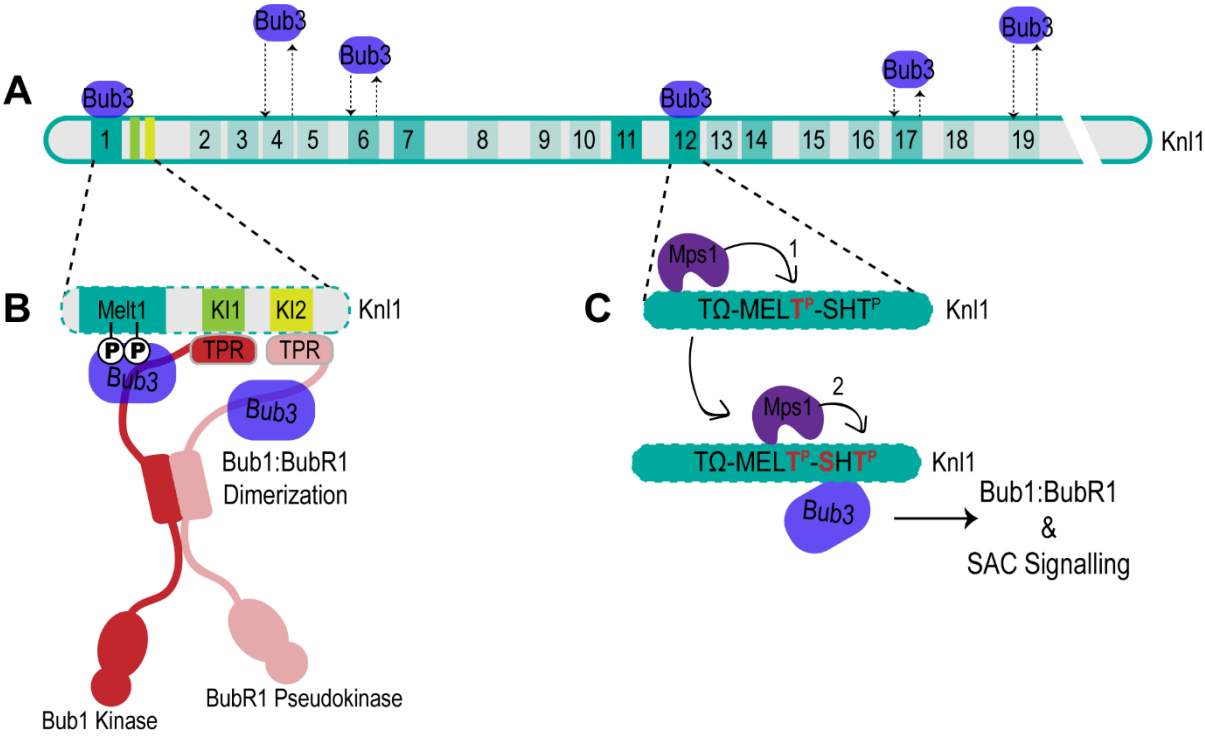

Figure 1.8: Knl1 MELTs and the KI1 and KI2 motifs in SAC signalling. (A) *A schematic depiction of Knl1 with 19 MELT repeats. The activity of each MELT, as defined by the ability of the MELT to recruit the Bub3:Bub1 complex for SAC signalling, corresponds to a colour gradient (the darker the more active* (Vleugel *et al*, 2015)*. The strength of the Bub3 (blue) and MELT interaction is also depicted by the arrow length.* ***(B)*** *A close up of the N-terminus of Knl1 where MELT1 is immediately proceeded by the KI1 and KI2 motifs which bind to the TPR lobes of Bub1 and BubR1, respectively. This mechanism enhances Bub1/BubR1 recruitment and is unique to some metazoans including humans.* ***(C)*** *Strong repeat activity requires sequential multisite phosphorylation of the Knl1:Bub3 interface by Mps1. Mps1 first phosphorylates the threonine MELT residue which enhances Mps1 phosphorylation at the SHT motif. Strong recruiters of Bub3:Bub1 require the SHT to enhance the Bub3:MELT interaction.*

In humans, 10 MELTs have a N-terminal TxxΩ motif (x, any amino acid; Ω, aromatic) which is critical for Bub1 recruitment by an unknown mechanism (Vleugel *et al*, 2013) (Fig 1.8C).

The most active MELTs also have an indispensable SHT motif C-terminal to the MELT (Vleugel *et al*, 2015) (Fig 1.8C). This SHT motif, first recruits Mps1 and its phosphorylation primes MELT phosphorylation and Bub3 recruitment. This mechanism is thought to be unique to vertebrate Knl1. Furthermore, in vertebrate orthologs, the N-terminal most MELT, MELT1, has two 12 residue upstream KI motifs which can recruit Bub1 and BubR1 TPR lobes (Kiyomitsu *et al*, 2007; Bolanos-Garcia & Blundell, 2011; Krenn *et al*, 2012) (Fig 1.8B). However, KI motif mutants do not abolish Bub1/BubR1 kinetochore localization and are not required for the checkpoint (Krenn *et al*, 2012; Yamagishi *et al*, 2012). Detailed analyses have shown that KI motifs are MELT enhancers, making MELT1 the strongest recruiter of Bub1:Bub3 and the only MELT which can sustain the SAC by itself (Krenn *et al*, 2014). Therefore, it is suggested that MELT1 and its KI motifs can recruit Bub1/BubR1 when their kinetochore levels are low, enabling efficient SAC activation when no or only mild defects are present. Overall, the abundance of MELTs and the difference in their affinities suggests a mechanism by which eukaryotic cells are able to control the strength of SAC signalling in various scenarios of segregation errors.

1.10 Bub1 and BubR1 Kinetochore Targeting

Bub1 and BubR1 evolved from several duplication events with a common ancestral gene (Vleugel *et al*, 2012). They share similar domains, including TPR, GLEBS, KEN, and ABBA motifs, and yet have very different roles in SAC signalling (Fig 1.6). Both Bub1 and BubR1 form stable mutually exclusive complexes with Bub3, both using the GLEBS domain (Wang *et al*, 2001; Larsen *et al*, 2007). Initially, it was thought that both Bub1 and BubR1 were recruited to Knl1 through Bub3. However, Bub3 was not found to be essential for BubR1 recruitment and BubR1 does not stabilize the Bub3-Knl1 interaction as Bub1 does (Primorac *et al*, 2013; Krenn *et al*, 2014). This is because Bub1 contains a loop upstream of the GLEBS Bub3 binding domain which enhances Bub3 binding to phosphorylated MELTs on Knl1 (Overlack *et al*, 2015). Interestingly the same loop in BubR1 is required for enhancing the ability of the MCC to inhibit APC/C^{Cdc20} (Zhang *et al*, 2016a). This suggests alternative recruitment methods are present for BubR1.

Subsequently, it was discovered that Bub1 and BubR1 form a tight dimer at kinetochores through a novel domain in the centre of each (Overlack *et al*, 2015) (Fig 1.6). Cells which lack the Bub1:BubR1 interaction still have an active but impaired SAC (Zhang *et al*, 2016a). Interestingly, the Bub1:BubR1 complex is conserved in fission yeast where Mad3 (BubR1) is

able to dimerize with Bub1 using their tetratricopeptide repeat (TPR) domains instead (Leontiou *et al*, 2019). The TPR domains in human Bub1 and BubR1 are not involved in their dimerization. Even more elusive to how Bub1 and BubR1 are recruited for SAC signalling in humans was the previously mentioned discovery that the N-terminus of Knl1 has two lysine-isoleucine (KI) motifs which are conserved in only a few vertebrates, and of which binds to the TPR motifs of Bub1 and BubR1 (Ghongane *et al*, 2014; Krenn *et al*, 2014) (Fig 1.8B).

Therefore, these results suggest that multiple pathways for BubR1 recruitment exist, which may be redundant or may be used in specific circumstances. Because Bub1 and BubR1, like Knl1 are fast evolving proteins with several recent gene duplication events, it may be that certain localization pathways are remnants of ancestral organisms. Further work into Bub1 and BubR1 localization will be necessary to complete our understanding of the SAC signalling cascade.

1.11 The ABBA and KEN motifs of Bub1

Bub1 contains a N-terminal TPR domain, followed by a GLEBS motif, BubR1 dimerization domain, CD1 domain, and a C-terminal kinase domain. Bub1 also contains three Cdc20 binding sequences. In the centre of Bub1 there is an ABBA motif immediately followed by a KEN box (KEN1) and a second KEN box (KEN2) just before the kinase domain (Schematic in Fig 1.6).

ABBA and KEN motifs both allow substrate recognition by APC/C$^{Cdc20/Cdh1}$ for ubiquitin-mediated degradation (DiFiore *et al*, 2015; Alfieri *et al*, 2017; Diaz-Martinez *et al*, 2015). Both Bub1 KEN boxes have been shown to be important for Bub1 ubiquitin-mediated degradation by APC/C^{Cdh1} during SAC silencing (Qi & Yu, 2007). KEN1 was the predominant recognition site but removal of both was required to completely eliminate ubiquitination.

The KEN and ABBA motifs of Bub1 are also thought to be required for SAC signaling, although the specific role of each is largely unknown. Evidence suggests that KEN2, which is directly N-terminal to the start of the kinase domain of Bub1, mainly functions in the recruitment and phosphorylation of Cdc20 (Kang *et al*, 2008). These results suggest KEN1 is

also involved but that KEN2 is more crucial to this function. Abolishing both KEN motifs eliminated Bub1-dependent Cdc20 phosphorylation.

It was not until several years later that an ABBA motif, immediately preceding the KEN1 box was discovered in Bub1 (DiFiore *et al*, 2015) (Fig 1.6). Removal of the ABBA motif in Bub1 has a dramatic effect on SAC signaling and is more pronounced than KEN removal. Interestingly, using a 1-550 truncation, removal of KEN2 and the Bub1 kinase domain did not affect SAC signaling. Even more surprising, Zhang et al., 2017, recently showed that when a minimal kinetochore targeting region of Bub1 (residues 1-280) is fused to Mad1, which does not contain either the KEN1 or ABBA motifs, the checkpoint is still robust, suggesting that the MCC can form without the Bub1:Cdc20 interaction. This is likely because of the redundancy in the ABBA and KEN motifs of BubR1 as discussed earlier. As this truncation of Bub1 still includes the Bub1:BubR1 dimerization domain, it would be interesting to know if a smaller truncation of Bub1 also lacking this domain would have a stronger checkpoint defect.

Despite these data, it is still probable that the Bub1 ABBA/KEN1 region is important in facilitating efficient transfer of the C-Mad2:Cdc20 complex to BubR1, which is why the checkpoint is reduced but still viable upon their removal (Diaz-Martinez *et al*, 2015). Relatedly, it would also be interesting to test whether a single molecule of CDC20 can bind both the ABBA and KEN1 motifs or if they are temporally and/or spatially regulated during the checkpoint.

1.12 The Bub1:Mad1 Interaction

Historical Background

In 2000, Brady and Hardwick, suggested that a complex between phosphorylated Mad1, Bub1 and Bub3 was required for spindle checkpoint function in yeast (Brady & Hardwick, 2000). They identified that a conserved RLK motif, which forms a basic patch on the outside of the Mad1 coiled-coil, was essential for this complex. They subsequently found that an RLK/AAA mutation prevented Mad1 kinetochore association and created a defective checkpoint. This was later recapitulated in human cells (Kim *et al*, 2012).

It was not until 2014 that London and Biggins, identified a direct interaction between Bub1 CD1 and Mad1 RLK in budding yeast (London & Biggins, 2014b). They discovered that

Mad1 associated with kinetochore preparations from cells and that this was dependent on Knl1 (Spc105). Subsequently they identified that it was not due to a direct interaction between Knl1 and Mad1, but an interaction between Bub1 and Mad1. They found the RLK motif of Mad1 was required and that lambda phosphatase released Mad1 from Bub1. Mass spectrometry and a phospho-mutant screen subsequently determined that phosphorylation sites within the Bub1 CD1 domain were required for the Mad1:Bub1 interaction. Specifically, they identified two essential sites, T453 and T455. Mps1 was confirmed as the phosphorylating kinase through a radio-labelled assay (Weiss & Winey, 1996) and further *in vivo* studies. Later ITC experiments suggest a moderate affinity of 2.2 μM for this interaction (Ji *et al*, 2017).

In the same year, another study published from the Desai lab, found the same direct interaction between Bub1:Mad1 in *C. elegans* (Moyle *et al*, 2014). *C. elegans* present an unusual case as they lack both the Bub1 CD1 domain and any Mps1 homologue. Here the Bub1 kinase domain directly binds Mad1, suggesting that Mad1 can be recruited to kinetochores by different mechanisms. It is hypothesized that other kinases, including polo-like kinase 1 (Plk1) may fulfil the roles of Mps1 in MCC assembly in *C. elegans* (Espeut *et al*, 2015).

The Human Bub1:Mad1 Interaction

Even after determining the mechanism for the Bub1:Mad1 interaction in yeast, it took several years to reproduce the direct interaction between Bub1 and Mad1 in humans. Part of the difficulty arose from the discovery that there were two modes of Mad1 recruitment, the Bub1 pathway and the metazoan specific Rod/Zwilch/Zw10 (RZZ) pathway (Karess, 2005).

In 2017, two studies were the first to confirm the direct interaction of human Bub1 and Mad1 *in vitro* (Zhang *et al*, 2017; Ji *et al*, 2017). Importantly they discovered sequential phosphorylation by first Cdk1 at Ser459 and then Mps1 at Thr461, was required to capture a robust interaction. Bub1 Ser459 is followed by a proline and matches the minimal Cdk1 substrate consensus of [S/T]P. The negatively charged phosphorylated Ser459 then primes Mps1 phosphorylation at Thr461, as Mps1 prefers to phosphorylate sites with an acidic residue at the -2 position (Dou *et al*, 2011). A Bub1 S459A/T461A mutant could not rescue mitotic arrest deficiency caused by Bub1 depletion (Ji *et al*, 2017), while phospho-mimetic mutants S459E and T461D could mostly restore the arrest (Zhang *et al*, 2017). The Nilsson

lab further confirmed this interaction *in vivo*, using a doubly phosphorylated pSpT antibody to detect staining in nocodazole arrested cells, and by using a proximity-dependent ligation assay (Zhang *et al*, 2017).

ITC and SPR suggest that the interaction between human Bub1 and Mad1 is lower affinity than in yeast. ITC suggests the singly phosphorylated pThr461 Bub1 CD1 peptide binds the $Mad1^{CTD}$ with an affinity of 15.7 μM, whereas the doubly phosphorylated peptide has an affinity of 3.1 μM (Ji *et al*, 2017). Using SPR, singly phosphorylated Thr461 had a K_D of 32 μM while doubly phosphorylated CD1 had a K_D of 16 μM. Phosphorylation by Cdk1 alone at Ser459 does not create a Bub1-Mad1 interaction which can sustain the checkpoint (Zhang *et al*, 2017).

It is important to note that other than when a doubly phosphorylated $Bub1^{CD1}$ peptide is used, a strong Bub1-Mad1 interaction has yet to be captured by longer Bub1 truncations in any biophysical studies. Numerous labs have reported an inability to capture the full-length complex in size-exclusion, and almost all pull-down studies with full-length Bub1 and/or other Bub1 truncations have very low occupancy of Mad1. This might suggest that the Bub1-Mad1 interaction becomes weaker when larger Bub1 constructs are used or that some sort of autoinhibition is occurring. Additionally, there exists no structure of Mad1 bound to Bub1 and thus the molecular details of this phospho-specific interaction are unknown.

The Bub1:Mad1 interaction has been shown to be important for more than just targeting the Mad1:C-Mad2 complex to kinetochores, however the details of this remain to be elucidated. In fission yeast, Bub1 was found to be required even when Mad1 was tethered to Mis12 of the outer kinetochore (Heinrich *et al*, 2014). Fusion of human Mad1 to kinetochores or to Bub1 bypasses the requirement for the CD1:RLK interaction in targeting Mad1 to kinetochores, but Bub1 is still required for proper checkpoint function (Zhang *et al*, 2017). This is likely because Bub1 acts as a scaffold by which it not only recruits Mad1 but also Cdc20 and BubR1, as well as repositioning these checkpoint proteins for efficient MCC assembly.

1.13 RZZ-mediated Mad1 Kinetochore Recruitment

As mentioned, another reason for the complication in understanding the human Bub1:Mad1 interaction at kinetochores was the discovery that there were two modes of recruitment. In

humans, depletion of Bub1 or removal of its CD1 domain, does not completely remove Mad1 from kinetochores, as is the case in yeast, because a second pool was found to be targeted by the RZZ complex (Karess, 2005; Zhang *et al*, 2015; Calda *et al*, 2015; Silió *et al*, 2015; Zhang *et al*, 2019).

The RZZ complex is a metazoan specific pathway for Mad1 kinetochore recruitment (Karess, 2005). RZZ localizes to kinetochores soon after nuclear envelope breakdown through Knl1-Zwint recruitment (Starr *et al*, 1998; Wang *et al*, 2004; Kops *et al*, 2005). RZZ has been shown to be required for proper Mad1 kinetochore recruitment and a fully robust checkpoint (Buffin *et al*, 2005; Silió *et al*, 2015; Qian *et al*, 2017; Calda *et al*, 2015; Zhang *et al*, 2015, 2019). Mad1 has been found in RZZ immunoprecipitants in Drosophila but a direct interaction between Mad1 and RZZ subunits remains to be established (Défachelles *et al*, 2015b, 2015a). Recent works suggests Cdk1-cyclin B1 localises to the corona through an interaction with RZZ and cyclin B1 scaffolds the SAC by binding directly to the N-terminus of Mad1 which may suggest that RZZ may only indirectly recruit Mad1 to kinetochores (Allan *et al*, 2020).

Recent data from the Nilsson lab has suggested that Mad1 kinetochore recruitment mediated by RZZ is actually synergistic with the Bub1 pathway, rather than being separate (Zhang *et al*, 2015, 2019). Interestingly the N-terminal region of Knl1 was required for this RZZ dependent localization of Mad1 in a Bub1^{CD1}-dependent manner. There is also another kinetochore pool of RZZ whose localisation is not dependent on Knl1 or Bub1, but instead associated to the Ndc80:CenpT complex (Calda *et al*, 2015; Samejima *et al*, 2015). However, it is unknown if this pool of RZZ helps to maintain Mad1 at kinetochores.

1.14 The Mad1-Mad2 Complex

Mitotic arrest deficiency 1 (Mad1) was first discovered in *S. cerevisiae* using a genetic screen (Li & Murray, 1991). Mad1 mutant cells divide faster when exposed to Benomyl, a drug that perturbs microtubule polymerisation (Li & Murray, 1991; Hardwick & Murray, 1995). The importance of Mad1 targeting to kinetochores was first demonstrated when it was shown that artificially tethering Mad1 to kinetochores could maintain an active checkpoint even after all kinetochores were attached (Maldonado & Kapoor, 2011). Additionally, reactivation of the checkpoint after SAC silencing could be achieved by using an FRB/FKBP rapamycin system to conditionally target Mad1 to kinetochores (Kuijt *et al*, 2014). Several studies have also

shown that the strength of the SAC response is dictated by Mad1:C-Mad2 kinetochore levels (Collin *et al*, 2013; Dick & Gerlich, 2013).

The major role of Mad1 in the SAC is believed to be recruitment of Mad2 to unattached kinetochores where the Mad1:C-Mad2 tetramer acts as the platform for Mad2 open-to-closed template conversion and subsequent MCC activation. However, in recent years the role of Mad1 in the SAC has expanded, to a view that Mad1 is not only important for Mad2 recruitment, but also has key catalytic roles in MCC formation which is dependent upon its C-terminal domain (discussed further in section 1.18 and in chapters 4 and 5).

Mad1:C-Mad2 Localization

The Mad1:C-Mad2 complex is first targeted to the nuclear envelope during interphase, and this targeting depends on the very N-terminus of Mad1 (Heinrich *et al*, 2014; Chen *et al*, 1998; Liu *et al*, 2003; Sang *et al*, 2008). The nuclear basket nucleoporin Megator protein is required for Mad1 nuclear envelope targeting (Lince-Faria *et al*, 2009; Schweizer *et al*, 2013; Rodriguez-Bravo *et al*, 2014). Evidence suggests that interphase Mad1 nuclear pore targeting helps ensure a sufficient amount of Mad1:C-Mad2 complex is produced before mitosis (Schweizer *et al*, 2013; Rodriguez-Bravo *et al*, 2014). Cellular Mad1:C-Mad2 levels then dramatically increase during prometaphase when the complex is targeted to kinetochores (Chen *et al*, 1998; Tipton *et al*, 2011). Mad1 not only requires Mps1 to be targeted to kinetochores but also to be released from nuclear pore complexes as Mps1 phosphorylates Megator which then disrupts its interaction with Mad1 (Cunha-Silva *et al*, 2020).

As previously mentioned, there is a debate about whether or not Mad1 is targeted to outer kinetochores for the purpose of MCC formation by Bub1 or RZZ or a synergy of both. The NTD domain of Mad1 also has several suggested kinetochore recruiters, including Plk1 (Chi *et al*, 2008), Nek2A (Lou *et al*, 2004), Cenp-E (Akera *et al*, 2015), Cdk1-Cyclin B (Alfonso-Pérez *et al*, 2019), and Spindly (Yamamoto *et al*, 2008). It is however unclear if NTD mediated kinetochore targeting of Mad1 is synergistic with the Bub1 and RZZ pathways. This is particularly interesting in light of the fact that Mad1 is an extremely elongated coiled-coil protein spanning approximately 80 nm in length, and therefore it is plausible that Mad1 targeted by its NTD could reach the outer kinetochore with its CTD. Nevertheless, the general consensus is that for MCC assembly, Mad1 kinetochore localisation happens in a Cenp-I>Ndc80>Mps1>Bub1>Mad1 hierarchy. Cenp-I is located on the inner kinetochore and

targets Ndc80 to the outer kinetochore, which then targets Mps1, and finally Bub1 phosphorylation by Mps1 recruits Mad1 (Martin-Lluesma *et al*, 2002; Liu *et al*, 2003; Matson & Stukenberg, 2014).

1.15 Mad1 Structure

Mad1 is an 83 kDa protein, which forms a constitutive dimer that primarily consists of an elongated coiled-coil (Fig 1.9). The structure of Mad1 is discussed extensively in chapter 5. There is no full-length structure of Mad1, largely due to low solubility and expression of full-length Mad1. However, two recent studies have finally reported full-length MBP-tagged Mad1 purification co-expressed with Mad2 in Tna83 insect cells (Alfonso-Pérez *et al*, 2019; Piano *et al*, 2021).

The N-terminus of Mad1, residues 1-485, is largely unstudied, but believed to consist mostly of long coiled-coil regions separated by several disordered loops (Fig 1.9A). In contrast, the C-terminus of Mad1 is well studied. Mad1 residues 485-584 have been crystallized with a Mad2 R133A mutant (PDB: 1GO4; Sironi *et al*, 2002) (Fig. 1.9B-C). Mad2 R133A is self-dimerization deficient and was necessary to obtain a homogenous sample for crystallization. In this structure Mad1 forms a dimer through its coiled-coil α-helices. This coiled-coil is disrupted by a short-disordered loop, named the 'Mad2 interacting motif' (MIM), spanning residues 530-550, which traps one molecule of C-Mad2 per chain to make a Mad1:C-Mad2 heterotetramer. Each C-Mad2 molecule can then dimerize with an O-Mad2 molecule, to make a Mad1:C-Mad2:O-Mad2 hexamer (Fig 1.9B-C).

The very C-terminus of Mad1, residues 597-718, has also be crystallized presenting an N-terminal coiled-coil (597-637), ending in a globular head domain (PDB 4DZO; Kim *et al*, 2012) (Fig 1.9B). The C-terminal head, residues 638-718, forms homo-dimeric RWD folds, a fold found in the kinetochore binding domains of several other checkpoint proteins, including Spc25/24 and Csm1. The RWD fold is part of a ubiquitin-conjugating enzyme class, however, RWD domains lack the proper machinery for covalent ubiquitin transfer (Doerks *et al*, 2002). RWD domains are usually involved in protein-protein interactions (Páez-Pereda & Arzt, 2015; Schmitzberger & Harrison, 2012).

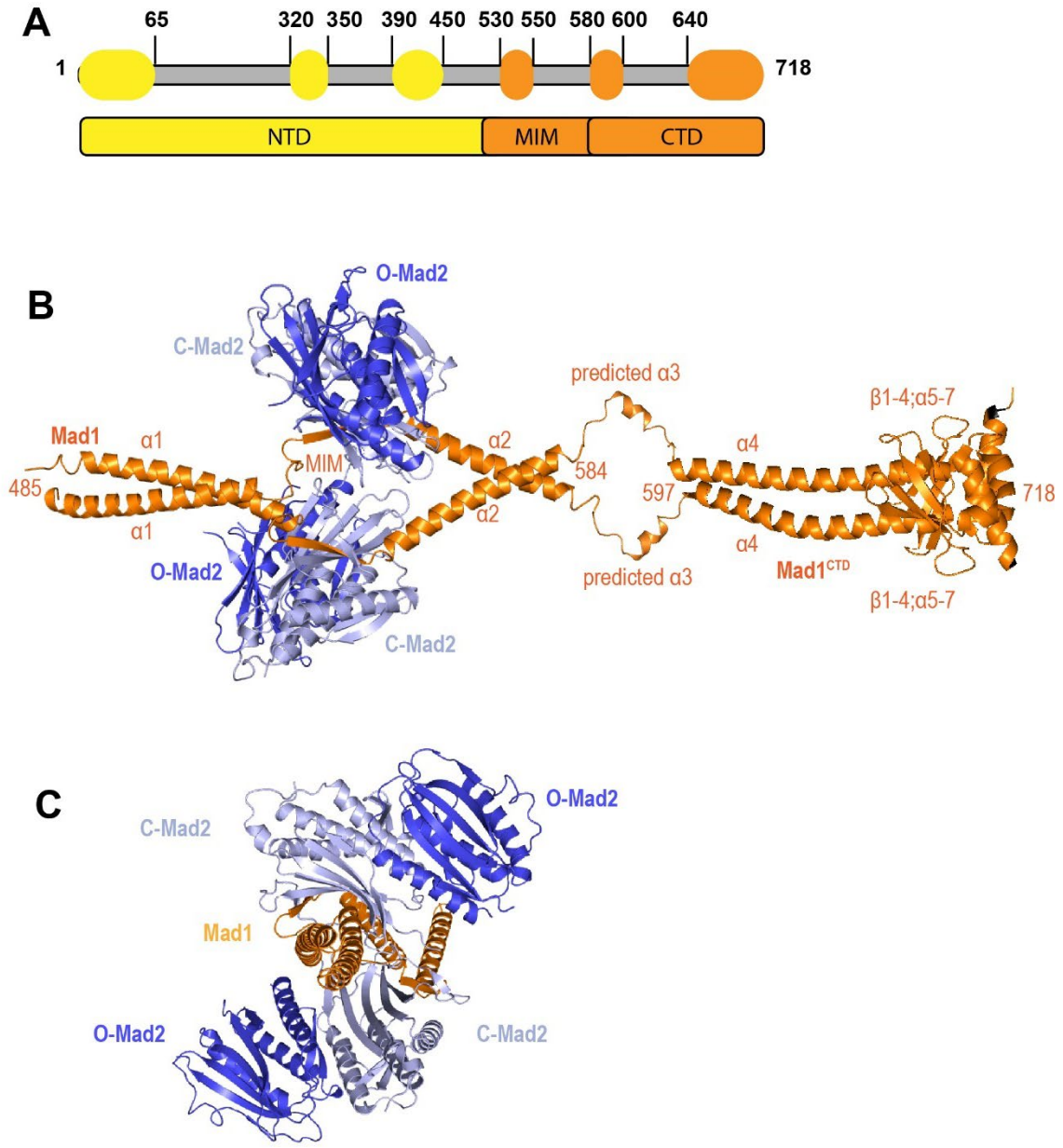

Figure 1.9: Characterisation of Mad1 and the Mad1:C-Mad2:O-Mad2 complex. ***(A)*** *Schematic diagram of Mad1. Non-coiled coil segments are depicted by ovals as predicted by COIS program (Lupas et al, 1991). Mad1 contains three distinct regions. The NTD (yellow) of which there is no structure, composed of a long coiled-coil interrupted by several loops. The MIM (orange) which dimerises and binds two C-Mad2 molecules, and the CTD (orange).* ***(B)*** *A side view of the Mad1Δ485-718:C-Mad2:O-Mad2 complex. The Mad1 dimer encompassing residues 485-584 is depicted in light orange (PDB 1GO4; Sironi et al, 2002), bound to two C-Mad2 molecules in light blue. Two O-Mad2 molecules (dark blue) dimerised to C-Mad2 are fitted using the structure of the O-C Mad2 dimer (PDB 2V64; Mapelli et al, 2007). The coiled-coil is then interrupted by a 16 amino acid segment, which is predicted by AlphaFold2 to have a short α-helix (residues 586-592). The coiled-coil then resumes and the structure of the C-terminal head domain of Mad1, residues 597-718, is depicted in dark orange (PDB 4DZO).* ***(C)*** *Top view of the Mad1:C-Mad2:O-Mad2 complex, not including the flexible head domain.*

A few studies have suggested additional importance of the CTD of Mad1 in MCC formation, including interaction with Cdc20, and a possible fold-over mechanism using the disordered

loop between residues 584 and 597 to fold back onto the Mad1:C-Mad2 core (Ji *et al*, 2017; Piano *et al*, 2021; Sironi *et al*, 2002). However, the functional importance if any of these interactions have yet to be confirmed. Interestingly, the N-terminus of Mad1 is not required for catalytic MCC formation *in vitro*, as a Mad1 420-718 truncation forms MCC at the same levels as Mad1 full-length (Faesen *et al*, 2017). The better studied Mad1 485-718 truncation was slightly worse at MCC catalysis, suggesting a region between residues 420 and 485 is important for the checkpoint in an unknown manner.

1.16 MCC Assembly Requires Mad2 Conversion

As previously mentioned, a key requirement of MCC formation is the conformational change of Mad2 from an open to closed (O-to-C) state. O-Mad2 is the predominant conformation in interphase cells. In mitosis, two pools of Mad2 exist, cytosolic O-Mad2 which is unbound and inactive and C-Mad2 which is active and bound to either of its ligands (Mad1 and Cdc20), by means of their MIM motif (Shah *et al*, 2004; Luo *et al*, 2004).

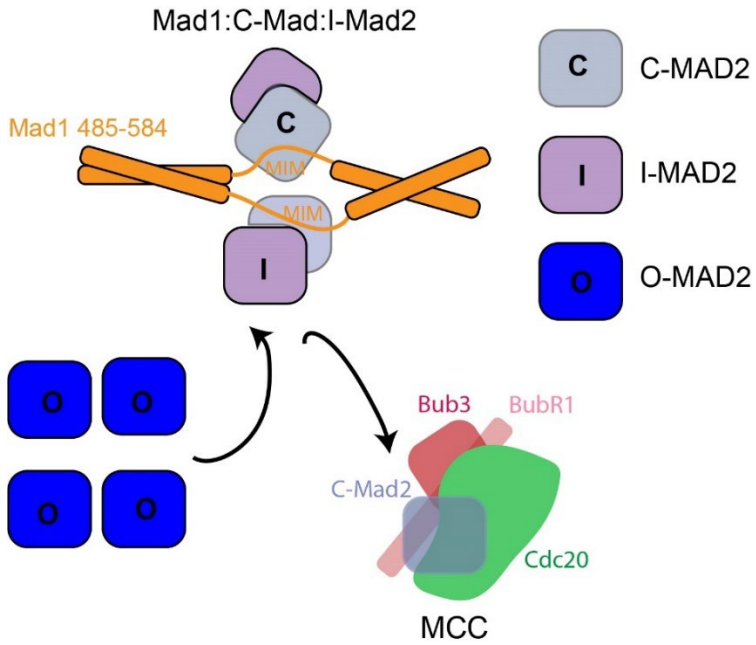

Figure 1.10: A schematic of Mad2 template conversion during MCC formation. *The C-Mad2 molecule, which is part the MCC, requires the Mad1:C-Mad2 platform to form, a process by which cytosolic O-Mad2 (dark blue) binds to C-Mad2 (light blue) already bound to Mad1. C-Mad2 bound to Mad1 then acts as a template by which O-Mad2 is converted into C-Mad2 in a catalytic manner. A transient intermediate state of Mad2 (I-Mad2 coloured purple) likely forms upon O-Mad2 dimerization to C-Mad2. The newly formed C-Mad2 then rapidly binds Cdc20 (green) and BubR1:Bub3 (pink and red) to form the MCC.*

Several experiments were fundamental to establishing that MCC formation requires O-to-C Mad2 conversion (Fig 1.10). The checkpoint requires cytosolic O-Mad2, not Mad2 that is already part of the Mad1:C-Mad2 complex, and Mad1 overexpression will titrate away free O-Mad2 and abrogate the checkpoint (Chung & Chen, 2002). $P31_{comet}$, an adaptor protein important for MCC disassembly, which is homologous to O-Mad2 and can bind the Mad1:C-Mad2 complex, can prevent formation of the MCC by blocking cytosolic O-Mad2 binding to the Mad1:C-Mad2 tetramer and preventing C-Mad2 formation (Nezi *et al*, 2006; Mapelli *et al*, 200) . It has also been reported that $P31_{comet}$ may instead extract Mad2 from the MCC (Westhorpe *et al*, 2011). Checkpoint dysfunction also occurs if a Mad1 MIM mutant (K541A/L543A), which cannot bind Mad2 is used (Ji *et al*, 2018). Additionally, the checkpoint is abrogated if a Mad2ΔLL mutant (O-Mad2 locked), is targeted to kinetochores, or by targeting a Mad2 R133A mutant which is dimerization deficient (Kruse *et al*, 2014).

Because Mad1:C-Mad2 seems to act as the platform for conversion of O-Mad2 into C-Mad2, a template model has been proposed by which the C-Mad2 molecule bound to Mad1, not only acts as a platform for recruitment of O-Mad2 to unattached kinetochores, but also acts as a template for catalytic conversion of O-Mad2 into C-Mad2 (Simonetta *et al*, 2009; De Antoni *et al*, 2005; Nezi *et al*, 2006; Mapelli *et al*, 2007) (Fig 1.10). This model suggests that some sort of transient intermediate Mad2 (I-Mad2) occurs during O-Mad2 conversion on the Mad1:C-Mad2 platform, however the existence and properties of this intermediate state have yet to be confirmed (Hara *et al*, 2015; Luo & Yu, 2008; Mapelli *et al*, 2007).

Structural Analysis of Mad2 Conversion

A detailed analysis of the conformational change which occurs during the O-Mad2 to C-Mad2 transition is shown in Fig 1.11. Mad2 contains a central core (coloured yellow in Fig 1.11), which includes a three-stranded anti-parallel β-sheet (β4-6), and three α-helices (αA-C), with a β-hairpin (β2-3) between the αA and αB helices. The core of Mad2 is preserved during Mad2 conversion while both the N- and C-termini of Mad2 undergo metamorphosis. The disordered segment at the very C-terminus of O-Mad2, as well as the two adjacent β-strands (β8 and β7 coloured red) which form a C-terminal β-hairpin, swing across the central face of Mad2, displacing the N-terminal β-strand in O-Mad2 (β1 coloured blue in O-Mad2). This ejected N-terminal β-strand then refolds as an α-helix and an extended α-helix in C-Mad2. The rearrangement of the C-terminal β-hairpin and its adjacent loop (the 'safety-belt'), ultimately enables Mad2 to entrap the β-stranded MIM motif of Cdc20 (coloured green). This

entrapment of Cdc20^{MIM} during the Mad2 O-to-C transition has thus been coined the 'safety-belt' mechanism and results in a dramatic alteration of the hydrogen bond network in the periphery of Mad2 (Sironi *et al*, 2002; Mapelli *et al*, 2007).

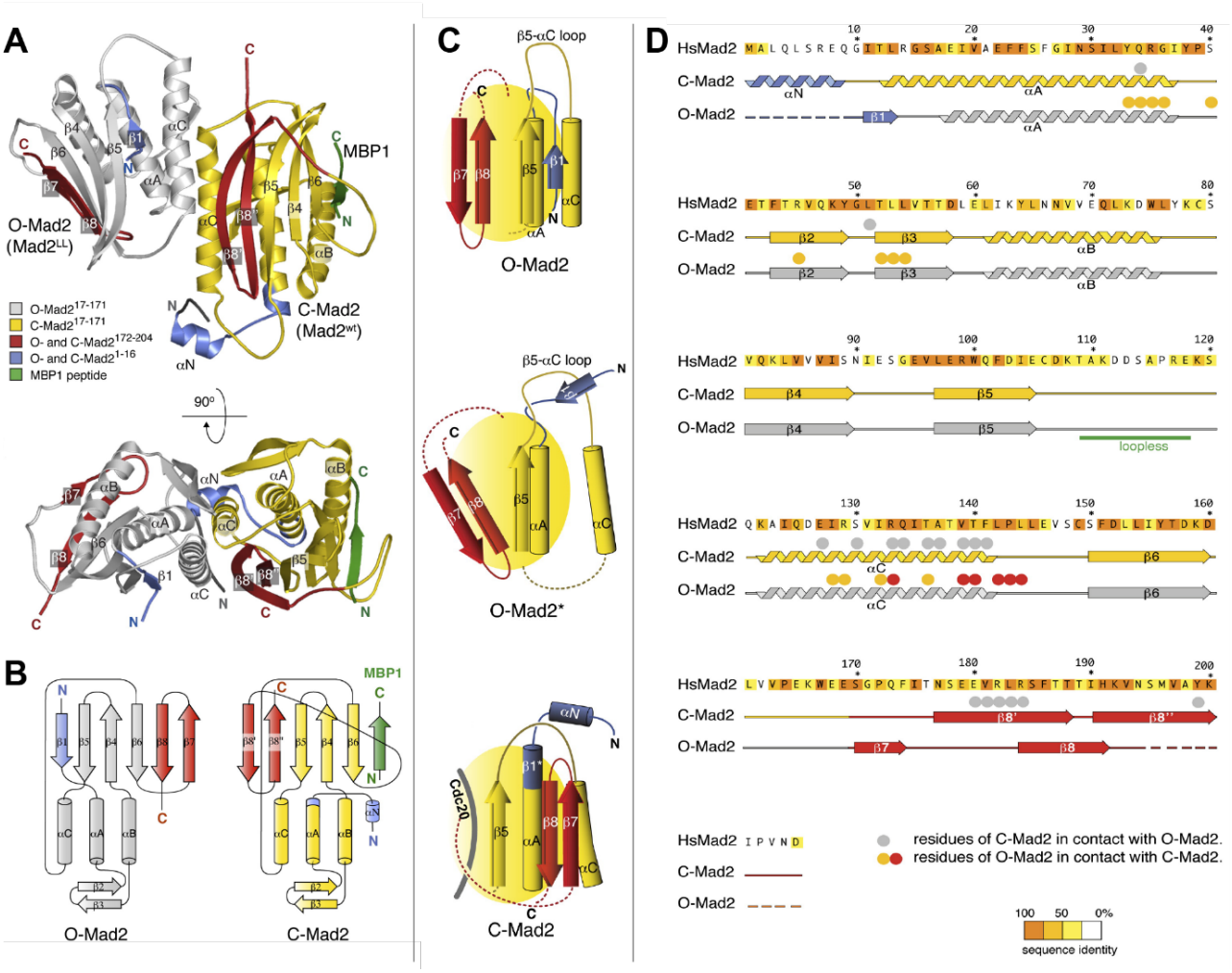

Figure 1.11: Structural comparison of the open and closed states of Mad2. *Figures taken and adapted from Mapelli et al, 2007.* ***(A)*** *A top and side view of the crystal structure of the O-Mad2:C-Mad2 dimer with the MIM motif of Cdc20 bound to the C-Mad2 molecule (PDB: 2V64).* ***(B)*** *A topology diagram of O-Mad2 and C-Mad2:Cdc20^{MIM}.* ***(C)*** *From top to bottom, steps in the conversion of O-Mad2 into C-Mad2, specifically the conformational rearrangement of β1 and αN segments (coloured blue) and the C-terminal β sheets (coloured red). O-Mad2* represents a suggested intermediate state which must occur to allow the O-to-C transition.* ***(D)*** *Schematic diagram of the sequence and secondary structure of O-Mad2 versus C-Mad2. Ribbons are coloured according to a conservation bar displayed below. The circles mark residues where O-Mad2 and C-Mad2 make contact.*

1.17 Catalysis is Required for Mad2 Conversion

The conformational change of Mad2 from the open-to-closed state requires a large activation energy and therefore spontaneous conversion is extremely slow and rate-limiting for MCC formation (Simonetta *et al*, 2009). In cells, SAC activation takes only minutes (Dick & Gerlich, 2013; Clute & Pines, 1999), and mixing C-Mad2 with BubR1 and Cdc20 allows

spontaneous formation of the MCC at 4°C *in vitro* (Ji *et al*, 2017; Faesen *et al*, 2017). However, mixing O-Mad2 with BubR1 and Cdc20 does not spontaneously form the MCC *in vitro*. The half-life of this reaction is about 220 mins and requires overnight incubation to reach equilibrium (Faesen *et al*, 2017). Thus, the reorganization of the Mad2 'safety-belt' seems to be the rate-limiting step of MCC assembly, and as in cells this happens within minutes during an active SAC, one or more mechanisms of catalysis must be occurring.

Several recent studies have investigated the kinetics of Mad2 conversion by establishing assays to measure MCC formation (Faesen *et al*, 2017; Ji *et al*, 2017; Piano *et al*, 2021). The Musacchio lab established a FRET system to measure MCC formation by assessing CFP-BubR1 or CFP-Cdc20 binding to Mad2 conjugated to a TAMRA fluorophore (Faesen *et al*, 2017; Piano *et al*, 2021). The Yu lab utilized MCC-mediated APC/C inhibition which leads to less efficient substrate ubiquitination as a read out for MCC assembly and thus Mad2 conversion (Ji *et al*, 2017). These studies and others have identified several key factors contributing to MCC catalysis, including the Mad1:C-Mad2 tetramer, Mad2 dimerization, phosphorylation of Mad1 by Mps1, phosphorylated Bub1, the N-terminus of Cdc20, and the Mad2 PEG motif. However, the molecular mechanisms and sequence of events for how each components catalyzes MCC assembly is not yet understood.

1.18 Phosphorylated Mad1 Stimulates MCC Formation

Previously, the importance of the Mad1:C-Mad2 complex in checkpoint formation was believed to solely be the ability of Mad1:C-Mad2 to both recruit O-Mad2 and act as a platform for template-based C-Mad2 formation. However, several recent studies suggest that the Mad1:C-Mad2 complex, when triggered by Mps1-dependent Mad1 phosphorylation, enhances Mad2 conversion. The specific details of how Mad1 phosphorylation by Mps1 catalyzes MCC formation are not yet known and will be a key focus in this thesis.

The first evidence to suggest an important role of Mad1 outside of targeting Mad2 to kinetochores was the identification that Mad1 constitutively targeted to kinetochores still required Mps1 to produce an efficient checkpoint response (Hewitt *et al*, 2010; Maldonado & Kapoor, 2011; Tighe *et al*, 2008; Heinrich *et al*, 2014). Additionally, truncating the RWD head of Mad1, while maintaining the RLK motif, creates a defective checkpoint despite the targeting of Mad1:C-Mad2 to kinetochores being maintained (Kruse *et al*, 2014).

Additionally, a Bub1-Mad1 fusion, when the Bub1 CD1 domain is deleted, still requires the C-terminal domain of Mad1 for proper checkpoint signaling (Zhang *et al*, 2017). In fission yeast, the Hauf laboratory mutated residues, E670, D673, and D676, to QNN respectively, within $Mad1^{CTD}$ and found that the checkpoint was defective despite preserving Mad2 and Mad1 at kinetochores (Heinrich *et al*, 2014). The same mutants in human Mad1 create a similar phenotype (Ji *et al*, 2017; Zhang *et al*, 2017).

As previously explained, the Musacchio lab, using a FRET system for MCC formation, found that when adding Mad1:C-Mad2 after being phosphorylated by Mps1, the MCC formed within a few minutes, whereas it otherwise required overnight incubation. This supports experiments showing that Mps1 inhibition by reversine creates checkpoint dysfunction even when Mad1 is forcibly targeted to kinetochores, and this can only be rescued by using a Mad2 L13A mutant which preferentially forms the closed state and thus does not require conversion (Yang *et al*, 2008; Tipton *et al*, 2011, 2013). Therefore, Mad1 functions as key catalyst in MCC formation, and this role is functionally distinct from the requirement of Mad1 in targeting Mad2 to kinetochores.

Mad1 Phosphorylation Sites

Mass spectrometry has been used by several labs to identify several phosphorylation sites present in mitotic Mad1. Functionally significant sites were found in both the N- and C-terminal domains, however only the C-terminal sites were found to be important for MCC activation (Ji *et al*, 2017; Zhang *et al*, 2017; Ji *et al*, 2018). Interestingly, all three studies found that a single residue, Thr716, two residues from the C-terminus of Mad1, was the most critical for Mad1 phosphorylation-dependent checkpoint activation. Mutating Thr716A abrogated the SAC, and significantly diminished APC/C^{MCC} inhibition of securin ubiquitination *in vitro* (Ji *et al*, 2017). Phosphorylation of Mad1 at Thr716 has been implicated in promoting an interaction with the N-terminus of Cdc20, and this will be discussed further in chapter 4 (Piano *et al*, 2021; Ji *et al*, 2017).

Additionally, Thr644, Ser610, and Tyr634 phosphorylation mutants also negatively impacted the checkpoint response by yet unknown mechanisms (Ji *et al*, 2018). An additional study identified Mps1-dependent phosphorylation at Ser699, Ser713 and Thr716 (Piano *et al*, 2021). Therefore, several residues and multiple surfaces within the C-terminus of Mad1 are

crucial for the SAC, but the mechanisms behind how each specific phosphorylation site contributes, and whether it contributes directly to MCC catalysis, is not yet clear.

1.19 SAC Silencing

Reviewed in Bokros & Wang, 2016; Benzi & Piatti, 2020.

Once microtubule-kinetochore attachments are successful and the checkpoint has been satisfied, the SAC signaling cascade must be rapidly shutoff and APC/C inhibition needs to be reversed. There are several key steps in this process, including but not limited to, Mad1 and Mps1 removal, PP2A and PP1 phosphatase signaling, halting MCC formation, and disassembling existing MCC.

Mps1 Silencing

Mps1 binds to Ndc80 and shares this binding site with microtubules. It has been suggested that as microtubules bind, they displace Mps1 and prevent phosphorylation of Knl1, Bub1, and Mad1 which is required to maintain the checkpoint (Hiruma *et al*, 2015; Ji *et al*, 2015). In budding yeast, it has also been suggested that end-on microtubule attachments to kinetochores physically separates Mps1 from its downstream substrates, a mechanism which has also been suggested for Aurora B inhibition (Aravamudhan *et al*, 2015). Consequently, tethering Mps1 to kinetochores causes persistent Mad1 kinetochore localisation and an inability to shut off the checkpoint (Koch *et al*, 2019; Ito *et al*, 2012; Jelluma *et al*, 2010).

PP1 Signaling

The conserved protein phosphatase 1 (PP1) is a crucial player in silencing the checkpoint (Lesage *et al*, 2011). It is recruited to kinetochores through the N-terminal SILK and RVSF motifs of Knl1 and directly opposes Mps1 and Aurora B activity in activating the checkpoint (Aravamudhan *et al*, 2015; Welburn *et al*, 2010; Liu *et al*, 2010; Vanoosthuyse & Hardwick, 2009a). Mutation of the RVSF or SILK motifs in Knl1, creates a prolonged checkpoint and subsequent cell death.

Removal of Mad1

Removal of Mad1 is a key step in shutting down SAC signaling (Gassmann *et al*, 2010; Barisic & Geley, 2011; Vanoosthuyse & Hardwick, 2009b). If Mad1 kinetochore release is prevented by tethering Mad1 to Mis12, cells present severely delayed anaphase onset (Jelluma *et al*, 2010). Stripping of the Mad1:C-Mad2 complex from kinetochores is believed

to happen through RZZ-associated Spindly, which enables minus-end directed dynein-dynactin transport of Mad1:C-Mad2 away from kinetochores (Gassmann *et al*, 2010; Barisic & Geley, 2011; Griffis *et al*, 2007; Silva *et al*, 2014).

MCC Disassembly

There are two independent mechanisms for MCC disassembly. Firstly, APC/C bound MCC can be ubiquitinated by the APC/C resulting in MCC degradation (Uzunova *et al*, 2012; Foe *et al*, 2011; Reddy *et al*, 2007). Secondly, the MCC can be disassembled in an energy-dependent mechanism involving $p31_{comet}$ and the AAA+ ATPase Trip13 (Teichner *et al*, 2011; Eytan *et al*, 2014; Ye *et al*, 2015). It is well established that the hexameric ring of AAA+ ATPases utilize the energy of ATP-hydrolysis to power substrate translocation through their central pore and is a mechanism which often functions to unravel protein complexes (Erzberger & Berger, 2006; Snider *et al*, 2008; Puchades *et al*, 2020). In the case of Mad2, $p31_{comet}$ recruits C-Mad2 to Trip13 which then catalyzes the conversion of C-Mad2 into O-Mad2. Dr. Claudio Alfieri while in the Barford group, solved the cryo-EM structure of nucleotide-bound Trip13 with and without the p31:C-Mad2:Cdc20 complex (Alfieri *et al*, 2018). These structures showed that the $p31_{comet}$ adaptor is able to recognize the HORMA domain of C-Mad2 and deliver its N-terminus to the central pore of Trip13. This translocation of the Mad2 N-terminus through the Trip13 pore, is coupled with the rotary motion of the AAA+ ATPase upon ATP-hydrolysis, resulting in remodeling of the C-Mad2 β-sheet necessary for O-Mad2 conversion. This remodeling releases Mad2 from Cdc20 and disassembles the MCC (Alfieri *et al*, 2018).

Two other functions of $p31_{comet}$

As part of the MCC remodeling process, another interesting aspect of $p31_{comet}$ is that it can disrupt the binding of BubR1:Bub3 to Cdc20:C-Mad2 in a way that is independent of ATP-hydrolysis. Mad2 normally stabilizes the MCC by optimally positioning the KEN box of BubR1 to bind Cdc20 (Chao *et al*, 2012). $p31_{comet}$ competes with BubR1 for Mad2 binding, and therefore antagonizes MCC formation. $p31_{comet}$ also antagonizes MCC formation in a second way. Like Mad2, $p31_{comet}$ is a HORMA domain protein which structurally mimics the O-Mad2 state and blocks the conversion of Mad2 by binding the Mad1:C-Mad2 complex and preventing cytosolic O-Mad2 from binding and undergoing conversion (Xia *et al*, 2004; Yang *et al*, 2007).

1.20 Initial objectives of this thesis

The initial aim of my PhD project was to investigate further how checkpoint proteins are recruited to kinetochores and how Mps1 phosphorylation empowers Bub1 and Mad1 as catalysts in the generation of MCC. This would be accomplished by reconstituting the entire 'pre-MCC' complex, composed of Knl1:Zwint:Bub3:Bub1:C-Mad2:O-Mad2:Mad1:Cdc20, through combining the phosphorylated pKnl1:pBub1:Bub3:Cdc20 complex with the phosphorylated pMad1:C-Mad2:O-Mad2 complex. After successful reconstitution, a combination of biochemical assays and cryo-electron microscopy would be used to analyse both the structure and function of this complex. The major questions I hoped to address included:

1) How phosphorylation promotes both the Bub1-Mad1 interaction as well as the Mad1:Cdc20 interaction.
2) How the overall architecture of the complex creates a juxtaposition of each component to promote efficient MCC assembly.
3) How these events, including Mad1 phosphorylation catalyse Mad2 conversion.

Cryo-EM is currently undergoing an exponential resolution revolution (discussed in chapter 2) and therefore solving the structure of what we predicted was likely to be a very flexible and heterogenous complex seemed challenging but feasible. In particular, we were aware that the Bub1-Mad1 interaction would likely be difficult to capture, as other labs had reported an inability to form a stable Bub1-Mad1 complex. We hoped that by combining all components of the pre-MCC scaffold, as well as utilising the recent advancements in our understanding of i) sequential Bub1 phosphorylation by Cdk1 and Mps1, ii) the Mad1-Cdc20 interaction promoted by Mad1 phosphorylation, iii) a possible synergistic tripartite complex of Bub1-Mad1-RZZ at kinetochores, that we would be able to stabilise the Bub1-Mad1 interaction and capture the entire pre-MCC complex.

After purifying all pre-MCC components and successfully recapitulating Bub1 Ser459 and Thr461 and Mad1 Thr716 phosphorylation *in vitro*, I spent the greater part of the first two years of my thesis trying to reconstitute the entire complex. However, I was largely unsuccessful due to an inability to stabilise the Bub1-Mad1 interaction despite multiple attempts to enhance their affinity. Due to word limit constraints, I will only include a summary of these attempts below:

- Co-expression of all pre-MCC subunits in the baculovirus expression system in the presence of Mps1 and okadaic acid. Okadaic acid is a phosphatase inhibitor which specifically targets PP2A, but also PP1 at higher concentrations, and its presence during baculovirus protein expression has been shown to be a reliable way to promote mitotic protein phosphorylation (Alfieri *et al*, 2018).
- Inclusion of the RZZ complex.
- Enhancing the Bub1-Mad1 interaction through fusing together Bub1 and Mad1 or forcing dimerization using the FRB-FKBP-Rapamycin system.
- Adding multiple sequential CD1 repeats within Bub1, as this has been shown to be an effective way to enhance the Bub1-Mad1 interaction *in vivo* and additionally to bypass the requirement of RZZ in human Mad1 kinetochore recruitment (Zhang *et al*, 2019).
- Using several types of Knl1, Mad1 and/or Bub1 truncations.
- Cross-linking

Thus, the revised aim of my thesis was to investigate specific parts of the MCC assembly scaffold using a more diverse mixture of techniques which were better suited to addressing each individual question and with the hope that a more complete picture of catalytic MCC assembly could be achieved.

1.21 Revised Objectives

Chapter 3 combines X-ray crystallography, NMR spectroscopy, and biophysics to explore the structure and function of the Bub1-Mad1 complex. This includes examining:

- How phosphorylation by Cdk1 and Mps1 specifically regulates the Bub1-Mad1 interaction.
- Whether this interaction serves simply to target Mad1 to kinetochores or if it repositions and/or alters the structure of the Mad1:C-Mad2 complex to promote MCC assembly.

Chapter 4 investigates how Mad1 phosphorylation by Mps1 catalyses MCC assembly. This includes exploring:

- The specific sites of Mps1 phosphorylation on Mad1.

- How Mad1 phosphorylation promotes the Mad1^{CTD}-Cdc20^{NTD} interaction, including analysing the recently identified Box1 and Box2 motifs within the N-terminus of Cdc20.
- The structure of phosphorylated Mad1^{CTD} bound to Cdc20.
- Does Mad1 phosphorylation serve any other purpose than to promote interaction with Cdc20.

Chapter 5 investigates the structure of the Mad1:C-Mad2:O-Mad2 platform in the phosphorylated and non-phosphorylated states by cryo-electron microscopy.

Chapter 6 sets the premise for ongoing work which investigates the mechanisms underlying Mad2 conversion from the open to closed state by NMR. This includes examining:

- The specific steps and sequence of these steps which occur during Mad2 conversion
- If any true intermediate states exist.

Chapter Two
Materials and Methods

2.1 Composition of frequently used medias and buffers.

Buffer	Composition
4x SDS-PAGE	50 mM Tris pH 6.6, 10% SDS, 40% glycerol, 0.8% bromophenolblue, 0.5 mM DTT
LB	10 g/l tryptone, 5 g/l yeast extract, 10 g/l NaCl
Low salt LB	10 g/l tryptone, 5 g/l yeast extract, 2 g/l NaCl
2xTY	16 g/l tryptone, 10 g/l yeast extract, 6 g/l NaCl
TBE	90 mM Tris Base, 3 mM EDTA, 90 mM Boric acid
MES SDS	9.76 g/l MES, 6.06 g/l Tris Base, 1 g/l SDS, 0.3 g/l EDTA
PBS	7.325 g/L NaCl, 2.36 g/l Na_2HPO_4, 1.163 g/l $NaH_2PO_4 \cdot 2H_2O$
PBS-T	1x PBS, 0.2 % Triton-X
Lysis	25 mM HEPES pH 8.3, 250 mM NaCl, 2 mM TCEP, 10% Glycerol, 1 mM PMSF (Sigma), cOmplete™ EDTA-free protease tablets (Roche), 5 units/ml Benzonase® Nuclease (Sigma)
Wash	25 mM HEPES pH 8.0, 250 mM NaCl, 2 mM TCEP
ATP wash	25 mM HEPES pH 8.0, 250 mM NaCl, 2 mM TCEP, 5 mM ATP, 15 mM $MgCl_2$
Strep elution	25 mM HEPES pH 8.0, 50 mM NaCl, 2 mM TCEP, 4 mM Desthiobiotin
SEC	15 mM HEPES pH 8.0, 200 mM NaCl, 1 mM TCEP
NMR	20 mM HEPES pH 7.0, 100 mM NaCl, 1 mM TCEP
RQ Low	15 mM HEPES pH 8.2, 25 mM NaCl, 1 mM TCEP
RQ High	15 mM HEPES pH 8.2, 1000 mM NaCl, 1 mM TCEP
RS Low	15 mM HEPES pH 7.3, 50 mM NaCl, 1 mM TCEP
RS High	15 mM HEPES pH 7.3, 1000 mM NaCl, 1 mM TCEP
ITC	25 mM HEPES pH 7.5, 100 mM NaCl, 1 mM TCEP
Phosphorylation	25 mM HEPES pH 8.0, 5% glycerol, 0.1 µM Okadaic Acid, 15 mM BGP, 2 mM ATP, 10 mM $MgCl_2$, 0.5 mM TCEP

Table 2.1: Composition of commonly used buffers and medias.

2.2 Molecular Cloning

All recombinant proteins used in this study, unless otherwise denoted, are of human origin.

Polymerase chain reaction (PCR)

DNA fragments containing the gene of interest were amplified by PCR using PfuTurbo C_x Hotstart DNA Polymerase (Agilent). Oligonucleotides were obtained from Sigma-Aldrich. An 80 µl reaction was setup using components outlined in Table 2.2, then split into four times 20 µl reactions, and the PCR was run across a temperature gradient.

Volume	Components	Final Concentration
8 µl	10x PfuTurbo C_x buffer	1x
2 µl	dNTP (10 mM)	250 µM
1.2 µl	Primer 1 (100 µM)	1.5 µM
1.2 µl	Primer 2 (100 µM)	1.5 µM
1.6 µl	PfuTurbo C_x polymerase (2.5 U/µl)	4 units
1.6 µl	DNA template (100 ng/µl)	2 ng
64.4 µl	H_2O	

Table 2.2: Concentration of individual components used in a typical PCR reaction.

The PCR reaction was carried out in a Mastercycle Nexus PCR machine (Eppendorf) using the PCR protocol below.

Cycles	Temperature	Duration
1	95°C	2 mins
30	95°C	25 s
	62-52°C gradient	30 s
	68°C	1 min for targets ≤1 kb 1 min per kb for targets >1 kb
1	72°C	10 mins

Table 2.3: Standard PCR protocol

USER® Cloning

USER® cloning was used for all cloning and DNA manipulations following methods outlined in Zhang et al., 2016. PCR fragments were isolated from an agarose gel using a Qiagen gel extraction kit and eluted in 100 µl of H_2O. Fragments were combined and precipitated using 300 µl of 100 mM NaAc pH 5.2 dissolved in 100% EtOH. The DNA pellet was then re-suspended with 10 µl of ice-cold USER® reaction outlined in Table 2.4, incubated for 20 mins at 37 °C, followed by an additional 20 mins at RT, and then placed on ice and transformed into competent *E. coli* cells. All plasmids were transformed into homemade DH5α (NEB) chemically competent cells, except for plasmids containing the modified multibac pU1, and pU2 backbones (Zhang *et al*, 2016c), which were transformed into homemade One Shot™ *PIR1 cells* (ThermoFisher). One Shot™ *PIR1 cells* were used because pU1 and pU2 incorporate a conditional origin of replication derived from R6Kγ phage. Transformed One Shot™ *PIR1 cells* were immediately plated onto LB plates supplemented with 25 µg/ml chloramphenicol, whereas plasmids transformed into DH5α were incubated in 300 µl of LB for 45 mins at 37 °C before plating onto LB plates with appropriate antibiotics.

Volume	Components
1.0 µl	10x CutSmart® Buffer (NEB)
0.5 µl	USER® Enzyme (NEB)
0.5 µl	DpnI (NEB)
8.0 µl	dH_2O

Table 2.4: Components of USER® reaction

Site-directed mutagenesis

Mutants were generated using the QuikChange™ Lightning Site-Directed Mutagenesis Kit (Agilent), developed by Stratagene Inc. (Xia & Xun, 2017).

Plasmid preparation

Single colonies were picked and inoculated in 5 ml 2XTY medium (One Shot™ *PIR1 cells)* or LB medium (all other strains) with appropriate antibiotics. The culture was shaken at 37 °C overnight at 220 rpm. The plasmids were then purified using the QIAprep Spin Miniprep Kit (Qiagen), and eluted in 50 µl H_2O and stored at -20 °C.

2.3 DNA constructs used in this study

Proteins were tagged with one or more DS-, Flag- or His-tags with or without a TEV or 3C protease site. The tag sequences and protease sequence sites used are outlined in Table 2.5. For DNA manipulations, several start plasmids were acquired from lab stocks (Table 2.6) that were then used to clone all subsequent constructs. For baculovirus expression, recombinant proteins were cloned into a modified multibac pUCDM (pU1 & pU2) or pFastBac1 HTa vectors to create a baculovirus transfer vector for insect cell expression as previously described (Zhang *et al*, 2016c). For *E.coli* expression, the coding regions were generally always cloned by USER® (NEB) into a modified pRSFDuet-1 vector (71341-3, Sigma-Aldrich) unless otherwise denoted. A colon (:) punctuation between genes denotes multiple genes within the same vector.

DS (Double Strep)	PQLAMWSHPQFEKGGGSGGGSGGGSWSHPQFEK
Flag	DYKDHDGDYKDHDIDYKDDDDK
TEV	ENLYFQ/S
3C	LEVLFQ/GP
His	HHHHHH

Table 2.5: Protein sequences of purification tags and cleavage sites used in this study

Construct	Vector
His-MBP-TEV-Cdc20 (S.Z.)	pFastBac1 HTa
Bub3-Mad2 (Z.Z.)	pU2
Flag-TEV-BubR1-DS (C.A.)	pFastBac HTa
His-TEV-Cyclin A2 (S.Z)	pFastBac HTa
GST-3C-Cdk2 (S.Z)	pGEX
Mps1-TEV-His (Z.Z.)	pU1
Bub1:DS-TEV-Mad1 (Z.Z.)	pU1
$Mps1^{KD}$-TEV-His6	pNIC28-Bsa4
Mad2-3C-His6 (C.A.)	pET11a
GST-3C-Mps1	pU1
3xFlag-3C-Bub3:His6-DS-TEV-Bub1	pU1
His6-DS-TEV-Mad1:Mad2	pU1
His6-TEV-Mad2	pU2
His6-MBP-TEV-$Cdc20^{1-73}$	pRSF-Duet

Table 2.6: A summary of constructs used for expression and molecular cloning as well as initial wild-type constructs made for all subsequent mutagenesis. *The initials specify if the construct was obtained and previously cloned by either Ziguo Zhang (ZZ), Suyang Zhang (SZ) or Claudio Alfieri (CA) of the Barford group. The $Mps1^{KD}$ construct contains only the Mps1 kinase domain (residues 519-808). A colon (:) punctuation between genes denotes multiple genes within the same vector.*

Abbreviation	Construct	Vector	Description
Mad1Δ485	His6-DS-TEV-Mad1Δ485-718:Mad2	pU1	Tetrameric Mad1:C-Mad2 complex which includes Mad1 residues 485-718 (MIM + RLK + RWD domains).
Mad1Δ420	His6-DS-TEV-Mad1Δ420-718:Mad2	pU1	Same as Mad1Δ485 but includes an elongated N-terminus.
$Mad1^{CTD}$	His6-DS-TEV-Mad1Δ597-718	pRSF-Duet	CTD construct crystallized in PDB: 4DZO.
$Mad1^{Core}$	His6-DS-TEV-Mad1Δ485-584	pU1	Dimerizes and binds to two C-Mad2 molecules to form a tetramer. Crystallized in PDB:1GO4.
Mad1Δ485-5A	His6-DS-Mad1Δ485-718-5A:Mad2	pU1	S538A, T540A, T500A, S551A, T716A. Phosphorylation mutations.
Mad1Δ420-6A	His6-DS-Mad1Δ420-718-6A:Mad2	pU1	T432A, S538A, T540A, T500A, S551A, T716A. Phosphorylation mutations.
Mad1Δ485:C-Mad2ΔR133A	His6-DS-Mad1Δ485-718:Mad2ΔR133A	pU1	Mad1:C-Mad2 with a Mad2ΔR133A dimerization mutant which ensures only tetrameric Mad1:C-Mad2 forms.

Table 2.7 A summary of Mad1 constructs and Mad1:C-Mad2 complexes used*. A colon (:) punctuation between genes denotes multiple genes within the same vector. Additional point mutants within $Mad1^{CTD}$ were made for ITC experiments using the QuikChange™ Lightning Site-Directed Mutagenesis Kit and are outlined in Figure 3.12A of chapter 3.*

Abbreviation	Construct	Vector	Description
Mad2ΔLL*	DS-TEV-Mad2Δ109-117	pRSF-Duet	Prefers O-Mad2. Can dimerize with C-Mad2.
Mad2 R133A	DS-TEV-Mad2 R133A	pRSF-Duet	Dimerization deficient Mad2
Mad2 L13A	DS-TEV-Mad2 L13A	pRSF-Duet	Prefers C-Mad2. Can form O:C or C:C dimers.
Mad2 LPETG	DS-TEV-Mad2-LPETG	pRSF-Duet	Mad2 WT with a sortase site for TAMRA addition.
Mad2 R133A L13A	DS-TEV-Mad2 R133A	pRSF-Duet	Prefers C-Mad2 which is also dimerization deficient.
Mad2ΔC10	DS-TEV-Mad2 1-195	pRSF-Duet	Mad2 with the C-terminal 10 residues deleted. O-Mad2 locked.
Mad2ΔDO	DS-TEV-Mad2Δ109-117, Δ195-205	pRSF-Duet	Mad2 'double open'. A combination of MadLL and Mad2ΔC10

Table 2.8: A summary of all Mad2 mutants used in this project. **Mad2 loop-less mutant (Mad2LL) is a stabilized form of open Mad2 where 109-117 residues are deleted form the loop that connects strand β5 to helix αC and are substituted with a Gly-Ser-Gly triplet, preventing conversion of open-Mad2 into closed-Mad2 (Mapelli et al, 2007).*

2.4 Unlabelled Protein Expression in Bacteria

Bacterial transformation

Generally, 0.5 µl of plasmid at 100 ng/µl was transformed with 50 µl of homemade chemically competent BL21 (DE3) Star cells or B834 (DE3) pRARE cells, left on ice for 15 mins, followed by heat shock at 42 °C for 40 s, and incubated on ice for 1 min. Cells were made competent in-house using standard TB buffer protocols. For bacterial expression, the transformation mixture was added to 100 ml of LB media with appropriate antibiotics and incubated at 200 rpm and 37 °C overnight.

Bacterial protein expression

10 ml of overnight pre-culture was used to inoculate each litre of LB medium, supplemented with appropriate antibiotics, and shaken at 37 °C and 200 rpm in a 2.0 L baffled flask. Once an OD between 0.4-0.8 was reached, the temperature was switched to 18°C and each flask was supplemented with 0.25 mM of IPTG. The culture was then grown overnight at 18°C after which it was harvested by centrifugation at 4500 rpm for 15 min, before being flash-frozen in liquid nitrogen and stored at -80 °C.

For purification of Mad2 in the open confirmation, when cells reached an OD of 0.5 the temperature was reduced to 15°C, and the cells were grown for a further 45 mins, after which the culture was induced with 0.33 mM IPTG. Expression was then completed for 6-12 hrs at 15°C. An expression temperature of 16 °C has previously been reported to reduce

spontaneous conversion of O-Mad2 into C-Mad2 (Mapelli *et al,* 2007). The cells were harvested at 4 °C and the pellet was always kept on ice until flash-frozen in liquid nitrogen to ensure no spontaneous conversion of Mad2 to the closed state occurred.

2.5 Baculovirus Expression

All recombinant proteins for baculovirus expression were cloned into either a modified multibac pUCDM (pU1) vector (Zhang *et al,* 2016) or pFastBac1 HTa. Bacmid generation and virus amplification was completed following the protocol outlined in Zhang *et al*, 2016, unless otherwise indicated.

Bacmid transformation of pU1 or pU2

6 µl of plasmid was transformed in 150 µl of DH10MultiBac^{Cre} chemically competent *E.coli* cells and incubated on ice for 20 mins before being heat shocked for 40 s at 42 °C. The mixture was then incubated on ice for a further 2 mins after which it was incubated overnight in 5-10 ml of LB media without antibiotic resistance. The culture was then spun down and plated onto pre-warmed LB plates supplemented with 50 µg/ml kanamycin (ThermoFisher), 10 µg/ml tetracycline (MP-Biomed 103012), 100 µg/ml Bluo-Gal (Melford MB1030) and 40 µg/ml IPTG. In the case of pU1 and pU2 plasmids the LB plates were further selected with chloramphenicol, whereas pFastBac1 HTa vectors were selected with 10 µg/ml gentamycin (Sigma G1914).

Bacmid preparation of pU1 or pU2 alone

When selecting for bacmids containing only pU1 or pU2, several blue colonies were selected from the LB plates after incubating them for 48 hrs at 37 °C. Selected colonies were cultured overnight in 10 ml of LB with appropriate antibiotics. The overnight culture was pelleted at 4,000 rpm for 10 mins after which the supernatant was removed. The pellet was re-suspended in 500 µl P1 buffer (QIAGEN Miniprep Kit), transferred to a 2 ml autoclaved Eppendorf, and vortexed for an additional 30 s. Next, 250 µl of P2 buffer was added, mixed, and incubated at RT for 5 mins before adding 350 µl N3 buffer. Cell debris was removed by centrifugation at 13k rpm for 30 mins. 700 µl of the supernatant was transferred to an Eppendorf and ethanol precipitated with 3-times excess isopropanol and spun at 4 °C at 13k rpm for 1 hr and then dissolved in 100 µl sterile water. To ensure that there was no bacterial contamination during transfection, the resuspended plasmid was spun for a further 15 mins at 13k rpm, after which 80 µl was transferred into a new Eppendorf tube. Bacmid DNA concentration was measured

on a nanodrop to ensure a concentration above 5000 ng/µl was achieved before storing at 4 °C.

Bacmid Preparation of pU1 together with pFastBac HTa

To generate a recombinant MultiBac bacmid integrated with gene cassettes from both pU1, pU2 and pFastBac, a two-step transposition procedure was used following Zhang *et al*, 2016. First pU1 or pU2 were integrated into MultiBac bacmid present in DH10Multibac^{Cre} *E. coli* chemically competent cells as described above. Next blue colonies were picked from the LB plates containing integrated pU1/U2 bacmid and chemically competent cells were made from these colonies using a standard TB protocol. The pFastBac HTa plasmid was then transformed into 100 µl of pU1/U2 competent cells, incubated overnight in 10 ml LB without antibiotic selection and then plated onto bacmid LB plates supplemented with gentamycin to select for the pFastBac HTa gene. As recombinant pFastbac HTa are integrated into the MultiBac bacmid at the Tn7 locus site, disruption of the lacZ gene occurs, allowing white colonies containing the dual-integrated vector to be distinguished from blue colonies only containing the pU1/U2. Plates were left to grow for two days after which a 10 ml LB culture with a single white colony was grown overnight at 37 °C and 200 rpm to be used for bacmid preparation as described above.

P1 virus transfection

2.5 ml of SF9 insect cells at 0.3 million/ml were pipetted into a 6-well plate and left at RT for 30 min to allow cell attachment. 200 µl of Sf900-II medium (Life Technologies no. 10902-104) was added to a 1.5 ml Eppendorf and 6 µl of Cellfectin-II reagent (Life Technologies 10362-100) was mixed with 10 µl of bacmid DNA. This mixture was incubated at RT for 15 mins after which the medium in the 6-well plate was aspirated and 800 µl of Sf900-II medium was added to the Cellfectin/Bacmid DNA mixture before being pipetted onto the wall of the 6-well plate so as not to disturb the cell monolayer. The plate was then incubated at 27 °C in a humidified atmosphere. After the first day, 1 ml of Sf900-II medium was added to each well of the 6-well plate and the plates were then left for a further 4 days before proceeding onto virus amplification.

Virus amplification and protein expression

The 2 ml of transfection in the 6-well plates were individually added to 40 ml of SF9 insect cells at 1.2 million/ml. The cells were shaken at 27 °C at 140 rpm until cell viability dropped

to 80 % (normally after 3 days). The amplified virus (P2 virus) was then harvested by spinning the cells at 2000 g for 5 mins, the supernatant was decanted into a sterile 50 ml Falcon tube supplemented with 2 % FBS, and stored in the dark at 4 °C. For protein expression, 1 ml of P2 virus was added to 100 ml of SF9 cells at 2 million/ml and incubated until viability dropped to 80% (about 3 days). This generated a P3 virus which was then used for infecting High Five (H5) cells for protein expression, by adding 13 ml of P3 virus per 400 ml of H5 cells at 1.5 million/ml. Cells were harvested once viability dropped below 85 % (normally 40 hrs). The cells were then pelleted at 1000 g for 10 mins and the pellet was flash-frozen in liquid nitrogen. For co-expression of multiple proteins in different viruses, 13 ml of each individually amplified P3 virus was used to co-infect 400 ml of H5 cells.

Hi5 Expression with Okadaic Acid

Proteins were expressed in Hi5 cells in the presence of okadaic acid to promote natural mitotic phosphorylation (Alfieri *et al*, 2016). Hi5 cells were infected with the amplified SF9 virus and grown until viability had dropped to 90 % (about 30 hrs). Okadaic acid at a final concentration of 0.1 μM was added to the media and the cells were grown for an additional 5 hrs and then harvested and immediately re-suspended in lysis buffer supplemented with 0.1 μM okadaic acid and 10 mM BGP. The specific phosphorylation sites required were confirmed by mass spectrometry or phospho-antibody detection.

2.6 Protein Purification

All protein purification buffers unless otherwise denoted are outlined in Table 2.1. Generally, all cell pellets were re-suspended in 250 ml of lysis buffer per 8 L of *E. coli* cells or 4 L of Hi5 insect cells at 4 °C, supplemented with 5 mM EDTA unless purified over a HiTrap TALON® Crude column. All *E. coli* preparations were supplemented with 25 mg/ml of lysozyme (Sigma-Aldrich). Cell lysis was performed by sonication, after which the lysate was centrifuged at 48,000 g for 1 hr at 4 °C. The cleared supernatant was filtered with a 5 μM syringe filter before being applied to an affinity column.

TEV and 3C Proteases

Recombinant TEV and 3C protease plasmids for *E. coli* protein expression were obtained from Jing Yang of the Barford group. His6-TEV lysate was applied to 15 ml of HiTrap TALON® Crude columns (Cytiva), washed with 15 CV of wash buffer, and eluted with 5 CV of wash buffer supplemented with 50 mM imidazole. The eluate was concentrated and

further purified with a Superdex 75 Increase column (GE Healthcare) and stored at -80 °C in 50% glycerol at 2 mg/ml. The 3C protease was purified over 15 ml of GST-resin, washed with 20 CV of wash buffer, and eluted in the wash buffer supplemented with 25 mM reduced glutathione, and then further purified with a HiLoad 16/600 Superdex 200 column (GE Healthcare) pre-equilibrated in the SEC buffer. Both proteases were kept with their tags on to aid in protease removal during target protein cleavage and purification.

DS-tagged protein purification

All DS-TEV-tagged proteins and protein complexes unless otherwise described were purified over 25 ml of Strep-Tactin Superflow Plus cartridges (Qiagen) at 1.2 ml/min, washed with 75 ml of strep ATP wash buffer at 1.0 ml/min, followed by 75 ml of wash buffer at 3.5 ml/min, before eluting with 100 ml of strep elution buffer at 2 ml/min. The eluate was then concentrated and cleaved overnight with 2 mg of TEV protease at 4°C. The cleaved protein was then diluted to 25 mM NaCl and further purified by an anion-exchange resource Q (GE Healthcare), using a gradient of the low to high RQ buffers over 40 CV. Fractions from the resource Q were concentrated and then purified further by size-exclusion chromatography (SEC) using either a HiLoad 16/600 Superdex 200 (GE Healthcare), Superdex 75 Increase column (GE Healthcare), or Superose 6 Increase Column (GE Healthcare), pre-equilibrated in the SEC buffer.

Full-length Cdc20

Cdc20 cloned into a pFastbac1HTA in frame with a His6-tag followed by MBP and a TEV cleavage site (His6-MBP-TEV-Cdc20) was acquired from Dr. Alfieri of the Barford group and purified as previously described (Alfieri *et al*, 2016). Aliquots of His6-MBP-TEV-Cdc20 and cleaved Cdc20 were stored at -80 °C in 25 mM HEPES pH 7.5, 200 mM NaCl, 5 % glycerol, and 2 mM DTT.

Cdc20$^{1-73}$

His-MBP-Cdc20$^{1-73}$ was purified over two 5 ml HiTrap TALON® Crude columns (Cytiva) in a buffer of 25 mM HEPES pH 8.0, 350 mM NaCl, and 5 % glycerol. The lysis buffer was supplemented with EDTA-free protease tablets (Roche), 25 mg/ml lysozyme, and 2 mM PMSF. His-MBP-Cdc20$^{1-73}$ was washed with 5 CV of wash buffer supplemented with 10 mM imidazole, then eluted over 10 CV with 100 mM imidazole and cleaved overnight with 5 mg of TEV while undergoing dialysis into 25 mM HEPES pH 7.3, 40 mM NaCl, 1 mM TCEP,

and 5 % glycerol. Cdc20$^{1-73}$ was purified away from cleaved His-MBP using a 6 ml cation-exchange Resource S column (GE Healthcare) and eluted with a gradient of the low and high RS buffers over 20 CV. Fractions containing Cdc20$^{1-73}$ were concentrated and run over a 120 ml Superdex 75 column (GE Healthcare) pre-equilibrated in the SEC buffer. For crystallisation and NMR experiments, a second round of cation-exchange and SEC was performed to eliminate all contaminants.

Cdk2:Cyclin A2^{trunc}

An N-terminal truncation, consisting of residues 174-432, of His-tagged human cyclin A2 was used together with GST-tagged Cdk2 to perform Cdk1 phosphorylation of Bub1. Pellets were co-lysed, and the supernatant was applied to 12 ml of Glutathione Sepharose™ 4B (GE Healthcare) and washed with 30 CV of wash buffer. Both His6 and GST tags were then cleaved in parallel with TEV and 3C proteases overnight at 4 °C in the SEC buffer. The flow-through from the resin was then collected, concentrated, and further purified by a Superdex 200 16/600 column (GE Healthcare) pre-equilibrated in the SEC buffer.

GST-Mps1

GST-Mps1-TEV-His6 pellet was resuspended in lysis buffer, supplemented with 500 mM NaCl, 25 mg/ml lysozyme, and 0.05% NP-40. The supernatant was applied to 10 ml of Glutathione Sepharose™ 4B resin and washed with 25 CV of wash buffer supplemented with 500 mM NaCl. GST-Mps1-TEV-His6 was eluted overnight at 4 °C without removal of the GST-tag to keep full-length Mps1 soluble, using an elution buffer containing 25 mM HEPES pH 8.0, 500 mM NaCl, 2 mM DTT, and 20 mM reduced glutathione. The eluate was concentrated and then run over a Superdex 200 16/600 column in the SEC buffer.

Mps1^{KD}

The Mps1 kinase domain pellet was re-suspended in lysis buffer and the supernatant was run over a 5 ml HiTrap TALON® crude column (Cytiva), washed with wash buffer supplemented with 5 mM imidazole and eluted in 100 mM imidazole. The eluate was cleaved with TEV overnight and run over a HisTrap HP column and then concentrated and purified further by a Superdex 75 16/600 column (GE Healthcare)

Purification of O-Mad2 and C-Mad2 states

Purification was completed using the standard DS-tagged protein purification protocol described above, however, Mad2 was diluted to 15 mM NaCl prior to anion-exchange purification and a slower gradient of 30 CV from 25-400 mM NaCl was performed. O-Mad2 eluted around 50-75 mM NaCl, while C-Mad2 eluted around 175-220 mM. A second anion-exchange step was always performed using a 1 ml Resource Q (GE Healthcare) to ensure the sample had complete conformational homogeneity before being run over a Superdex 75 16/600 column pre-equilibrated in NMR or SEC buffers. The conformational specificity of Mad2 anion-exchange elution, has been previously shown by several groups to be an effective way to purify O-Mad2 from C-Mad2 (Mapelli *et al*, 2007; Ji *et al*, 2018; Ye *et al*, 2015), and we further confirmed the homogeneity of our O-Mad2 and C-Mad2 purifications by NMR spectroscopy.

2.7 Peptide Synthesis

Peptides were ordered from Designer Bioscience UK, at 95 % purity, with amidation and acetylation modifications. Peptides were resuspended in 500 mM HEPES pH 8.0, 100 mM NaCl, before undergoing dialysis overnight in either ITC, SEC, or NMR buffer.

Peptide Name	Peptide Sequence
Bub1 pSpT CD1	(W)KVQP{pS}P{pT}VHTKEALGFIMNMFQAPTS
Bub1 CD1	(W)KVQPSPTVHTKEALGFIMNMFQAPTS
Bub1 SpT CD1	(W)KVQPSP{pThr}VHTKEALGFIMNMFQAPTS
Bub1 post-CD1	DDKDEWQSLDQNEDAFEAQFQKNVRS
Sc Bub1 pTpT CD1	QSRSP{pThr}V{pThr}AFSKDAINEVFSMFNQHYS
Cdc20 Box1	RWQRKAKE
Cdc20 Box2	RTPGKSSSKVQT
$Cdc20^{1-35}$	MAQFAFESDLHSLLQLDAPIPNAPPARWQRKAKEA
MBP1	SWYSYPPPQRAV
Cdc20 MIM	EHQKAWALNLNGFDVEEAKILRLSGKPQ

Table 2.9: Sequences of synthesized peptides from Designer Bioscience.

2.8 *In vitro* phosphorylation

Pure Bub1 and Mad1 fragments or complexes were phosphorylated essentially as previously described (Ji *et al*, 2017). For Bub1 phosphorylation by both Mps1 and Cdk2, proteins were mixed in parallel at a 4:1 molar ratio of Bub1 to each kinase. This mixture was then buffer exchanged into the phosphorylation buffer (outlined in Table 2.1) using a PD-10 column (GE healthcare). The reaction was incubated at 25 °C for 1.5 hrs before the reaction was stopped by either adding Cdk1/2 inhibitor iii (ENZO life sciences) and Reversine (Sigma) or by a

size-exclusion step. Phosphorylation of Mad1 by Mps1 was performed similar to Bub1 however a 1:1 molar ratio of Mad1 to GST-Mps1 was used and the reaction was incubated for 4 hrs at 27 °C. Phosphorylation efficiency was assessed by intact mass spectrometry, or NMR spectroscopy.

2.9 ^{32}P Incorporation Assay

Activity of all kinase preps were tested through a radio-labelled phosphate incorporation assay (Weiss & Winey, 1996). ATP, [γ-32P]- 3000 Ci/mmol 10 mCi/ml EasyTide, (PerkinElmer) was used to quantitate kinase activity for Bub1 and Mad1 by Mps1^{KD}, GST-Mps1 as well as Cdk2-CycA. This ATP is radio-labelled on the gamma phosphate group with ^{32}P. All experiments were done under the supervision of Thomas Tischer (trained for radioactivity). 20 µl reactions were setup using a master mix of Bub1 or Mad1 at 1 µM in the phosphorylation buffer except ATP was reduced to 1 mM and supplemented with 5 µCi of ^{32}P ATP per 20 µl reaction. The reactions were left at room temperature for 2 hrs, mixed with SDS-PAGE loading dye and run on an SDS-PAGE gel for 45 mins at 200 v. Afterwards, the gel was washed two-times for 10 mins with H_2O to remove excess radio-labelled ATP and to decrease background. The gel was then dried using a gel dryer with a vacuum pump onto Whatman paper. The dried gel was then incubated with FUJIFILM Super RX for 1 hr in the dark room after which it was imaged with a X-OMAT Developer and Replenisher.

2.10 Lambda Phosphatase Treatment

Lambda phosphatase was obtained from Dr. Claudio Alfieri of the Barford Group and added to proteins in a 100:1 molar ratio of protein to lambda phosphatase. The reaction was carried out either for 2 hrs at RT or overnight at 4 °C in the SEC buffer supplemented with 2 mM $MnCl_2$. The lambda phosphatase was inactivated by addition of 30 mM EDTA.

2.11 Mass Spectrometry Phosphorylation Identification

Identification of phosphorylation sites on Bub and Mad complexes were performed by Sarah Maslen at the LMB mass spectrometry (MS) facility. Purified proteins were sent in solution or as SDS-PAGE Coomassie gel bands where the protein was extracted. After reduction with 10 mM DTT and alkylation with 55 mM iodoacetamide, the proteins were digested overnight at 37 °C at a 1:50 ratio of trypsin (Promega, UK). Tryptic peptides were analysed by nano-scale capillary LC-MS/MS with an Ultimate U3000 HPLC (Thermo Scientific Dionex, San Jose, USA) set to a flowrate of 300 nL/min. Peptides were trapped on a C18 Acclaim PepMap100 5 µm, 100 µm × 20 mm nanoViper (Thermo Scientific Dionex, San Jose, USA)

prior to separation on a C18 T3 1.8 µm, 75 µm × 250 mm nanoEase column (Waters, Manchester, UK). A gradient of acetonitrile eluted the peptides, and the analytical column outlet was directly interfaced using a nano-flow electrospray ionization source, with a quadrupole Orbitrap mass spectrometer (Q-Exactive HFX, ThermoScientific, USA). For data-dependent analysis a resolution of 60,000 for the full MS spectrum was used, followed by twelve MS/MS. MS spectra were collected over a *m*/*z* range of 300–1,800. The resultant LC-MS/MS spectra were searched against a protein database (UniProt KB) using the Mascot search engine program. Database search parameters were restricted to a precursor ion tolerance of 5 p.p.m with a fragmented ion tolerance of 0.1 Da. Multiple modifications were set in the search parameters: including two missed enzyme cleavages, and phosphorylation of serine, threonine, and tyrosine. The proteomics software Scaffold 4 was used to visualize the fragmented spectra.

2.12 Intact Protein Mass Spectrometry

Intact proteins were subjected to LC-MS analysis by Sarah Maslen at the MRC-LMB mass spectrometry facility. A modified NanoAcquity (Waters, UK) delivered a flow of approximately 50 µl/min, and proteins were injected directly on a C4 BEH 1.7 µm, 1.0 x 100 mm UPLC column (Waters, UK). Proteins were eluted with a 20-min gradient of acetonitrile (2 % to 80 %). The analytical column outlet was directly interfaced via an electrospray ionisation source, with a hybrid quadrupole time-of-flight (Q-TOF) mass spectrometer (Xevo G2, Waters, UK). Data were acquired over a m/z range of 350–2000, in positive ion mode with a cone voltage of 30 v. Scans were summed together manually and deconvoluted using MaxEnt1 (Masslynx, Waters, UK). The data were then searched against an LMB in-house database using a Mascot search engine (Matrix Science) (Perkins *et al*, 1999), and the peptide identifications validated using the Scaffold program (Proteome Software Inc.) (Keller *et al*, 2002).

2.13 Native Mass Spectrometry

Intact complexes were subjected to SEC-MS analysis. Briefly, a M-class LC (Waters, UK) delivered a flow of approximately 100 µl/min. Complexes were injected directly onto a BEH SEC column, 200 Å, 1.7 µm, 2.1 mm x 150 mm UPLC column (Waters, UK). Complexes were eluted with an isocratic gradient of 100 mM ammonium acetate. The analytical column outlet was directly interfaced via an electrospray ionisation source, with a hybrid quadrupole time-of-flight Synapt G2-Si mass spectrometer (Waters, UK). To maintain non-covalent

interactions in the gas phase temperatures were kept at 20 °C. Data were acquired over a m/z range of 1000-8000 m/z, in positive ion mode with a cone voltage of 150 v. Scans were summed together manually and deconvoluted using MaxEnt1 (Masslynx, Waters, UK).

2.14 Circular Dichroism

Circular Dichroism experiments were carried out with Dr. Stephen McLaughlin of the MRC-LMB biophysics facility. For each peptide tested, serial dilutions into H_2O were performed, and the far-UV CD spectra were recorded on a Jasco J-815 spectrometer in a thermostated cuvette holder maintained at 20 °C.

2.15 Isothermal Titration Calorimetry (ITC)

Isothermal titration calorimetry (ITC) assays were performed with an Auto-iTC200 instrument (Malvern Instruments, Malvern, UK) at either 10 °C, 20 °C, or 30 °C. Prior to analysis all samples were dialysed into the ITC buffer (Table 2.1) overnight at 4 °C. For each titration, 300 µl of one sample was added to calorimeter cell, while the titrating sample was injected into the cell consisting of one 0.5 µl injection followed by 19 injections of 2 µl each. Generally, 1 mM of peptide or protein was injected into 100 µM protein in the cell unless otherwise denoted. The changes in the heat were integrated over the entire titration and fitted to a single-site binding model using the PEAQ Analysis software package 1.0.0.1258 (Malvern Instruments). Titrations were repeated at least twice. For experiments containing Mad1, the stoichiometry was calculated assuming that the Mad unit is a dimer.

2.16 Sedimentation Velocity (AUC-SV)

Analytical ultracentrifugation sedimentation velocity (AUC-SV) experiments were carried out with Dr. Stephen McLaughlin at 20 °C in a Beckman Optima XL-A analytical ultracentrifuge following standard protocols (Zhao *et al*, 2013). Samples were analysed at 35,000 RPM. 430 µl of samples were loaded in 2-channel centrepiece cells and data were collected using the absorbance (280 nm) and interference (655 nm) optical detection systems. Sedimentation data were time-corrected and analysed in SEDFIT 15.01c (Cole *et al*, 2008).

2.17 Sedimentation Equilibrium (AUC-SE)

Analytical ultracentrifugation sedimentation equilibrium (AUC-SE) experiments were carried out with Dr. Stephen McLaughlin, in a buffer of 20 mM HEPES pH 7.5, 100 mM NaCl, 1 mM TCEP. Samples were loaded into 12 mm 6-sector cells, placed in an An-50Ti rotor and centrifugated at 10,200, 12,200 and 21,000 rpm at 20 ˚C until equilibrium had been reached

using an Optima XL-I analytical ultracentrifuge (Beckman). The data were analysed in SEDPHAT 15.2b (Schuck, 2003). The partial-specific volumes (v-bar) were calculated using Sednterp (Cole *et al*, 2008). The density and viscosity of the buffer were determined with a DMA 4500M density meter (Anton Parr) and a AMVn viscometer (Anton Paar). Data were plotted with the program GUSSI (Brautigam, 2015).

2.18 SEC-MALS

Size-exclusion was coupled with multi-angle light scattering (SEC-MALS). Experiments were performed using an Agilent 1200 series LC system with an online Dawn Helios ii system (Wyatt) equipped with a QELS+ module (Wyatt) and an Optilab rEX differential refractive index detector (Wyatt). In each experiment, 110 µl of purified protein from 0.5-3.0 mg/ml was auto-injected onto a Superdex 75 (or 200) 10/300 GL column (GE healthcare) or a Superose 6 increase 10/300 GL column (GE Healthcare) and run at 0.5 ml/min. The molecular masses were analysed with ASTRA 7.3.0.11 (Wyatt). Data were plotted using Prism 8.4.3 (GraphPad Software, Inc).

2.19 In-gel cross-linking mass spectrometry (IGX-MS)

Purified complexes of the tetrameric Mad1Δ485:C-Mad2ΔR133A complex, as well as the non-phosphorylated and phosphorylated hexameric Mad1Δ485:C-Mad2:O-Mad2 complexes were cross-linked following the published IGX-MS workflow (Hevler *et al*, 2021). Respective complexes were mixed with NativePAGE sample buffer, and subsequently, 15 µg of each sample was run onto a Bis-Tris gel (3–12%). For cross-linking, bands corresponding to tetrameric and hexameric Mad1:Mad2 complexes were excised, rinsed with distilled H2O and subsequently cross-linked (in triplicates) with either 1.5 mM DSS or 20 mM DMTMM for 30 mins at RT. The reaction was quenched by the addition of Tris to a final concentration of 50 mM. Following classical in-gel digestion (Shevchenko *et al*, 2007), cross-linked proteins were washed, reduced and alkylated prior to trypsin digestion. For MS analysis of cross-linked peptides, the samples were re-suspended in 2 % formic acid and analysed using an UltiMate™ 3000 RSLCnano System (ThermoFisher) coupled on-line to an Orbitrap Exploris 480 (ThermoFischer). Peptides were trapped for 5 mins in 0.1 % FA in water, using a 100-µm inner diameter 2-cm trap column (packed in-house with ReproSil-Pur C18-AQ, 3 µm) prior to separation on an analytical column (50 cm of length, 75 µM inner diameter; packed in-house with Poroshell 120 EC-C18, 2.7 µm). Trapped peptides were eluted following a 60 min gradient from 9-40 % of 80 % ACN, 0.1 % FA. Full scan MS spectra

from 350-1600 m/z were acquired in the Orbitrap at a resolution of 60,000 with a normalized AGC target of 300 % and maximum injection time of 120 ms. Only peptides with charged states 3-8 were fragmented, and dynamic exclusion properties were set to n = 1, for a duration of 30 s. Fragmentation was performed using a stepped HCD collision energy mode (27, 30, 33 %) in the ion trap and acquired in the Orbitrap at a resolution of 30,000 with an AGC target set to 500 %, an isolation window of 1.4 m/z and a maximum injection time of 54 ms. Raw files obtained for respective IGX-MS experiments were subsequently analysed with pLink2 (Chen *et al*, 2019). FDR (controlled at PSM level for cross-linked spectrum matches and separately computed for intra and inter cross-links) rate was set to 5%. The obtained cross-links were plotted onto previously published structures (PDB ID: 4DZO, 2V64, 1GO4) using an in-house python script for PyMOL (The PyMOL Molecular Graphics System, Version 1.2.3, Schrödinger, LLC) and further visualized using xiNET (Combe *et al*, 2015).

2.20 BS3 cross-linking for Cryo-EM

Purified homogenous Mad1:Mad2 complexes were crosslinked with the crosslinker BS3 (bis[sulfosuccinimidyl] suberate) (ThermoFisher). The specific crosslinking conditions for each complex was optimised by testing various temperatures, crosslinker concentrations, and reaction times which was then assessed by 4-12% NuPAGE Bis-Tris gels as well as by size-exclusion chromatography and SEC-MALS. Generally, 2 mM BS3 was incubated with Mad1:Mad2 complexes at 0.3 mg/ml for 1 hr at 4 °C. BS3 was then quenched by adding 100 mM Tris-HCl at pH 8.0 and incubated on ice for 30 min. The cross-linked complex was then concentrated to 3.5 mg/ml and re-purified by size-exclusion chromatography, first on a Superdex 200 15/300 column (GE Healthcare), and then again on a Superdex 200 5/150 (GE Healthcare). The complex was cross-linked at only 0.3 mg/ml and then concentrated prior to SEC because it was found this decreased formation of cross-linked aggregates forming in the sample.

2.21 Methods for Protein Structure Determination

There are three main techniques which are used to gain detailed insights into the 3D structures of proteins and protein complexes: nuclear magnetic resonance (NMR) spectroscopy, x-ray crystallography, and cryo-electron microscopy (cryo-EM). Each method has its own unique advantages and as well as limitations. In this thesis, all three were used extensively to investigate different characteristics of the assembly of the mitotic checkpoint

complex onto kinetochores and data from each method were integrated to create a more complete understanding of these molecular processes.

X-ray crystallography, accounting for approximately 80% of all deposited structures (as of 2021) to the PDB, is the gold-standard method, as in theory it is not limited by size, and is generally the quickest, cheapest, and most automated method to determine atomic and near-atomic resolution structures. However, protein crystallisation not only requires large and highly concentrated amounts of sample, but also that the protein or complexes are rigid and homogenous enough to crystallise. Ultimately this means that very little conformational heterogeneity is tolerated, and the resulting structure only represents a static form of the molecule, rather than a dynamic one.

Cryo-EM on the other hand has debatably become the most powerful structural biology technique. It requires tiny amounts of sample (generally < 0.1 mg), has no upper size limit, and allows for substantial amounts of both sample heterogeneity and conformational variability. Additionally, due to many recent technological and image processing breakthroughs, cryo-EM can regularly obtain sub-3-4 Å resolution which allows accurate modelling of 3D protein structures. However, cryo-EM is not without its limitations, in particular it is severely limited by size, whereby proteins less than 100 kDa often cannot be solved to high-resolution unless they are substantially structured and homogenous. Additionally, cryo-EM requires that individual components of the protein complexes need to have relatively high binding affinity (approximately < 10 μM) to remain stable and together on EM grids, and thus weak protein-protein interactions are often unable to be captured.

NMR is a technique which arguably does not receive enough appreciation in the structural biology field. This is because it is mostly limited to small proteins (< 50 kDa), it requires expensive isotopic labelling of proteins, and although best at handling conformational heterogeneity, like crystallography, it requires large quantities of highly pure sample. However, NMR is able to provide detailed structural insights that neither cryo-EM nor crystallography can obtain. For example, NMR can unveil protein dynamics at an exceptionally wide range of time scales (ranging from picoseconds to seconds), which includes individual side-chain motion to global conformational change, and it is able to provide a close to physiological solution structure. Additionally, NMR can provide high-

resolution information of protein-protein interactions, even if they have very weak (low mM range) affinity.

2.22 Brief Introduction to NMR Spectroscopy

Reviewed in: Purslow *et al*, 2020; Teng, 2013; Marion, 2013; Keeler, 2010.

The core principle of NMR relies on the fact that nuclei possess a magnetic field as they are spinning and charged particles, and this magnetism allows measurement of the resonance frequency of a particular atomic nucleus which will be affected by its composition and interaction with surrounding atoms both intra- and inter-molecularly. Importantly, the effect of secondary structure, as well as the lack thereof, the spacing of atomic nuclei within these domains, and the dynamics of these domains, causes specific changes in an atom's resonance frequency. These changes can then be measured and carefully analysed to obtain detailed 3D information about a protein or complexes structure in solution. In particular, NMR can report the local chemical environment of an individual nucleus, either through space or through bond, thereby providing atomic-level resolution of the conformational changes occurring in a protein's structure.

Sample Preparation

Generally, proteins are labelled biosynthetically in *E. coli*, where bacterial growth occurs in minimal media, which is enriched with NMR active isotopes of carbon, nitrogen, and/or hydrogen. Whether the sample needs to be single-labelled (^{15}N), double-labelled ($^{15}N/^{13}C$), or triple-labelled ($^{15}N/^{13}C/^{2}H$) depends on the protein(s) size and the nature of the experiments. While ^{15}N labelling allows detection of the backbone N-H that provides the fingerprint spectrum of a protein, ^{13}C labelling allows detection of Cα, Cβ and CO that provides key structural information including secondary structure propensities. ^{2}H labelling or deuteration of side chains is normally applied to larger proteins that suffer from rapid relaxation through Cα-Hα. Generally, 300-500 µl of sample at 0.1-0.5 mM is required, and the protein of interests needs to be stable throughout data acquisition (which can take days / weeks).

Data Acquisition

During data acquisition, isotopically labelled proteins are placed in a strong magnetic field (> 700 MHz), such that the magnetic spins of individual nuclei will align with the external field along the z-axis. Subsequent pulses of radio frequency electromagnetic radiation will induce

the individual spins to oscillate at specific frequencies. The most basic NMR spectrum is a one-dimensional (1D) spectrum which displays the resonance frequency of a nucleus relative to a standard (normally sodium trimethylsilylpropanesulfonate (DSS) for protein NMR) in a magnetic field, called the chemical shift. For example, protons in water have a chemical shift of 4.7 ppm in a ^{1}H 1D spectrum, which corresponds to ~3,290 Hz difference from DSS (which is defined as 0 ppm) in a 700 MHz magnet. In principle, each NMR-active nucleus will give its own unique peak based on their resonance frequencies, however, these peaks will heavily overlap due to lack of resolution in a 1D spectrum, so multi-dimensional, homonuclear (^{1}H, ^{1}H) or heteronuclear (^{1}H, ^{15}N or ^{13}C) spectra are almost always required to resolve the overlapping resonances.

Backbone Assignment

Triple resonance experiments are used to identify each backbone resonance to its corresponding residue along the polypeptide chain. This is done by means of 'through-bond' experiments, in which a H_NNCAB spectra can be used to correlate each NH group within its own Cα and Cβ chemical shifts, while a CBCA(CO)NH_N spectra will only correlate with the NH group of its preceding Cα and Cβ chemical shifts. Therefore, these experiments not only provide the chemical shift information for the identification of different amino acids, but also provides the connectivity between residues that are essential for a complete assignment.

Protein Structure in Solution

The primary means to obtain structural information by NMR is through the measurement of nuclear Overhauser effects (NOEs). NOEs refer to the changes to a nuclear spin upon saturation of a nearby nuclear spin. It is particularly useful as it allows transfer of magnetisation through space and therefore provides spatial information between two nuclei. NOEs are inversely proportional to r^{-6}, where r is the internuclear distance, and are observable up to 5 Å. Intensities of NOE cross-peaks can therefore be translated into, distance constraints, together the chemical restraint refined by the backbone resonances. A 3D structural model which satisfies all geometrical constraints can be generated. As the secondary structure of a protein is dominated by its Cα and Hα orientation, secondary structural information is also readily available upon backbone assignment, where Cα and Cβ chemical shifts are obtained.

Chemical Shift Perturbations (CSP)

When a protein undergoes conformational change or interacts with another molecule, the chemical environment of certain residues will change, resulting in distortions to their chemical shifts, and this effect is known as a chemical shift perturbation (CSP). To put this into perspective, if you consider a protein-ligand interaction; when the protein is in the apo-state, any particular nucleus of an amino acid will have a unique chemical shift, and if upon addition of the ligand, the ligand binds a specific residue or binding of adjacent residues changes its relative position in space, there will be a change in that residue's environment and thus its chemical shift. Depending on the nature of the interaction, for example, the strength and if it causes conformational change, different rates of chemical exchange exist, generally being classified as slow, intermediate, or fast. The type of exchange which occurs ultimately determines what kind of CSP is seen.

Very strong interactions are more likely to have **slow** exchange, and this will result in both the apo and bound populations remaining stable across the duration of the NMR experiment (typically in the millisecond regime), and these two populations will result in two distinct peaks in the spectra. In a slow exchange interaction, if only a limiting amount of ligand is added, two stable populations will exist, and therefore two peaks simultaneously will be seen for a specific residue, one at the original apo position and the other in the bound position. If the ligand is then titrated to saturation, the initial peak will gradually disappear, and the new peak will grow in intensity, until the initial peak is no longer visible.

Analysing CSPs becomes more complicated if the rate of the exchange is in the **intermediate** range, as this often means the two populations do not remain stable across the length of the NMR experiment. Therefore, as the ligand is titrated, the affected apo-peaks will become significantly weaker or even no longer observable, and this phenomenon is called line-broadening. Line-broadened peaks may reappear, likely at new positions, when only one new state exists which lasts across the length of the experiment, usually as the ligand reaches saturation.

Lastly, CSPs are generally the most dramatic and easy to interpret when the interactions are weak, in the mM range, as these interactions give rise to **fast** exchange, such that a particular state only exists for part of the time it takes to record the spectra and therefore the observed

CSP will be a weighted average of the two states whose position can easily be tracked across ligand titration.

Ultimately, CSPs and line-broadening can both be analysed to give detailed insight into the location and strength of a binding event, as well as if any conformational change occurs upon binding. It is important however to remember that for any given CSP or line-broadening event, one cannot decipher if it comes from conformational change of those residues or actual binding.

2.23 NMR Spectroscopy Methods

Isotopic labelling for NMR spectroscopy

Expression of uniformly-labelled ^{15}N and/or ^{13}C proteins was done in M9 minimal media (6 g/L Na_2HPO_4, 3 g/L KH_2PO_4, 0.5 g/L NaCl) supplemented with 1.7 g/L yeast nitrogen base without NH_4Cl and amino acids (Sigma Y1251). 1 g/L $^{15}NH_4Cl$ and 4 g/L unlabelled glucose were supplemented for ^{15}N labelling. For $^{15}N/^{3}C$ double-labelled samples, the unlabelled glucose was replaced with 3 g/L $^{2}H^{13}C$-glucose. For the deuteration of nonlabile sidechain protons, cells were adapted for growth in first 10 %, then 44 % and finally 78 % deuterated media on agar plates before large-scale cultures were grown and supplemented with 1 g/L $^{15}NH_4Cl$ and 4 g/L $^{2}H^{13}C$-glucose in 99 % D_2O (Sigma).

NMR Spectroscopy

Prior to all NMR experiments, proteins were dialysed into 20 mM HEPES, pH 7.0, 100 mM NaCl, 1 mM TCEP. All NMR experiments were conducted by Dr Conny Yu and Dr Stefan Freund at the MRC-LMB NMR Facility. ^{1}H-detected experiments were performed on 600 MHz and 800 MHz Avance III spectrometers, both equipped with triple resonance TCI CryoProbes (Bruker). ^{31}P 1D NMR spectra were recorded on a 500 MHz Avance II spectrometer equipped with a broadband BBO cryoprobe (Bruker). ^{31}P 1D spectra were recorded using a standard ^{1}H decoupled sequence with power-gated decoupling and 30˚ flip angle. Some data were also acquired on a Bruker Avance III HD 950 at the MRC Biomolecular NMR centre at the Francis Crick Institute. All spectra unless otherwise denoted were collected in 20 mM HEPES, pH 7.0, 100 mM NaCl, 1 mM TCEP, 0.02% NaN_3 at 298K. Topspin 3.6 (Bruker) was used for processing and NMRFAM-Sparky 1.47 for data analysis (Lee *et al*, 2015).

Standard ^{2}H decoupled TROSY-based triple resonance experiments were used for backbone resonance assignments: HNCO, HN(CA)CO, HNCA, HN(CO)CA, HNCACB, HN(CO)CACB and HN(COCA)NNH (Pervushin, 2000). Backbone datasets were collected with 20-25 % non-uniform sampling and reconstructed using compressed sensing in MddNMR (Mayzel *et al*, 2014). Backbone assignments were obtained in Mars (Jung & Zweckstetter, 2004).

For binding studies, the relative peak intensities were normalized to the C-terminal residue Ala718 of $Mad1^{CTD}$ or Gly73 of $Cdc20^{1-73}$ and expressed as PI_{bound}/PI_{free}, with PI_{bound} and PI_{free} being the peak heights of the free and bound forms, respectively. Weighted chemical shift perturbations were calculated using the equation $\sqrt{(\Delta\delta^{1}H)^{2}+(0.2(\Delta\delta^{15}N)^{2})}$ with $\Delta\delta^{1}H$ and $\Delta\delta^{15}N$ being the chemical shift differences between free and bound states.

$^{15}N\{^{1}H\}$-heteronuclear NOE values are expressed as I/I_0 ratio and measured using standard Bruker pulse sequences, with interleaved on- (I) and off-resonance (I_0) saturation. Secondary chemical shifts were calculated from the differences between observed Cα/Cβ chemical shifts and Cα/Cβ chemical shifts for random coils (Kjaergaard & Poulsen, 2011).

2.24 Brief Introduction to X-Ray Crystallography

Reviewed in: (Wlodawer *et al*, 2013; McPherson & Gavira, 2014)

Protein structure determination by x-ray crystallography requires that the sample is first crystallised, then individual crystals are harvested and frozen in liquid nitrogen, exposed to X-rays to produce a diffraction pattern which can then be analysed to determine the structure of the repeating unit cell (which contains the protein or complex) within the crystal.

Crystallization

Protein crystallization is usually the rate-limiting step in X-ray crystallography. Crystallization requires that the protein(s) of interest be not only highly concentrated but also homogenous in both composition and conformation, such that when they reach a super-saturated state, normally by means of vapour diffusion, the molecules will be forced into a three-dimensional repeating lattice, which then forms a crystal. Generally, this is accomplished by systematically screening various buffers, pHs, protein concentrations, temperatures, and additives to find a potential hit. Once a hit, such as seeds, tiny crystals,

clusters or large but poorly diffracting crystals, is identified, further optimisation centred around the initial hit condition can be done to achieve diffraction-quality single crystals.

Data Collection

Generally, a focused collimated X-ray beam, usually produced by means of a synchrotron storage ring or a rotating anode, is fired at a cryo-protected frozen crystal held in a low X-ray scattering plastic loop, which is kept in a stream of liquid nitrogen and mounted on a goniometer head. The diffracted X-rays are then recorded on a detector, such as a charged coupled device (CCD) or more likely nowadays, a hybrid pixel detector (e.g. Eiger detectors from Dectris). Adjustment of the distance of the crystal from the detector determines the maximum resolution at the edge of the detector based on Bragg's law, and 3D information is usually obtained by rotating the crystal on a spindle which is perpendicular to the beam. The specific strategy for data collection, including the beam flux and the total angle of rotation, depends on several factors, including the crystal resistance to radiation damage, the required resolution, and the crystal symmetry.

Structure Solution

Producing an electron density map from a diffraction pattern is mathematically complex but at present day many automated software packages are available which more often than not makes structure solution incredibly quick and simple. The diffraction pattern is created from interference of x-rays scattered from the molecules comprising the unit cell and amplified by the crystal, where the spots are formed when x-rays interfere constructively rather than being cancelled out. Each spot in the diffraction pattern carries some information of the fourier transform of the whole electron density contained in the unit cell. To calculate the inverse fourier transform to compute the electron density map each spot is assigned a Miller index (h, k, l), and the intensities (amplitudes) of these spots are measured and scaled relative to each other. However, the amplitudes alone are not sufficient as the phases of the diffracted beams must also be calculated, and because the phases cannot be directly measured from the diffraction images, this is known as the 'phase problem', which can be solved in a variety of ways.

The most common and easiest method to gain phase information is by molecular replacement where an initial model from either a homologous protein or an already solved part of the complex, is used in rotational and translational searches to identify how the protein of interest

is placed inside the unit cell. These searches are carried out in Patterson space, which conveniently only requires knowledge of the observed amplitudes but not the phases. Otherwise, the phases must be calculated by other means, including isomorphous replacement where heavier atoms (usually metals) are introduced into the crystal and the change in the amplitudes of the diffracted beams can be used to determine the positions of the heavy atoms and thus provide phase information.

Once both the amplitudes and the phases are known, the electron density map can be calculated using a fast fourier transform (FFT) method and the protein model can then be built. Software packages are then used to iteratively refine the model to find the best fit to the experimental data as well as known chemical and geometrical restraints.

2.25 X-ray Crystallography Methods

Crystallization

Crystallization of Bub1^{CD1}-Mad1^{CTD}

Purified Mad1^{CTD} was concentrated to 11 mg/mL in 20 mM HEPES pH 8.0, 100 mM NaCl, and 1mM TCEP. Bub1 pSpT peptide (Table 2.9) (Designer BioScience) was solubilised with 100% DMSO to 50 mM. Mad1^{CTD} was mixed with 5 or 2.5 mM Bub1^{CD1} which meant that the final concentration of DMSO was 10 % or 5 %, respectively. Crystallisation trays were setup using a series of screening plates from the UKRI Medical Research Council (MRC), Laboratory of Molecular Biology (LMB) Crystallisation Facility (Jancarik & Kim, 1991; Gorrec & Löwe, 2018). Single drops were setup with final volumes of either 200 nL or 1000 nL of a 1:1 ratio of protein to reservoir solution using a nanolitre-dispenser Mosquito robot (TTP labtech) at ambient temperature. Crystals were grown using the sitting-drop vapor diffusion method at 20 °C. An initial hit was found in 10% iso-propanol, 0.1 M HEPES pH 7.5, and 20 % PEG 4000, which was in the sparse matrix pH 4.6-8.5 and stochastic sampling pH 3.6-9.0, LMB plate 1 screen (Hampton Research: HR2-110 & HR2-112). A 4-corner screen of this condition was setup, varying isopropanol from 5 %-15 % and PEG 4000 from 10 %-30 % while HEPES was kept constant (the 4-corner screen is outlined in, Gorrec and Löwe, 2018). The optimised crystals were fished within 35 hrs, as after that the crystals started to dissolve rapidly. The harvested crystal was immediately flash-frozen in liquid nitrogen using the reservoir solution supplemented with 20 % glycerol as a cryo-protectant.

Crystallization of Phosphorylated Mad1^{CTD}

Purified GST-Mps1 phosphorylated Mad1^{CTD} was concentrated to 5.5 mg/mL in 20 mM HEPES pH 7.5, 100 mM NaCl, and 1 mM TCEP. Hits for phosphorylated apo Mad1^{CTD} grew in LMB plate 19 (Pi-PEG: CS-128, Jena Biosceince) position 43, containing 11.4 % v/v PEG 400, 50 mM HEPES 7.1, 12.9 % w/v PEG 2000 MME. A 4-corner screen of this condition was setup varying the concentrations of PEG 400 and PEG 2000 from 5 % to 25 %, while HEPES was kept constant. The crystal structure was subsequently solved from a well of the 4-corner screen containing 7 % PEG 400, 40 mM HEPES pH 7.1, 21 % w/v PEG 2000. The reservoir supplemented with 30 % glycerol was used as a cryo-protectant.

Crystallographic Data Collection, Structure Determination, and Refinement

High-resolution data sets were collected remotely at beamline I04 at the Diamond Light Source, Didcot, U.K. Selected data sets were auto processed using the XDS pipeline in Xia2 (Kabsch, 2010; Winter, 2010). Phenix version 1.18.2-3874 was used for structure solution with PHASER-MR molecular replacement against PDB: 4DZO (Kim *et al*, 2012; Liebschner *et al*, 2019). The peptide was manually built in Coot (Emsley *et al*, 2010). Refinement was performed using PHENIX and validation with MolProbity (Williams *et al*, 2018). Phosphorylated Mad1^{CTD} data were collected in-house, using FrE+ SuperBright (Rigaku) X-ray generator, equipped with a Mar345DTB image plate (Mar). Data collection was completed using 180 degrees with one image per degree and 4 mins of exposure.

Single-wavelength anomalous dispersion

The crystals were harvested using LithoLoop sample mounts on specialized I23 copper sample assemblies. Data were collected and processed by Dr. Armin Wagner and Dr. Christian Orr on the long-wavelength beamline I23 at Diamond Light Source with an X-ray energy of 4.5 keV using the semi-cylindrical PILATUS 12M (Dectris, CH) (Wagner *et al*, 2016). 4.5 keV (2.775 A) was selected as this energy provides a good balance of increased signal from P and S atoms and reduced X-ray absorption by the crystal and solvent. Each dataset consisted of 360° with an exposure time of 0.1 s per 0.1° image. Multiple datasets per crystal were taken at varying kappa and phi values to ensure completeness and increased multiplicity. Data integration were performed with XDS and XSCALE (Kabsch, 2010). The origin of the PDB model was corrected using POINTLESS, AIMLESS and MOLREP (Evans, 2006; Winn *et al*, 2011). Phased anomalous difference Fourier maps were produced

using ANODE (Thorn & Sheldrick, 2011). A sigma cut-off of 4.0 was used to identify sites of anomalous contribution.

2.26 Brief Introduction to Cryo-Electron Microscopy

Reviewed in: Williams & Carter, 2009; Wagner, 1993; Glaeser, 2016; Van Heel *et al*, 2000. In transmission electron microscopy (TEM), electrons are transmitted through a specimen and the scattering density is captured onto a detector to create a 2D projection. Two types of electron scattering occur: high-resolution elastic scattering and low-resolution inelastic scattering. Inelastic scattering causes irradiation, charging of the specimen, and creates a poor signal-to-noise ratio (SNR). Beam damage is the major limitation of EM and is primarily combated by collecting low dose images with poor SNR. Higher resolution data were obtained by computationally averaging together thousands if not millions of 'single-particles' within these low dose images to increase the SNR. Software packages (CryoSPARC and Relion) then assemble the 2D projections into reliable 3D models through a process termed single-particle reconstruction.

The layout of an electron microscope is similar to an optical microscope (Fig 2.0). A coherent electron beam is created at the top and is transmitted down the column, passing through the sample. At several stages, the beam is manipulated by both lenses (magnetic coils) and apertures which focus the beam onto the sample and then again onto the detector. A high-vacuum within the microscope column is required to minimise interactions between the electrons and air. Cryo-electron microscopy was introduced as way to preserve specimens in the high-vacuum column and reduce electron bombardment damage without having to use negative-staining (Lepault *et al*, 1983; Adrian *et al*, 1984). Cryogenic temperatures reduce radiation damage as much as 6-fold, primarily because low temperatures trap and localise free radicals that are produced during sample irradiation (Schultz, 1988; Dubochet *et al*, 1985). Initially, 2D crystals were used to solve high-resolution structures at cryogenic temperatures. This is because simply freezing a protein solution in liquid nitrogen creates diffracting cubic ice which obstructs specimen electron diffraction. However, as discussed in the previous section crystallisation requires a lot of material, and many samples are unable to form 2D crystals.

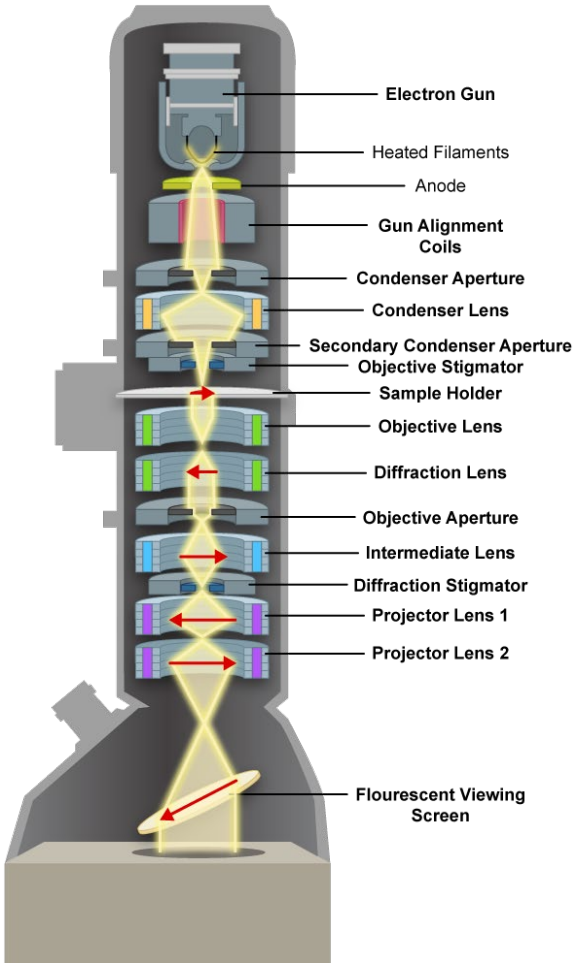

Figure 2.0: Image formation in TEM. *At the top, a coherent electron source is created using a field emission gun (FEG). To create a focused electron beam, a FEG uses one anode to create a strong electric field which is then applied to an ultra-thin tungsten needle and a second anode provides the accelerating force. Together, these two electrostatic lenses create a fine cross-over. The beam is first demagnetised through the condenser lens with the intensity of the beam being controlled by the condenser aperture. The transmitted electrons are then diffracted through the sample after which the objective lens refocuses the electron beam and the objective aperture creates amplitude contrast by excluding high-angled scattered electrons. The intermediate lens and projector lens further magnify and focus the beam onto a screen or detector. (Figure adapted from https://bio.libretexts.org/@go/page/10618)*

A huge breakthrough in cryo-EM, ultimately came from the discovery of amorphous ice by Dubochet and colleagues (Adrian *et al*, 1984; Schultz, 1988). When water freezes it forms a crystalline ice layer. However, if water is frozen sufficiently fast enough, it will solidify into an amorphous solid which does not significantly scatter electrons while the protein scattering intensity is sufficient enough to create contrast suitable for particle imaging. Amorphous ice also allows preserving proteins in a hydrated environment and therefore more native state. Although liquid nitrogen (-195 °C), is cold enough to quick freeze samples, its heat capacity is low enough that the water boils upon freezing, which slows down the freezing process enough to allow cubic ice to form. This is known as the leidenfrost effect (Dobro *et al*, 2010).

In contrast, liquid ethane (-180 °C) has a high enough heat capacity to create vitreous ice. This led to a now universally used plunge-freezing method for cryo-EM sample preparation. The sample is applied to a grid, excess liquid is blotted away, the grid is plunged into liquid ethane, and then transferred into liquid nitrogen for storage. Optimisation of sample blotting is key to creating a layer of ice which is thick enough to cover the protein and survive beam damage, but thin enough that the ice produces limited background signal.

Grid Preparation

Reviewed in: Russo & Passmore, 2016.

In electron microscopy, homogenous purified protein is applied to a grid of conductive material which is then inserted into the column under high-vacuum. Grids are normally 3.05 mm in diameter and contain a mesh with 200-400 squares per inch and contain a thin holey film (~12 nm) of carbon or gold with holes 1.2 μm in diameter and 1.3 μm spacing. These holes are important for attracting proteins and creating a thin ice layer. Gold grids have the advantage that they significantly reduce specimen movement and charging(Passmore & Russo, 2016). Typically, 3 μl of sample is applied to the grid and then blotted away prior to addition of negative stain or directly plunge-frozen in liquid ethane. EM grids are glow-discharged prior to sample addition to create a hydrophilic environment which attracts particles to the surface. Often a thin film of carbon is added on top of the grid as a specimen support layer prior to glow-discharging to increase the hydrophilicity and improve sample distribution.

Brief Introduction to Image Processing

As previously mentioned, to combat radiation damage, very low dose images with poor SNR are taken in cryo-EM. In simple terms, the 2D projections captured by the detector are the sum of the phase and amplitude contrasts of the scattered electrons. The amplitude contrast is determined by the loss of electrons due to inelastic scattering, however because biological samples mainly consist of light atoms such as H, C, N, O, which do not absorb or scatter electrons strongly, this renders the amplitude contrast almost negligible. Therefore, the phases which are created by the interference of unscattered and scattered electrons, provide most of the contrast and are the combined effect of collecting images slightly under focus and the spherical aberration of the lens. Unsurprisingly, these phase and amplitudes get distorted in several ways, including the contrast transfer function, the envelope function and beam-induced particle motion (Erickson and Klug, 1971). Software packages have therefore

evolved to correct for these artefacts which significantly increases the SNR. One of the most important improvements in the recent cryo-EM 'resolution revolution' has been direct electron detectors which makes it possible to account for beam-induced motion by tracking and correcting particle motion across multi-frame movies.

A 3D structure can then be solved from these corrected 2D projections in a process termed 'single-particle analysis' (SPA). First, hundreds of thousands, if not millions, of 2D projections are matched and aligned by orientation, confirmation, and homogeneity, to create 2D classes. 3D models are then generated using computer programs which determine the relative orientations of the 2D classes with respect to a 3D reference (Radermacher *et al*, 1986; Van Heel & Frank, 1981; Sigworth, 1998). A commonly used method to accomplish this is called 'projection-matching' whereby an initial reference structure is iteratively refined until it converges to the real structure (Penczek *et al*, 1994). Projecting-matching requires a good initial 3D reference, which for a long time was the rate-limiting step in SPA. Present day, one of the most popular methods is using a 'stochastic gradient descent-based' algorithm (SGD) (Mandt *et al*, 2017; Punjani *et al*, 2017). The SGD algorithm starts by making a random reconstruction from a small number of images and then over many small noisy steps, randomly selects a small subset of images and searches all possible 3D reconstructions while also evaluating their overall likelihood. One of the biggest advantages of SGD is that by only requiring the original particles it creates an unbiased reference.

After obtaining a good initial model, this model is then used to iteratively perform 3D refinement and classification. In each iteration, the initial model is used to create many different artificially high-signal projections which then each raw particle is then compared and aligned to its best match, after which all the projections are recombined in 3D space to create an improved 3D map. This process of re-projecting the 3D map and re-aligning each particle is iterated until convergence occurs and no further improvements can be made. Model building into the cryo-EM density map is then done in a very similar way to x-ray crystallography.

2.27 Electron Microscopy Methods

Grid Preparation

For Mad1-Mad2 complexes, copper Quantifoil 1.2/1.3, 300 mesh, grids were used. Grids were treated with a 9:1 argon: oxygen plasma for 45 s, after which 3.5 µl of purified complex

at 1.5-2.5 mg/ml supplemented with 0.05 % NP-40 was pipetted onto the grid at 4 °C and 100 % humidity before immediately blotting for 2 s and plunging into liquid ethane using a FEI Vitrobot Mark III (ThermoFisher).

Data Collection

Grids were generally screened on a 200 kv Glacios (ThermoFisher) equipped with Falcon 3 (ThermoFisher). Data were then collected at 300kv on a Titan Krios, equipped with a K2 or K3 detector (Gatan).

Image Processing Protocols

Image processing was carried out using Warp, CryoSPARC, and Relion 3.0 or 4.0 (Zivanov *et al*, 2018; Punjani *et al*, 2017; Tegunov & Cramer, 2019). The specifics of each complexes image processing are outlined in their respective results section. Beam-induced motion correction was used to align movies into a single micrograph in UCSF motioncorr2 (Zheng *et al*, 2017). CTF-correction was completed with Gctf (Zhang, 2016). Particle picking was done by manually training and then implementing a model in crYOLO (Wagner *et al*, 2019) or WARP (Tegunov & Cramer, 2019). Initial 3D reconstructions were created in CryoSPARC using an SGD algorithm (Punjani *et al*, 2017). 3D classification was usually completed in Relion. Once the best classes were found, a fine-angle search was conducted to further separate different confirmations within each class. Non-uniform refinement in cryoSPARC was generally used for 3D refinement (Punjani *et al*, 2020). 3D variability analysis was also completed in cryoSPARC. After 3D models with limited heterogeneity were found, Bayesian polishing was done to correct for beam-tilt induced particle motion (Bai *et al*, 2013; Zivanov *et al*, 2019). Bayesian polishing in addition to beam-induced motion correction sets a hypothetical value of particle trajectories to prior likelihood and sets a 'smooth' motion. Final maps were sharpened and filtered in a post-processing program within Relion and the local resolution of maps was estimated. The reported estimated final map resolutions were calculated based on the gold standard FSC = 0.143 or 0.5 criterion (GS-FSC) (Scheres & Chen, 2012; Chen *et al*, 2013; Neumann *et al*, 2018; Ramírez-Aportela *et al*, 2021).

2.28 Computational methods

Molecular analyses and structure alignments were performed with the UCSF Chimera package (Pettersen *et al*, 2004). Chimera is developed by the Resource for Biocomputing,

Visualization, and Informatics at the University of California, San Francisco (supported by NIGMS P41-GM103311). Molecular graphics were produced in PyMOL Molecular Graphics System, Version 2.3.3 Schrödinger, LLC. Protein structure predictions were completed using AlphaFold2 (Jumper *et al*, 2021) using the Notebook based environment (Mirdita *et al*, 2021). The majority of protein secondary structure predictions were performed with PHYRE2 or PSIPRED proteins sequence analysis workbench (Kelley *et al*, 2015; Jones, 1999; Buchan & Jones, 2019). Multiple sequence alignments were completed in BLAST (Altschul *et al*, 1990).

Gallery of Purified Proteins

Proteins were purified in accordance with section 2.6 and purified proteins used in this thesis are displayed in figure 2.1 below using SDS-PAGE analysis. Gels were stained with InstantBlue™ Protein stain (Expedeon). All proteins are of human origin.

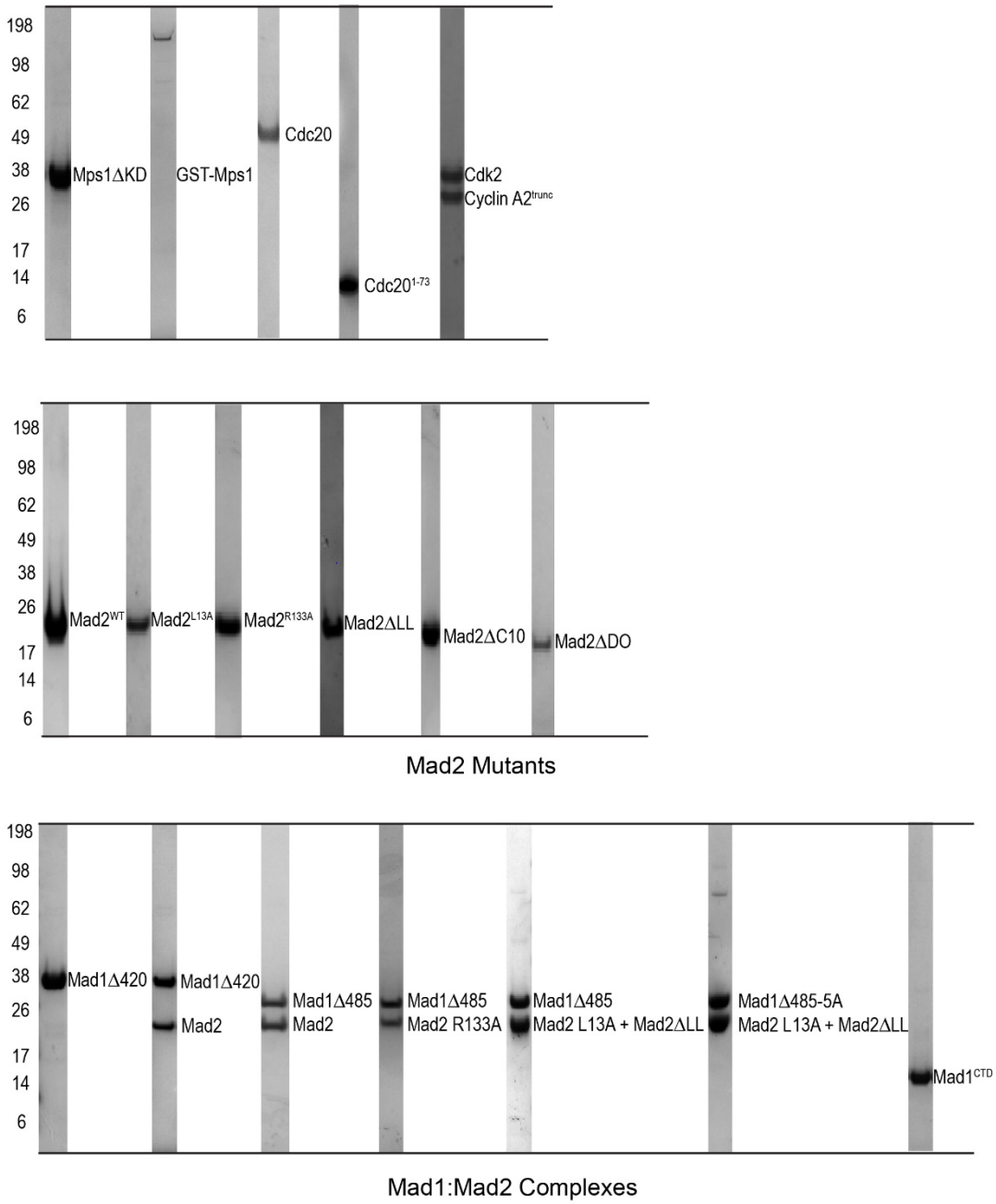

Figure 2.1: Gallery of key purified human proteins used in this thesis. *All proteins were analysed by SDS-PAGE using a 4-12% Bis-Tris Glycine gel with the SeeBlue™ Plus2 Protein Ladder (ThermoFisher).*

Chapter 3
The Bub1-Mad1 Interaction

This chapter contains work which has been published in Fischer et al, 2021. Any experiments or analyses which were not completed by me are duly acknowledged. Any sections of the manuscript not completed by me are rewritten.

3.1 Chapter Abstract

During the metaphase to anaphase transition, in response to improper kinetochore-microtubule attachments, the spindle assembly checkpoint (SAC), activates assembly of the mitotic checkpoint complex (MCC), an inhibitor of the anaphase promoting complex/cyclosome (APC/C). MCC assembly is under the control of the mitotic kinase Mps1, which orchestrates a phosphorylation-dependent signalling cascade to assemble the MCC at kinetochores. Key to this process is the Mad1-Mad2 complex, which when targeted to kinetochores through a direct interaction with the phosphorylated conserved domain 1 (CD1) of Bub1, acts as the platform for catalytic MCC formation. This chapter covers work completed which describes the molecular mechanism of Mad1 kinetochore targeting by phosphorylated Bub1. This includes a crystal structure of $Mad1^{CTD}$ bound to $Bub1^{CD1}$, unveiling how phosphorylation of Bub1 Thr461, not only creates a direct interaction with Arg617 of the conserved Mad1 RLK (Arg-Leu-Lys) motif, but also acts as an N-terminal cap to the CD1 α-helix dipole. We also discovered that surprisingly only one $Bub1^{CD1}$ peptide binds to the Mad1 homodimer in solution, and we suggest that this stoichiometry is due to inherent asymmetry within the coiled-coil of $Mad1^{CTD}$ and controls the $Bub1^{CD1}$-$Mad1^{CTD}$ interaction.

3.2 Chapter Background

Faithful chromosome segregation requires surveillance by the SAC, which in response to improper kinetochore-microtubule attachments, delays premature chromosome segregation until all errors can be fixed (Foley & Kapoor, 2013; Musacchio, 2015; Sacristan & Kops, 2015). Improper attachments activate the SAC, which then triggers production of the mitotic checkpoint complex (MCC), consisting of BubR1, Bub3, Mad2, and Cdc20 (Sudakin *et al*, 2001; Chao *et al*, 2012). The MCC functions by binding and inhibiting the E3 ubiquitin ligase, the anaphase promoting complex/cyclosome (APC/C), when the APC/C is bound and activated by a second molecule of Cdc20 (Alfieri *et al*, 2016; Herzog *et al*, 2009; Izawa &

Pines, 2015; Yamaguchi *et al*, 2016) . Inhibition of the APC/C then delays premature chromosome segregation by preventing APC/C-mediated degradation of two key cell cycle regulators, cyclin B and securin (Clute & Pines, 1999; Cohen-Fix *et al*, 1996).

Recent work points towards hierarchical recruitment of SAC proteins onto the outer kinetochore, by means of an Mps1-dependent phosphorylation cascade, which creates a catalytic platform for MCC assembly (Dou *et al*, 2019; Faesen *et al*, 2017; Ji *et al*, 2017). However, the precise molecular mechanisms for how hierarchical recruitment of the various checkpoint proteins onto the kinetochore and how each protein contributes to the localization and stimulation of downstream components remains a major unresolved question in the field.

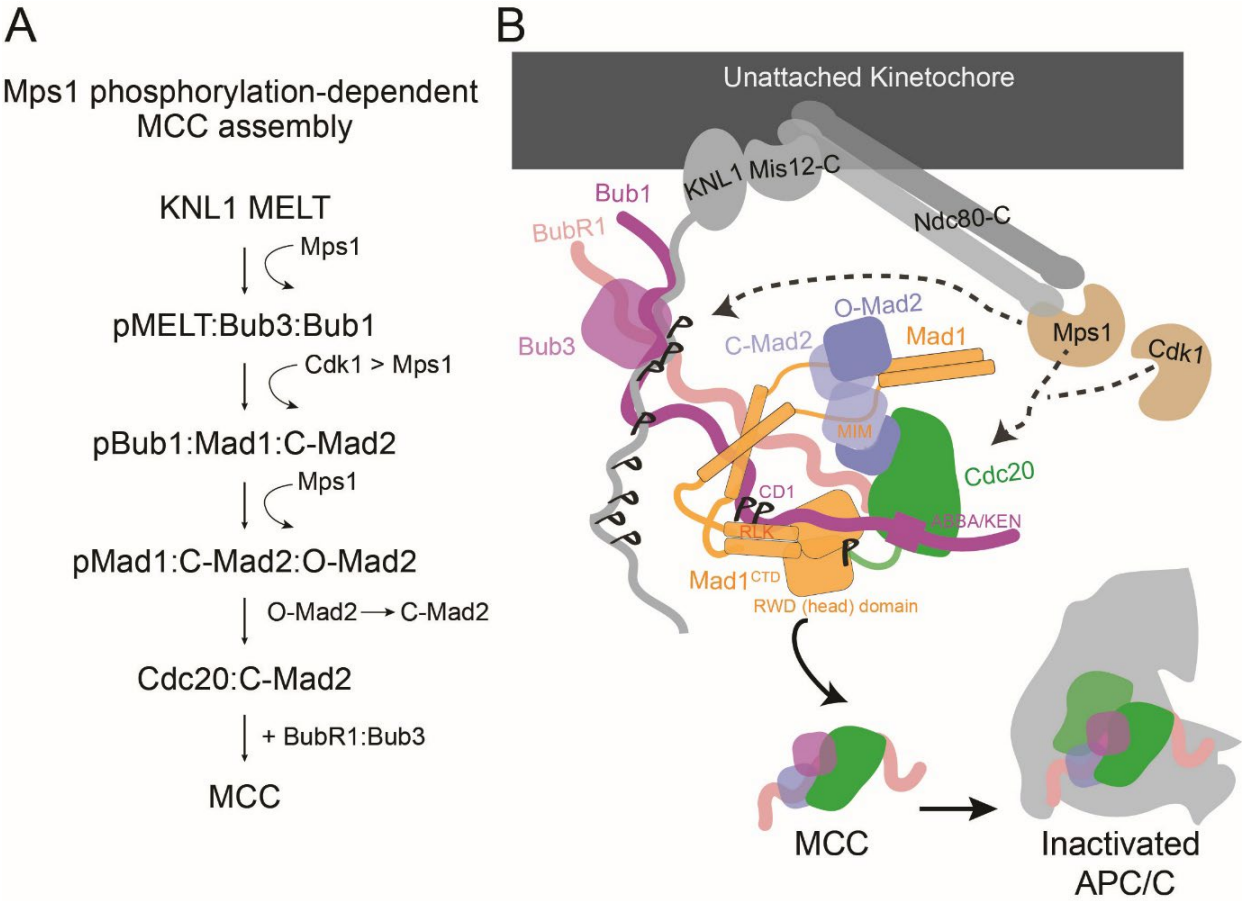

Figure 3.1: MCC assembly and the Bub1-Mad1-Mad2-Cdc20 complex at kinetochores. (A) *Outline of the crucial sequential steps of MCC assembly onto the outer kinetochore.* ***(B)*** *A schematic model of MCC assembly onto the outer kinetochore. All steps explained in detailed within the text below.*

The current consensus is that the signalling cascade starts with Mps1 phosphorylating several MELT (methionine-glutamate-leucine-threonine) motifs on the outer kinetochore protein Knl1, which then recruits Bub1 through its interaction with Bub3, as Bub3 preferentially binds phosphorylated MELT sequences (London *et al*, 2012; Primorac *et al*, 2013; Shepperd

et al, 2012; Vleugel *et al*, 2015; Yamagishi *et al*, 2012). Next, Mps1 phosphorylates Bub1 at a central conserved domain 1 (CD1), which then recruits the Mad1:C-Mad2 complex, likely through a direct interaction with the RLK motif of Mad1 (London & Biggins, 2014b, 2014a; Ji *et al*, 2017; Zhang *et al*, 2017). Schematics of human Bub1 and Mad1 are shown in Fig 3.2. Recently, a third phosphorylation event by Mps1 has also been identified in the C-terminal head of the Mad1 dimer, and this phosphorylation has been shown to significantly enhance the rate of MCC formation, possibly by promoting an interaction between Mad1 and Cdc20 (Ji *et al*, 2017; Ji *et al,* 2018).

Although the precise recruitment pathway of Cdc20 for MCC formation is still debated, it is likely that Bub1, through its ABBA and KEN1 motifs just C-terminal to the CD1 domain, plays a role in recruiting and repositioning Cdc20 close to the Mad1:C-Mad2 complex (Diaz-Martinez *et al*, 2015; Di Fiore *et al*, 2016; Lischetti & Nilsson, 2015; Zhang *et al*, 2019). In the last step of MCC assembly, cytosolic open-Mad2 (O-Mad2) is recruited to the Mad1:C-Mad2 complex through dimerization with closed-Mad2 (C-Mad2), and this O-Mad2 is then converted to C-Mad2 through what is believed to be a template conversion mechanism (De Antoni *et al*, 2005; Luo *et al*, 2004; Mapelli *et al*, 2007; Simonetta *et al*, 2009; Sironi *et al*, 2002). The newly converted C-Mad2 is then released from the Mad1:C-Mad2 complex and entraps the MIM motif of Cdc20. The MIM motif of Cdc20 is likely optimally positioned nearby by means of its interaction with Bub1 that is bound to Mad1. The Cdc20:C-Mad2 complex then has high affinity for BubR1, which is also thought to be positioned close-by through dimerization with Bub1, to generate the MCC (Chao *et al*, 2012; Faesen *et al*, 2017; Kulukian *et al*, 2009).

Altogether this suggests that activation of the MCC requires a finely tuned phosphorylation-dependent signalling cascade which utilises Bub1 as a key platform which not only targets Mad1:C-Mad2, BubR1, and Cdc20 to kinetochores but also repositions these components in close spatial proximity to allow efficient MCC assembly.

The importance of Bub1 phosphorylation to create the Bub1-Mad1 complex in SAC activation was discovered over two decades ago and it was at this time that the RLK motif of Mad1 was also identified as being essential for proper Mad1 kinetochore association and checkpoint activation (Brady & Hardwick, 2000). However, it was not until 2014, that a direct interaction between Bub1 and Mad1 was captured. London and Biggins identified in

budding yeast that Mad1^{CTD} only interacted with Bub1^{CD1} when it was phosphorylated by Mps1 at Thr453 and Thr455 (London & Biggins, 2014). Recapitulating this interaction in humans was initially more difficult, however several years later two independent studies confirmed this mechanism in human Bub1 and Mad1 whereby the Bub1-Mad1 interaction was dependent on sequential phosphorylation of Bub1 at Ser459 and Thr461 by Cdk1 and Mps1 kinases respectively (Ji *et al*, 2017; Zhang *et al*, 2017).

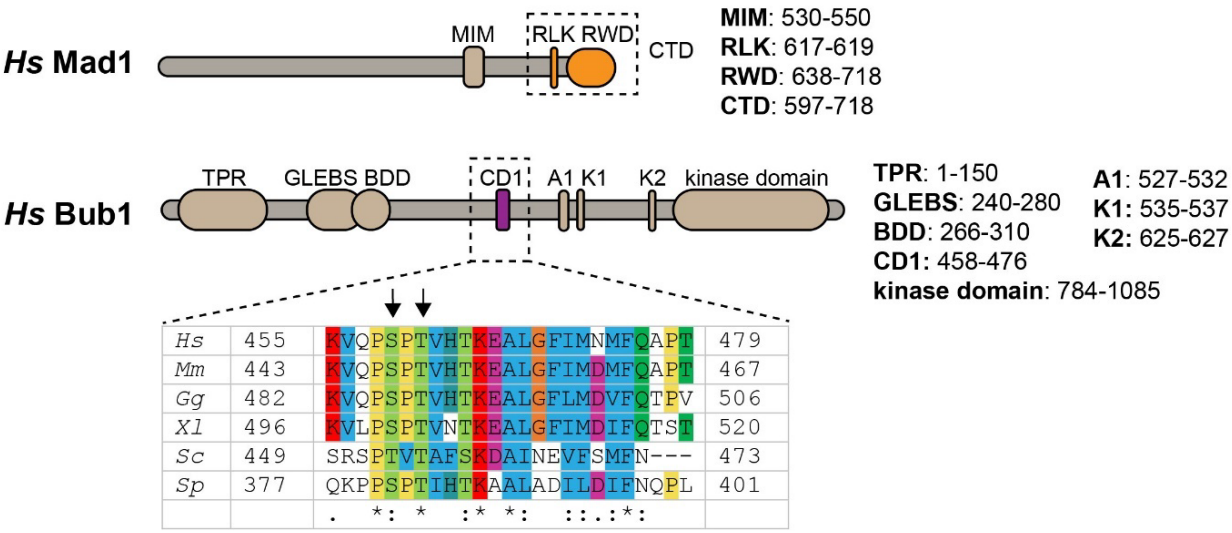

Figure 3.2: Schematics of full-length human Mad1 and Bub1*. The domains crystallized in this study are highlighted by dashed boxes. A sequence conservation map produced by ClustalX2 is shown for the Bub1^{CD1} domain. The two sites of phosphorylation (pSer459/pThr461) are highlighted by black arrows. A1: ABBA motif. K1/2: KEN box motifs. MIM: Mad2 interacting motif. CD1: conserved domain 1. BDD: Bub dimerization domain. GLEBS: Gle2-binding-sequence. TPR: Tetratricopeptide repeat. RLK: Arg-Leu-Lys motif. RWD: RING, WD40, DEAD domain.*

3.3 Chapter Aims

As previously mentioned, the initial goal when this project was started was to reconstitute Knl1:Mad1:C-Mad2:O-Mad2:Cdc20:Bub1:Bub3 complex and then use cryo-electron microscopy to investigate the molecular interactions of these components. Unfortunately, these efforts failed because a stable Bub1-Mad1 complex could not be captured, despite many attempts to enhance their interaction. Thus, the aim became to investigate the Bub1-Mad1 interaction in more detail and as there was no structure of the Bub1-Mad1 complex at all, we aimed to crystallise a peptide comprising the CD1 domain of Bub1 to Mad1 in the hopes it would reveal the overall architecture of the Bub1-Mad1 interaction and how sequential phosphorylation of Bub1 promotes Mad1 kinetochore targeting.

3.4 In solution only one Bub1^{CD1} binds to the Mad1^{CTD} homodimer

Before proceeding with crystallographic studies, ITC was performed to investigate the Mad1^{CTD}-Bub1^{CD1} interaction and to compare our results with the two prior studies which performed ITC and SPR on similar constructs (Ji *et al*, 2017; Zhang *et al*, 2017). The Bub1^{CD1} peptide sequence (residues 455-479) is shown in Fig 3.2, with the two sites of phosphorylation (Ser459 and Thr461) indicated. Using the doubly phosphorylated pSer459-pThr461 Bub1^{CD1} peptide binding to Mad1^{CTD} we obtained a K_D of 2.7 ± 1.2 μM which is similar to previous reports (Fig 3.3A). We were however surprised to find that only one Bub1^{CD1} peptide bound to the Mad1^{CTD} dimer. Neither prior study reported the stoichiometry of this interaction so we could not compare our results. This stoichiometry of only one peptide per Mad1 dimer was reproducible across eight repeat experiments including when a N-terminal tryptophan was added to the peptide to ensure accurate peptide concentration measurements and this N-terminal tryptophan did not alter the K_D of the interaction. Additionally, loading the peptide into the calorimeter cell rather than Mad1^{CTD} and titrating Mad1^{CTD}, resulted in the same stoichiometry (Fig 3.3B). We additionally, tested Bub1^{CD1} binding to the Mad1:C-Mad2 complex where the Mad1 truncation was extended to contain either residues 485-718 or 420-718 of Mad1, and although there was a slight decrease in the binding affinity for the tetrameric complex, the stoichiometry was clearly still conserved (Fig 3.3C-D). This suggests that the 1:1 ratio of Bub1^{CD1} to Mad1^{CTD} homodimer is likely to be conserved within full-length Bub1 and Mad1, however, we cannot exclude the possibility that the stoichiometry would differ when full-length constructs are used.

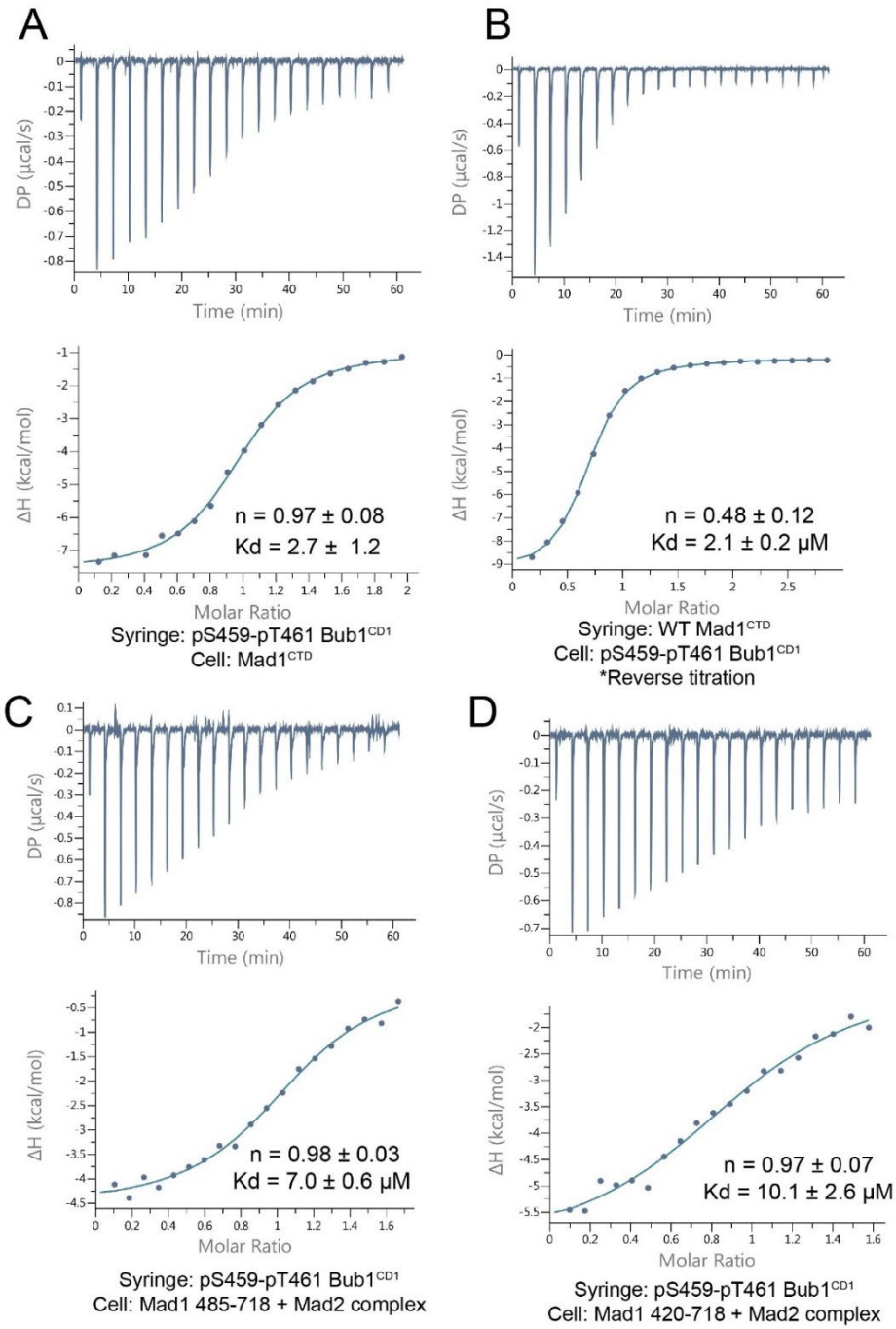

Figure 3.3: ITC of the Mad1^{CTD}-Bub1^{CD1} Interaction. *The KD and stoichiometry (n) values were obtained by averaging at least three experiments. The reported error values are calculated standard deviations.* ***(A)*** *Isothermal calorimetry (ITC) of Mad1^{CTD} binding to doubly phosphorylated Bub1^{CD1}. Bub1^{CD1} was injected into 0.45 µM Mad1^{CTD} in 19 injections of 2 µl, revealing a dissociation constant (K_D) of approximately 2.7 µM and a stoichiometry of 1:1 Mad1^{CTD} dimer to Bub1^{CD1} peptide.* ***(B)*** *Reverse titration of Mad1^{CTD} to doubly phosphorylated pThr461-pSer459 Bub1^{CD1} where Mad1^{CTD} concentration is stated as total monomer.* ***(C)*** *Titration of doubly phosphorylated pThr461-pSer459 Bub1^{CD1} to the Mad1:C-Mad2 tetramer with the Mad1 485-718 truncation.* ***(D)*** *Titration of doubly phosphorylated pThr461-pSer459 Bub1^{CD1} to the Mad1:C-Mad2 tetramer using the Mad1 420-718 truncation.*

The stoichiometry of the Mad1^{CTD}-Bub1^{CD1} interaction was further analysed using analytical ultracentrifugation sedimentation equilibrium (AUC-SE) with Dr. Stephen McLaughlin of the MRC-LMB biophysics facility (Fig 3.4). Mad1^{CTD} at 20 µM was tested by itself or mixed with either 20 µM or 40 µM of Bub1^{CD1} peptide. The calculated mass of Mad1^{CTD} alone was nearly identical to the expected mass of the Mad1^{CTD} homodimer, while both samples mixed with either a 1:1 or 1:2 molar ratio of Mad1^{CTD} to Bub1^{CD1}, had a calculated mass which was close to the expected mass of only one Mad1^{CTD} homodimer bound to a single Bub1^{CD1} peptide. This further confirms the 1:1 Mad1^{CTD} dimer to Bub1^{CD1} stoichiometry observed in our ITC experiments.

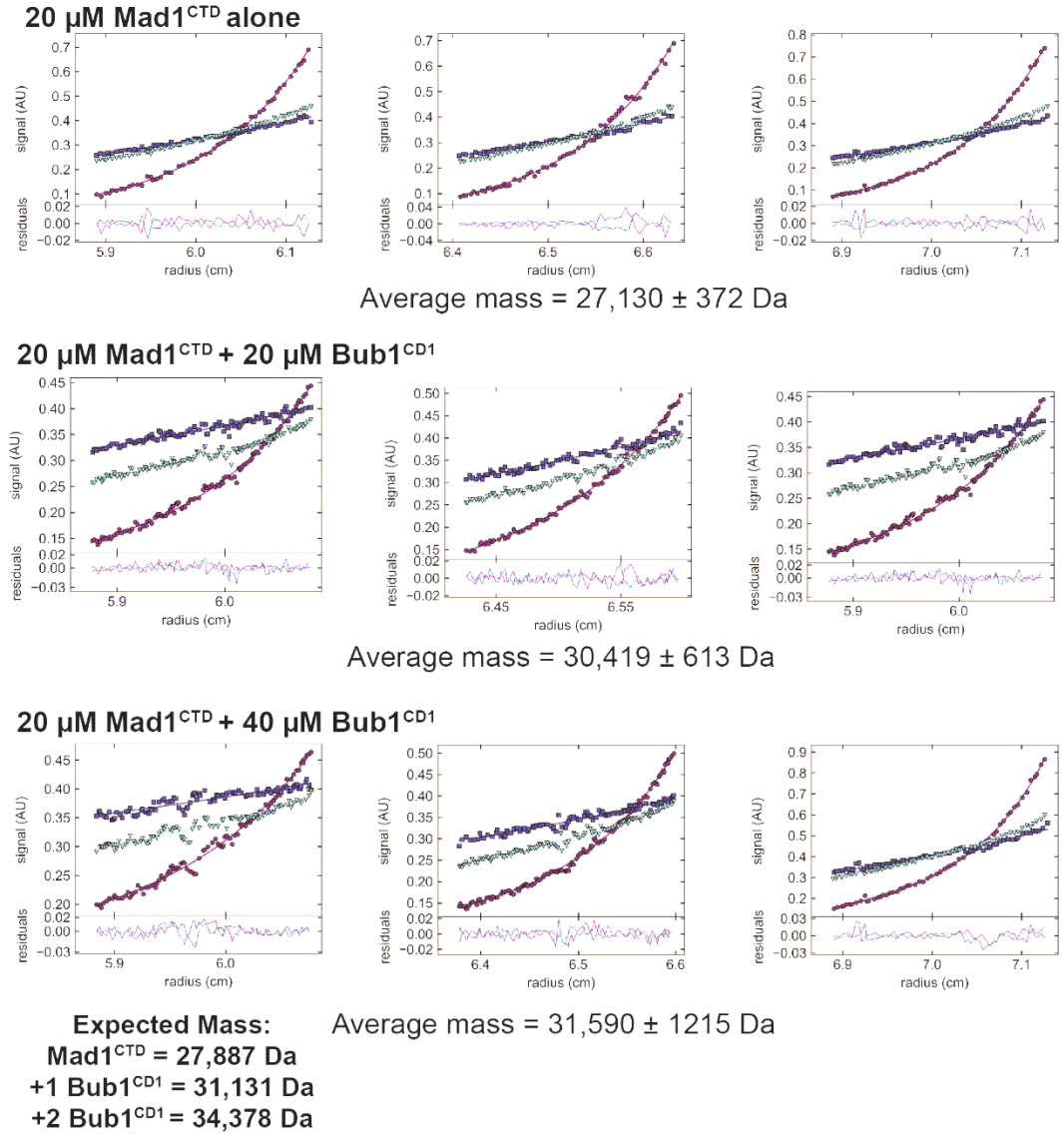

Figure 3.4: Analytical ultracentrifugation sedimentation equilibrium of Mad1^{CTD}-Bub1^{CD1} complexes. *Samples were run in triplicate. The data were fitted to a two species model where the mass of the Bub1^{CD1} peptide with an N-terminal tryptophan residue (3247 Da) was fixed. Standard errors are shown.*

We additionally used NMR spectroscopy to probe the Bub1^{CD1}-Mad1^{CTD} interaction. These experiments were completed by Dr. Conny Yu at the MRC-LMB NMR facility. By using ^{31}P phosphate 1D NMR, unique signals can be observed for pSer459 and pThr461 in the Bub1^{CD1} peptide (Fig 3.5). Bub1^{CD1} alone yielded not only two distinct peaks for the two phosphorylated residues but also splitting of the subsequently confirmed pSer459 signal. The two sites of phosphorylation are part of a Ser-Pro-Thr sequence and cis-trans proline isomerization of the Ser-Pro amide bond was identified as the result of the splitting of the pSer459 signal. At a 1:1 molar ratio of Bub1^{CD1} to Mad1^{CTD} dimer, the free pThr461 signal completely disappeared, while the pSer459 signal remained largely unchanged except for a small shift. This suggests that pThr461 is a key residue in the Bub1^{CTD}-Mad1^{CTD} interaction, while the pSer459 remains highly flexible and its chemical environment is only marginally altered by Mad1^{CTD} binding. We next added more Bub1^{CD1} peptide such that a 2:1 ratio relative to Mad1^{CTD} dimer was achieved, and this resulted in a spectrum with multiple signals for both phosphorylated residues. By overlaying the free and bound phosphorylated Bub1^{CD1} peptide peaks, it became clear that this spectrum showed the presence of unbound peptide, such that there is a reappearance of signal at the chemical shift position for unbound pThr461 and pS459 positions, as well as the bound peaks are still retained. Taken together, our ^{31}P NMR experiments support our ITC and AUC-SE data and suggest that at least for these truncations of Mad1 and Bub1, only one Bub1^{CD1} domain is able to bind to the Mad1^{CTD} homodimer.

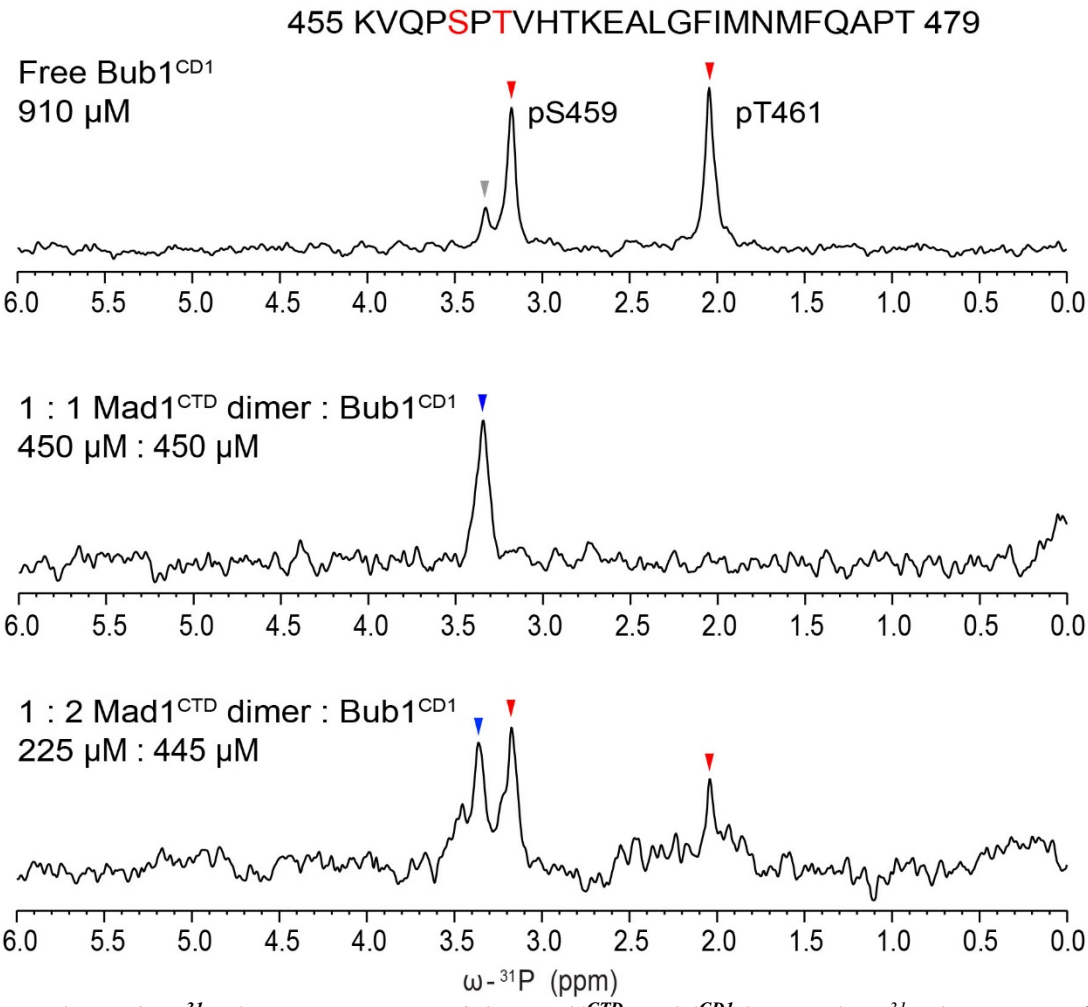

Figure 3.5: ^{31}P 1D NMR spectra of the Mad1^{CTD}-Bub1^{CD1} interaction. *^{31}P 1D spectra showing phosphorylated Bub1^{CD1} peptide titrated with an increasing concentration of Mad1^{CTD} dimer. The peptide sequence is shown above with the two phosphorylated residues highlighted in red. Peaks corresponding to pSer459 and pThr461 are marked with red arrows. The major pSer459 peak represents pSer459 in a trans Ser-Pro bond and the minor pSer459 peak (marked grey) represents pSer459 in a cis Ser-Pro bond. In the 1:1 molar ratio of Mad1^{CTD} dimer to Bub1^{CD1}, the pThr461 peak is significantly line broadened and the pSer459 peak (marked blue) is perturbed. In the 1:2 molar ratio of Mad1^{CTD} dimer to Bub1^{CD1}, in addition to signal for the bound pSer459, there is reappearance of the original free position of pS459 and unbound pThr461 supporting the presence of unbound peptide.*

We cannot exclude the possibility that the Bub1-Mad1 complex would present a different stoichiometry *in vivo*, however our results strongly point towards a mechanism by which only one Bub1 molecule binds to the Mad1 homodimer. This has interesting implications for how MCC is catalytically assembled onto the outer kinetochore, and this will be discussed more later on in this thesis. For example, it has been suggested that Mad1^{CTD} might fold back onto the Mad1:C-Mad2 core to promote template conversion of Mad2 from an open to closed state (De Antoni *et al*, 2005; Mapelli *et al*, 2007). If this fold-over model is correct, it might imply that only one site is either available or favourable for Bub1 binding. Our model of the Bub1-

Mad1-Cdc20 interaction at kinetochores (Fig 3.1) also might suggest that only one Cdc20 molecule can be accommodated at the head domain of Mad1^{CTD} proximal to the Thr716 phosphorylation site, especially if one side of the Mad1 head is already contacting the Mad1:C-Mad2 core. Therefore, this could be another reason only one Bub1 binds. Ultimately, this unusual stoichiometry made solving a structure of the Bub1-Mad1 complex all the more exciting in the hopes that the molecular details could answer some of these questions.

3.5 Crystallization of Mad1^{CTD}-Bub1^{CD1}

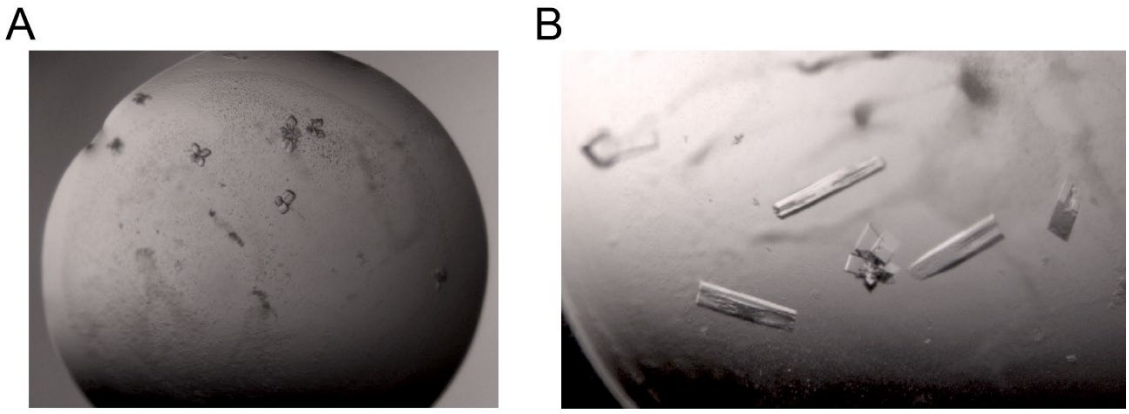

Figure 3.6: Crystallization of Mad1^{CTD}-Bub1^{CD1}. (A) *Initial Mad1^{CTD}-Bub1^{CD1} hits in LMB plate 1, position D5, which contained 10 % Isopropanol, 20 % w/v, PEG 4000, 0.1 M HEPES pH 7.5.* ***(B)*** *Optimised Mad1^{CTD}-Bub1^{CD1} hits used for high-resolution data collection at the Diamond Light Source.*

Co-crystallization Mad1^{CTD} and Bub1^{CD1} was initially tried using a screen based on the condition in which Apo Mad1^{CTD} was previously crystallised (20 mM Tris, 100 mM KCl, 1 mM TCEP, 26% (w/v) PEG1500, 0.1 M Na Cacodylate, pH 6.2, 1 mM reduced L-Glutathione), however no crystal hits were obtained. Next, apo Mad1^{CTD} crystals were obtained in this condition and soaking with either 1 mM Bub1^{CD1} dissolved in the crystallisation buffer or 2.5 or 5.0 mM Bub1^{CD1} which required 5 % and 10 % DMSO respectively. The DMSO was required as the pSpT Bub1^{CD1} peptide requires DMSO to remain soluble above 1.0-1.5 mM. In both cases the apo Mad1^{CTD} crystals dissolved after 4 hrs of soaking. Next 0.35 mM Mad1^{CTD} was mixed with 5 mM Bub1^{CD1} and screened using the entire LMB library of crystallisation plates (Gorrec and Löwe, 2018). Mad1^{CTD} was in a buffer containing 25 mM HEPES pH 7.5, 100 mM NaCl, 1 mM TCEP, while a 50 mM Bub1^{CD1} stock in 100 % DMSO was used, resulting in 10 % DMSO in the Bub1-Mad1 mixture and thus 5 % DMSO in the crystallisation drop after the sample was mixed with the reservoir solution. Hits were found in LMB plate 1, position D5, which contained 10 %

Isopropanol, 20 % w/v PEG 4000, 0.1 M HEPES pH 7.5 (Fig 3.6A). A 4-corner screen (outlined in Gorrec and Löwe, 2018) based on this condition was setup and larger hits were obtained and harvested for data collection (Fig 3.6B).

3.6 Overall Architecture of the Mad1^{CTD}-Bub1^{CD1} complex

We were able to obtain a near-atomic resolution crystal structure of human Mad1^{CTD} dimer bound to two doubly phosphorylated Bub1^{CD1} peptides, termed the Mad1^{CTD}-Bub1^{CD1} complex (Fig 3.7) (PDB: 7B1F). This was the first reported structure of phosphorylated Bub1^{CD1} and the Mad1^{CTD}-Bub1^{CD1} complex. Several datasets were collected, but the highest resolution crystal structure diffracted to 1.75 Å and belonged to the space group $P2_12_12_1$ with one Mad1^{CTD}-Bub1^{CD1} complex per asymmetric unit. However, due to strong anisotropic diffraction the actual resolution is closer to 2.1 Å. A summary of the data collection and refinement statistics is given in Appendix Table 1.

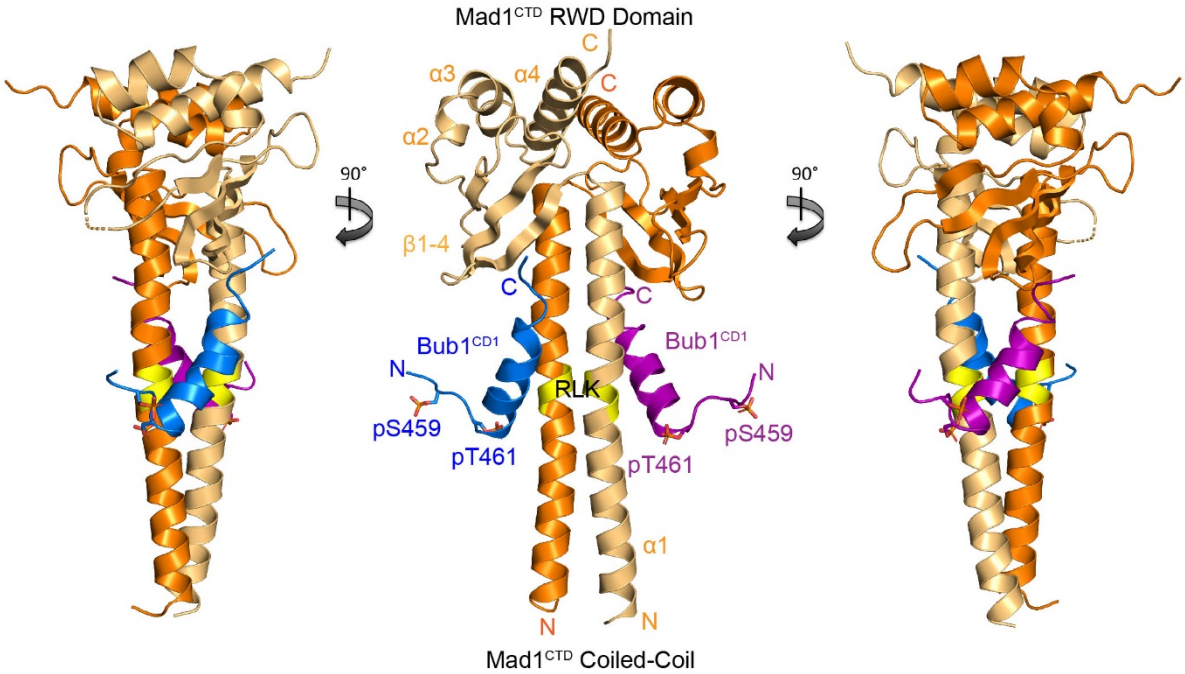

Figure 3.7: Overview of the human Mad1^{CTD}-Bub1^{CD1} interaction. *Three views of the crystal structure of Mad1^{CTD} homodimer (dark/light orange) bound to two Bub1^{CD1} peptides (purple/blue). The RLK motif of Mad1 is highlighted in yellow. The two phosphorylation sites are shown as sticks.*

The overall architecture of the Mad1^{CTD}-Bub1^{CD1} interaction is shown in Fig 3.7. We were surprised to see that the crystal structure contained two Bub1^{CD1} peptides bound to the Mad1^{CTD} homodimer, despite the clear 1:1 stoichiometry of Mad1^{CTD} to Bub1^{CD1} confirmed in solution by ITC, ^{31}P NMR and AUC-SE. This disparity in stoichiometry between the crystal structure and our biophysics data will be discussed later in section 3.11. In our crystal

structure, Mad1^{CTD} is comprised of an N-terminal elongated coiled-coil, followed by a globular head domain featuring a conserved RWD (RING, WD40, DEAD) fold, which agrees with the previously published crystal structure of apo Mad1^{CTD} (PDB:4DZO) (Fig 3.7) (Kim *et al*, 2012; Nameki *et al*, 2004; Petrovic *et al*, 2014a). Each chain of Mad1^{CTD} starts with an elongated stem formed by the N-terminal α-helix (α1), followed by a globular C-terminal head domain composed of an anti-parallel β-sheet of four β-strands (β1-4), a short helix (α2), and two C-terminal helices (α3/α4).

Each Bub1^{CD1} peptide is largely a single α-helix, consisting of almost four complete turns (Fig 3.7). We were able to build without ambiguity, 21 of the 26 residues of each Bub1^{CD1} peptide, while the first three and last two residues were not visible in the electron density map. Interestingly, each Bub1^{CD1} peptide contacts both Mad1^{CTD} monomers as the Bub1^{CD1} helix lies diagonally across the Mad1^{CTD} coiled-coil (Fig 3.7: left and right panels). The Bub1^{CD1} helix only starts with the second phosphorylation site, pThr461, while the six most N-terminal residues, including the first phosphorylation site pSer459, are disordered and do not directly contact Mad1. The diagonal interface of Bub1^{CD1}-Mad1^{CTD} results in the N-terminus of each CD1 helix contacting one Mad1^{CTD} monomer at the conserved Mad1 RLK motif by means of its interaction with the pThr461 site, whereas the C-terminal residues of Bub1^{CD1} contact the opposite Mad1 monomer starting from the top of the coiled-coil and its adjoining head domain β-sheet (Fig 3.7 and Fig 3.8A). The last three C-terminal residues of each peptide are disordered and seemed positioned to extend across the Mad1^{CTD} RWD-fold (Fig 3.8 A-B).

3.7 The Bub1-Mad1 interaction is mediated by pThr461

As previously discussed, SAC activation in response to unattached kinetochores promotes formation of the Mad1-Bub1 complex, a targeting mechanism which is conserved from yeast to humans and requires that Bub1 be phosphorylated at its central CD1 domain (Heinrich *et al*, 2014; London & Biggins, 2014b; Silió *et al*, 2015). Sequence alignment of the Bub1^{CD1} domain is shown in Fig 3.2. It is known that in *S. cerevisiae,* Mps1 phosphorylates the Bub1 CD1 domain at both Thr453 and Thr455 to promote an interaction between Mad1 and Bub1, with the pThr455 site alone being sufficient for a strong interaction (Ji *et al*, 2017; London & Biggins, 2014). In humans, it has been shown that the equivalent phosphorylation sites, Ser459 and Thr461, are also required, and similar to yeast, pThr461 alone is sufficient to promote the Bub1-Mad1 interaction, whereas pSer459 alone cannot

(Asghar *et al*, 2015; Daub *et al*, 2008; Ji *et al*, 2017; Zhang et al., 2017). Interestingly, in humans a more specific targeting mechanism has been identified where the Ser459 site is first phosphorylated by Cdk1 which then primes phosphorylation of the Thr461 site by Mps1 (Ji *et al*, 2017b; Qian *et al*, 2017). In contrast to yeast where a T453A mutation does not signficantly affect the Bub1-Mad1 interaction or checkpoint viability, a S459A mutant in human Bub1, inactivates Bub1-mediated Mad1 kinetochore recruitment (Zhang *et al*, 2017). This strongly suggests that this priming mechanism of Mps1 phosphorylation of Thr461 by Cdk1 phosphorylation at Ser459 is critical for $Bub1^{CD1}$ functionality.

Our crystal structure reveals that the phosphate group of pThr461 forms a strong interaction with Mad1 through a charged hydrogen bond with Arg617 of the Mad1 RLK motif (Fig 3.8 A and C). The phosphothreonine additionally makes further contacts with the amide backbone of its own chain, and this results in the Bub1 His463 imidazole sidechain hydrogen bonding with Ser610 of Mad1 (Fig 3.8C). This is in contrast with the phosphoserine site which does not contact Mad1, but is instead part of the disordered N-terminal tail of the CD1 helix (Fig 3.8 A and C).

We also performed phosphorus single-wavelength anomalous dispersion (SAD) at the Diamond Light Source with Dr. Christian Orr and Dr. Armin Wagner (Fig 3.9 A-D; Appendix Table 2). These data clearly show anomalous density for the phosphorous atom of the phosphothreonine at each site built in our structure (Fig 3.9 B-C). Furthermore, there are no clear signals for the phosphoserine on either chain which agrees with our crystal structure in which the pSer459 is not directly contributing to the $Mad1^{CTD}$-$Bub1^{CD1}$ interaction.

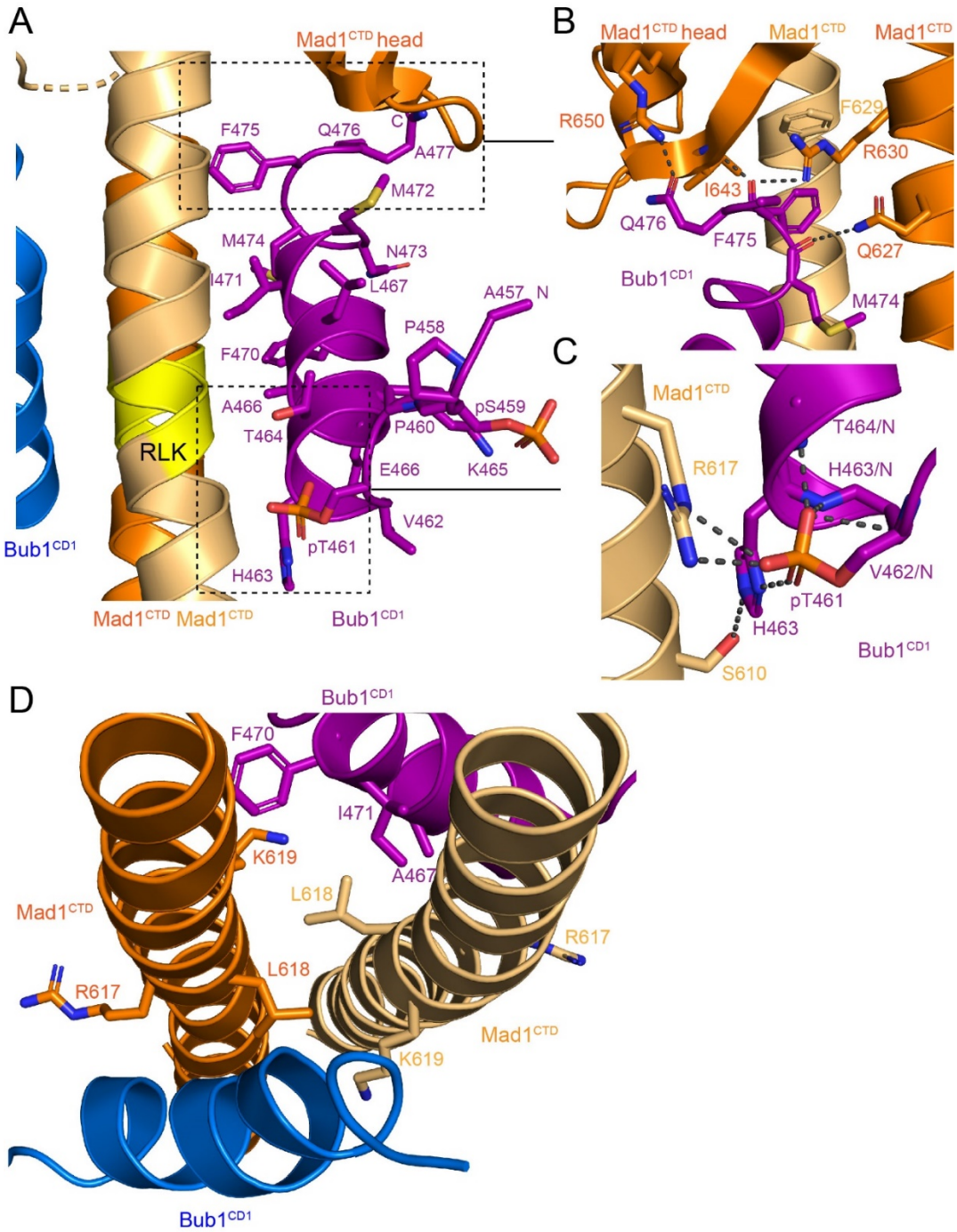

Figure 3.8: Molecular Interactions of the Mad1^{CTD}-Bub1^{CD1} complex. ***(A)*** *The extensive largely hydrophobic interface of the Mad1^{CTD}-Bub1^{CD1} interaction is highlighted with the higher occupancy CD1 peptide (purple). The RLK motif of Mad1 is coloured yellow.* ***(B)*** *Close up view of Bub1^{CD1} interactions with the head domain of Mad1^{CTD}. Hydrogen bonding interactions within 3.5 Å are highlighted by black dashes.* ***(C)*** *Close up view of the Mad1 Arg617 and Bub1 pThr461 interaction. An additional contact occurs between the phosphate of pThr461 and Bub1 His463 which then forms a hydrogen bond with Mad1 Ser610. Additional stabilizing hydrogen bonding occurs between the pThr461 phosphate and the amide nitrogen of Val462, His463, and Thr464. Hydrogen bonding interactions within 3.5 Å are highlighted by black dashes.* ***(D)*** *Top view of the conserved RLK motifs of the Mad1 homodimer which are shown as sticks. The sidechains of hydrophobic residues near the RLK site at the surface of Bub1^{CD1} are shown as purple sticks which form a hydrophobic pocket.*

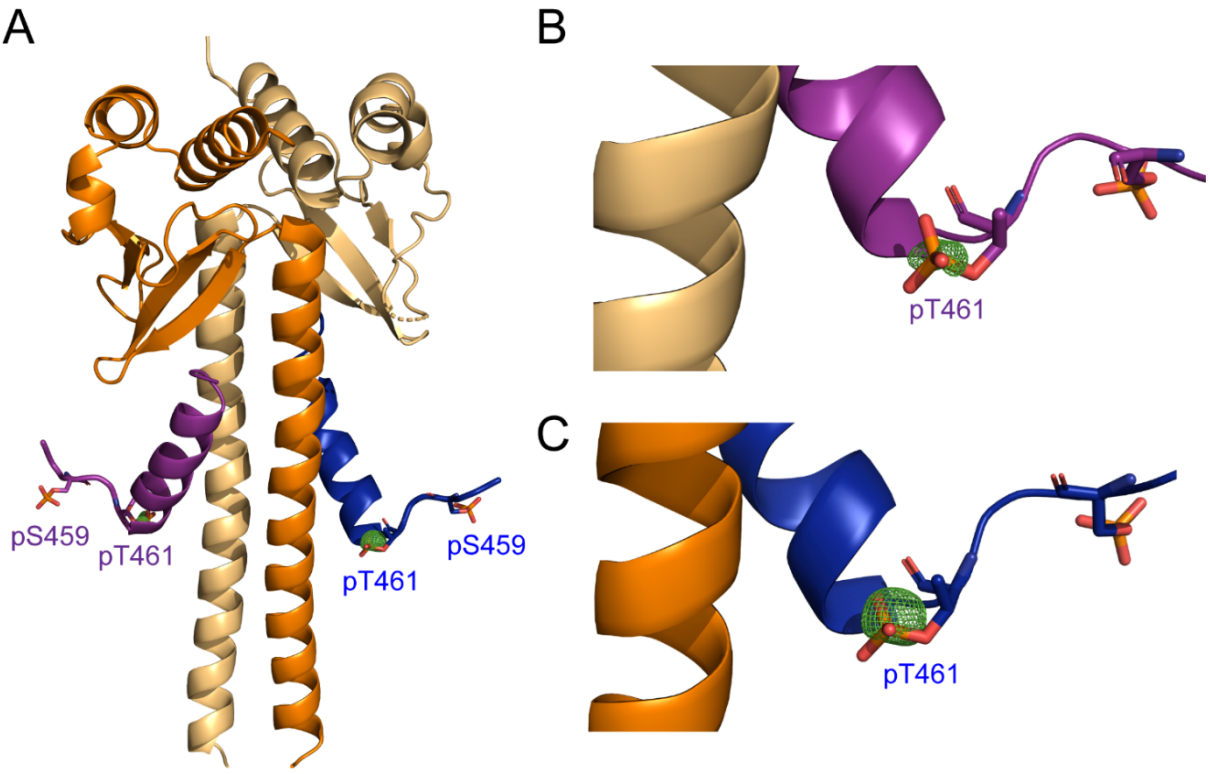

D

Nearest Atom	Distance to closest atom (Å)	Anomalous peak height (sig)
SG A:CYS65	0.605	15.30
SD A:MET78	1.040	10.24
SG B:CYS65	0.880	7.17
SG B:CYS36	0.481	6.95
CE B:MET78	0.824	6.25
SG A:CYS36	0.782	5.67
O B:GLY63	2.226	5.18
CB A:CYS36	1.876	5.14
O2P C:TPO4	1.165	5.06
O2P D:TPO4	1.595	4.82
CG D:MET17	2.352	4.45
OG1 D:TPO4	0.847	4.42
CG C:MET17	0.713	4.41
CA A:THR27	1.213	4.40
O2P C:TPO4	2.544	4.26
CG2 A:VAL24	2.315	4.17

Figure 3.9: Phosphate SAD of the Bub1^{CD1}-Mad1^{CTD} complex. (A) *The crystal structure of Bub1^{CD1}-Mad1^{CTD} with the anomalous signal for the phosphate groups of the two phosphorylated threonine residues shown as green mesh.* ***(B)*** *Close-up view of the phosphothreonine anomalous signal on subunit D.* ***(C)*** *Close-up view of the phosphothreonine anomalous signal on subunit C.* ***(D)*** *The strongest unique anomalous peaks as reported by ANODE with a cut off of 4.0 sigma (Thorn & Sheldrick, 2011). The anomalous peak heights corresponding to the phosphate of the phosphothreonine are highlighted in red.*

A striking feature of the Mad1^{CTD}-Bub1^{CD1} interaction is that the pThr461 is positioned at the start of the CD1 helix such that the phosphate group caps the N-terminus of the helix and stabilizes the positively-charged helix dipole with its bulky negative charge (Fig 3.8 A and C). The stabilization of α-helices through compensation of the α-helix macro-dipole by

capping residues is widely recognized (Chakrabartty *et al*, 1993; Hol *et al*, 1978; Wada, 1976). Our study reveals how this helix-dipole capping can be achieved and regulated by phosphorylation, and is reminiscent of α-helix stabilization by phosphorylation of Ser46 in the bacterial protein HPr (Pullen *et al*, 1995; Thapar *et al*, 1996). Interestingly, secondary structure prediction of the Bub1^{CD1} domain suggests that the helix of unphosphorylated CD1 would only start from Thr464, further hinting that pThr461 helps to stabilize an extended helix (Fig 3.10). Additionally, examination of the ^{1}H 1D spectra of the non-phosphorylated and phosphorylated Bub1^{CD1} peptides reveals that both peptides are disordered when unbound in solution based on the narrow dispersion of their amide peaks (Fig 3.11A). Previous circular dichroism experiments also suggested that the unbound Bub1^{CD1} peptide is unstructured but might have helical propensity that is increased with Thr461 phosphorylation (Zhang *et al*, 2017). This implies that Mad1 binding induces the Bub1^{CD1} domain to adopt a helical conformation, a mechanism which likely enhances the specificity of Thr461 phosphorylation as a regulatory mechanism in promoting the Mad1^{CTD}-Bub1^{CD1} interaction.

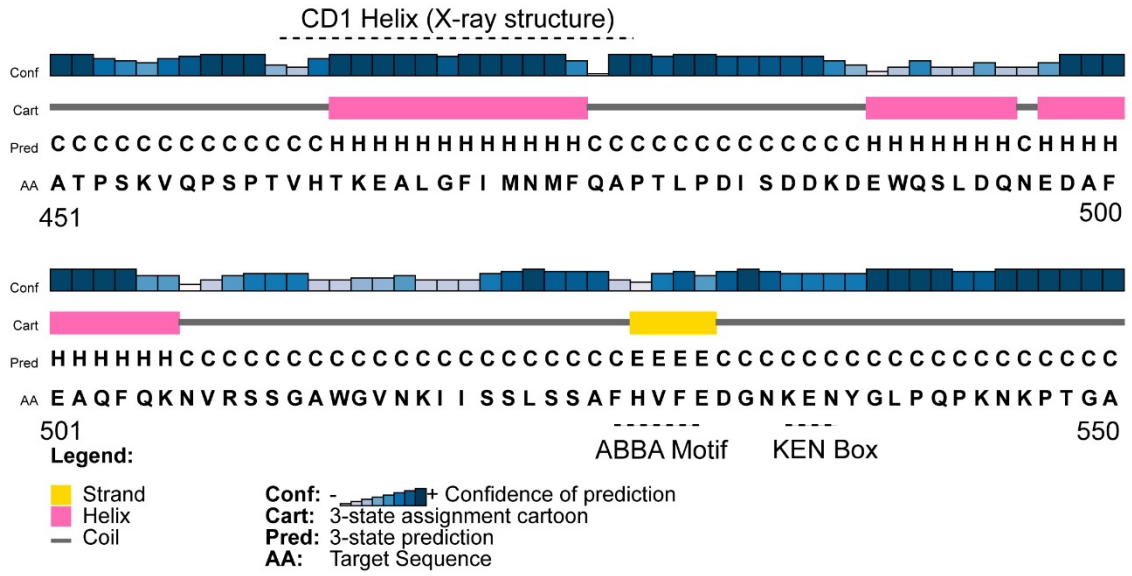

Figure 3.10: Secondary structure prediction of Human Bub1 (residues 448-553) *which includes the CD1, ABBA, and KEN1 domains of Bub1 (Buchan and Jones, 2019). The length of the CD1 helix present in the X-ray structure is shown as well as the location of the ABBA and KEN1 motifs.*

We also assessed binding of the non-phosphorylated Bub1^{CD1} peptide to Mad1^{CTD} using ITC and observed no binding (Fig 3.12). Additionally, as assessed using NMR spectroscopy completed by Dr. Conny Yu, titration of the non-phosphorylated peptide into ^{15}N labelled Mad1^{CTD} also failed to reveal Bub1-Mad1 interactions (Fig 3.11B). NMR can readily detect weak binding in the mM range further highlighting the essential role of phosphorylating

Thr461 in order to promote the Bub1-Mad1 interaction. We additionally tested the binding of an R617A mutant of Mad1 by ITC and found that it severely weakened the Bub1^{CD1}-Mad1^{CTD} interaction to the millimolar range (Fig 3.12). However, as it does not completely abolish binding, unlike the non-phosphorylated peptide, this further confirms the additional effects of the phosphothreonine on the Bub1^{CD1}-Mad1^{CTD} interaction.

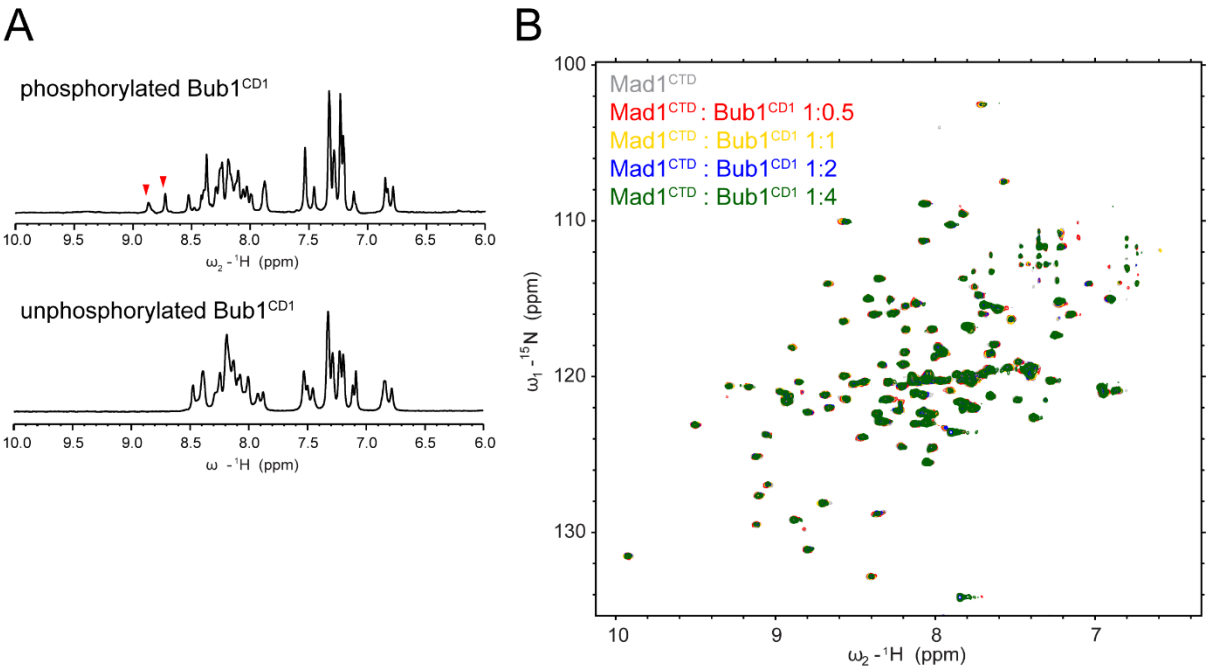

Figure 3.11: Titration of phosphorylated Bub1^{CD1} peptide into Mad1^{CTD}. *(A) ^{1}H 1D spectra showing the amide regions of phosphorylated and unphosphorylated Bub1^{CD1} peptides. The narrow dispersion of the amide peaks suggests both peptides are unstructured. The red arrows highlight two peaks that were shifted downfield upon phosphorylation, most likely corresponding to the phosphorylated Ser459 and Thr461.* ***(B)*** *^{1}H,^{15}N-2D HSQC showing ^{15}N-labelled Mad1^{CTD} with an increasing concentration of unphosphorylated Bub1^{CD1} peptide. In molar ratios of Mad1^{CTD} dimer to Bub1^{CD1}, peptides were added at 1:0.5 (red), 1:1 (yellow), 1:2 (blue) and 1:4 (green) ratios. There is no observable change in chemical shifts or peak intensities.*

Altogether, this work strongly suggests that the phosphate group of pThr461 promotes a direct interaction to Mad1 through not only its interaction with Arg617 as suggested by the crystal structure, but also by promoting conformational changes within the Bub1 CD1 motif. This work, together with the fact that Cdk1 phosphorylation of Ser459 primes Mps1 phosphorylation at Thr461, nicely explains how phosphorylation by Mps1 creates a highly specific interaction between Bub1 and Mad1 and allows for a finely-tuned regulation of the mitotic checkpoint complex.

We also note that phosphorylation of Bub1 CD1 Thr464, three residues C-terminal to the Thr461 phosphorylation, has been previously reported (Fig 3.8A) (Ji *et al*, 2017). *In vitro* analysis suggests that a triply phosphorylated pSer459-pThr461-pThr464 peptide had significantly lower affinity for Mad1 than the doubly phosphorylated peptide (Ji *et al*, 2017). Our crystal structure explains that a bulky phosphate at Thr464 would clash with the Bub1-Mad1 interface which could explain this. It is therefore possible that negative regulation of the Bub1-Mad1 interaction could be accomplished by Thr464 phosphorylation in response to certain checkpoint signals.

3.8 Contribution of the phosphoserine site

Both previous studies which investigated the contribution of the phosphothreonine and phosphoserine in the Bub1-Mad1 interaction, found a signficant reduction in binding for the singly phosphorylated pThr461 peptide, but also showed that pSer459 alone could not establish a strong Bub1-Mad1 interaction (Zhang *et al*, 2017; Ji *et al*, 2017). By SPR, the Nilsson group found that the pS459-pT461 peptide bound with an affinity of 16 μM, while the pT461 peptide was reduced two-fold to 32 μM (Zhang *et al*, 2017). By ITC, the Yu group found that the pS459-pT461 peptide had a K_D of 3.1 μM while the pT461 peptide had a K_D of 15.7 μM (Ji *et al*, 2017). These experiments would suggest that although the phosphothreonine is the main point of contact for the Bub1-Mad1 interaction, that the phosphoserine is not only required for priming Thr461 phosphorylation but also contributes directly to the Bub1-Mad1 interaction.

In contrast, our ITC experiments did not show a difference between the pT461 and pS459-pT461 interaction, as the singly phosphorylated peptide had an observed K_D of 3.3 ± 0.3 μM, which is nearly identical to the doubly phosphorylated peptide (Fig 3.12A). We did however notice a significant reduction in the solubility of the singly phosphorylated peptide, likely due to the absence of the charged bulky phosphate to an otherwise very hydrophobic peptide. It therefore seems likely that the reduce solubility and/or the differences in our experimental conditions could be why our results varied. We had to lower the concentration of the singly phosphorylated peptide and $Mad1^{CTD}$ used in our ITC experiments in order to ensure the singly phosphorylated peptide remained soluble. We also point out that our results fit with our crystal structure which shows that the pS459 site does not directly contribute to the Bub1-Mad1 interaction and this additionally supports the suggested mechanism by which the primary role of the phosphoserine site is to prime phosphorylation at Thr461.

A

Mad1^{CTD}	Bub1 Peptide	Kd (μM)	Stoichiometry (Dimer:Peptide)
WT	CD1	-	-
WT	SpT* CD1	3.3 ± 0.30	0.91 ± 0.04
WT	pSpT CD1	2.7 ± 1.20	0.97 ± 0.08
K614A	pSpT CD1	2.4 ± 0.43	1.05 ± 0.21
R617A	pSpT CD1	3003 ± 786	0.91 ± 0.14
L618A	pSpT CD1	-	-
K619A	pSpT CD1	10.1 ± 5.40	1.07 ± 0.10
Q627A	pSpT CD1	2.4 ± 0.40	0.94 ± 0.01
F629A	pSpT CD1	-	-
R630A	pSpT CD1	10.1 ± 1.30	0.97 ± 0.03
I643A	pSpT CD1	1.4 ± 0.53	0.91 ± 0.03
R650A	pSpT CD1	1.1 ± 0.30	0.91 ± 0.04
QRI**	pSpT CD1	14.5 ± 3.50	0.94 ± 0.03
QRRI**	pSpT CD1	24.9 ± 1.30	0.85 ± 0.05

B

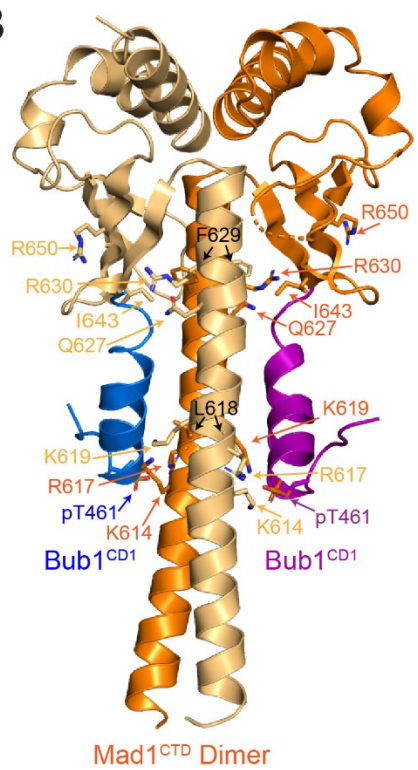

Figure 3.12: ITC of Bub1^{CD1} and Mad1^{CTD} mutants. (A) *Summary of all ITC experiments performed in this study. The K_D and stoichiometry (n) values were obtained by averaging at least three experiments. The reported error values are calculated standard deviations. The mutations of Mad1^{CTD} are highlighted in the Bub1^{CD1}-Mad1^{CTD} crystal structure in (B). Mutants which do not bind, are marked with a dash. Raw data for each ITC reaction are shown in the Appendix Figs 1-3. SpT* CD1 peptide is a peptide which is phosphorylated at Thr461 and not at Ser459. QRI** and QRRI** are triple and quadruple mutants of Mad1 which contact the C-terminus of Bub1^{CD1}. The QRI triple mutant contains Q627A, R650A and I643A, while the QQRI quadruple mutant additionally contains R630A.* ***(B)*** *The crystal structure of Bub1^{CD1}-Mad1^{CTD} with the Mad1 residues which were mutated in our ITC experiments shown as sticks. Residues from both monomers are shown. The lower occupancy peptide is shown as blue and the higher occupancy peptide as purple.*

3.9 The role of the Mad1 RLK motif

As previously discussed, Mad1 contains a conserved RLK motif (R617-L618-K619) within its C-terminal coiled-coil. A sequence conservation map of Mad1^{CTD} is shown in Fig 3.13. Except in a few species, such as *C. elegans* and *X. laevis*, the RLK motif is highly conserved. This motif has been shown by several groups to be essential for Mad1 SAC-dependent kinetochore targeting through its interaction with Bub1 (Brady & Hardwick, 2000; Heinrich *et al*, 2014; Kim *et al*, 2012). Guided by our crystal structure (Fig 3.8D), we investigated the role of individual residues of the RLK motif and how they contribute to the Bub1-Mad1 interaction.

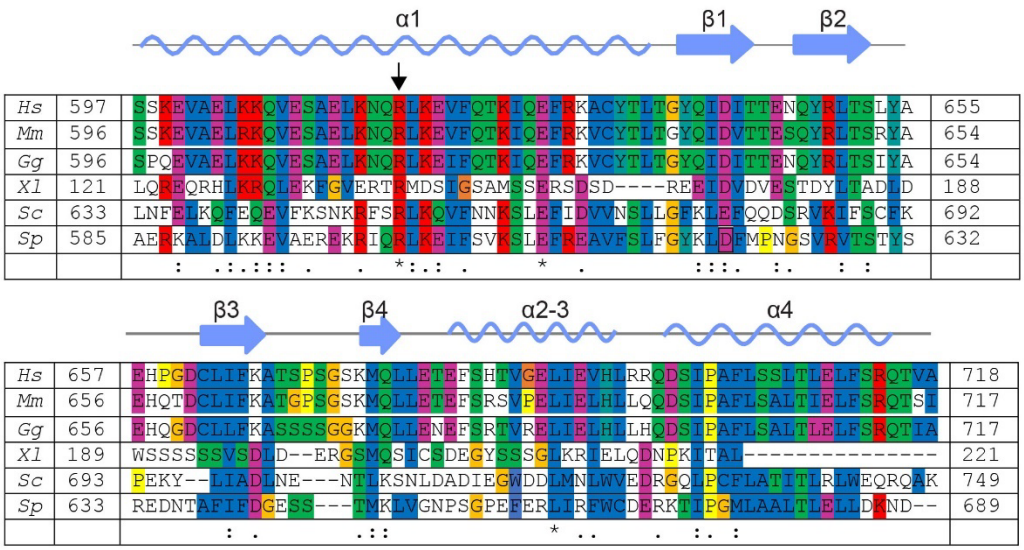

Figure 3.13: Mad1^{CTD} sequence alignment. *The sequence alignment of Mad1^{CTD} was created using ClustalX2 of Mad1^{CTD} (human Mad1 residues 597-718) (Larkin et al., 2007). Mad1 secondary structural elements are shown above and the Arg617 residue of the RLK motif is highlighted with a black arrow.*

As previously discussed, the interface between Mad1 and Bub1 is mediated by a strong hydrogen bonding interaction between Mad1 Arg617 of the RLK motif and the phosphothreonine site of Bub1^{CD1} (Fig 3.8C). An R617A mutation nearly abolishes Mad1^{CTD}-Bub1^{CD1} interaction by decreasing the infinity over 1000-fold and confirms the crucial role of this residue (Fig 3.12).

Surprisingly, a L618A mutation of the RLK motif had an even stronger effect than an R617A mutation, as it completely abolished interaction with Bub1^{CD1} (Fig 3.12). However, Mad1^{CTD} L618A had very poor expression compared to wild-type Mad1^{CTD} which has high expression levels. Mad1^{CTD} L618A also aggregated easily and eluted strangely from a size-exclusion column (Fig 3.14). As Leu618 lies between the hydrophobic coiled-coil dimerization interface of Mad1^{CTD} we thought this mutant might be impairing Mad1^{CTD} dimerization (Fig 3.8D). However, a subsequent SEC-MALS experiments verified that the purified L618A mutant was still dimeric (Fig 3.14). We therefore speculate that this mutant perturbs the Mad1 dimerization interface, and more importantly as it directly connected to Arg617, it likely disrupts this key interaction. Furthermore, much of the Bub1^{CD1}-Mad1^{CTD} interface is formed from hydrophobic interactions, including a hydrophobic pocket formed by Phe470 and Ile471 residues on the outside of the Bub1^{CD1} helix (Fig 3.8A and D). A L618A mutant would therefore also perturb the Bub1-Mad1 interaction by weakening these hydrophobic

interactions. Consequently, the lack of detectable interaction between Mad1^{CTD} L618A and Bub1^{CD1} likely results from mis-folding of the Mad1^{CTD} dimer and disrupted Mad1^{CTD}-Bub1^{CD1} contacts.

A previously reported kinetochore localisation study by the Yu group, found that a single K619A mutation of the Lys within the RLK motif was defective in kinetochore targeting (Kim *et al*, 2012). To our knowledge no other study has specifically explored the function of Mad1 Lys619 in the Mad1^{CTD}-Bub1^{CD1} interaction. Surprisingly, in our structure Lys619 of either Mad1 subunit does not strongly contact Bub1 (Fig 3.8D). Similar to the apo structure of Mad1^{CTD}, the Lys619 sidechain reaches across the Mad1^{CTD} dimer to the opposite coiled-coil, and forms only weak contacts with the opposite Bub1^{CD1} peptide, likely through a π-cation interaction between Mad1 Lys619 and Bub1 Phe470 (Fig 3.8D). Substituting Ala for Lys619 moderately reduced the Bub1^{CD1}-Mad1^{CTD} affinity from 3 μM to 10 μM (Fig 3.12). These results suggest that the lysine of the RLK motif, although important, is not essential for the Bub1-Mad1 interaction *in vitro* and might point to an additional unknown role of Lys619 in Mad1 kinetochore recruitment.

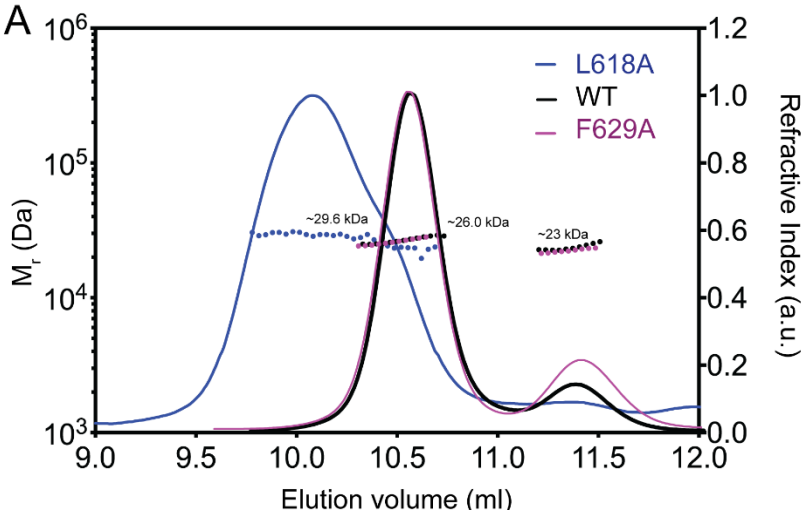

Figure 3.14: Size-exclusion multi-angle light scattering (SEC-MALS) of Mad1^{CTD} wild-type and L618A and F629A mutants. *All eluted as monodispersed species. The average mass of WT Mad1^{CTD} was 26.2 kDa. The average mass for the L618A and F629A mutants was 29.6 kDa and 26.7 kDa respectively. The tailing peak of about 23 kDa comes from residual TEV protease in the sample.*

3.10 Bub1^{CD1} interactions with the Mad1^{CTD} head domain

An important and novel feature of the Bub1^{CD1}-Mad1^{CTD} complex is that the C-terminus of each Bub1^{CD1} peptide contacts both the top of the coiled-coil and head domain of Mad1 of the opposite subunit to which the phosphorylated threonine interacts (Fig 3.8A and B). In order to probe to what extent these contacts contribute to the Bub1^{CD1}-Mad1^{CTD} interaction,

we created individual or combined alanine substitutions for several of these residues within Mad1^{CTD} (Q627, F629, R630, I643, R650; highlighted in Fig 3.8B and Fig 3.12B) to test by ITC (Fig 3.12A).

Two of the individual mutations, F629A and R630A, had a significant effect on Bub1^{CD1} binding. The R630A mutant impaired the Bub1^{CD1}-Mad1^{CTD} interaction over 3-fold, while the F629A mutant completely abolished Bub1^{CD1} binding (Fig 3.12A). Phe629 is a buried hydrophobic residue which contacts the opposite Phe629 of the Mad1 dimer and therefore contributes to the hydrophobic dimerization interface (Fig 3.12B). Phe629 also contributes to the hydrophobic interface of the Bub1^{CD1}-Mad1^{CTD} complex by stacking with Bub1 Phe475 (Fig 3.8B). Because the F629A mutant was poorly expressed but by SEC-MALS still dimeric, we speculate that similar to the L618A mutant previously discussed, the complete disruption of Bub1^{CD1} binding in the F629A mutant is a result of a mis-folded Mad1^{CTD} dimer (Fig 3.14A). The significant effects of both the F629A and R630A mutants agree with previous kinetochore localization experiments from the Yu group which found both mutants had defective kinetochore targeting (Ji et al., 2017).

While individual alanine substitutions of Gln627, Ile643, and Arg650 had no noticeable effect on Bub1^{CD1} binding, a triple alanine mutant (termed QRI*) significantly reduced Bub1^{CD1} affinity 5-fold (to 14.5 μM), indicating that in combination they contribute to the Bub1^{CD1}-Mad1^{CTD} interaction (Fig 3.12). A quadruple mutant (termed QRRI*) which also includes the R630A mutation, further reduced the affinity of the interaction to 25 μM, confirming the significant contribution of R630A to the Bub1^{CD1}-Mad1^{CTD} interaction (Fig 3.12). We also note that mutation of the hydrophobic MFQ sequence (Bub1 residues 474-476) to RRK, located near the C-terminus of Bub1^{CD1} (highlighted in Fig 3.8A-B), has been previously shown to abolish Bub1^{CD1} binding to Mad1^{CTD} (Zhang *et al*, 2017).

Taken together, our ITC analyses confirm the importance of these residues in mediating Bub1^{CD1} interactions with the head domain of Mad1, as further revealed by our crystal structure. These experiments however also indicate that they contribute less binding energy than the pThr461:Arg617 interaction, further highlighting the importance of phosphorylation in the Bub1-Mad1 interaction. In relation to the model of the Bub1:Mad1:C-Mad2:Cdc20 complex at kinetochores (Fig 3.1), it is possible that the contacts of the C-terminus of the Bub1^{CD1} peptide with the head domain of Mad1 are primarily important for positioning

Cdc20 in close proximity to the Mad1:C-Mad2 complex, such that the newly converted C-Mad2 can readily entrap the MIM motif of Cdc20. This theory will be explored further in chapter 4 of this thesis.

3.11 Disparity between the crystal structure and in-solution stoichiometry

As previously mentioned, after confirming through several methods (ITC/NMR/AUC-SE) that only one Bub1^{CD1} peptide can bind to the Mad1^{CTD} dimer in solution, we were surprised to see two peptides bound in our crystal structure (Fig 3.7). This led us to investigate why this might be. Our ITC and sedimentation equilibrium experiments were performed with Mad1, at 100 µM or lower, and titrating Bub1^{CD1} until a 2-4-fold molar excess was obtained. Our ^{31}P NMR experiments were conducted with around 0.25 to 0.5 mM of each, and still only one binding event was detected. Additionally, NMR is an excellent technique to analyse weak, even millimolar range interactions, and thus our data suggest that a second weaker binding event does not occur in-solution.

In contrast, our Mad1^{CTD}-Bub1^{CD1} crystal structure was obtained through co-crystallization of Mad1^{CTD} and Bub1^{CD1} at final concentrations of 0.35 mM and 2.5 mM respectively in 5 % DMSO. We note that these concentrations of Mad1 and Bub1 greatly exceeds their reported sub-micromolar concentrations at kinetochores (Faesen *et al*, 2017). The use of millimolar concentrations of peptide, and the presence of DMSO and isopropanol which was required for Mad1^{CTD}-Bub1^{CD1} crystallization, may explain the association of a second peptide in the crystallized complex. The poor solubility of the peptide over 1 mM made it unfeasible to test Bub1^{CD1} binding at higher concentrations in our in-solution experiments without the addition of DMSO or isopropanol. The addition of either interfered with ITC enthalpy changes and created a strong signal in our ^{1}H NMR experiments which obscures the protein peaks.

Further examination of our crystal structure reveals interesting findings. Firstly, there is a complete absence of crystal contacts involving the Bub1^{CD1} peptide which would suggest that the 2:2 stoichiometry of the Mad1^{CTD}-Bub1^{CD1} complex is not a crystallization artefact. Secondly, despite Bub1^{CD1} and Mad1^{CTD} being co-crystallized at concentrations over 100 times their $K_{D,}$ including using a seven-fold molar excess of the peptide, we still saw clear differential occupancy of the two peptides in the electron density map and the 2Fo-Fc omit map (Fig 3.15A and C-D). This suggests that despite Mad1^{CTD} being a homodimer, the two peptides have different affinities for Mad1^{CTD}. We also collected a dataset of Mad1^{CTD}-

Bub1^{CD1} with a two-fold higher peptide concentration of 5 mM and this led to a lower resolution structure, most likely due to the two-fold increase in DMSO, and the differential occupancy, although reduced, was still observed (Fig 3.15B). We tried to lower the peptide and/or DMSO concentration to obtain a crystal structure with only one peptide bound, however, this always resulted in either an increase in the differential occupancy of the two peptides or crystallisation of apo Mad1^{CTD} (Fig 3.18, discussed further in section 3.13). We additionally tried to soak the Bub1^{CD1} peptide at high concentration into apo Mad1^{CTD} crystals but were unsuccessful. It is therefore likely that the close packing of the Mad1^{CTD} in the apo $P6_5$ space group blocks Bub1^{CD1} peptide binding, and that peptide binding only occurs when the concentration is forced very high.

Altogether these results led us to examine the Mad1^{CTD}-Bub1^{CD1} crystal structure in more detail, as well as to further investigate the Bub1-Mad1 interaction in solution by NMR, to explain why one peptide would have preferential binding to the Mad1 homodimer.

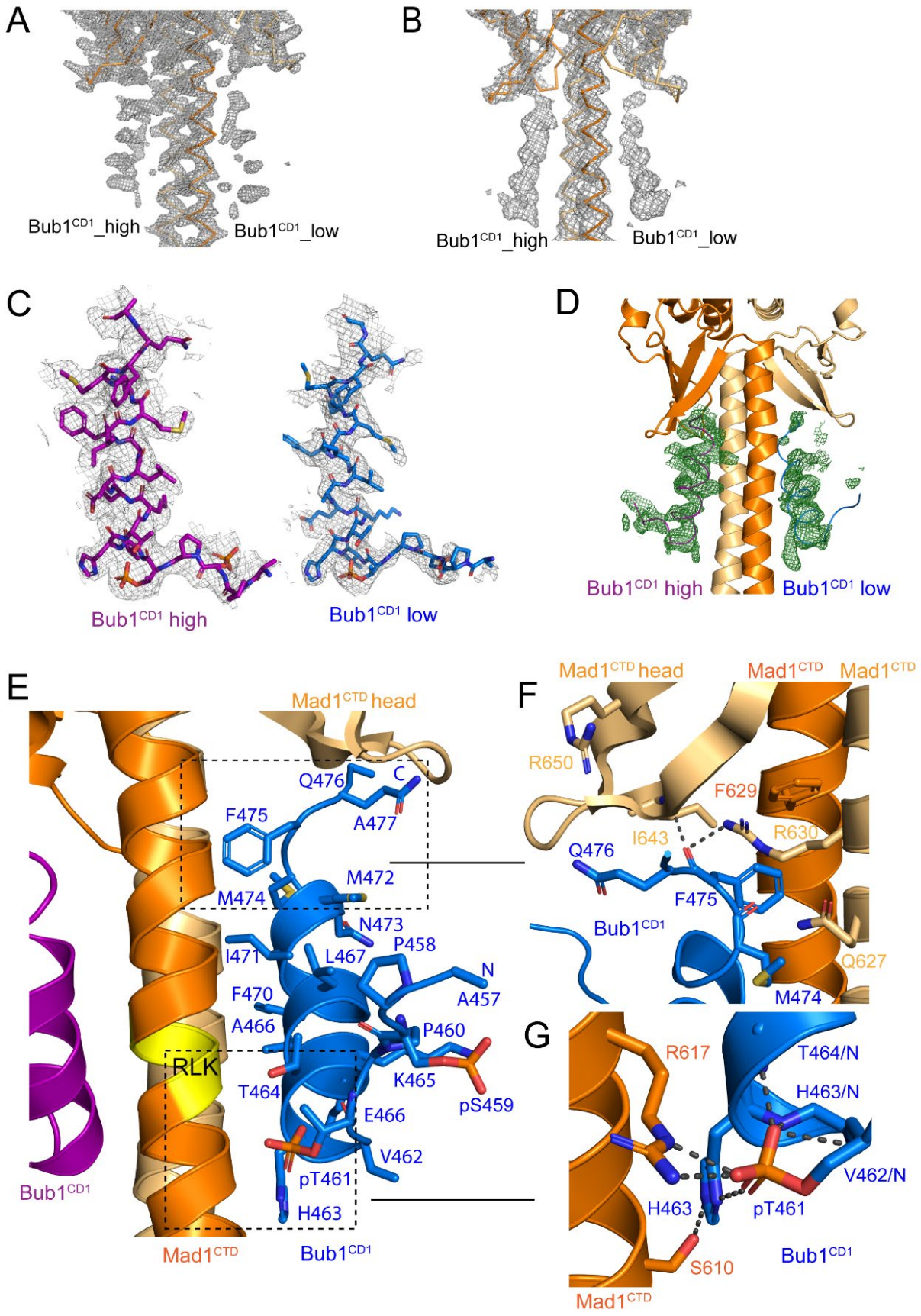
A
Bub1CD1_high
Bub1CD1_low
B
Bub1CD1_high
Bub1CD1_low
C
Bub1CD1 high
Bub1CD1 low
D
Bub1CD1 high
Bub1CD1 low
E
Mad1CTD head
Q476
C
F475
A477
M472
M474
N473
I471
L467
P458
N
A457
F470
A466
P460
RLK
T464
K465
pS459
E466
V462
pT461
H463
Bub1CD1
Mad1CTD
Bub1CD1
F
Mad1CTD head
Mad1CTD
Mad1CTD
R650
F629
I643
R630
Q476
F475
Bub1CD1
Q627
M474
G
R617
T464/N
H463/N
V462/N
H463
pT461
S610
Bub1CD1
Mad1CTD

Figure 3.15: Differential peptide occupancy in the Mad1^{CTD}-Bub1^{CD1} crystal structure. (A) *A snapshot of the electron density map of Mad1^{CTD}-Bub1^{CD1} visualized in Coot (Emsley et al, 2010) which shows the differential Bub1^{CD1} peptide occupancy. Both Mad1^{CTD} subunits are depicted as ribbons in shades of oranges.* ***(B)*** *Electron density map visualized in Coot for a lower resolution Mad1^{CTD}-Bub1^{CD1} structure showing more equivalent peptide occupancy (Emsley et al., 2010). Two times the peptide concentration as compared to the complex crystallized in (A) was used during co-crystallization (5 mM total) requiring 10 % DMSO.* ***(C)*** *Electron density map for each peptide is shown using Isomesh in PYMOL. The same threshold for each peptide is displayed.* ***(D)*** *The 2Fo-Fc omit map (green) for both Bub1^{CD1} peptides in the Bub1^{CD1}-Mad1^{CTD} crystal structure. Created with Phenix (Liebschner et al, 2019).* ***(E)*** *The extensive interface of the Mad1^{CTD}-Bub1^{CD1} interaction is highlighted with the lower occupancy Bub1^{CD1} peptide (blue). The RLK motif of Mad1^{CTD} is coloured yellow.* ***(F)*** *Close-up view of the lower occupancy Bub1^{CD1} peptide (blue) interactions with the head domain of Mad1^{CTD} (orange/light orange). Hydrogen bonding interactions within 3.5 Å are highlighted by black dashes.* ***(G)*** *Close-up view of the Mad1^{CTD} Arg617 and Bub1^{CD1} pThr461 interaction in the lower occupancy peptide (blue). Hydrogen bonding interactions within 3.5 Å are highlighted by black dashes. Additional contact occurs between the phosphate of pThr461 and Bub1^{CD1} H463 which then forms a hydrogen bond with Mad1^{CTD} S610. Additional stabilising hydrogen bonding occurs between the pThr461 phosphate and the amide nitrogen of Val462, His463, and Thr464.*

3.12 The apo Mad1^{CTD} homodimer is asymmetric

Although it was not pointed out in the original study which crystallized apo Mad1^{CTD}, the homodimer is markedly asymmetric (Kim et al., 2012) (Fig 3.16A-B). By aligning apo Mad1^{CTD} onto itself, the extent of this asymmetry can be appreciated (Fig 3.16C-D). In particular, there is a large asymmetric curvature in the coiled-coil, such that one coiled-coil α-helix (apoB) is relatively straight whereas its counterpart (apoA) is significantly bent. Interestingly, the hinge of this bending occurs at the RLK motif (Fig 3.16A-B), and alignment of the RLK motif of both subunits of the apo homodimer reveals that the head domain is rotated inwards towards the more bent α-helix (Fig 3.16C). By aligning the head domain onto itself it is possible to see that this is actually due to a change in the angle at which both helices of the coiled-coil are curved with respect to the head domain, rather than a change in the conformation of the head domain itself (Fig 3.16D). This asymmetry of apo Mad1 is also reflected in the relative B-factors, with the protomer containing the more bent stem (apoA) exhibiting higher flexibility as does its adjacent head domain (apoB_head) of the opposite protomer, as compared to the less bent helix and its adjacent head domain which are quite rigid (apoB and apoA_head) (Fig 3.16E).

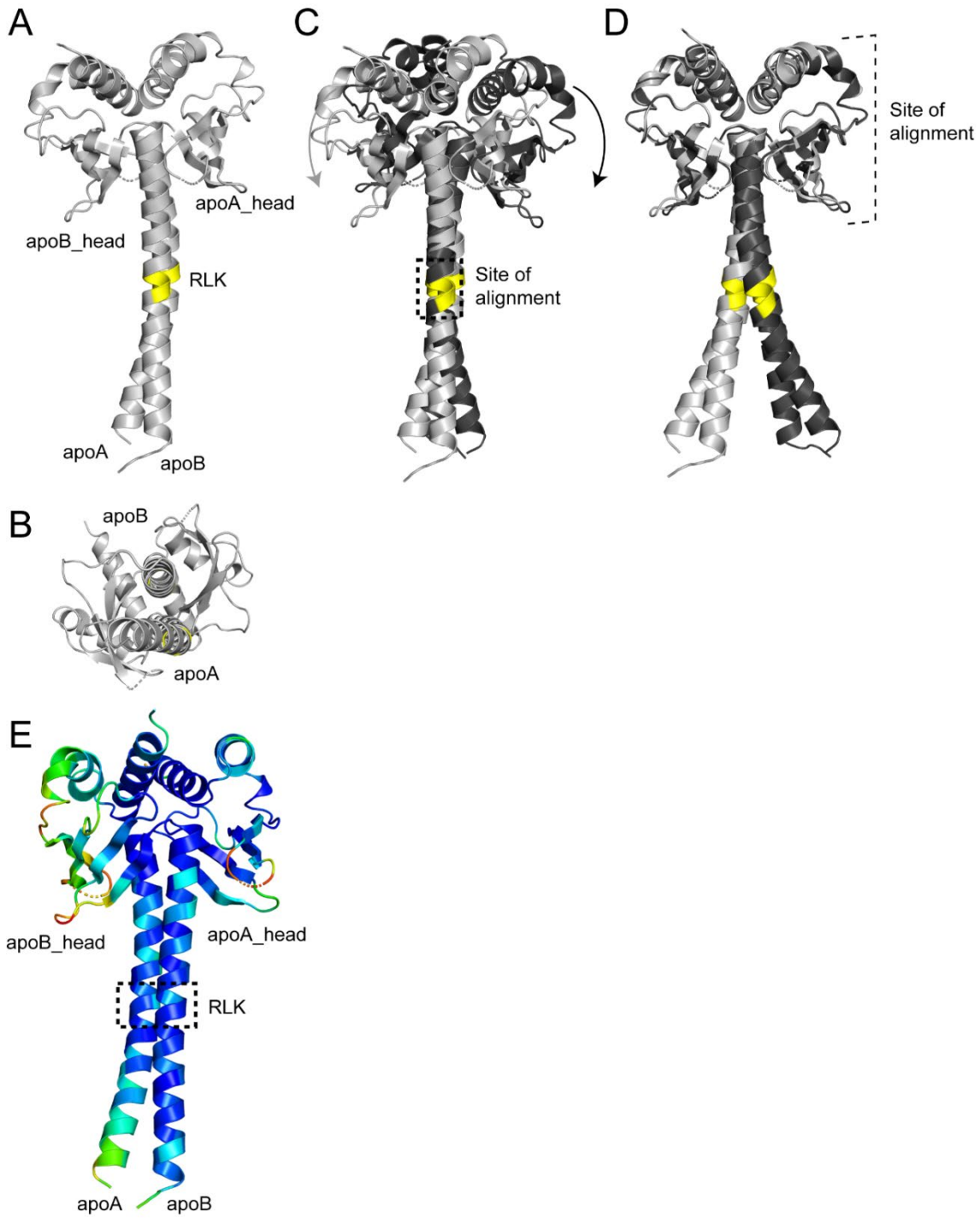

Figure 3.16: Apo Mad1^{CTD} homodimer is asymmetric. (A) *Crystal structure of apo Mad1^{CTD} (grey) with the RLK motif highlighted in yellow. PDB ID: 4DZO (Kim et al, 2012).* ***(B)*** *Bottom view of the crystal structure of apo Mad1^{CTD} showing the extent of the bending of the apoA helix.* ***(C)*** *Opposite subunits of two copies of apo Mad1^{CTD} homodimer aligned onto their respective RLK motifs (yellow). One copy is in grey, the other in black. The arrows highlight the rotation of the head domain inwards towards the inside of the coiled-coil curvature.* ***(D)*** *Alignment of opposite subunits of the head domain of two apo Mad1^{CTD} copies. One copy is in grey, the other in black. E) Apo Mad1^{CTD} coloured by relative B-factors. The more bent helix (apoA) and its adjacent head domain (apoB_head) exhibit higher flexibility.*

3.13 Bub1^{CD1}-bound Mad1^{CTD} is also asymmetric

Our structure of Bub1^{CD1}-bound Mad1^{CTD} is also asymmetric, with one Mad1^{CTD} protomer being slightly more curved than the other, but there is an overall straightening of the more bent subunit as compared to the apo structure (Fig 3.17A-B). Similar to the apo structure, both protomers of the coiled-coil are strikingly arched to one side (Fig 3.17B). Interestingly, this asymmetry likely explains the differential occupancy of the two peptides. The side of the coiled-coil which angles inwards is the site of the higher occupancy peptide, whereas the lower occupancy peptide binds to the outside of the bend (Fig 3.17A-B). The curvature of the coiled-coil results in stronger engagement of both the hydrophobic coiled-coil and the head domain of Mad1 with the higher occupancy peptide.

Closer examination of how each side of the Mad1 head domain engages with its adjacent peptide shows that there are additional hydrogen bonds with the C-terminus of the higher occupancy peptide as compared to the lower occupancy peptide (Fig 3.17C). This includes contacts between Bub1 Gln476 and Mad1 Arg650, as well as Bub1 Met474 and Mad1 Gln627, in the higher occupancy peptide which do not exist in the lower occupancy peptide (Fig 3.17C). However, it is unlikely that the differential peptide occupancy is solely the result of how the head domain engages each peptide, as our previously discussed ITC experiments in section 3.9 show that neither Arg650 nor Gln627 participate significantly to the Bub1^{CD1}-Mad1^{CTD} interaction (Fig 3.12A). What is more likely is that the differential occupancy is a result of the net effect of the peptide binding to the inside of the bent coiled-coil, rather than the outside of the bend, combined with the enhanced contacts to the head domain. As with apo Mad1^{CTD}, mapping the B-factors onto Bub1^{CD1}-Mad1^{CTD} clearly shows how asymmetric the homodimer is, with the side of the homodimer (bound_A and head_B) which contacts the higher occupancy peptide (high_CD1) having higher rigidity as does the peptide itself (Fig 3.17D). Altogether, this suggests that even bound Mad1^{CTD} is asymmetric and more interestingly that there is a direct relationship between the asymmetry of Bub1^{CD1}-Mad1^{CTD} complex and the differential peptide occupancy.

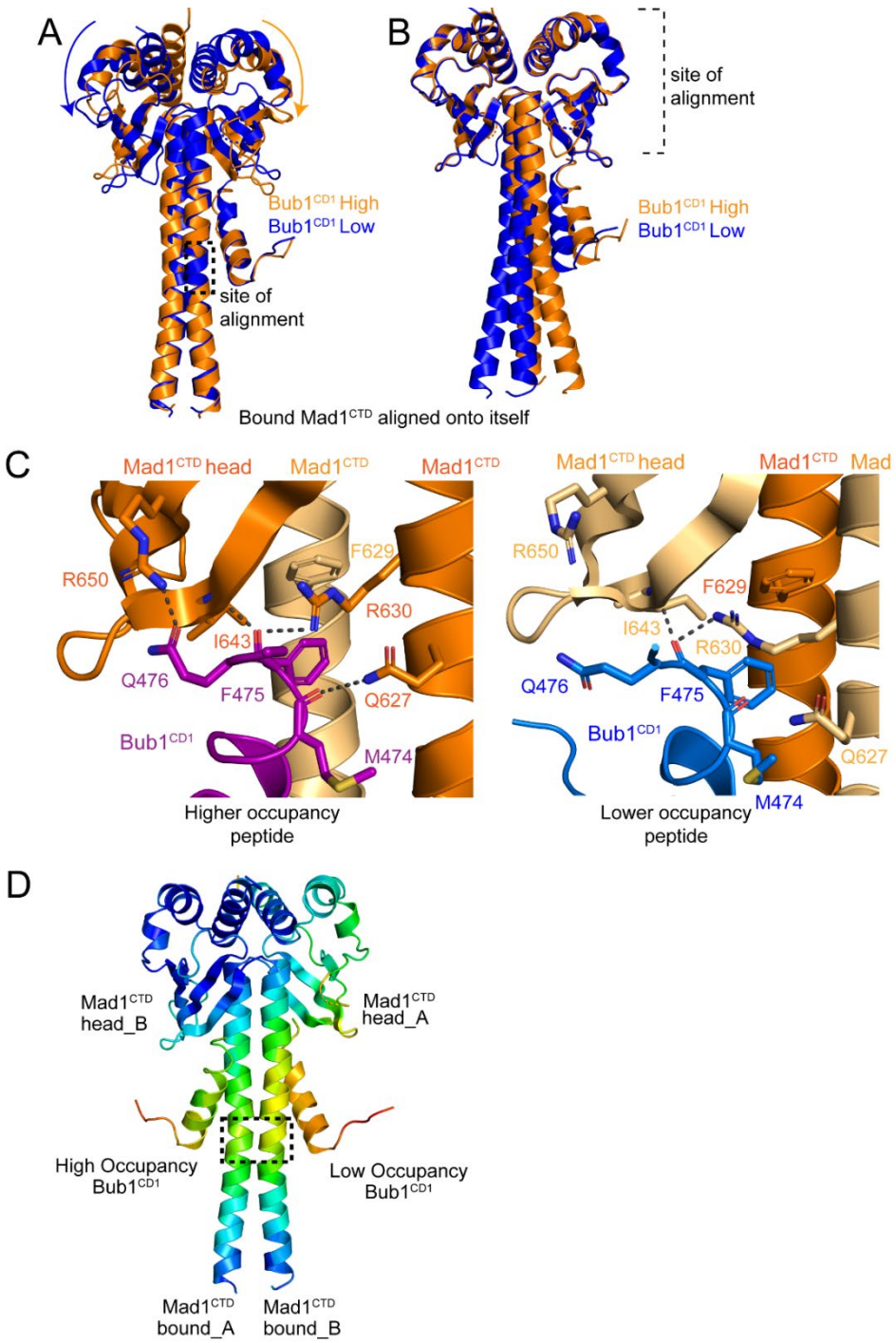

Figure 3.17: Bub1^{CD1} bound Mad1^{CTD} homodimer is asymmetric. (A) *Alignment of the RLK motif of opposite subunits of the Mad1^{CTD}-Bub1^{CD1} structure. The site on Mad1 which is aligned is highlighted by the dashed box. In one dimer (coloured orange), the higher occupancy peptide is depicted as an orange cartoon. In the other dimer (coloured blue), the lower occupancy peptide is depicted as a blue cartoon. The orange and blue arrows highlight the stronger engagement of the head domain with the higher occupancy peptide.* ***(B)*** *Alignment of the head domain of opposite subunits of the Mad1^{CTD}-Bub1^{CD1} structure. In one dimer (coloured orange), the higher occupancy peptide is depicted as an orange cartoon. In the other dimer (coloured blue), the lower occupancy peptide is depicted as a blue cartoon.* ***(C)*** *Comparison of the high and low occupancy Bub1^{CD1} peptide contacts with the opposite sides of the Mad1 head domain and top of the coiled-coil. Hydrogen bonds within 3.5 Å are shown as black dashes.* ***(D)*** *Temperature factors mapped onto the Mad1^{CTD}-Bub1^{CD1} crystal structure.*

3.14 Mad1^{CTD} asymmetry is likely to be inherent to Mad1

Our data suggest that crystallographic packing is unlikely to be the cause of the asymmetry present in the apo Mad1^{CTD} and Bub1^{CD1}-bound Mad1^{CTD} structures. For one, both the apo and Bub1^{CD1}-bound states are asymmetric, despite being crystallized in different space groups ($P6_5$ versus $P2_12_12_1$). Furthermore, we solved several crystal structures of the Mad1^{CTD}-Bub1^{CD1} complex using the same crystallization conditions but in different space groups and in each case the asymmetry of the homodimer was retained (Fig 3.18). The asymmetric unit of the monoclinic space group ($P2_1$) comprises two Mad1^{CTD}-Bub1^{CD1} complexes (PDB: 7B1H). Both complexes display clear asymmetry, but to dramatically different degrees (Fig 3.18C-D). In the more asymmetric complex, there is a stronger difference in Bub1^{CD1} peptide occupancy, and as with our crystal structure in the $P2_12_12_1$ space group, the higher occupancy peptide binds to the concave side of the Mad1^{CTD} coiled-coil, and while the lower occupancy Bub1^{CD1} peptide binds to the convex side of the Mad1^{CTD} coiled-coil. Alignment of all four Mad1^{CTD} homodimers from the three different space group structures nicely presents the extent of the flexibility within the Mad1^{CTD} coiled-coil and head domain (Fig 3.18E). Altogether, we think this is very compelling evidence that this asymmetry is intrinsic to the Mad1^{CTD} homodimer and contributes to the differential occupancy of Bub1^{CD1} peptides in our crystal structures.

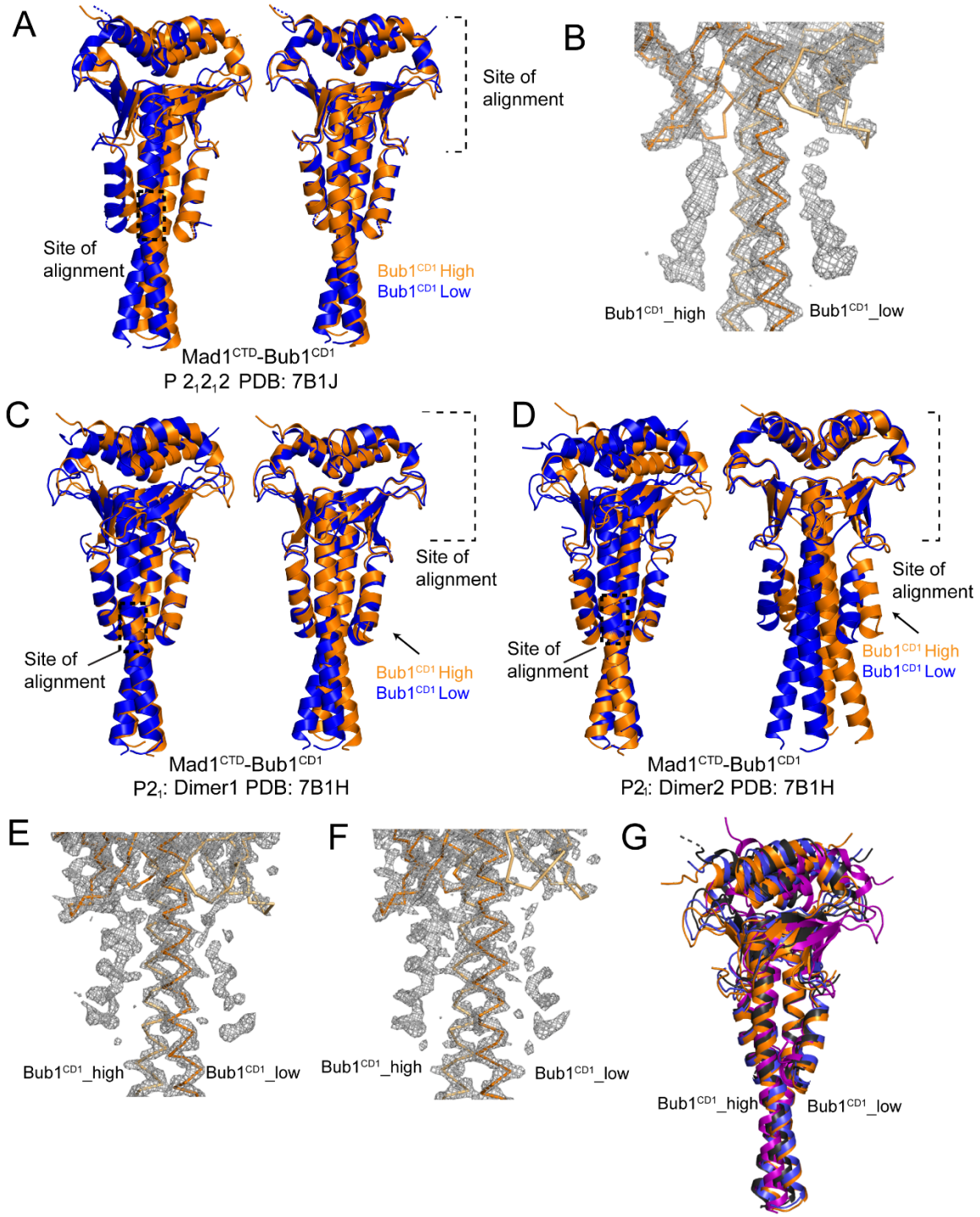
A
Site of alignment
Site of alignment
Bub1CD1 High
Bub1CD1 Low
Mad1CTD-Bub1CD1
P 2₁2₁2 PDB: 7B1J
B
Bub1CD1_high
Bub1CD1_low
C
Site of alignment
Site of alignment
Bub1CD1 High
Bub1CD1 Low
Mad1CTD-Bub1CD1
P2₁: Dimer1 PDB: 7B1H
D
Site of alignment
Site of alignment
Bub1CD1 High
Bub1CD1 Low
Mad1CTD-Bub1CD1
P2₁: Dimer2 PDB: 7B1H
E
Bub1CD1_high
Bub1CD1_low
F
Bub1CD1_high
Bub1CD1_low
G
Bub1CD1_high
Bub1CD1_low

Figure 3.18: Mad1^{CTD}-Bub1^{CD1} asymmetry and differential Bub1^{CD1} occupancy is conserved across structures from different space groups. (A) *Alignment of Mad1^{CTD}-Bub1^{CD1} structure from the $P2_12_12$ space group (PDB: 7B1J). Left panel: Alignment of opposite subunits of the homodimer on the RLK site. Right panel: Alignment of opposite subunits on the head domain. The duplicated dimers are coloured in orange or blue.* ***(B)*** *Electron density map of the Mad1^{CTD}-Bub1^{CD1} structure from the $P2_12_12$ space group (PDB: 7B1J) visualized in Coot (Emsley et al, 2010) which shows near equivalent peptide occupancy. The Mad1^{CTD} homodimer is represented as a ribbon in orange and yellow.* ***(C)*** *Alignment of one homodimer from the Mad1^{CTD}-Bub1^{CD1} structure from the $P2_1$ space group (PDB: 7B1H). Left panel: Alignment of opposite subunits of the homodimer on the RLK site. Right panel: Alignment of opposite subunits on the head domain. The duplicated dimers are coloured in orange or blue.* ***(D)*** *Alignment of the second homodimer from the Mad1^{CTD}-Bub1^{CD1} structure from the $P2_1$ space group (PDB: 7B1H). Left panel: Alignment of opposite subunits of the homodimer on the RLK site. Right panel: Alignment of opposite subunits on the head domain. The duplicated dimers are coloured in orange or blue.* ***(E)*** *Electron density map of one homodimer from the Mad1^{CTD}-Bub1^{CD1} structure (shown directly above) from $P2_1$ space group visualized in Coot (Emsley et al, 2010). The Mad1^{CTD} homodimer is represented as a ribbon in green and yellow.* ***(F)*** *Electron density map of the second homodimer from the Mad1^{CTD}-Bub1^{CD1} structure (shown directly above) from the $P2_1$ space group visualized in Coot (Emsley et al, 2010). The Mad1^{CTD} homodimer is represented as a ribbon in pink and blue. The occupancy of the peptide on the right is extremely poor as is the density for the head domain it contacts.* ***(G)*** *All four Mad1^{CTD} homodimers from the three different space group structures are aligned onto their Mad1^{CTD} RLK motif which is bound to the higher occupancy peptide. Blue = homodimer_1 from $P2_1$. Orange = homodimer_2 from $P2_1$. Purple = $P2_12_12_1$. Black = $P2_12_12$.*

3.15 Bub1 binding leads to substantial conformational changes of Mad1^{CTD}

In collaboration with Dr. Conny Yu and Dr. Stefan Freund of the MRC-LMB NMR facility, we investigated the Bub1^{CD1} interaction with Mad1^{CTD} in solution, using NMR. Because the Mad1^{CTD} dimer is relatively large by NMR standards (28 kDa) and contains an elongated coiled-coil, the slower overall tumbling of the complex in solution resulted in substantially lower resonance sensitivity. In order to achieve a near complete assignment of Mad1^{CTD} backbone resonances, we used uniformly sidechain deuterated ^{13}C,^{15}N labelled sample. As discussed in the methods section of this thesis, triple-labelling optimizes the relaxation rate of 3D experiments and provides higher sensitivity, and this allowed Conny and Stefan to assign 113 out of the 119 non-proline residues to create an almost complete assignment of Mad1^{CTD} (Fig 3.19A). Sequence assignment of Mad1^{CTD} then allowed us to analyse how each of these residues is affected upon Bub1^{CD1} binding in solution (Fig 3.19A-C).

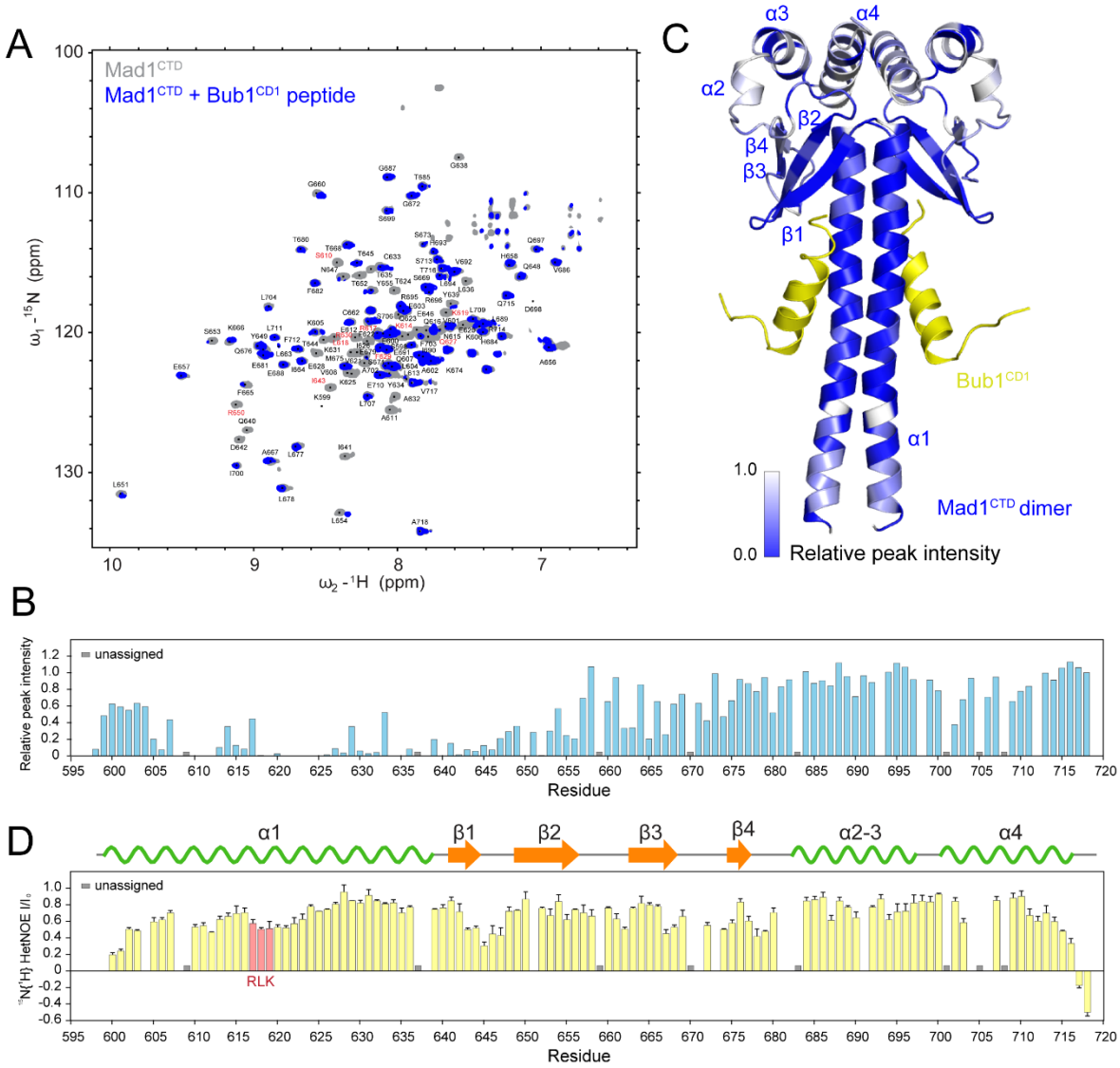

Figure 3.19: The Bub1-Mad1 interaction characterized by NMR. (A) *^{1}H,^{15}N-^{2}D HSQC showing ^{15}N-labelled Mad1^{CTD} with (blue) and without (grey) Bub1^{CD1} phosphorylated peptide. The peptide was added in excess at 1:2 molar ratio of Mad1^{CTD} dimer to Bub1^{CD1}. Assignments of the backbone resonances of Mad1^{CTD} are labelled on the spectra. Peaks which are mutated in the ITC experiments in Fig 3.12 are labelled in red.* ***(B)*** *Relative peak intensities (PI_{bound}/PI_{free}) of Mad1^{CTD} upon Bub1^{CD1} binding. Peak intensities were normalized to that of the C-terminal residue Ala718.* ***(C)*** *Relative peak intensities of Bub1^{CD1}-bound Mad1^{CTD} in B are mapped onto the Bub1^{CD1}-Mad1^{CTD} crystal structure. Residues are coloured using a scale of blue to grey, where regions with the most significant line broadening are highlighted in blue.* ***(D)*** *^{15}N{^{1}H}-heteronuclear NOE values were collected with interleaved on- (I) and off- (I0) resonance and expressed as I/I0. A higher value indicates higher rigidity of the backbone N-H bond. The Mad1 RLK motif is highlighted in red. The error bars are the calculated standard deviations of two technical replicates on the same sample.*

To analyse the Bub1^{CD1}-Mad1^{CTD} interaction in solution, we titrated unlabelled phosphorylated Bub1^{CD1} peptide into ^{15}N labelled Mad1^{CTD}. Dramatic and substantial attenuation for resonances corresponding residues 605 to 655 in the ^{1}H,^{15}N correlation spectra of Mad1^{CTD} which encompasses a vast majority of Mad1^{CTD} was seen (Fig 3.19A and

Fig 3.20A). The extent of the environmental changes upon Bub1^{CD1} binding is more easily examined by mapping the line broadened residues onto the crystal structure of Bub1^{CD1}-Mad1^{CTD} (Fig 3.19B). As previously discussed in the methods section (section 2.26) of this thesis, NMR titrations where there is some sort of protein-protein interaction generally result in either chemical shift perturbations of affected residues or as seen here, line broadening, especially in situations where binding is in the lower µM regime. It is important to note that changes can be indicative of both direct protein-protein interactions or conformational change as a result of complex formation which alters a residues chemical environment. Additionally, in a system such as this one, where Mad1 is a homodimer, only a single set of signals will be seen due to the conformational exchange between the two protomers. Nevertheless, because the attenuated signals correspond to a vast majority of the coiled-coil as well as the first two β-strands in the head domain, which is much more of Mad1 than is seen bound to Bub1^{CD1} in our crystal structures, it is possible to infer with high confidence that large structural elements of Mad1 undergo conformational change upon Bub1^{CD1} binding.

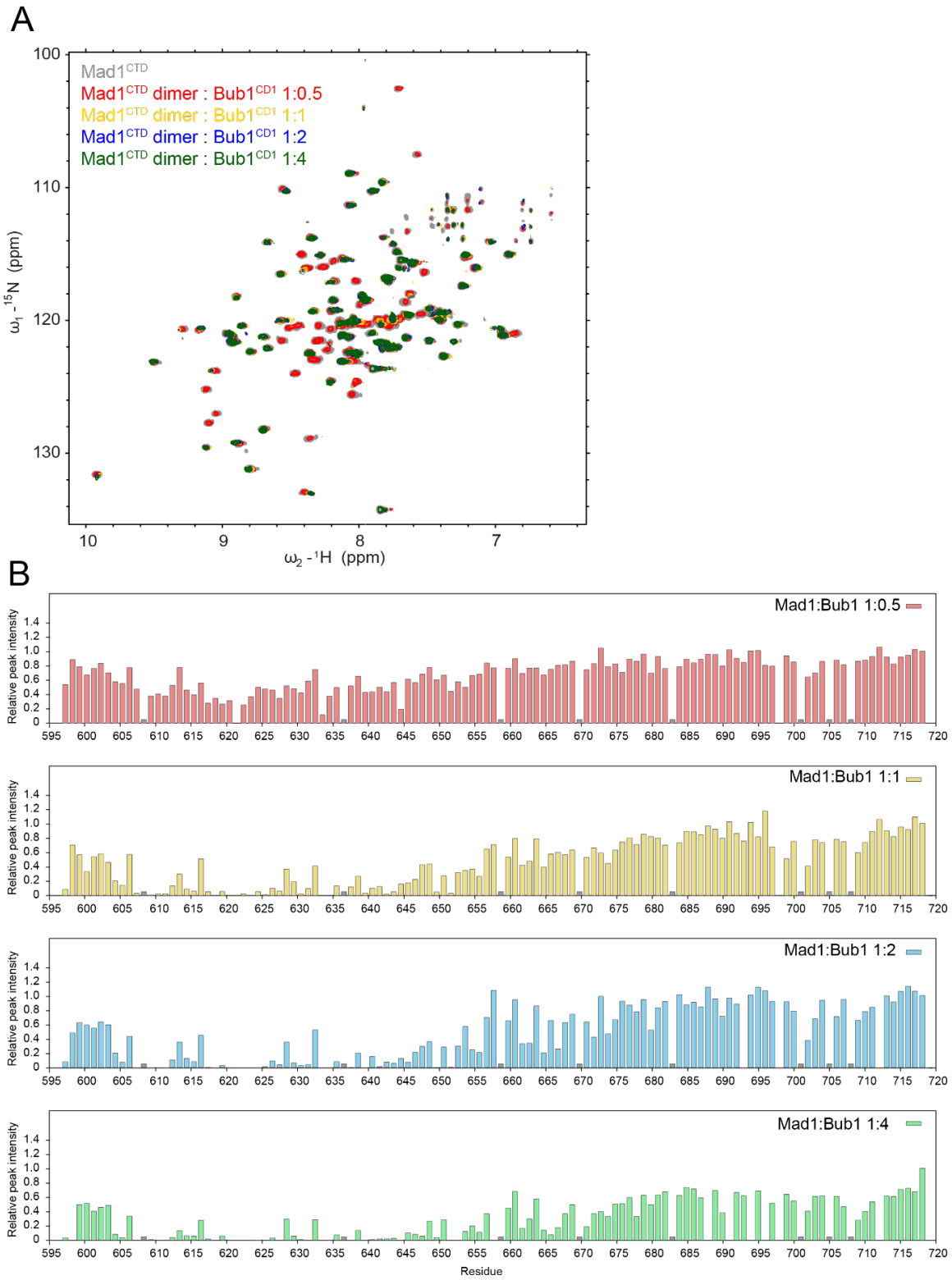

Figure 3.20: Titration of phosphorylated Bub1^{CD1} peptide into Mad1^{CTD}.(A) *^{1}H,^{15}N-2D HSQC showing ^{15}N-labelled Mad1^{CTD} with an increasing concentration of phosphorylated Bub1^{CD1} peptide. 1:0.5 (red), 1:1 (yellow), 1:2 (blue) and 1:4 (green) molar ratio of Mad1^{CTD} dimer to Bub1^{CD1} peptide.* ***(B)*** *Relative peak intensities of Mad1^{CTD} upon titration of phosphorylated Bub1^{CD1} peptide. The bar charts follow a similar colour scheme as the spectra in A, with the molar ratio of Mad1^{CTD} dimer to Bub1^{CD1} being 1:0.5 (red), 1:1 (yellow), 1:2 (blue) and 1:4 (green). Peak intensities were normalized to that of the C-terminal residue Ala718.*

Our NMR titrations also reveal that the dramatic signal attenuation occurs at a 1:1 molar ratio of Mad1^{CTD} dimer to Bub1^{CD1} peptide, after which further addition of peptide did not result in any more significant changes (Fig 3.20B). This further suggests that there is not a second peptide binding site in solution as already observed in our ITC, ^{31}P NMR and sedimentation equilibrium experiments. Conny and Stefan also completed ^{15}N{^{1}H} heteronuclear NOE experiments that samples ^{15}N backbone dynamics on a fast picosecond time scale which revealed that the RLK motif of free Mad1^{CTD} is actually the most flexible segment of the coiled-coil region (Fig 3.19D). This nicely supports our earlier observation that the RLK motif seems to be the dynamic hinge of the coiled-coil curvature. Unfortunately, the substantial line broadening that occurs in Bub1^{CD1}-bound Mad1^{CTD}, prevented us from obtaining similar dynamic data for the complex, but it seems likely that upon interaction with Bub1, the rigidity of the RLK motif would increase and that this in turn would result in an increase of the overall rigidity of the coiled-coil.

Altogether our NMR data suggest dynamic changes and local conformational rearrangements within Mad1^{CTD} upon Bub1^{CD1} binding. This is consistent with the multiple contacts observed in the Mad1^{CTD}-Bub1^{CD1} structure. In particular, the substantial line broadening observed in the coiled-coil region can be explained by the fact that the peptide is bound diagonally across the Mad1^{CTD} coiled-coil and therefore makes extensive contacts with both subunits. With the effect of Bub1 binding experienced in nearly the entire coiled-coil region, it is conceivable that a conformational rearrangement in the bend of the coiled-coil region of the apo Mad1^{CTD} is a requirement for efficient Bub1^{CD1} binding.

3.16 Mad1 asymmetry likely controls Bub1^{CD1} stoichiometry

During our analysis of Mad1^{CTD} asymmetry, we superimposed the apo and bound crystal structures of Mad1^{CTD} by aligning them on the RLK motif of each subunit, which results in four possible alignments (Fig 3.21). As a reminder, the higher occupancy peptide binds to the inside of coiled-coil bend of bound Mad1^{CTD} while the lower occupancy peptide binds to the outside (Fig 3.17). Alignments which place either of the two bound Bub1 peptides on the concave side of the apo structure results in severe clashes with the coiled-coil of Mad1 (Fig 3.21A and C), while alignment to the convex side of the coiled-coil, results in a loss of contacts between the Mad1^{CTD} head domain and Bub1^{CD1} peptide (Fig 3.21B and D), which is more pronounced for the higher occupancy peptide (Fig 3.21B). These analyses strongly

imply that Bub1^{CD1} would be unable to interact efficiently with either apo Mad1^{CTD} promoter without some sort of conformational change occurring.

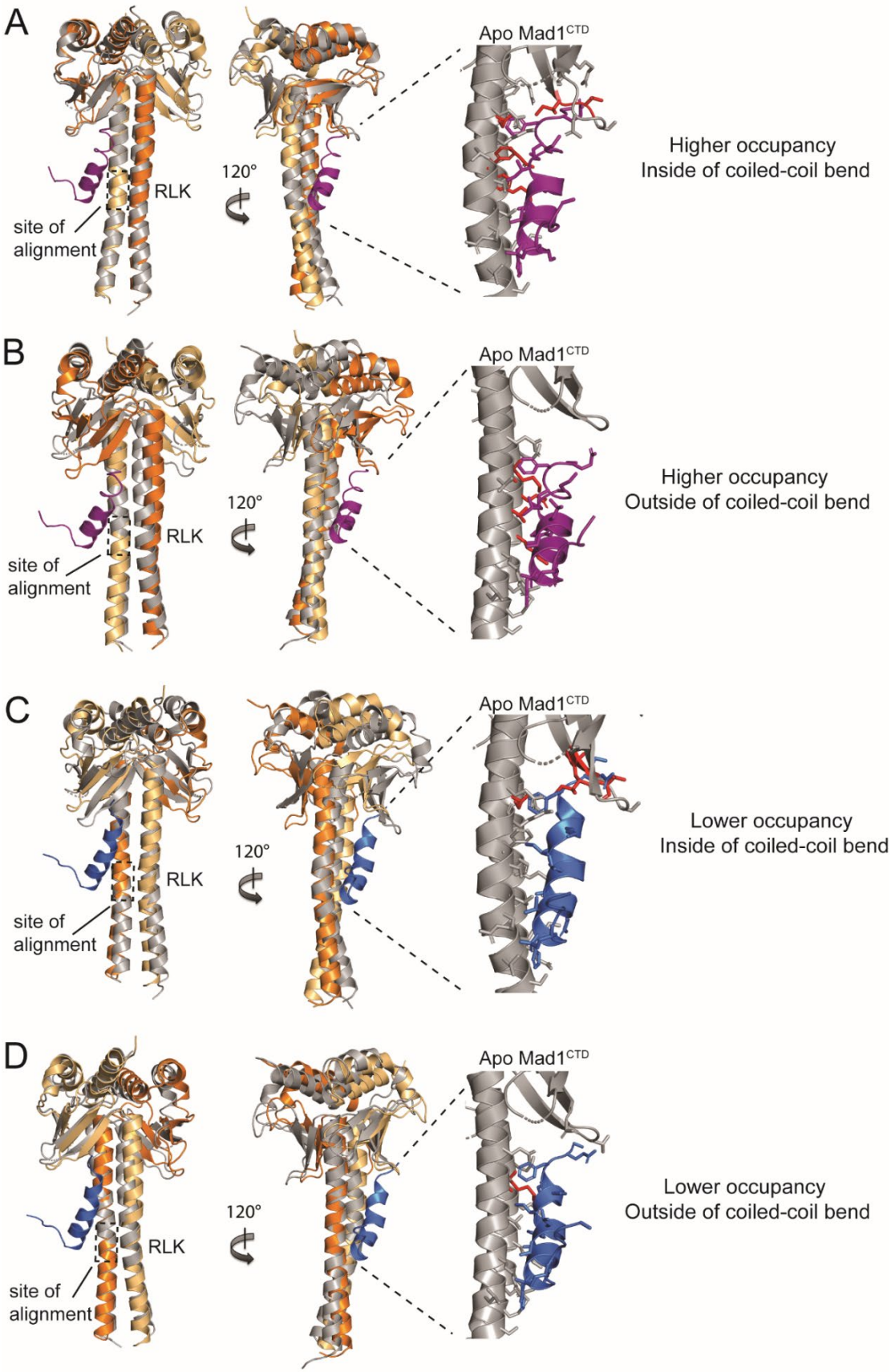

Figure 3.21: Alignments of apo and bound Mad1^{CTD}. *The various subunits of apo and bound Mad1^{CTD} are aligned by means of their RLK sites and the respective peptide bound is shown. For each alignment a close-up view of how the peptide fits onto the apo state is shown, with clashes highlighted by residues coloured red. Bound and apo Mad1^{CTD} are coloured orange and grey correspondingly. The higher and lower occupancy peptides are coloured purple and blue correspondingly.* ***(A)*** *The RLK site of subunit B of bound Mad1^{CTD} (bound to the higher occupancy peptide) aligned onto the RLK site of subunit A of apo Mad1^{CTD}. Severe clashes occur with the coiled-coil and head.* ***(B)*** *The RLK site of subunit B of bound Mad1^{CTD} (bound to the higher occupancy peptide) aligned onto the RLK site of subunit in B of apo Mad1^{CTD}. Severe clashes occur with the coiled-coil and loss of contact with the head.* ***(C)*** *The RLK site of subunit A of bound Mad1^{CTD} (bound to the lower occupancy peptide) aligned onto the RLK site of subunit A of apo Mad1^{CTD}. Severe clashes occur with the head.* ***(D)*** *The RLK site of subunit A of bound Mad1^{CTD} (bound to the lower occupancy peptide) aligned onto the RLK site of subunit B of apo Mad1^{CTD}. Slight clashes occur with the coiled-coil and there is a partial loss of contact with the head of Mad1^{CTD}.*

The conformational change observed between the apo and bound Mad1^{CTD} crystal structures, as well as the changes revealed in solution by NMR, points towards a mechanism by which the inherent asymmetry of Mad1 likely results in the unusual stoichiometry of the Bub1^{CD1}-Mad1^{CTD} complex, in which the more curved side of Mad1 favours Bub1 binding and is likely to represent the site of the single peptide which binds in solution. In fact, the higher occupancy peptide within the Mad1^{CTD}-Bub1^{CD1} crystal structure is indeed the one at the concave side of the coiled-coil forming more contacts to the Mad1^{CTD} head domain, consistent with our mutagenesis and ITC data. This suggested mechanism is further supported by our Mad1^{CTD}-Bub1^{CD1} structures from various space groups where higher occupancy of the second Bub1^{CD1} peptide correlates with a more symmetric Mad1^{CTD} dimer (Fig 3.18). Lastly, our analyses also suggest a requirement of apo Mad1^{CTD} to transition to a more symmetric state, which involves a conformational change centred on the dynamic RLK motif, which lessens the curvature of the coiled-coil, in order to allow for favourable Bub1^{CD1} binding.

3.17 Concluding Remarks

This chapter provides insights into the mechanism of how the Mad1:C-Mad2 complex is targeted to kinetochores in response to SAC activation, a process regulated by a sequential Mps1-dependent phosphorylation cascade (Fig 3.1). Cdk1 and Mps1 phosphorylate the Bub1 CD1 domain to create a direct interaction with the C-terminal coiled-coil of the Mad1 dimer. Our Mad1^{CTD}-Bub1^{CD1} crystal structures explain the molecular interactions of this highly specific targeting mechanism. We find that the first Bub1 phosphorylation site, pSer459, does not make direct contact with Mad1, consistent with the suggested mechanism by which the

primary role of Cdk1 phosphorylation of Ser459 is to prime Mps1 phosphorylation of Thr461 (Ji *et al*, 2017). We also show that pThr461 directly binds to Mad1 Arg617 of the conserved RLK motif, and we suggest that the high specificity of this interaction required to control MCC assembly results from the ability of the phosphate of pThr461 to stabilize the N-terminal α-helix dipole of Bub1^{CD1}. Additionally, using a variety of biophysical techniques, we confidently determined that only one Bub1^{CD1} peptide binds to the Mad1^{CTD} homodimer in solution. Analysis of apo and bound Mad1^{CTD} crystal structures indicates that the homodimer is intrinsically asymmetric, whereby the Mad1^{CTD} coiled-coil has significant curvature which also causes stronger engagement of the head domain with the peptide bound to the side of the coiled-coil with the concave bend. We suggest that this asymmetry is the reason only one peptide binds in solution. This also explains the differential occupancy of the two peptides bound to the Mad1^{CTD} homodimer in our crystal structure. The use of millimolar concentrations of peptide, and the presence of DMSO and isopropanol, required for Mad1^{CTD}-Bub1^{CD1} crystallization, may explain the association of a second peptide in the crystallized complex. Altogether we propose that the asymmetry of the Mad1^{CTD}-Bub1^{CD1} complex is an intrinsic and functional feature that plays an important role in generating the correct juxtaposition of SAC proteins required to catalyse MCC assembly.

Chapter 4
Juxtaposition of SAC proteins on phosphorylated Mad1

4.1 Chapter Abstract

Recently it was shown that C-terminal Mad1 phosphorylation by Mps1 is required for efficient SAC signalling (Ji *et al*, 2017; Piano *et al*, 2021). Phosphorylated Mad1 interacts with the N-terminus of Cdc20, and this seems to enable Cdc20 to catalyse its own incorporation into the MCC. This chapter examines how Mad1 phosphorylation regulates its interaction with Cdc20 using a variety of biophysical and structural studies. We determined that Thr716 is the only predominant Mps1 phosphorylation site within $Mad1^{CTD}$ *in vitro* and further confirmed that the N-terminus of Cdc20 preferentially binds phosphorylated Mad1, with the Box1 motif directly contacting pThr716. We then used NMR to gain detailed structural insights into the $pMad1^{CTD}$:$Cdc20^{1-73}$ interaction. Our findings suggest that only one $Cdc20^{1-73}$ molecule can bind to the $Mad1^{CTD}$ homodimer, and strikingly its interaction affects a significant portion of the $Mad1^{CTD}$ coiled-coil adjacent to the head domain, as well as the head domain β-sheet and C-terminal α-helix including the pThr716 site. We then acquired a complete backbone assignment of ^{15}N, ^{13}C-labelled $Cdc20^{1-73}$ and analysed which residues are involved in this interaction. This revealed that the entire N-terminal half of $Cdc20^{1-73}$, including the Box1 motif, is involved in binding, whereas the C-terminal half including Box2 is largely not. Our data also suggest that binding promotes helical formation within the otherwise disordered $Cdc20^{1-73}$. Lastly, we discovered a novel interaction between $Mad1^{CTD}$ and a region of Bub1 just C-terminal to the CD1 domain which is specific to phosphorylated Mad1. Altogether this highlights the key role Mps1 phosphorylation of Mad1 plays in targeting and repositioning SAC proteins for catalytic MCC formation.

4.2 Chapter Background

As discussed in the introduction of this thesis (section 1.18), C-terminal Mad1 phosphorylation by Mps1 is required for SAC activation, and this is presently believed to be because it promotes MCC formation by catalysing the conversion of open-Mad2 into closed-Mad2. However, the molecular mechanisms of how Mps1 phosphorylation enables Mad1 to perform its role as a catalyst remains unclear and will of be of key interest in this chapter.

Cdc20 interaction with Mad1^{CTD}

In 2017, Hongtao Yu's group identified a novel interaction between human Mad1 and Cdc20, which seemed to be dependent on several Mad1 phosphorylation sites within the C-terminal domain of Mad1 (Ji *et al*, 2017). The Cdc20 binding site of phosphorylated Mad1^{CTD} was mapped to the N-terminus of Cdc20 (27-RWQRK-31), which is part of a conserved Box1 motif (Fig. 4.1A-B).

Unpublished work from the doctoral thesis of Dr. Priya Amin of the Hardwick lab partially corroborated this finding in *S. pombe* (Amin, 2019). *S. pombe* Mad1 was found to interact with Slp1 (*S. pombe* Cdc20) in mitosis, and *S. pombe* Mad1 Thr668, which corresponds closely with human Mad1 Thr716, was found to be phosphorylated *in vivo* and functionally important for SAC activation. A T668A phosphorylation mutation caused sensitivity to benomyl induced spindle perturbation, however, contradictory to a T716A mutant in humans, T668A actually increased, by an unknown mechanism, the Slp1:Mad1 interaction.

Cdc20 catalyzes its own incorporation into the MCC

Very recently, two papers came out back-to-back which hypothesized that Cdc20 actually catalyzes its own incorporation into the MCC (Piano *et al*, 2021; Lara-Gonzalez *et al*, 2021a). The original model for template-based Mad2 conversion, suggests that docking of O-Mad2 onto the Mad1:C-Mad2 platform, promotes Mad2 conversion into a ligand-free state (C-Mad2^{empty}), which then binds rapidly to Cdc20 (De Antoni *et al*, 2005). However, the Musacchio lab using their FRET assay to analyze MCC conversion kinetics (originally developed in Faesen *et al*, 2017), found that C-Mad2^{empty} did not bind appreciably to the MIM motif of full-length Cdc20 (Cdc20^{FL}). In contrast, C-Mad2^{empty} bound spontaneously to a Cdc20 MIM peptide (Cdc20^{MIM}), or when the first 110 residues of the N-terminus of Cdc20 was truncated (Cdc20$^{111\text{-}C}$). O-Mad2 could bind to both Cdc20^{MIM} and Cdc20^{FL}, although at a much slower rate than C-Mad2^{empty} to Cdc20^{MIM}, with O-Mad2:Cdc20^{MIM} and O-Mad2:Cdc20^{FL} forming 50x and 100x slower, respectively. Only the rate of O-Mad2 binding to Cdc20^{FL} could be augmented (35-fold) by catalysts (Mad1:C-Mad2, Bub1 and their phosphorylation by Mps1). Interestingly, O-Mad2 or C-Mad2^{empty} binding to Cdc20^{MIM}, and C-Mad2^{empty} binding to Cdc20^{FL} could not be catalyzed, while catalysis was present but reduced for O-Mad2 binding to Cdc20$^{111\text{-}C}$, Cdc20$^{1\text{-}180}$, and Cdc20$^{PEG/AAA}$. Additionally, disruption of the Cdc20:pMad1^{CTD} interaction impaired catalysis.

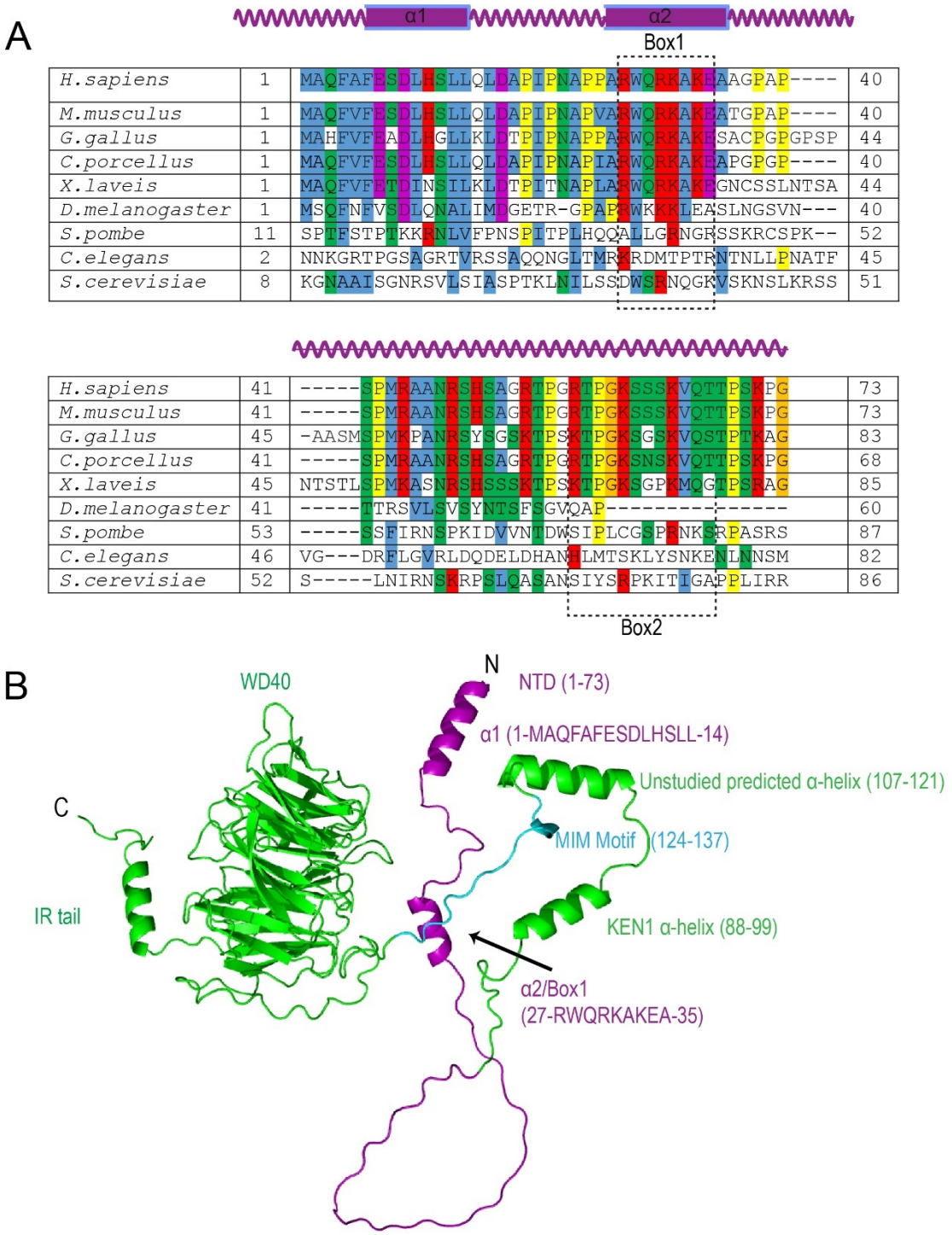

Figure 4.1: Sequence alignment and structure prediction for Cdc20. (A) *A multiple sequence alignment of Cdc20 N-terminal residues 1-73. The conserved Box1 and Box2 motifs are highlighted by the dashed boxes. Secondary structure prediction of two α-helices in this N-terminal region of human Cdc20 is shown above the sequence alignment in blue.* ***(B)*** *Protein structure prediction of full-length Cdc20 using AlphaFold2 (Jumper et al, 2021). The N-terminus of Cdc20 studied in this chapter (residues of 1-73) is coloured in purple. The MIM motif is coloured in cyan, while the rest of the protein is coloured green.*

These experiments indicate several important features of MCC formation. Firstly, $Cdc20^{MIM}$ and $Cdc20^{111\text{-}C}$ can 'thread' into the latched safety-belt of C-$Mad2^{empty}$ and therefore complex formation is spontaneous and unaffected by catalysis. The MIM motif of $Cdc20^{FL}$ is not readily able to thread into C-$Mad2^{empty}$, even in the presence of catalysts. Thus, the process of Mad2 conversion seems to be required for the safety-belt of Mad2 to entrap the MIM motif of $Cdc20^{FL}$. Optimal acceleration of Mad2 conversion requires several regions within Cdc20, including the $Cdc20^{NTD}$:$pMad1^{CTD}$ interaction, and therefore Mad1 phosphorylation by Mps1 seems to function by enabling Cdc20 to catalyze its own incorporation into the MCC.

Self-association of Cdc20

During MCC formation, Cdc20 autoinhibition, induced by self-association of its N- and C-termini, has been previously reported to block BubR1 binding to Cdc20 until Mad2 binds to Cdc20 which helps relieve this inhibition (Davenport *et al*, 2006; Han *et al*, 2013). Cdc20 self-association has also been seen in *C. elegans* and was found to be disrupted by Plk1 phosphorylation of Mad1 (Lara-Gonzalez *et al*, 2021a). Additionally, as several studies have shown that O-Mad2 binds much slower to full-length Cdc20 than N- or C- terminal truncations of Cdc20, it is therefore possible that Cdc20 self-association not only regulates BubR1 binding to Cdc20 but also C-Mad2 binding (Zhang & Lees, 2001; Piano *et al*, 2021; Tang *et al*, 2001). This points toward a mechanism by which the pMad1:$Cdc20^{NTD}$ interaction in humans may disrupt Cdc20 self-association and improve MIM accessibility and/or allow Mad1 to position Cdc20 close to Mad2.

Altogether these studies provide an updated view of MCC assembly, whereby, Bub1 scaffolds Mad1:C-Mad2, Cdc20 and O-Mad2, such that as O-Mad2 docks onto the Mad1:C-Mad2 platform and undergoes conversion to C-Mad2, the Mad2 safety-belt can entrap the MIM motif of Cdc20, which is made readily available by the $pMad1^{CTD}$:Cdc20 interaction.

4.3 Chapter Aims

As discussed, several Mps1-dependent phosphorylation sites within the C-terminus of Mad1 seem to play a role in enhancing MCC formation. This chapter aims to further explore the functional importance of these various sites, using a variety of biophysical and structural biology techniques. Of particular interest is the interaction of $pMad1^{CTD}$ and $Cdc20^{NTD}$. This includes how phosphorylation of Mad1 promotes its interaction with Cdc20, which specific

residues are involved, and the molecular mechanisms for how their association catalyses the formation of C-Mad2:Cdc20.

4.4 Phosphorylation of Mad1 by Mps1

The kinase domain of Mps1 ($Mps1^{KD}$) and full-length GST-Mps1 were purified (Fig 2.1), and the activity of both was confirmed by a ^{32}P incorporation assay (Fig 4.2). Next, we investigated the phosphorylation of the $Mad1^{420-718}$:Mad2 complex and $Mad1^{CTD}$ using either full-length GST-Mps1 or $Mps1^{KD}$, as well as when the $Mad1^{420-718}$:Mad2 complex was co-expressed with Mps1 in the baculovirus expression system and in the presence of okadaic acid. Okadaic acid is a phosphatase inhibitor which specifically targets PP2A but also has been shown to inhibit PP1 at higher concentrations (Takai *et al*, 1987). A previous post-doc in the Barford lab, Dr. Claudio Alfieri, established that addition of okadaic acid during baculovirus expression is a reliable way to promote mitotic protein phosphorylation (Zhang *et al*, 2016b; Alfieri *et al*, 2016).

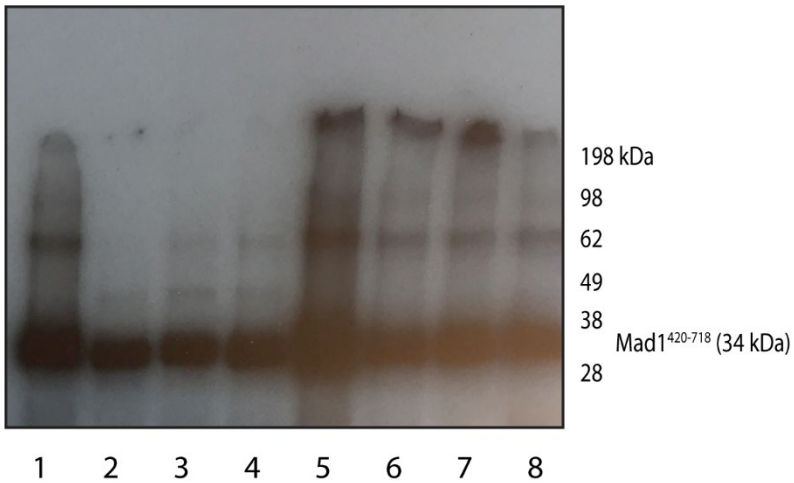

Figure 4.2: Confirmation of Mps1 phosphorylation activity. *A ^{32}P incorporation assay for $Mad1^{420-718}$ phosphorylation using (1) GST-Mps1 prior to SEC at 3 hrs, (2-4) SEC purified GST-Mps1 at 0.5, 1, 3 hr timepoints, (5) $Mps1^{KD}$ prior to SEC at 3 hr (6-8) SEC purified $Mps1^{KD}$ at 0.5, 1, 3 hr time points. In all samples, Mad1 shows a strong radio-labelled band at the position of Mad1 confirming phosphorylation by Mps1. A SeeBlue™ Plus2 ladder (ThermoFisher) was used to identify the molecular weights of radio-labelled bands.*

A summary of the phosphorylation sites identified by mass spectrometry, as well as the abundance of non-phosphorylated versus phosphorylated peptides in each sample, is shown in Appendix Table 3. These results suggest that GST-Mps1 has a higher specificity than the Mps1 kinase domain alone, and that the only major phosphorylation site within $Mad1^{CTD}$ is Thr716. Several sites of phosphorylation were picked up when $Mad1^{420-718}$ was expressed in the presence of Mps1 and okadaic acid, however, for unknown reasons phosphorylation at

Thr716 was not seen. We found the previously identified Thr644 phosphorylation site in all our samples phosphorylated by Mps1 *in vitro*, however only five phosphorylated peptides out of over 800 non-phosphorylated peptides were found, which might suggest that Mps1 does not have a strong preference for this site *in vitro* (Ji *et al*, 2017). We did not find any significant number of peptides for the previously identified Ser610, Ser598, Ser546, Thr550, Tyr535, Ser494, and Thr624 residues (Ji *et al,* 2017, 2018). The only other residue within Mad1 which seemed to have a significant amount of phosphorylation was Thr540, which was also identified in Ji *et al*, 2017, and is N-terminal to Mad1^{CTD} (residues 597-718).

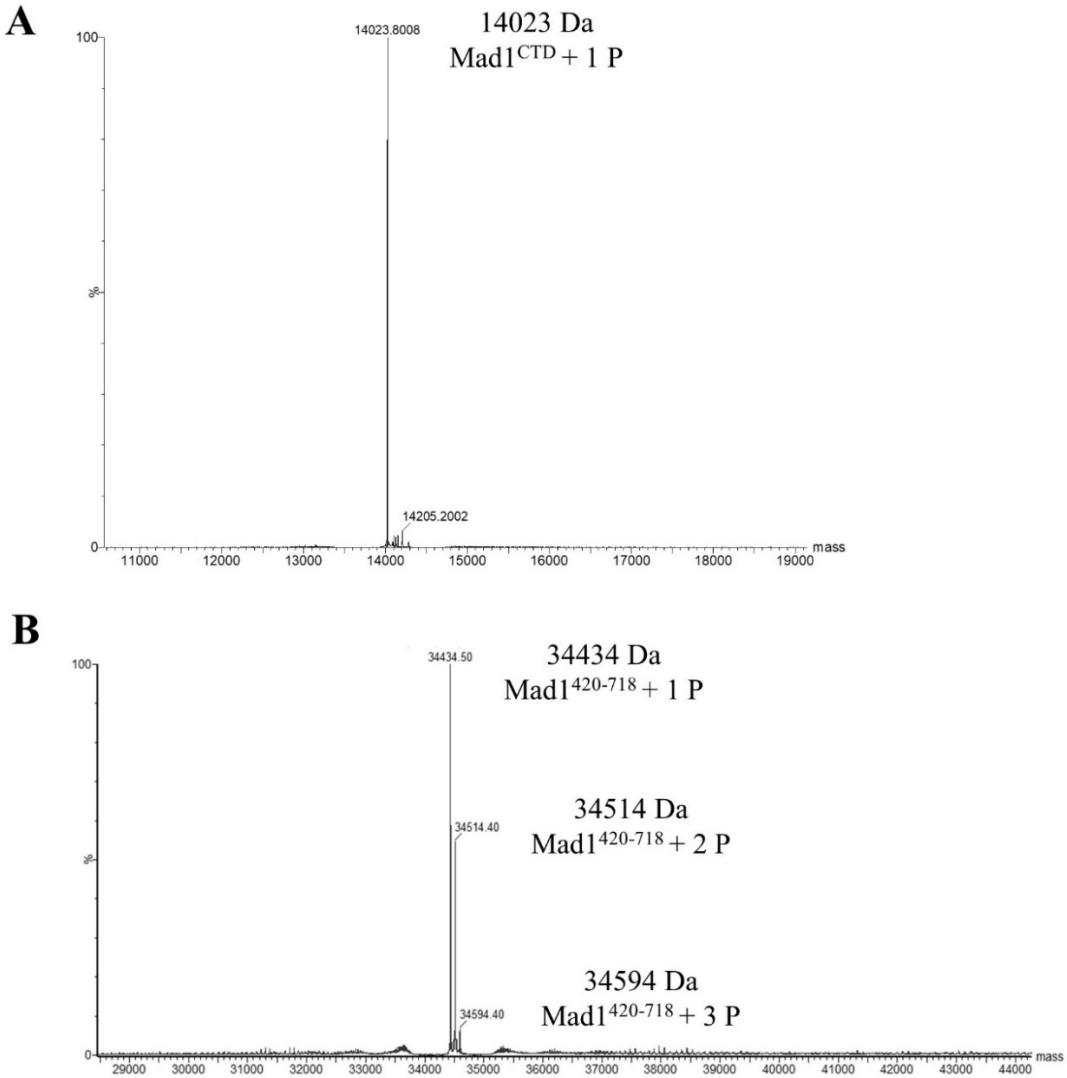

Figure 4.3: Intact mass spectrometry of phosphorylated Mad1. *Mad1^{CTD} and Mad1$^{420-718}$ were phosphorylated by GST-Mps1 and then analysed by intact mass spectrometry to determine the amount of phosphorylation sites present.* ***(A)*** *Mad1^{CTD} contains one major phosphorylation site as the major peak is 14,023 Da which is 80 Da larger than the expected mass of unphosphorylated Mad1^{CTD} (13,943 Da).* ***(B)*** *Mad1$^{420-718}$ contains either one (34,434 Da), two (34,514 Da), or three (34,594 Da) phosphorylation sites per Mad1$^{420-718}$ protomer as the expected mass of unphosphorylated Mad1$^{420-718}$ is 34,354 Da.*

Intact mass spectrometry of Mad1^{CTD} phosphorylation by GST-Mps1 strongly suggests that there is only a single phosphorylation site within each protomer and no significant unphosphorylated Mad1 is present (Fig 4.3A). Phosphorylation of the Mad1$^{420-718}$:C-Mad2 tetramer suggests each Mad1$^{420-718}$ protomer is predominantly phosphorylated at one site, but that a significant portion contain two and three phosphorylation sites (Fig 4.3B).

Using our previously completed backbone assignment of Mad1^{CTD} by NMR (Fig 3.19A), we analysed phosphorylated ^{15}N-labelled Mad1^{CTD} in a ^{1}H, ^{15}N 2D HSQC. A comparison of non-phosphorylated and phosphorylated Mad1^{CTD} is shown in Fig 4.4A, and the chemical shift perturbation of each residue is plotted in Fig 4.4B. Major CSP was observed for the backbone resonances corresponding to the Thr716 residue, and the effect of the phosphorylation was confined to the C-terminus as a significant CSP was only observed for residues 713-718. Together with our mass spectrometry analysis this strongly suggests that Thr716 is the only significant Mps1 phosphorylation site within Mad1^{CTD} *in vitro* and based on the complete disappearance of the original Thr716 peak position, phosphorylation is 100% efficient at this site. We however cannot rule out that *in vivo* Mps1 phosphorylates other sites on Mad1^{CTD}.

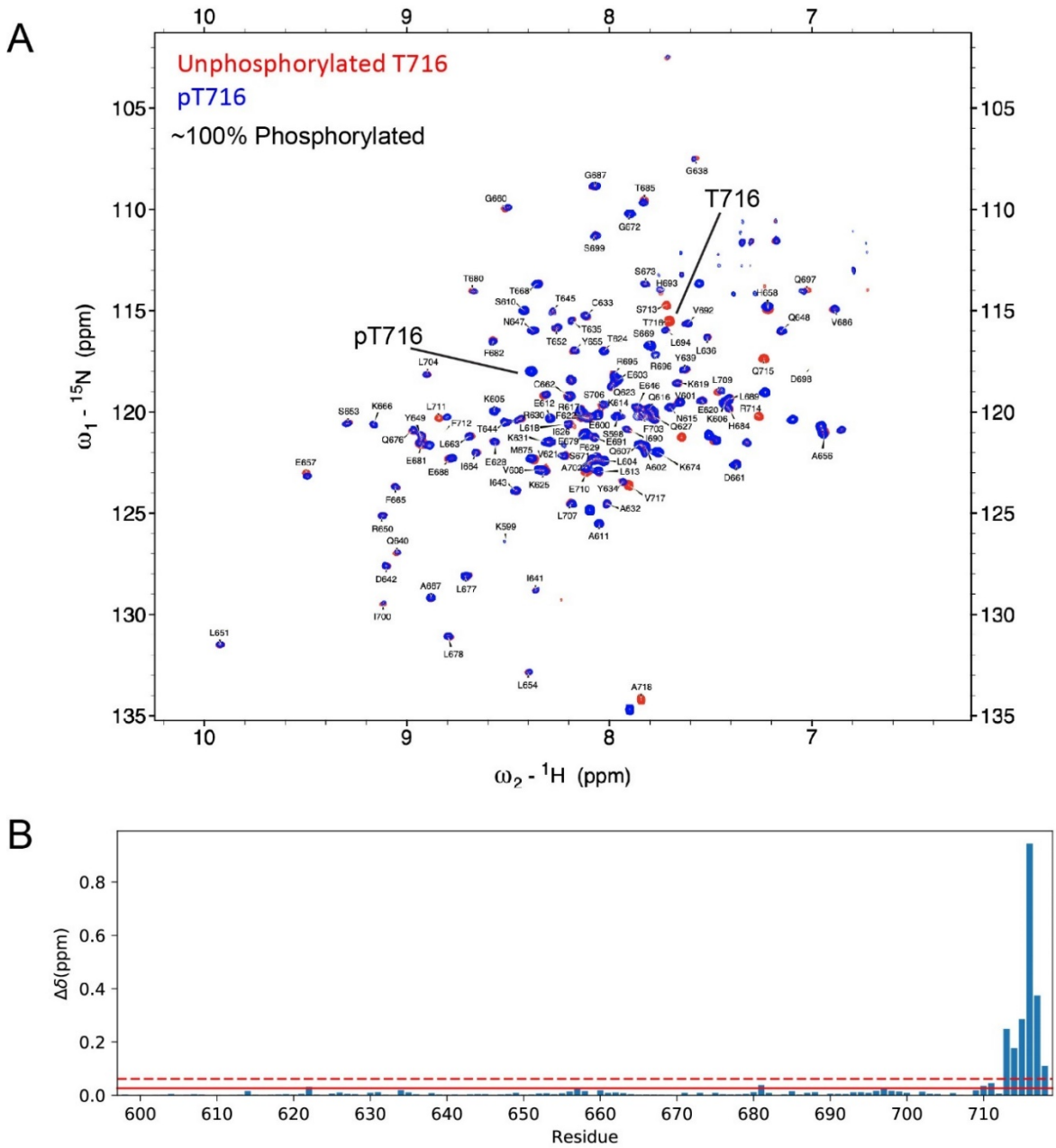

Figure 4.4: Phosphorylated Mad1^{CTD} by NMR. (A) *^{1}H, ^{15}N 2D HSQC of phosphorylated (blue) vs unphosphorylated (red) Mad1^{CTD}. As identified by the black lines, in the phosphorylated sample all of the original Thr716 peak has disappeared, and a new peak has appeared which can be assigned to pT716.* ***(B)*** *The relative CSPs of residues within pMad1^{CTD} as compared to non-phosphorylated Mad1^{CTD}. The solid red line is the mean CSP, while the dotted redline is the standard deviation.*

4.5 Crystal Structure of Phosphorylated Mad1^{CTD}

We were able to obtain a crystal structure of phosphorylated Mad1^{CTD} (Fig 4.5). The data collection and refinement statistics are shown in Appendix Table 4. This structure is identical to the previously crystallised unphosphorylated Mad1^{CTD} in the space group P6$_5$ (PDB ID: 4DZO; Kim *et al*, 2012), except for the presence of phosphorylation at Thr716. We only see a phosphate group on one Thr716 of the Mad1^{CTD} dimer, however, as is the case in the non-phosphorylated Mad1^{CTD} crystal structure, the very C-terminus of one chain has significantly

higher flexibility, which results in the last two C-terminal residues, Val717 and Ala718, not being visible in the electron density map. As our intact mass spectrometry and NMR suggests 100 % phosphorylation on a single site on every Mad1 promoter, we suspect that the greater flexibility of this chain is why the phosphate group is not visible. Overall, this structure further confirms phosphorylation at Thr716, and agrees with our NMR data that most peaks show no or little CSP upon phosphorylation of Thr716, confirming that no major conformational change occurs within the head domain of Mad1^{CTD} upon Mps1 phosphorylation.

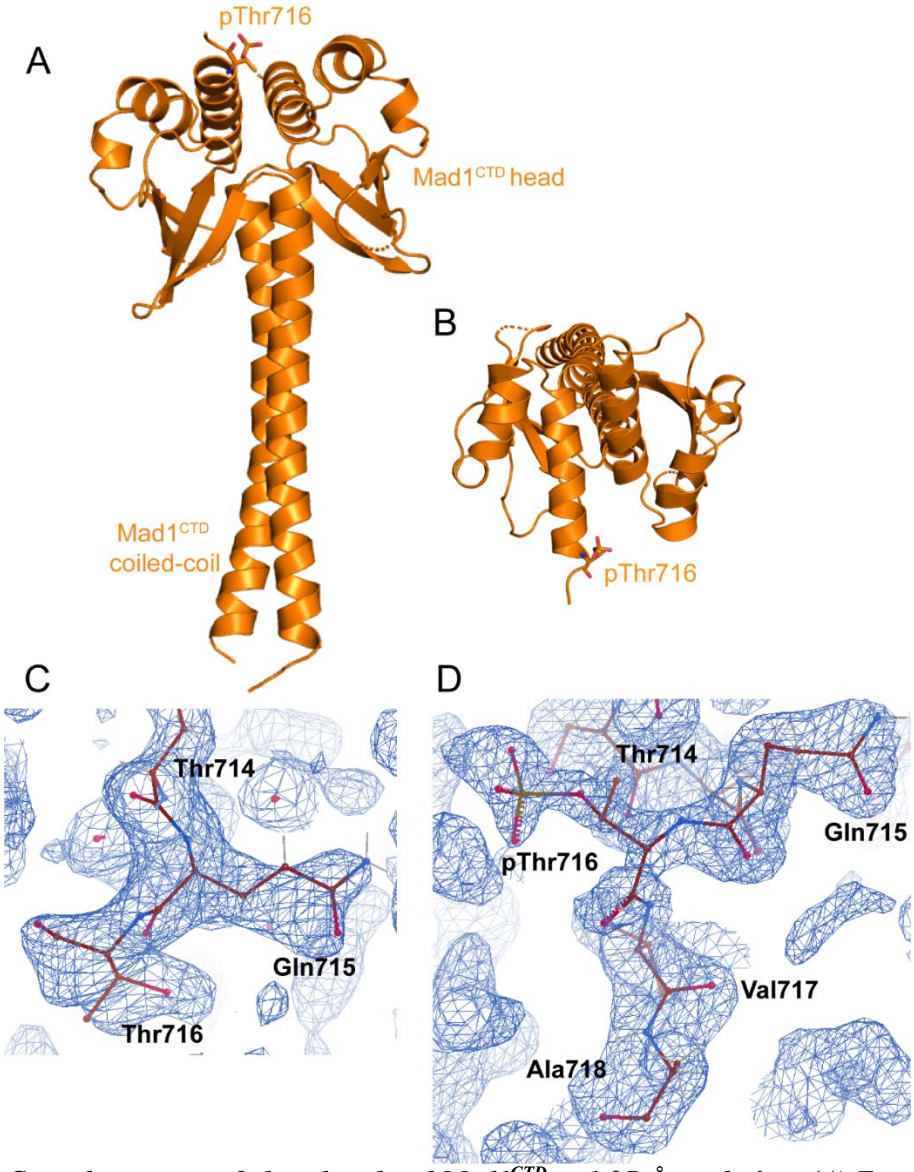

Figure 4.5: Crystal structure of phosphorylated Mad1^{CTD} at 1.87 Å resolution. ***(A)*** *Front view of the Mad1^{CTD} dimer with the single pThr716 site represented as a stick model.* ***(B)*** *Top view of the Mad1^{CTD} head domain with the pThr716 site shown.* ***(C)*** *Electron density for the more flexible C-terminus of chain where the last two residues (Val717 and Ala718) are not seen.* ***(D)*** *Electron density for the more rigid chain, with the phosphate group of pThr716 shown.*

4.6 Binding of Box1 and Box2 to Mad1^{CTD}

Peptides comprised of either the minimal Box1 or Box2 sequences implicated in the Cdc20-Mad1^{CTD} interaction (Box1 = 27-RWQRKAKE-34; Box2 = 58-RTPGKSSSKVQT-69) were synthesized (Table 2.9). The interactions of both with either Mad1^{CTD} or pThr716 Mad1^{CTD} were analysed by ITC. Box1 and Box2 into buffer alone did not produce any significant heat changes (Appendix Fig 4A-B). Box1 did not bind to non-phosphorylated Mad1^{CTD} (Appendix Fig 4C) but bound to pThr716 Mad1^{CTD} with an approximate K_D of 145 µM ± 35 µM (Appendix Fig 4D). Box2 also did not bind to unphosphorylated Mad1^{CTD}, and although binding to phosphorylated Mad1^{CTD} was seen, the affinity was extremely weak (low mM range) (Appendix Fig 4E-F). This suggests that both Box1 and Box2 bind preferentially to phosphorylated Mad1^{CTD}, albeit very weakly, and that Box1 has a higher affinity than Box2. These interactions were too weak to allow accurate measurement of the stoichiometry of Box1 and Box2 to Mad1^{CTD} by ITC.

Next, we used NMR to analyse the interaction of Box1 and Box2 to Mad1^{CTD} in further detail. Titration of Box1 and Box2 up to an 8-molar excess into 100 µM of unphosphorylated and phosphorylated ^{15}N Mad1^{CTD} is shown in Fig 4.6 and 4.7, respectively. The chemical shift perturbations of all assigned Mad1^{CTD} residues in all four spectra are summarised in Fig 4.8A. We also mapped these CSPs onto the crystal structure of pMad1^{CTD} (Fig 4.8 B-C). In all samples CSPs were observed for resonances at the very N-terminus of Mad1^{CTD} and within the RLK motif. These two regions were previously identified as the most flexible parts of Mad1^{CTD} which likely explains why CSPs at these residues are seen rather than actual binding (previously discussed in section 3.15). Additionally, CSPs were also observed for resonances from the three histidine residues within Mad1^{CTD} (His658, His684 and His693, highlighted by black arrows), and this is most likely due to subtle changes of histidine protonation upon small changes in pH and salt concentration during peptide titration (Fig 4.8A). The resonance for phosphorylated Thr716 is perturbated when Box1 is titrated into pMad1^{CTD}, while increased CSPs occur between residues 690-710 of Mad1^{CTD} when Box2 is titrated, with these CSPs being more pronounced when Box2 is titrated into phosphorylated Mad1^{CTD}. This suggests that Box1 binds directly to the phosphorylated Thr716 residue and that Box2 binds across the RWD-fold of Mad1^{CTD}. However, either the binding is very weak or not physiologically relevant as these CSPs were only observable at very high ligand concentrations.

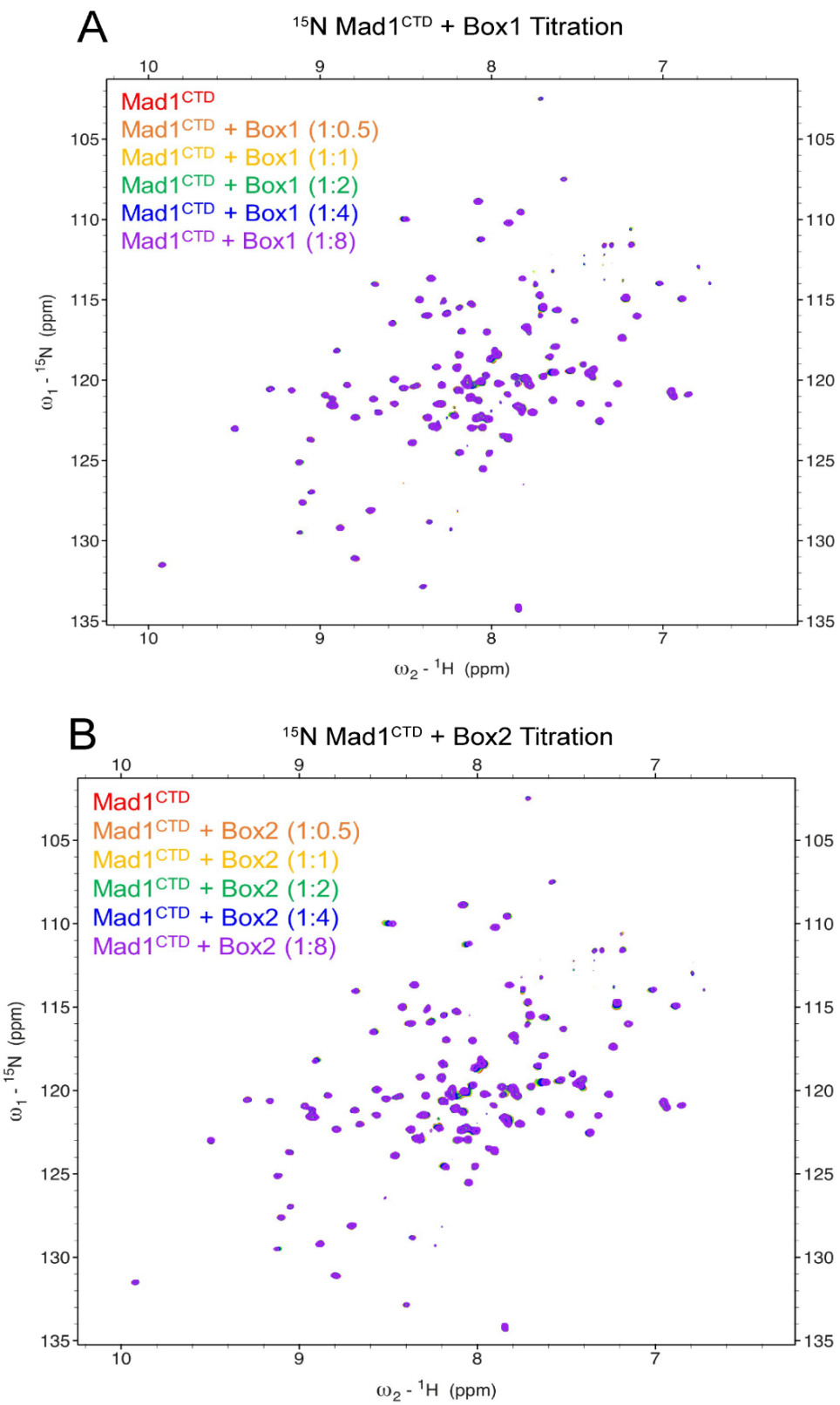

Figure 4.6: A ^{1}H, ^{15}N 2D HSQC showing ^{15}N-labelled Mad1^{CTD} at 100 µM before and after titration with either Box 1 (A) or Box2 (B) peptides up to an 8-molar excess of peptide.

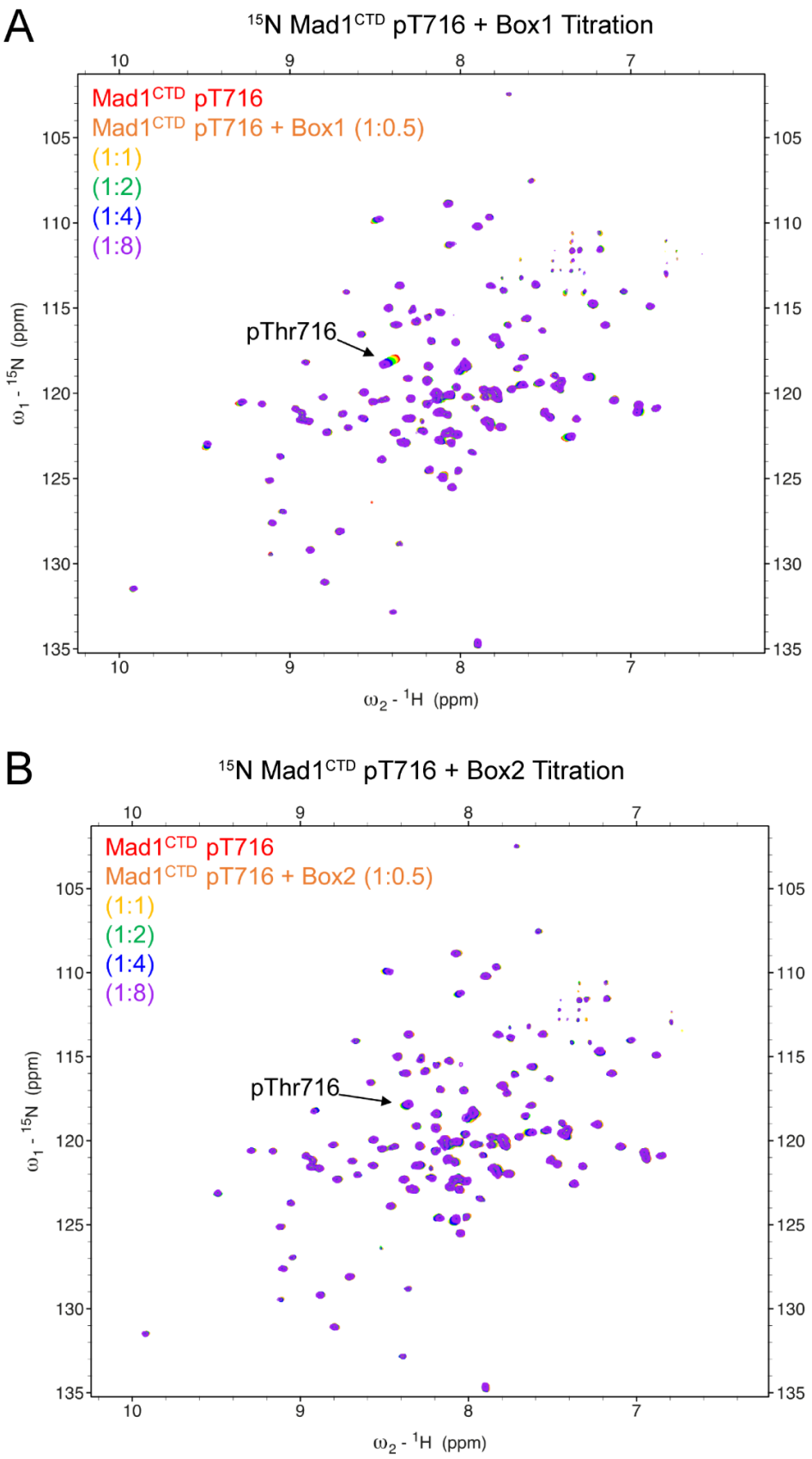

Figure 4.7: A ^{1}H, ^{15}N 2D HSQC showing phosphorylated (pThr716) ^{15}N-labelled Mad1^{CTD} at 100 µM before and after titration with either Box 1 (A) or Box2 (B) peptides up to an 8-molar excess of peptide.

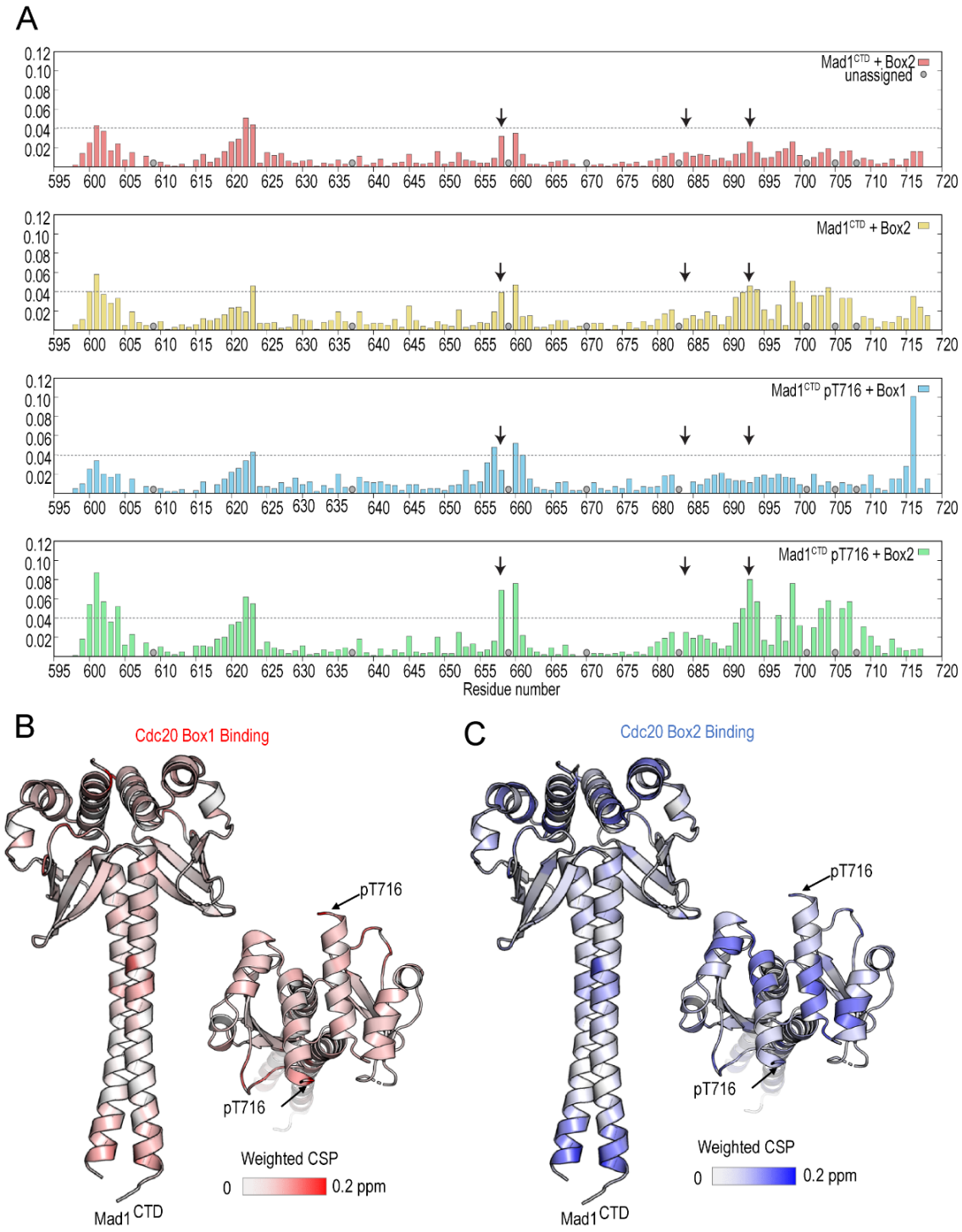

Figure 4.8: Chemical shift perturbations within Mad1^{CTD} upon Box1 and Box2 binding. (A) *Analysis of the weighted chemical shift perturbations of Box1 and Box2 binding to phosphorylated or unphosphorylated Mad1^{CTD} using the difference between apo Mad1^{CTD} compared to Mad1^{CTD} with an 8-molar excess of Box1 or Box2. The black arrows highlight CSPs which are likely a result of histidine residue sensitivity to small changes in pH and protonation. CSPs for Mad1^{CTD} + Box1 (Red), Mad1^{CTD} + Box2 (yellow), pMad1^{CTD} + Box1 (Blue), pMad1^{CTD} + Box2 (Green). CSPs above the grey dashed line (0.04 ppm) are considered significant.* ***(B)*** *The weighted CSPs of Box1 + pMad1^{CTD} are mapped onto the crystal structure of pMad1^{CTD}.* ***(C)*** *The weighted CSPs of Box2 + pMad1^{CTD} are mapped onto the crystal structure of pMad1^{CTD}.*

4.7 Only one Cdc20$^{1-73}$ can bind to the Mad1^{CTD} dimer

We were able to purify an N-terminal truncation of Cdc20 (residues 1-73), which includes the Box1 and Box2 motifs as well as a predicted α-helix at the very N-terminus of Cdc20 that is predicted to be helical by PSIPRED and AlphaFold2 (Fig 4.1A-B). We used SEC-MALS to explore binding of Cdc20$^{1-73}$ to phosphorylated and non-phosphorylated Mad1^{CTD} (Fig 4.9). Cdc20$^{1-73}$ did not bind to unphosphorylated Mad1^{CTD} (Fig 4.9A) but did to phosphorylated Mad1^{CTD} (Fig 4.9B). This further confirms the importance of the pThr716 site in promoting the Mad1:Cdc20 interaction. Cdc20$^{1-73}$ alone (8 kDa) elutes as a single peak later than the Mad1^{CTD} dimer (28 kDa), although by SEC-MALS the perceived molecular mass of this peak is very polydisperse (Fig 4.9B; blue peak). This strange elution of intrinsically disordered proteins has been observed previously in our lab and could suggest that Cdc20$^{1-73}$ is either aggregating or oligomerising during SEC. However, upon addition of pMad1^{CTD} and Cdc20 in a 1:2 molar ratio respectively, there is a clear shift in the elution of pMad1^{CTD} and a disappearance of the free Cdc20$^{1-73}$ peak (Fig 4.9B; pink peak). The peak corresponding to Mad1^{CTD}:Cdc20$^{1-73}$ is monodispersed with a calculated mass of 37 kDa, which is close to the expected mass of a Mad1^{CTD} dimer with only a single Cdc20$^{1-73}$ molecule bound (36 kDa).

Several attempts were made to add higher amounts of excess Cdc20$^{1-73}$ to see if the mass would increase and suggest a second Cdc20$^{1-73}$ could bind, however, these efforts failed because excess Cdc20$^{1-73}$ brought most all of the Mad1^{CTD}:Cdc20$^{1-73}$ complex into the void. Similar to the strange results seen for Cdc20$^{1-73}$ elution alone, we suspect the complex is aggregating on SEC when excess Cdc20$^{1-73}$ is present. The stability of the Mad1^{CTD}:Cdc20$^{1-73}$ complex in SEC would suggest a low μM affinity interaction, which is much stronger than that between Mad1^{CTD} and Box1 or Box2. Despite repeated efforts we were unable to obtained informative ITC data for Cdc20$^{1-73}$, also likely caused by aggregation of Cdc20$^{1-73}$ at the high concentrations required for ITC. Thus, we were unable to measure the K_D or stoichiometry of this interaction by ITC.

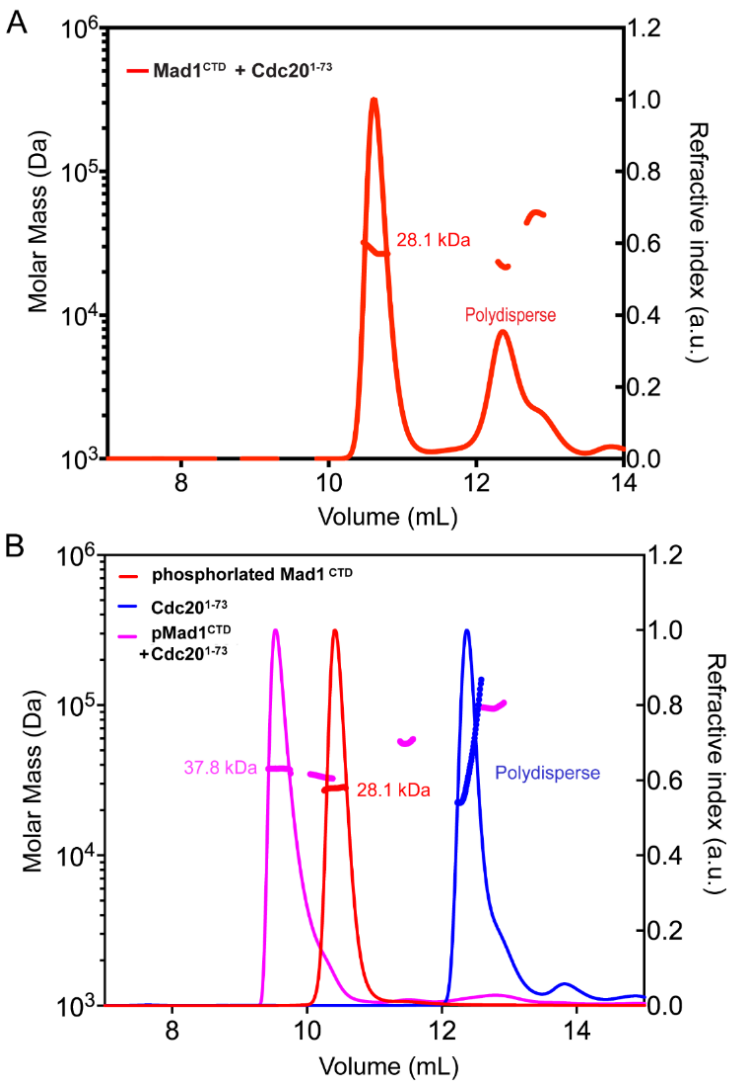

Figure 4.9: SEC-MALS of Mad1^{CTD} and Cdc20$^{1-73}$. (A) *Non-phosphorylated Mad1^{CTD} + Cdc20$^{1-73}$. The main peak has a mass of 28.1 kDa. This is nearly identical to the expected mass of Mad1^{CTD} alone (27, 887 Da), suggesting that no binding occurs.* ***(B)*** *Mad1^{CTD} alone (red) elutes as one monodispersed species with a mass of 28.1 kDa as expected for dimeric Mad1^{CTD} (27,887 Da). Cdc20$^{1-73}$ alone (blue) elutes quite late, as a single major peak, suggesting a single small species, however SEC-MALS suggests the peak is very polydisperse giving a variety of masses representing a range of oligomers. Mad1^{CTD}+ Cdc20$^{1-73}$ (pink), shows a main monodispersed species of 37.8 kDa with a shoulder of 31 kDa. This suggests that the complex of Mad1 and Cdc20 contains a 1:1 ratio of Mad1^{CTD} dimer (28 kDa) to Cdc20$^{1-73}$ (8 kDa).*

To overcome this technical difficulty, we used AUC-SE to further investigate the stoichiometry of Mad1^{CTD} dimer to Cdc20$^{1-73}$ (Fig 4.10). These experiments confirm that only a single Cdc20$^{1-73}$ molecule can bind to the Mad1^{CTD} homodimer, and that Cdc20$^{1-73}$ exists as a homogenous monomer in solution up to 80 µM despite the polydispersity suggested by SEC-MALS. Given that Mad1^{CTD} is a homodimer this stoichiometry is surprising, however we have previously shown that only a single molecule of Bub1^{CD1} can bind to the Mad1^{CTD} dimer (section 3.4), so it seems likely that these two phenomena are

related. It could be that the 1:1 stoichiometry of Cdc20$^{1-73}$ to Mad1^{CTD} dimer is also a result of the inherent asymmetry present in Mad1^{CTD} or it could be caused by another unknown mechanism. Similar to Bub1^{CD1} binding to Mad1^{CTD}, we cannot rule out that this interaction with full-length constructs and *in vivo* might produce a different stoichiometry, but it seems likely that the ability of only one Cdc20$^{1-73}$ to bind the Mad1^{CTD} dimer is physiologically and functionally relevant.

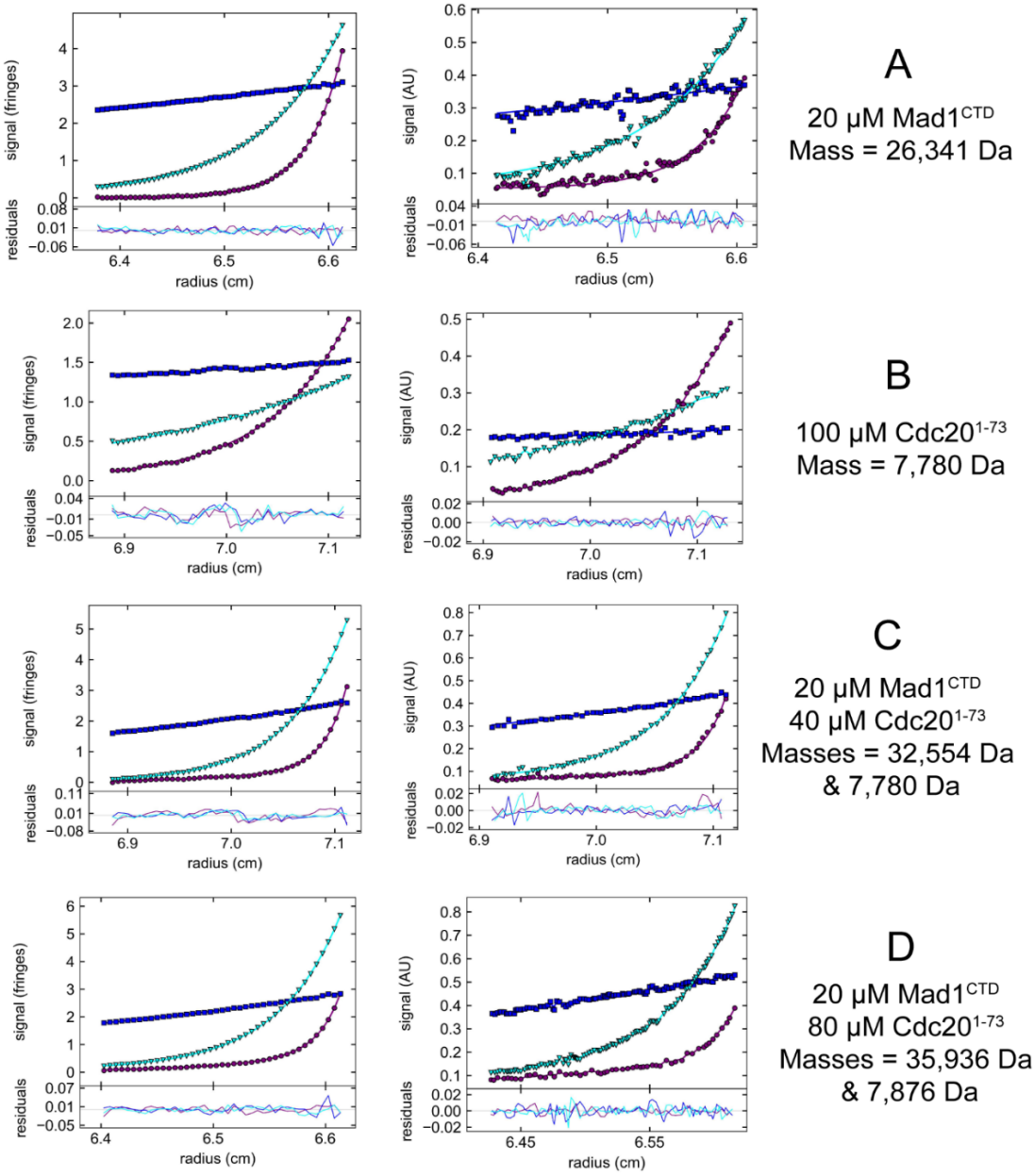

Figure 4.10: Sedimentation equilibrium (AUC-SE) of Mad1^{CTD} and Cdc20$^{1-73}$. *The interference data are on the left, and the absorbance data are on the right. Scans were initially fitted to single species exponentials. When there was found to be a poor fit, the number of species was increased to two or three, and the mass of a known species (Cdc20$^{1-73}$) was fixed in the fit. The calculated mass for the major species in all the Mad1^{CTD} and Cdc20$^{1-73}$ mixtures is close to the expected value of a single Cdc20$^{1-73}$ molecule bound to the Mad1^{CTD} dimer (35,745 Da), with the average calculated mass being 34,651 ± 771 Da.*

4.8 Binding of Cdc20$^{1-73}$ to ^{15}N Mad1^{CTD}

We next analysed residues involved in Cdc20$^{1-73}$ binding using NMR, by titrating unlabelled Cdc20$^{1-73}$ into either phosphorylated or unphosphorylated ^{15}N-labelled Mad1^{CTD}. We observed significant signal attenuation for the resonances from a large portion of the sequence of Mad1^{CTD} (Fig 4.11), in contrast to the more regional changes when Box1 or Box2 were titrated (Fig 4.6 and 4.7). It should be noted that Cdc20$^{1-73}$ binding causes line broadening of the Mad1^{CTD} peaks, rather than CSPs. This could be due to an intermediate exchange regime in NMR time-scale and this would agree with the low µM affinity of Mad1^{CTD}:Cdc20$^{1-73}$ observed in SEC.

The relative peak intensity changes for the assigned ^{15}N-labelled Mad1^{CTD} residues are summarised in Fig 4.12A and are mapped onto the crystal structure of Mad1^{CTD} (Fig 4.12B-C). This demonstrates that in both the unphosphorylated and phosphorylated Mad1^{CTD} samples, Cdc20$^{1-73}$ binding results in substantial signal attenuation within Mad1^{CTD} spanning residues 616-660. This starts at the RLK motif, extends along the coiled-coil, and includes the first β-strand of the head domain. The extent of line broadening is more significant in phosphorylated Mad1^{CTD}, with signal attenuation observed in all four β -strands in the anti-parallel β-sheet, as well as the last α-helix and the C-terminal pThr716 site. These data fit well with a cross-linking study which suggested that the pMad1:Cdc20 interaction was disrupted by a Q648A-R650A mutation which lies within the conserved QYRL motif within the anti-parallel β-sheet of Mad1^{CTD} (Piano *et al*, 2021). Overall, the strikingly large number of residues affected by Cdc20$^{1-73}$ binding suggests that Cdc20$^{1-73}$ has a very extensive binding interface with Mad1^{CTD} and/or that it induces a global conformational change within Mad1^{CTD}.

We find these data interesting in light of the fact that like the Bub1^{CD1}-Mad1^{CTD} interaction, only a single molecule of Cdc20$^{1-73}$ can bind to the Mad1^{CTD} homodimer. Our data for Bub1^{CD1} suggest that this stoichiometry is controlled by inherent asymmetry within Mad1^{CTD}, such that the curvature of the coiled-coil with respect to the head domain, makes one face of Mad1 more favourable than the other (chapter 3). Thus, this makes us wonder if Cdc20$^{1-73}$ is binding to the curved coiled-coil, and this is controlling Cdc20$^{1-73}$ stoichiometry or if some other mechanism is occurring. However, as it is not possible to differentiate if the changes in relative peak intensities are from binding or conformational change, without structures of the complex, we can only speculate.

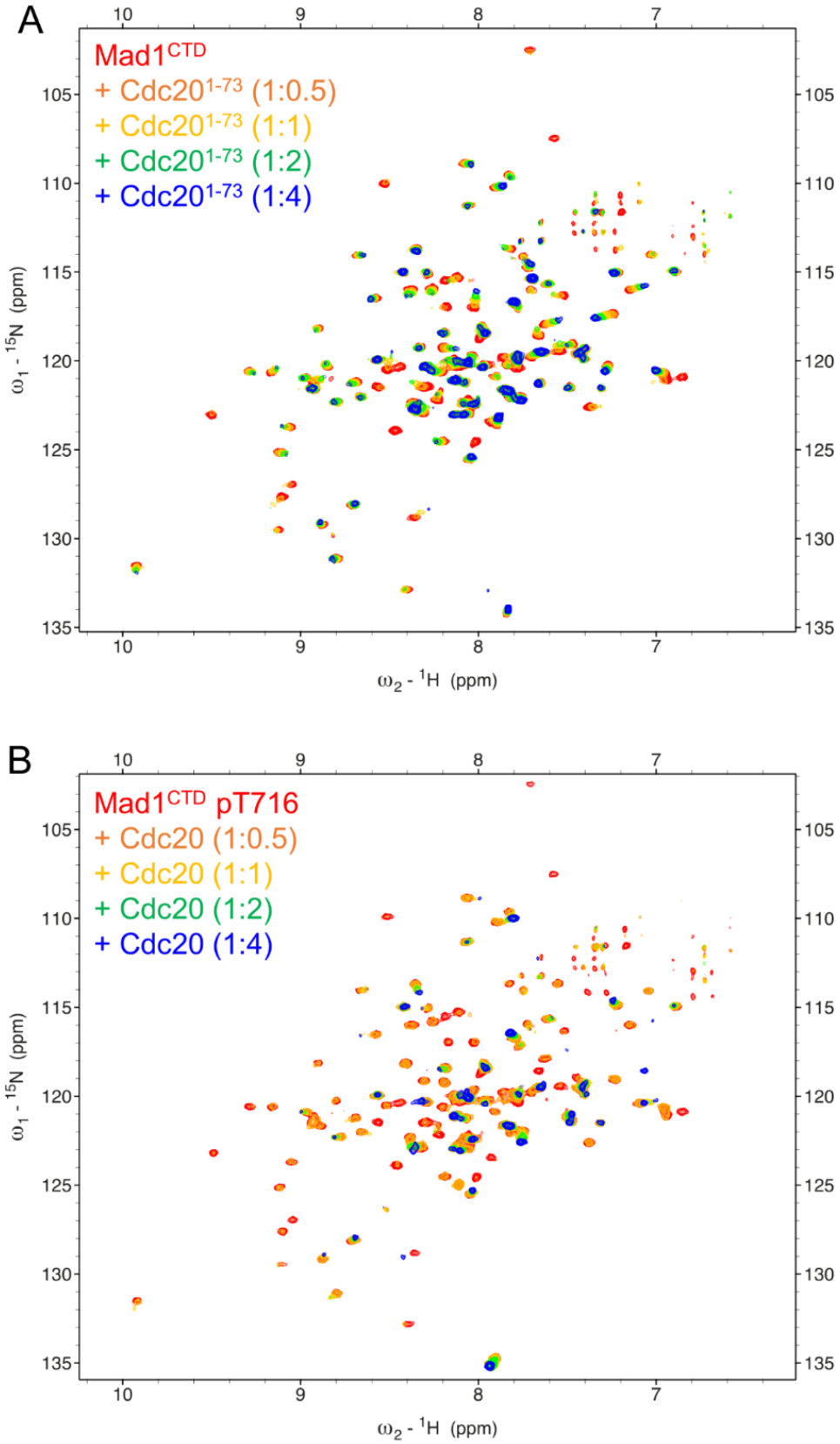

Figure 4.11: A ^{1}H ,^{15}N 2D HSQC showing titration of unlabelled Cdc20$^{1-73}$ into (A) *^{15}N-labelled non-phosphorylated Mad1^{CTD} or* ***(B)*** *^{15}N-labelled phosphorylated Mad1^{CTD}.*

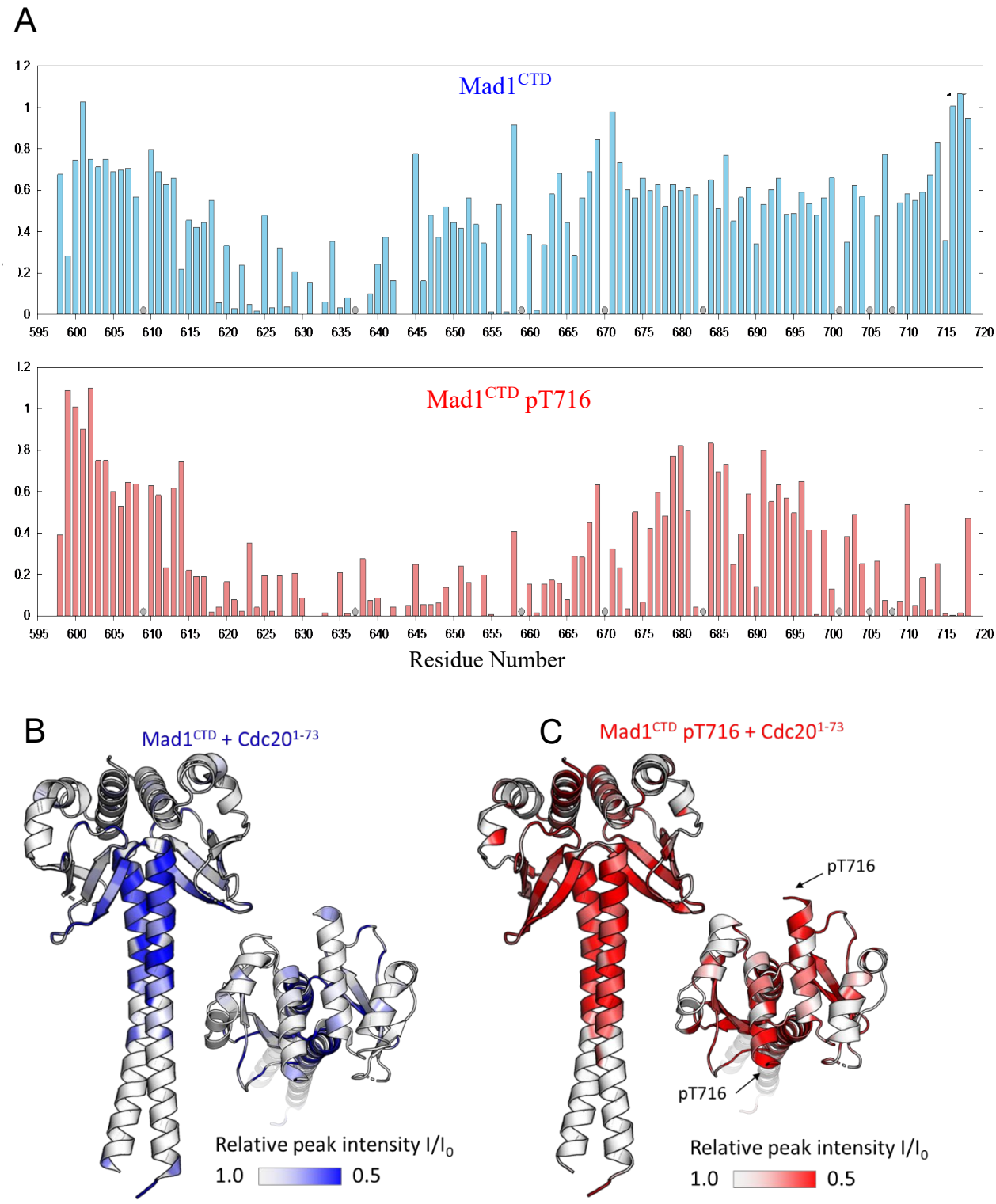

Figure 4.12: Analysis of the Cdc20$^{1-73}$ and Mad1^{CTD} interaction by NMR. ***(A)*** *Relative peak intensity changes from the ^{1}H, ^{15}N 2D HSQC of ^{15}N-labelled unphosphorylated Mad1^{CTD} + unlabelled Cdc20$^{1-73}$ at a 1:1 molar ratio (blue) or ^{15}N-labelled phosphorylated Mad1^{CTD} (red) + unlabelled Cdc20$^{1-73}$ at a 1:1 molar ratio. Unassigned peaks are denoted as grey circles. Lower peak intensity (line-broadening) means those residues are experiencing either conformational change or binding. Cdc20$^{1-73}$ binding induced line-broadening is mapped onto the crystal structure of Mad1^{CTD} when in the non-phosphorylated* ***(B)*** *or phosphorylated* ***(C)*** *states.*

4.9 Backbone Assignment of Cdc20$^{1-73}$

Next, in order to obtain structural information for Cdc20$^{1-73}$ and to analyse which residues are involved in Mad1^{CTD} binding, we expressed and purified ^{15}N, ^{13}C-labelled Cdc20$^{1-73}$ for backbone assignment of Cdc20$^{1-73}$. The assignment of Cdc20$^{1-73}$ in a ^{1}H, ^{15}N 2D HSQC, as completed by Dr. Conny Yu, is shown in Fig 4.13. Signals from prolines are absent in ^{1}H, ^{15}N 2D HSQC as they do not contain amide protons, and 10 of the 73 residues in this N-terminal truncation of Cdc20 are prolines. Additionally, several peaks were exchange broadened and not observable in the ^{1}H, ^{15}N 2D HSQC spectrum. Therefore, a carbon-detect ^{13}C, ^{15}N 2D CON spectrum was used to retrieve these missing signals (Fig 4.14). A ^{13}C, ^{15}N 2D CON experiment observes resonances from ^{13}CO which are attached to ^{15}N such that all backbone resonances including prolines can be acquired (Kragelund & Skriver, 2020). Carbon-detect experiments are also less susceptible to line broadening caused by solvent exchange of amide protons, therefore allowing a complete assignment of all residues of Cdc20$^{1-73}$.

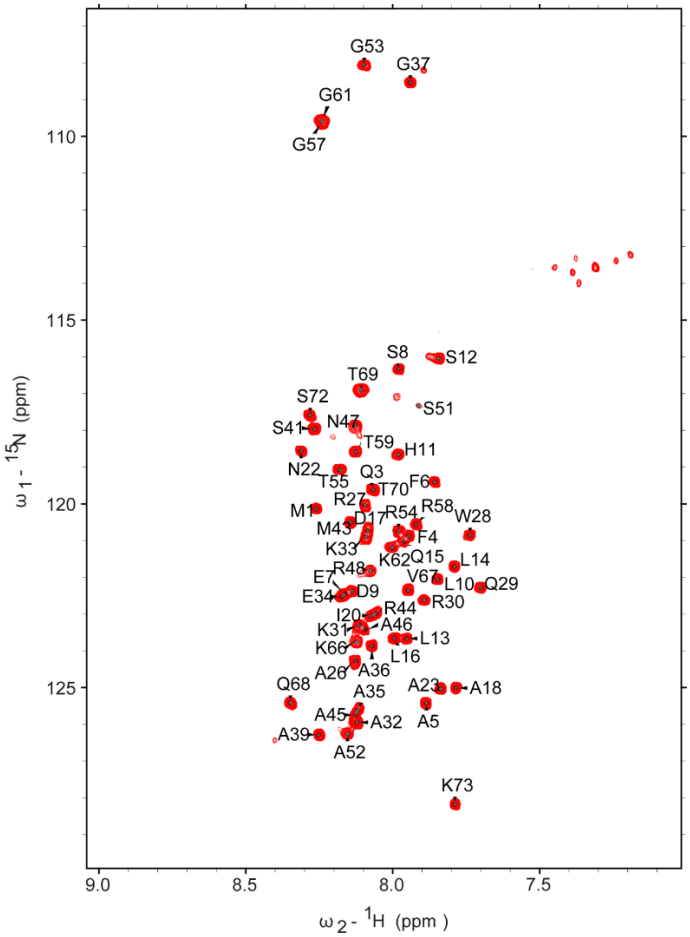

Figure 4.13: A ^{1}H, ^{15}N-2D HSQC (proton-detect) spectrum showing ^{15}N-labelled Cdc20$^{1-73}$ *with assignments of backbone resonances completed by Dr. Conny Yu labelled on the spectra.*

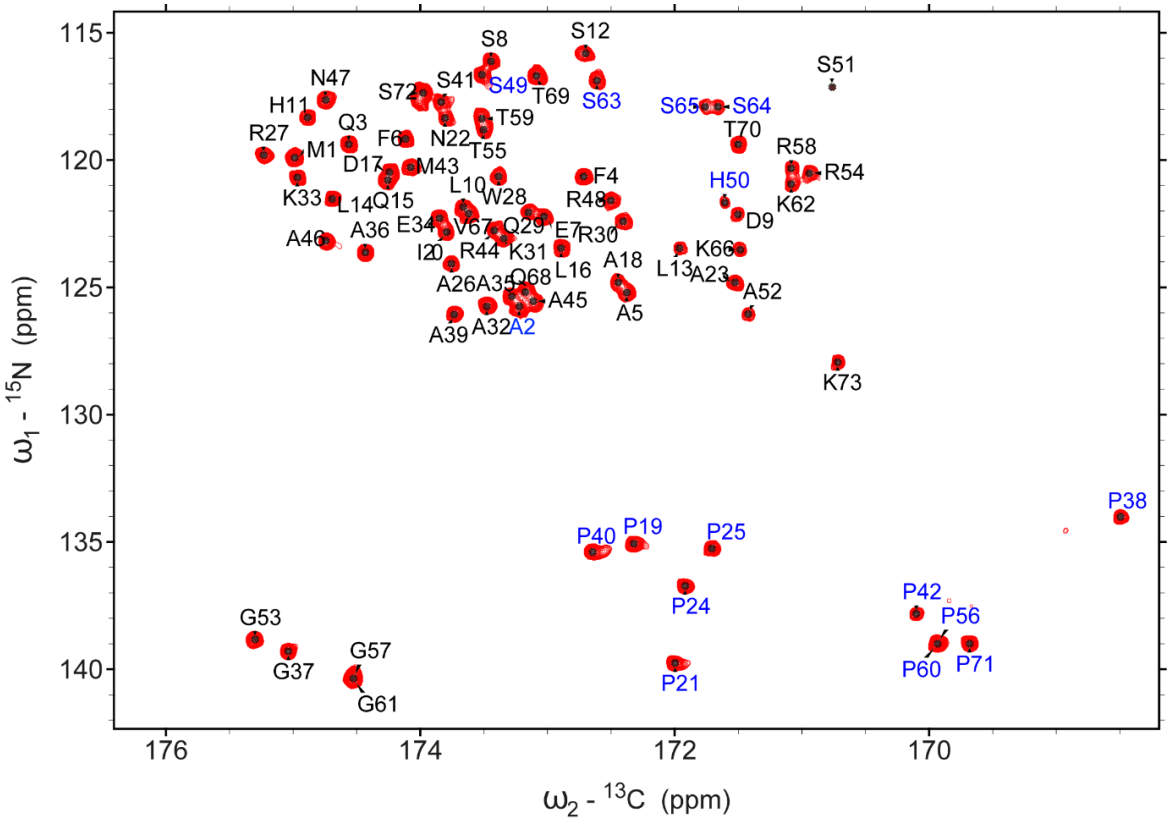

Figure 4.14: A ^{13}C, ^{15}N 2D CON (carbon-detect) spectrum showing ^{13}C, ^{15}N-labelled Cdc20$^{1-73}$ *with assignments of backbone resonances completed by Dr. Conny Yu labelled on the spectra. Residues coloured in blue are ones which were not seen in the ^{1}H, ^{15}N HSQC due to being either exchange broadened or proline residues.*

4.10 Investigating the binding of Mad1^{CTD} to labelled Cdc20$^{1-73}$

Having a complete sequence assignment of Cdc20$^{1-73}$ allowed us to analyse how each of these residues is affected upon titration of unphosphorylated or phosphorylated Mad1^{CTD} using a ^{1}H, ^{15}N correlation spectra of Cdc20$^{1-73}$ (Fig 4.15A-B). As was the case for titration of Cdc20$^{1-73}$ into ^{15}N-labelled Mad1^{CTD}, the ^{15}N-labelled Cdc20$^{1-73}$ peaks experience line broadening upon Mad1^{CTD} addition. We mapped these relative peak intensity changes to the sequence of Cdc20$^{1-73}$, with the secondary structure prediction of these residues shown below (Fig 4.15C). When either phosphorylated or unphosphorylated Mad1^{CTD} is titrated, substantial signal attenuation in the N-terminal half of Cdc20$^{1-73}$ occurs, whereas the C-terminal half, which includes the Box2 motif, is largely unaffected. This aligns with our ITC and NMR data which suggested that Box2 had very weak if any affinity for Mad1^{CTD} (section 4.6). Strikingly more signal attenuation occurs when pMad1^{CTD} is titrated, further confirming the importance of Mad1 phosphorylation by Mps1 in promoting this interaction (Fig 4.15B). In the non-phosphorylated sample, the more substantial line broadening occurs between

Cdc20$^{1-73}$ residues 10-30, which is centred on the two predicted α-helices, while when phosphorylated Mad1^{CTD} is titrated, the entire N-terminal half of Cdc20$^{1-73}$ is affected (Fig 4.15C).

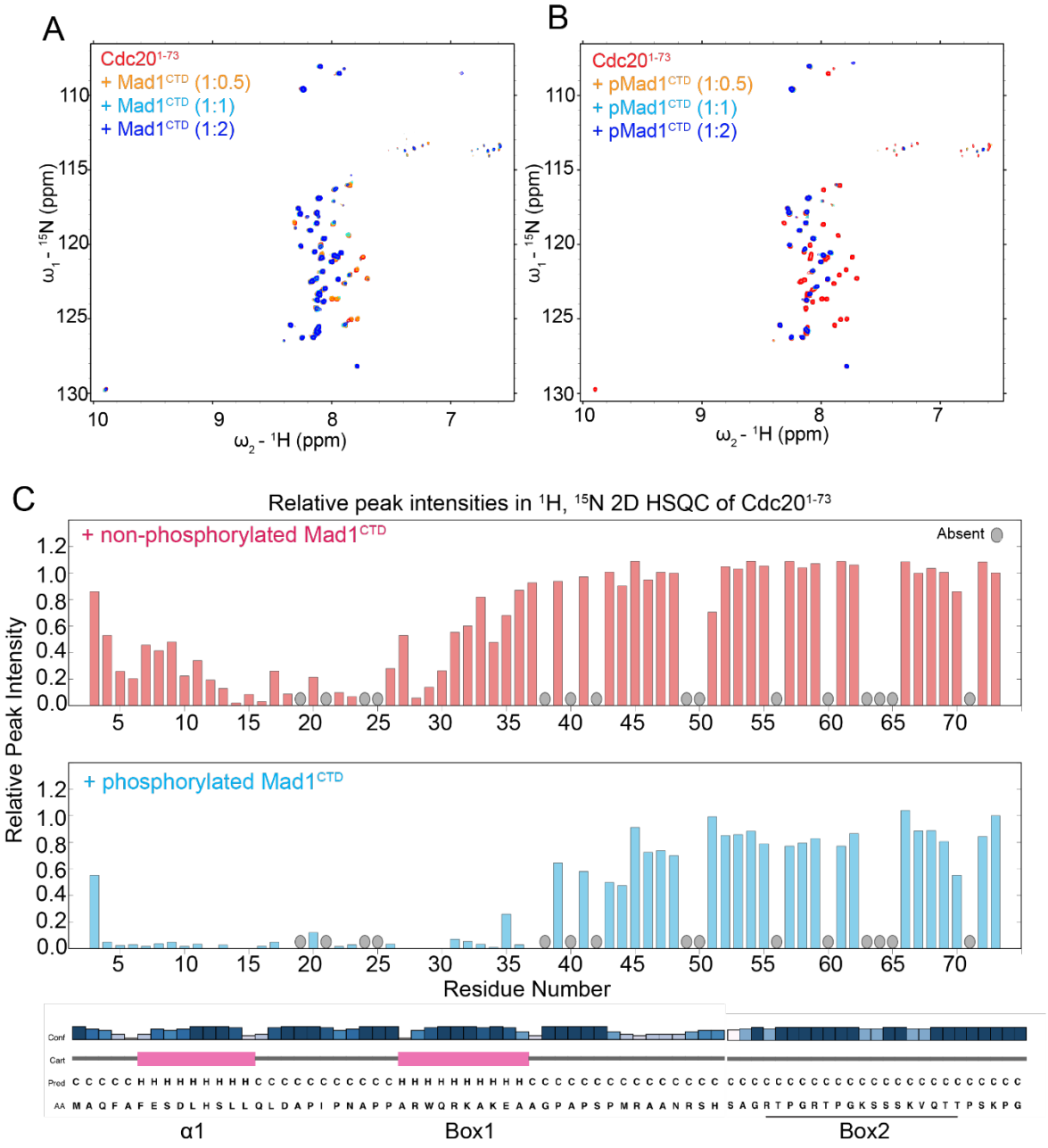

Figure 4.15: Binding of Mad1^{CTD} to ^{15}N-labelled Cdc20$^{1-73}$. (A) *A ^{1}H, ^{15}N 2D HSQC of non-phosphorylated Mad1^{CTD} titrated into ^{15}N-labelled Cdc20$^{1-73}$.* ***(B)*** *A ^{1}H, ^{15}N 2D HSQC of phosphorylated Mad1^{CTD} titrated into ^{15}N-labelled Cdc20$^{1-73}$.* ***(C)*** *The relative peak intensity changes within the ^{1}H, ^{15}N 2D HSQC spectra in (A) and (B) are mapped on to the sequence of Cdc20$^{1-73}$ based on the backbone assignments shown in Fig 4.13. The peak intensity changes are normalised to the Cdc20$^{1-73}$ C' residue Gly73. Peaks which are absent in the ^{1}H, ^{15}N 2D HSQC spectrum of Cdc20$^{1-73}$ are denoted as grey circles.*

As our NMR data suggest that the Box1 peptide binds very specifically to the pThr716 residue of pMad1^{CTD}, it seems plausible that Cdc20 lies in a parallel orientation to Mad1^{CTD},

such that Box1 binds to the top of the head domain at the flexible pThr716 site two residues from the C-terminus, while the N-terminus of Cdc20, including the first α-helix binds across the head domain β-sheet of $Mad1^{CTD}$ and possibly extends along the top of the coiled-coil. We find it interesting that our structure of $Bub1^{CD1}$-$Mad1^{CTD}$ (discussed in chapter 3), identified that Bub1 and Mad1 bind in a parallel orientation also, with the C-terminus of $Bub1^{CD1}$ posed to extend across the head domain of $Mad1^{CTD}$. This would position the ABBA and KEN1 motifs of Bub1 which are C-terminal to the Bub1 CD1 domain, in close proximity to the C-terminal β-propeller of Cdc20, and in the same orientation relative to one another. This Bub1-Cdc20 interaction has been shown to be important for SAC signalling, likely by repositioning Cdc20 in close proximity to the Mad1:C-Mad2 complex for MCC formation and may also be how Cdc20 is recruited to kinetochores for MCC formation (Chang *et al*, 2015; Di Fiore *et al*, 2016; Zhang *et al*, 2019; Diaz-Martinez *et al*, 2015).

We additionally analysed ^{15}N, ^{13}C-labelled $Cdc20^{1-73}$ upon titration of phosphorylated $Mad1^{CTD}$ in a ^{13}C, ^{15}N 2D CON experiment where resonances from all 73 residues of $Cdc20^{1-73}$ can be observed (Fig 4.16A). Plotting these relative peak intensity changes onto the sequence of $Cdc20^{1-73}$ provides a more complete analysis, which confirms that essentially all residues in the N-terminal half of $Cdc20^{1-73}$, including five prolines are involved in $pMad1^{CTD}$ binding, while the C-terminal half is largely unaffected (Fig 4.16B).

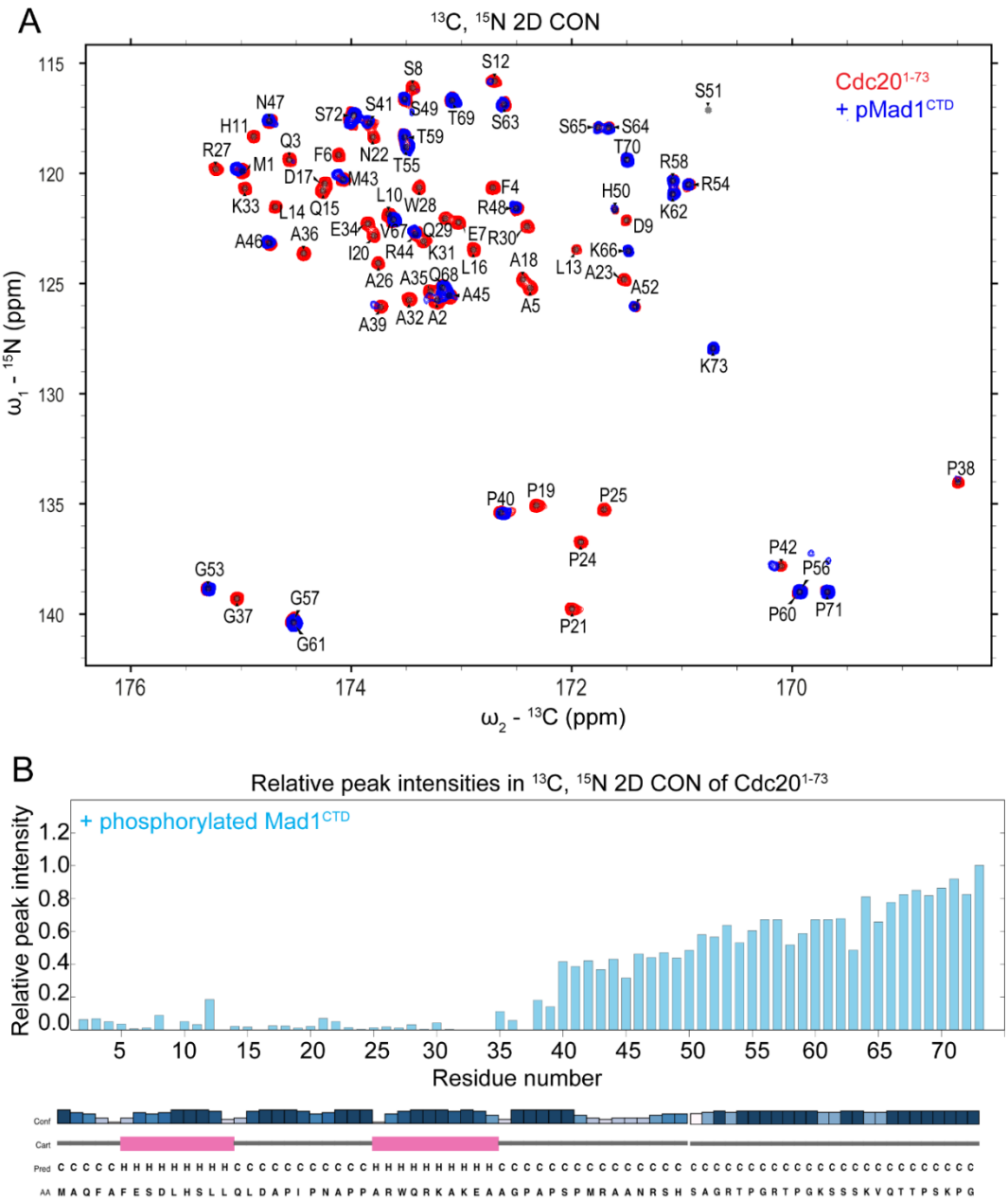

Figure 4.16: Binding of pMad1^{CTD} to ^{15}N, ^{13}C-labelled Cdc20$^{1-73}$. (A) *The ^{13}C, ^{15}N 2D CON spectrum of ^{15}N, ^{13}C-labelled Cdc20$^{1-73}$ before (red) and after (blue) pMad1^{CTD} addition at a 2-molar excess.* ***(B)*** *The relative peak intensity changes within ^{15}N, ^{13}C-labelled Cdc20$^{1-73}$, before and after pMad1^{CTD} addition. The peak intensity changes are normalised to the Cdc20$^{1-73}$ C-terminal residue Gly73.*

4.11 Mad1^{CTD} binding may promote helical formation within Cdc20$^{1-73}$

We performed ^{15}N{^{1}H}-heteronuclear NOE experiments that samples ^{15}N backbone dynamics on a fast picosecond timescale (Fig. 4.17A). Despite Cdc20$^{1-73}$ being disordered, our dynamics data revealed lower flexibility for the backbone N-H in the regions that were predicted to be helical. The termini and a middle segment of the sequence (around residues 35-40) were also determined to be highly dynamic.

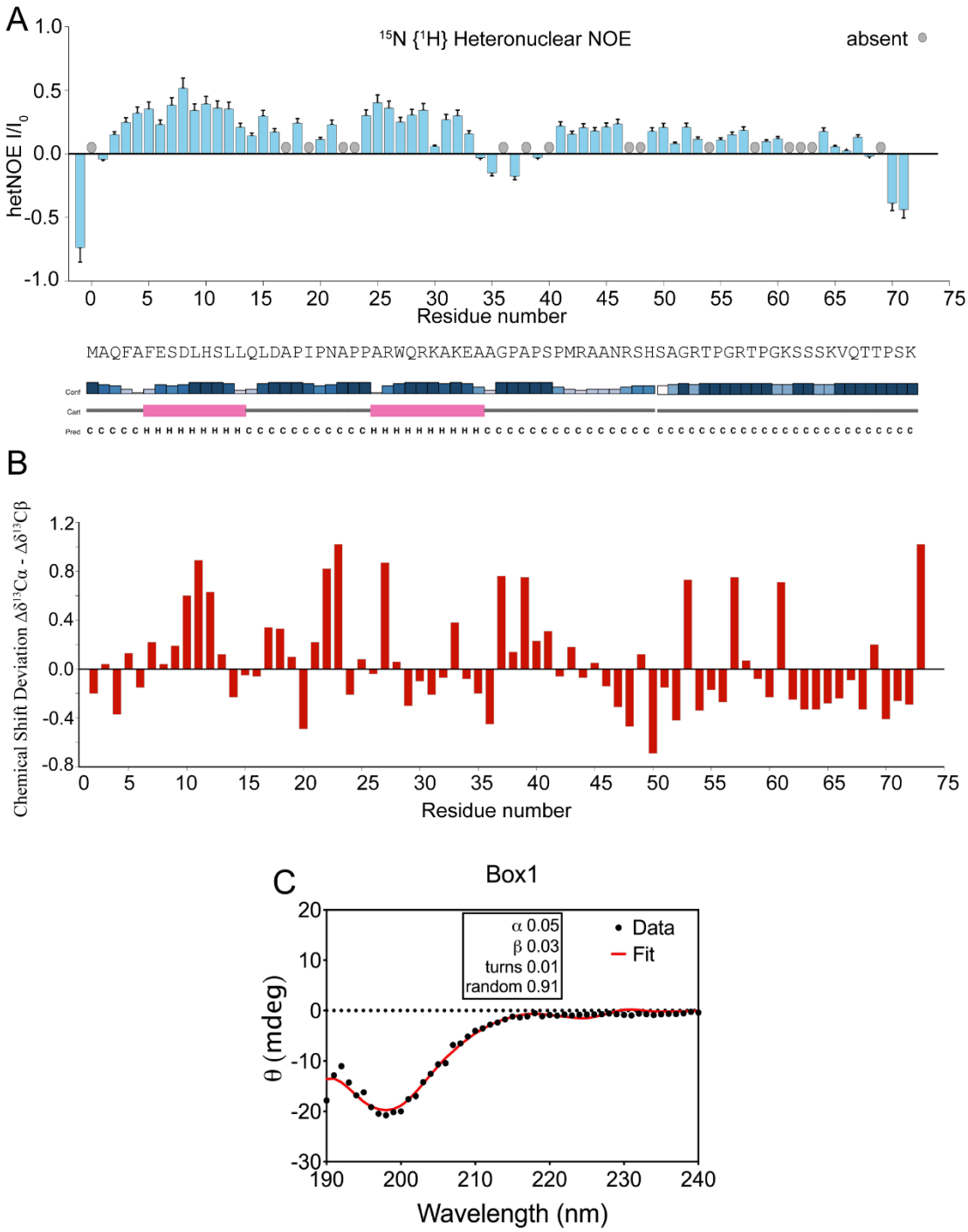

Figure 4.17: Dynamics and secondary structure analyses of Cdc20$^{1-73}$. (A) *^{15}N{^{1}H}-heteronuclear NOE values collected with interleaved on-(I) and off- (I^0) resonance and expressed as I/I_0. A higher value indicates higher rigidity of the backbone N-H bond. The error bars are the calculated standard deviations of the two technical replicates on the sample.* ***(B)*** *The calculated secondary chemical shifts of ^{15}N, ^{13}C-labelled Cdc20$^{1-73}$.* ***(C)*** *Circular dichroism of Box1 peptide in water.*

We also analysed the secondary chemical shifts for ^{15}N, ^{13}C-labelled Cdc20$^{1-73}$ (Fig 4.17B). The theoretical chemical shift of an amino acid in a completely random coil at a standard temperature and pH can be calculated, and how much a residues Cα or Cβ deviates from a random coil (the difference between the experimental Cα/β and the theoretical Cα/β) is called

the secondary chemical shift (Spera & Bax, 1991). The Cα deviation minus the Cβ deviation gives a good indication for whether a residue is part of a α-helix (positive values) or β-strand (negative values). Secondary chemical shifts are particularly powerful for disordered proteins, as they can also reveal if there is propensity for secondary structure. The secondary chemical shifts for $Cdc20^{1-73}$ suggests that there is very little secondary structure propensity for $Cdc20^{1-73}$ alone in solution (Fig 4.17B). We also performed circular dichroism on the Box1 peptide which confirmed that this region is not helical (Fig 4.17C). Unfortunately, the substantial line broadening which occurs upon $pMad1^{CTD}$ interaction with labelled $Cdc20^{1-73}$, prevented us from collecting similar backbone dynamics and secondary chemical shift analyses for labelled $Cdc20^{1-73}$ when in complex with $pMad1^{CTD}$.

Peaks with up-field chemical shifts in a ^{1}H, ^{15}N 2D HSQC experience more shielding and normally correspond to residues which adopt a helical conformation (Mielke & Krishnan, 2009). In the ^{1}H, ^{15}N 2D HSQC spectra of ^{15}N-labelled $Cdc20^{1-73}$, several peaks within the N-terminal half of Cdc20 are in the 7.5-8 ppm range. Interestingly, upon titration of non-phosphorylated or phosphorylated $Mad1^{CTD}$ into ^{15}N-labelled $Cdc20^{1-73}$, nearly all these peaks are line-broadened (Fig 4.15A-B). All of our experiments with ^{15}N or ^{15}N, ^{13}C-labelled $Cdc20^{1-73}$ were done at 5 °C. This is because at low temperatures the exchange rate between backbone NH and the solvent is significantly lower, giving solvent exposed residues improved signal, and for disordered proteins like $Cdc20^{1-73}$, the low temperature provides a significantly better signal-to-noise ratio (Waudby *et al*, 2020). Meanwhile at high temperatures faster rotational diffusion occurs which results in shorter tumbling time, and this normally gives an improved signal-to-noise ratio for structured proteins where the solvent exchange rate of amide protons is less of a problem. Therefore, we also attempted to study the interaction between $Cdc20^{1-73}$ and $pMad1^{CTD}$ at a higher temperature, in the hopes that we could obtain more information for the potentially structured regions (Fig 4.18). Strikingly, at 25 °C when ^{15}N-labelled $Cdc20^{1-73}$ is bound to $Mad1^{CTD}$ we can retrieve signals around 7.4 ppm, which strongly suggests that binding is inducing a portion of Cdc20 to become a folded α-helix. PSIPRED secondary structure prediction and AlphaFold2 structure prediction predicts two α-helices within the N-terminus of Cdc20, one of which is the Box1 motif (Fig 4.1A-B; Buchan and Jones, 2019; Jumper *et al*, 2021), it therefore seems likely that the binding of $Mad1^{CTD}$ to $Cdc20^{1-73}$ either stabilises or promotes formation of one or both of these helices.

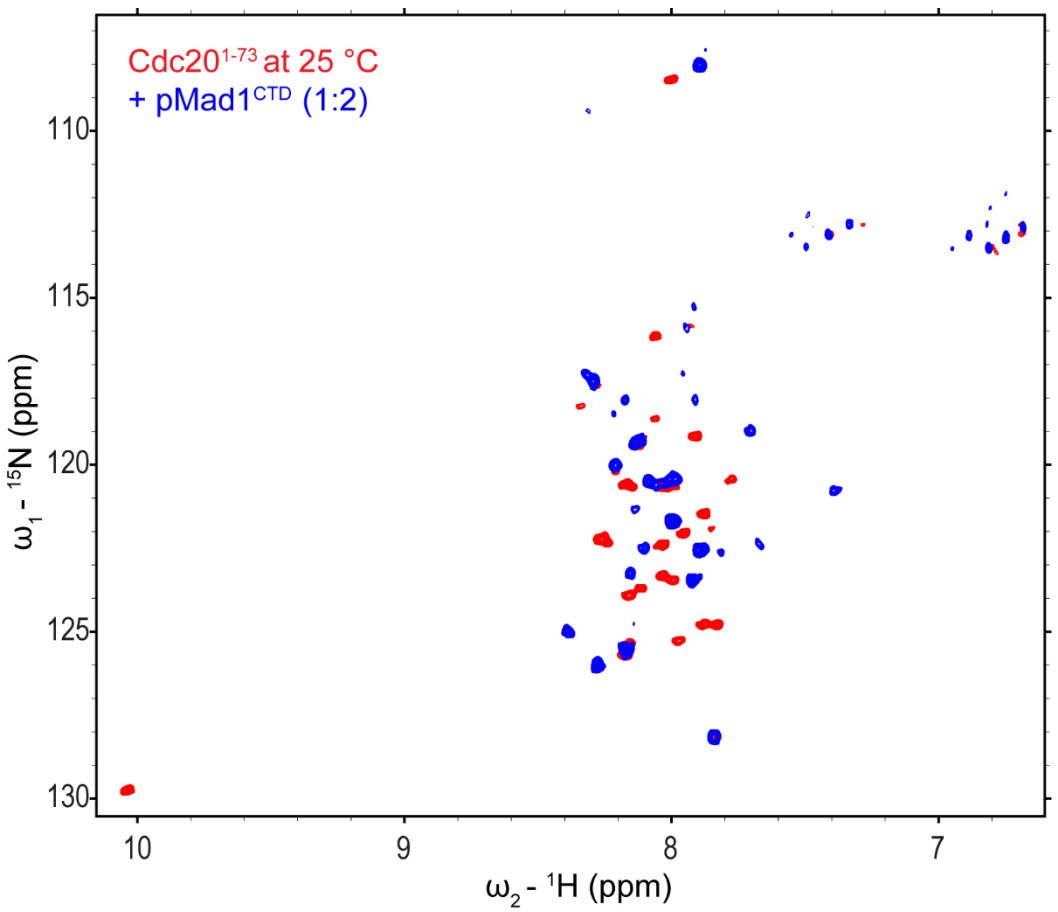

Figure 4.18: ***^{1}H, ^{15}N 2D HSQC of ^{15}N-labelled Cdc20$^{1-73}$ at 25 °C before and after pMad1^{CTD} addition.*** *Peaks in the region with helical propensity (7-8 ppm) are significantly line broadened. Additionally, at 25 °C as compared with 5 °C we can retrieve signals from folded regions, such that the peaks at 7.4 ppm likely comes from a folded α-helix.*

4.12 Mad1 phosphorylation also promotes Bub1 binding

In chapter 3, we presented the crystal structure of the Bub1^{CD1}-Mad1^{CTD} complex, which showed that the N-terminus of Bub1^{CD1}, which contains the pThr641 site, binds to the coiled-coil of Mad1^{CTD} at the conserved RLK motif, while the C-terminus of Bub1^{CD1} lies across the top of the Mad1^{CTD} coiled-coil and further contacts the head domain β-sheet. We additionally pointed out that the very C-terminus of Bub1^{CD1} seemed posed to extend across the top of the head domain of Mad1^{CTD}. We therefore speculated that further contacts with Mad1^{CTD} might exist C-terminal of Bub1^{CD1}, particularly as this region, which we have called Bub1$^{post-CD1}$, is predicted to be helical by PSIPRED and is directly followed by the ABBA and KEN1 motifs of Bub1 which bind Cdc20 (Fig 4.19A; Buchan and Jones, 2019). We therefore investigated whether any further contacts between Mad1^{CTD} and Bub1, C-terminal of the CD1 domain, might occur. Unfortunately, we were unable to purify a stable truncation of Bub1 which contains the CD1, post-CD1 and the ABBA and KEN1 motifs for analysis, due to problems

with the solubility of this truncation. This was despite trying several different lengths of truncations, as well as the addition of solubility tags to both termini. Therefore, we ordered a peptide which comprises the Bub1$^{post\text{-}CD1}$ domain (Fig 4.19A; the peptide sequence is shown in Table 2.9) and tested whether it bound to Mad1^{CTD} *in vitro.* We additionally used AlphaFold2, which was released just before submission of this thesis, to predict the structure of full-length Bub1, and the structure of residues 448-542 of this prediction is shown in Fig 4.19B (Jumper *et al*, 2021). The region comprising the post-CD1 peptide is coloured green while the ABBA/KEN1 motif is coloured cyan. AlphaFold2 predicts a much shorter α-helix than PSIPRED within post-CD1 (Fig 4.19A versus Fig 4.19B), as well as an additional α-helix between post-CD1 and the KEN motif (coloured grey, residues 517-523) which PSIPRED did not predict. Therefore, we ordered a peptide which additionally comprises this region to investigate if this α-helix also participates in Mad1^{CTD} binding (only to be investigated after this thesis has been submitted).

First we tested if Bub1$^{post\text{-}CD1}$ bound to Mad1^{CTD} using ITC (Fig 4.20). Bub1$^{post\text{-}CD1}$ titrated into buffer alone did not produce any significant heats (Fig 4.20A). Bub1$^{post\text{-}CD1}$ did not bind to non-phosphorylated Mad1^{CTD} (Fig 4.20B), but bound weakly to phosphorylated Mad1^{CTD} (Fig 4.20C). This suggests a novel interaction between Bub1 and Mad1 not previously identified and which is regulated by phosphorylation.

To investigate this further, we next analysed Bub1$^{post\text{-}CD1}$ interaction to ^{15}N-labelled Mad1^{CTD} and ^{15}N-labelled pMad1^{CTD} in a ^{1}H, ^{15}N 2D HSQC (Fig 4.21A-B). Very little, if any, changes occur in the non-phosphorylated Mad1^{CTD} sample, even when Bub1$^{post\text{-}CD1}$ was added at an 8-molar excess. However, a striking amount of CSPs were observed when Bub1$^{post\text{-}CD1}$ was titrated into phosphorylated ^{15}N-labelled Mad1^{CTD}, especially around pThr716. Therefore, our NMR data further confirms this novel interaction between Mad1^{CTD} and Bub1$^{post\text{-}CD1}$ and additionally highlights the role phosphorylation at pThr716 plays in promoting this interaction. We also plotted the CSPs which occur in non-phosphorylated and phosphorylated ^{15}N-labelled Mad1^{CTD} upon Bub1$^{post\text{-}CD1}$ titration (Fig 4.22A), and additionally mapped the CSPs which occur in phosphorylated Mad1^{CTD} onto the crystal structure (Fig 4.22B). This shows that Bub1$^{post\text{-}CD1}$ is likely binding to the two α-helices at the top of the Mad1^{CTD} head domain and fits nicely with our finding in the Bub1^{CD1}-Mad1^{CTD} crystal structure (Fig 3.8) that the C-terminus of Bub1^{CD1} was positioned to extend across the top of the head domain of Mad1^{CTD}.

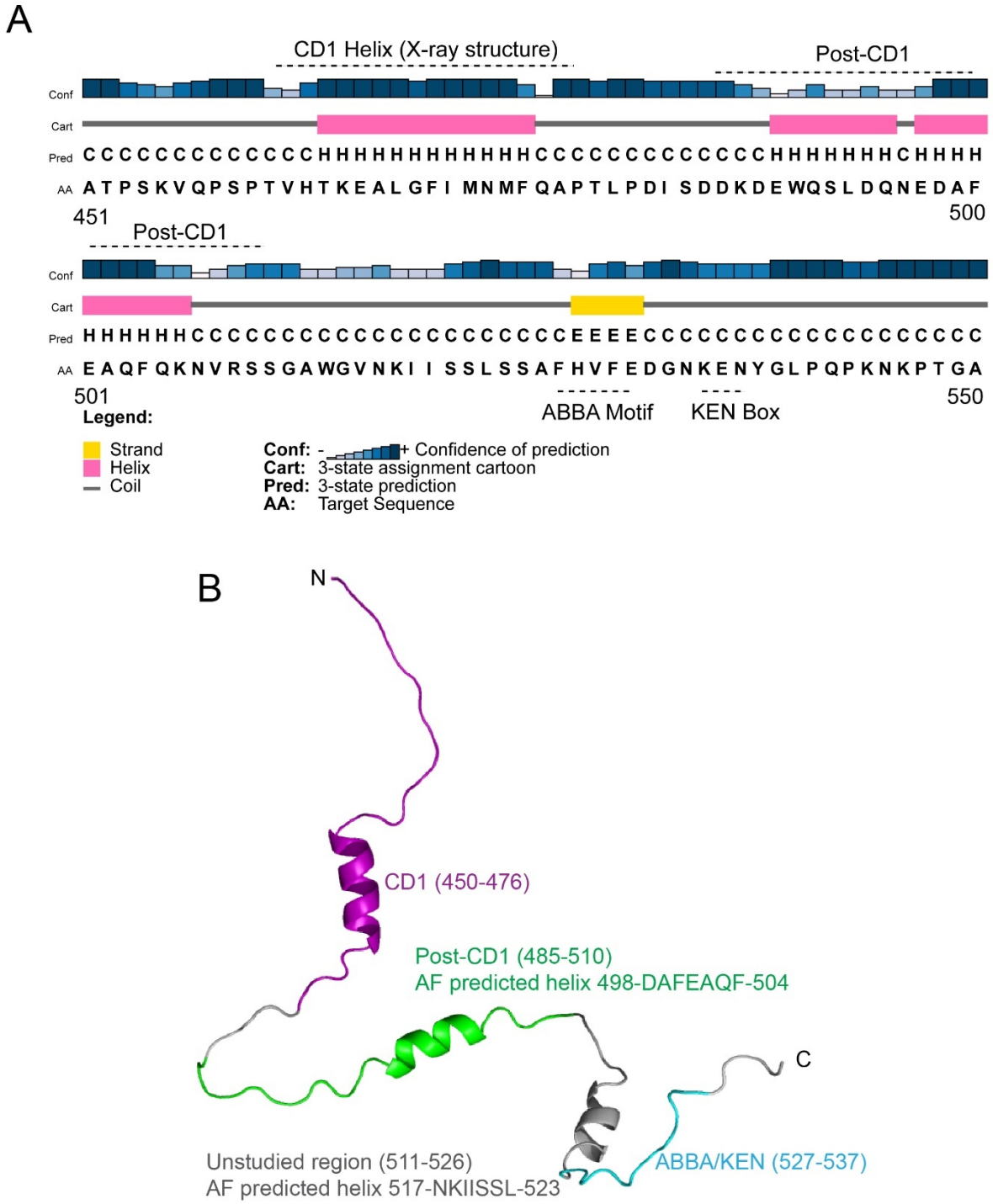

Figure 4.19: Secondary structure and structure prediction of Bub1. (A) *Secondary structure prediction of human Bub1 (residues 448-553) which includes the CD1, post-CD1, ABBA, and KEN1 domains of Bub1 (Buchan & Jones, 2019). The length of the CD1 α-helix seen in the X-ray structure as well as the post-CD1 peptide synthesized and used in this study is highlighted by the dashed lines as well as the location of the ABBA and KEN1 motifs.* ***(B)*** *Protein structure prediction of Bub1 (residues 448-542) using AlphaFold2 (Jumper et al, 2021). The region encompassing the post-CD1 peptide is shown in green, including a short α-helix predicted (residues 498-504). C-terminal to post-CD1 region another short α-helix (coloured grey, residues 517-523) is predicted just prior to the KEN1/ABBA motif.*

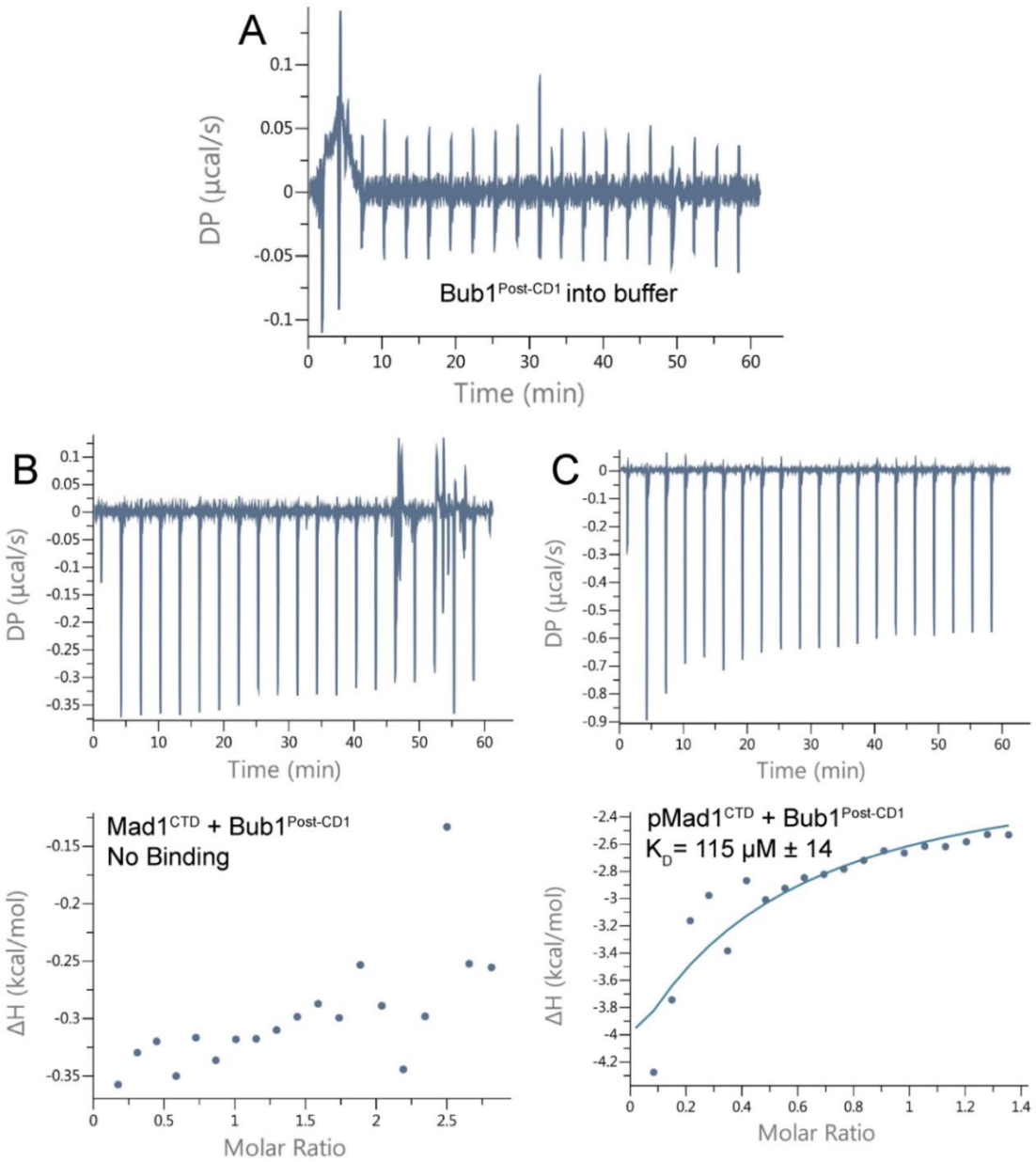

Figure 4.20: Isothermal calorimetry of Bub1$^{post\text{-}CD1}$ and Mad1^{CTD}. *The K_D and stoichiometry (n) values were obtained by averaging at least three experiments. The reported error values are calculated standard deviations.* ***(A)*** *Bub1$^{post\text{-}CD1}$ into buffer control.* ***(B)*** *Titration of Bub1$^{post\text{-}CD1}$ into non-phosphorylated Mad1^{CTD}.* ***(C)*** *Titration of Bub1$^{post\text{-}CD1}$ into phosphorylated Mad1^{CTD}.*

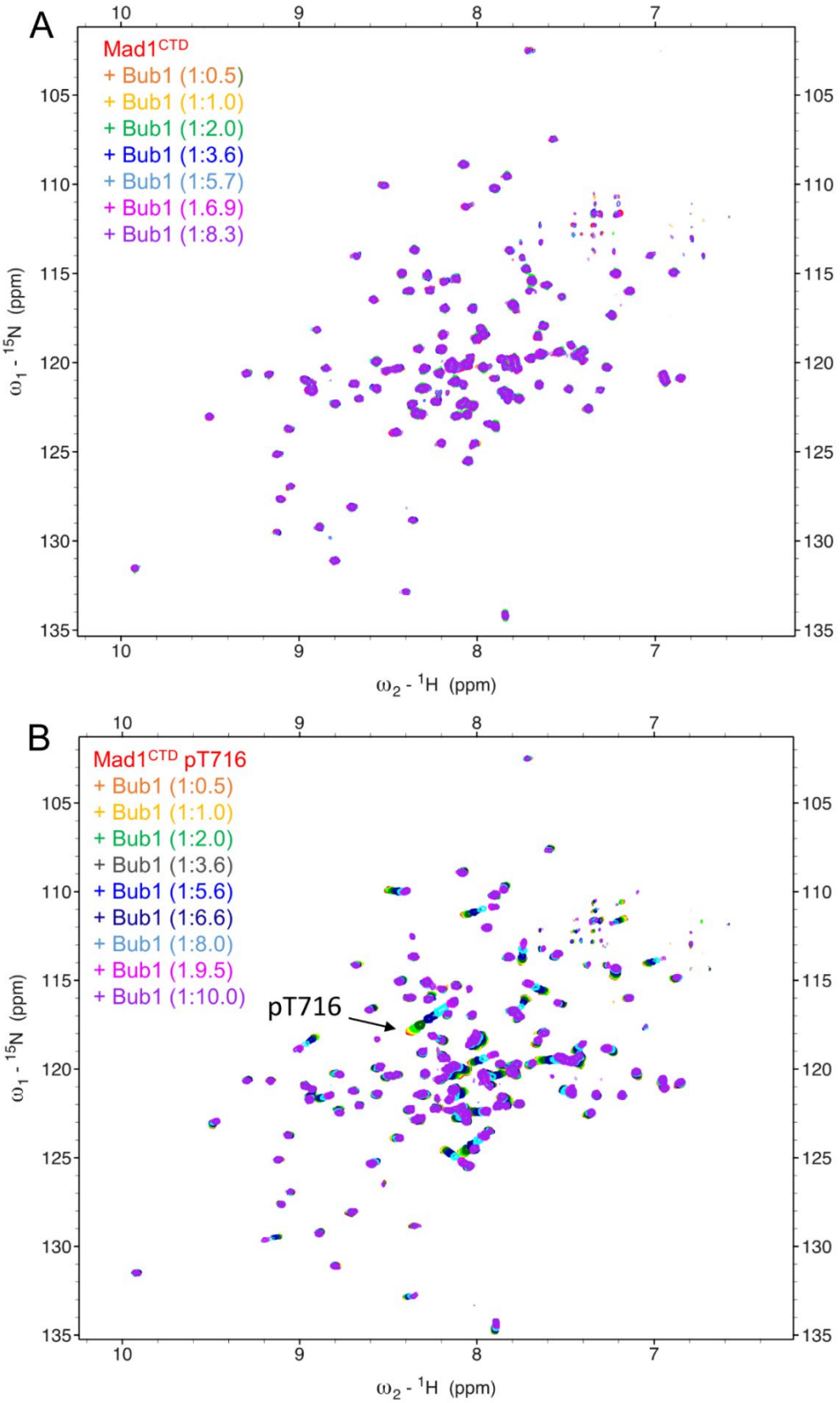

Figure 4.21: A $^{1}H,^{15}N$-^{2}D HSQC of Bub1$^{post\text{-}CD1}$ titrated into ^{15}N-labelled Mad1^{CTD}. (A) *Bub1$^{post\text{-}CD1}$ titrated into ^{15}N-labelled non-phosphorylated Mad1^{CTD}.* ***(B)*** *Bub1$^{post\text{-}CD1}$ titrated into ^{15}N-labelled phosphorylated Mad1^{CTD}.*

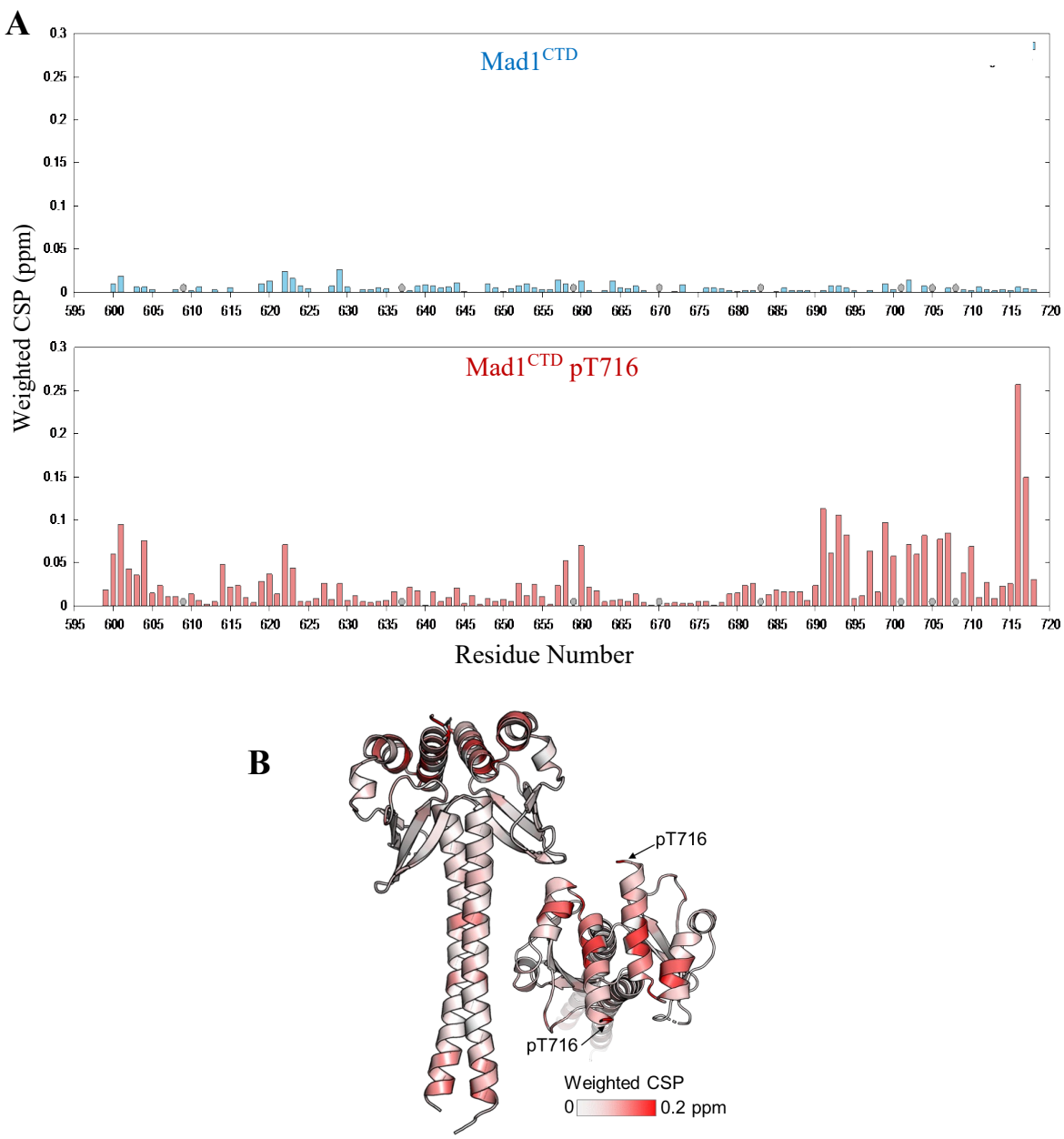

Figure 4.22: (A) *Weighted chemical shift perturbations of Bub1$^{post\text{-}CD1}$ peptide titrated into ^{15}N-labelled Mad1^{CTD} in the phosphorylated or unphosphorylated state. CSPs are calculated from the ^{1}H, ^{15}N 2D HSQC of Mad1^{CTD} at a 1:8 molar ratio of ^{15}N Mad1^{CTD} to Bub$^{post\text{-}CD1}$. Unassigned peaks are denoted as grey circles.* ***(B)*** *Bub1$^{post\text{-}CD1}$ binding to phosphorylated Mad1^{CTD} CSPs are mapped on to the crystal structure of phosphorylated Mad1^{CTD}.*

4.13 Summary and Future Directions

This work, along with two recently published papers (Piano *et al*, 2021; Lara-Gonzalez *et al*, 2021a), provides an updated view on how Mad1 phosphorylation by Mps1 promotes MCC assembly. Together Bub1 and Mad1 act as a scaffold which recruits and repositions Cdc20 and Mad2 in close proximity for MCC assembly (Fig 4.23). O-Mad2 docks onto the Mad1:C-Mad2 platform and as it undergoes conversion to C-Mad2, its safety-belt can entrap the MIM motif of Cdc20 which is made readily available by the pMad1^{CTD}:Cdc20 interaction. This

model fits well with the fact that the newly converted C-Mad2 cannot remain dimerized to C-Mad2 of the Mad1:C-Mad2 complex, and thus as it converts it is forcibly released onto Cdc20 which is positioned nearby (De Antoni *et al*, 2005).

We used a combination of mass spectrometry, crystallography, and NMR to confirm that the only predominant C-terminal Mad1 ($Mad1^{CTD}$) phosphorylation site *in vitro* by Mps1 is Thr716 and this site specifically regulates the $Mad1^{CTD}$:$Cdc20^{1-73}$ interaction. Binding of $Cdc20^{1-73}$ to $pMad1^{CTD}$ affects nearly every residue within the N-terminal half of $Cdc20^{1-73}$, with the conserved Box1 motif binding directly to Thr716 when phosphorylated. In contrast, the C-terminal half of $Cdc20^{1-73}$ including the Box2 motif contributes very little if at all to the interaction. Our work also suggests that although $Cdc20^{1-73}$ is almost entirely disordered in solution, that upon binding to $pMad1^{CTD}$ a folded α-helix likely forms which may provide further specificity to this interaction. Analysis of $Mad1^{CTD}$ residues involved in $Cdc20^{1-73}$ binding, suggests that nearly the entire top of the coiled-coil as well as the head domain β-sheet and last α-helix participate.

We and others have failed to capture a stable interaction of $Cdc20^{FL}$ and $pMad1^{CTD}$ despite this work showing that $pMad1^{CTD}$ and $Cdc20^{1-73}$ form a tight complex in SEC. Therefore, it is likely that the previously identified self-association of the N- and C-termini of Cdc20 is autoinhibiting this interaction and/or MIM accessibility. Future work will need to investigate specifically how this autoinhibition is relieved and whether the $pMad1^{CTD}$:Cdc20 interaction contributes to this and/or promotes MIM accessibility.

We additionally identified a novel interaction between $Mad1^{CTD}$ and a region just C-terminal to the $Bub1^{CD1}$ domain ($Bub1^{post\text{-}CD1}$), which also specifically binds to phosphorylated Thr716. It seems likely that this site is important for the juxtaposition of Bub1 and Cdc20 on phosphorylated $Mad1^{CTD}$. Additionally, we find it very intriguing that, like $Bub1^{CD1}$, only one $Cdc20^{1-73}$ can bind to the $Mad1^{CTD}$ homodimer. This might suggest that despite the binding sites of $Bub1^{post\text{-}CD1}$ and $Cdc20^{1-73}$ to the head domain of $Mad1^{CTD}$ and the pThr716 site overlapping, that a tripartite complex of Cdc20:Mad1:Bub1 could exist. Our studies also suggest the parallel binding of both Bub1 and Cdc20 to the head domain of $Mad1^{CTD}$ would place the KEN1 and ABBA motifs of Bub1 as well as the C-terminal β-propeller of Cdc20 in close proximity for their interaction which further suggests a tripartite complex might exist.

However, it is also possible that as only one copy of each can bind to the Mad1^{CTD} homodimer that their binding is competitive or regulated temporally. For example, it might be that a mechanism of transfer occurs whereby Bub1 targets both Mad1 and Cdc20 to kinetochores after which it then transfers Cdc20 to Mad1 during Mad2 conversion to form the C-Mad2:Cdc20 complex. It is also possible since the binding of Bub1^{CD1} promotes a global conformational change within Mad1^{CTD} that the binding of Bub1^{CD1} could alter Mad1^{CTD} such that Cdc20 can then bind at the same time to the opposite face of Mad1.

Ultimately, further biochemical, biophysical, and structural studies need to be completed to answer these questions and gain further insights into how the pMad1^{CTD}:Cdc20^{NTD} complex catalyses MCC assembly. For example, it would be interesting to test whether both Bub1^{CD1} and Cdc20$^{1-73}$ can bind to Mad1^{CTD} at the same time, or if their binding is competitive. Additionally, we wonder whether both pThr716 are being utilised in the 1:1 Bub1$^{post-CD1}$ or Cdc20$^{1-73}$ interaction with pMad1^{CTD}. We made several attempts to crystallise the Bub1$^{post-CD1}$ and Box1 peptides as well as the Cdc20$^{1-73}$ truncation to phosphorylated Mad1^{CTD}, but we were not yet successful. However, now that we have detailed structural insights into the Bub1^{CD1}:Mad1^{CTD} and Cdc20$^{1-73}$:Mad1^{CTD} interactions it may be possible to design constructs, such as cysteine-cysteine crosslinks, to capture the tripartite complex of pBub1^{CD1}:pMad1^{CTD}:Cdc20 for investigation by cryo-EM or X-ray crystallography.

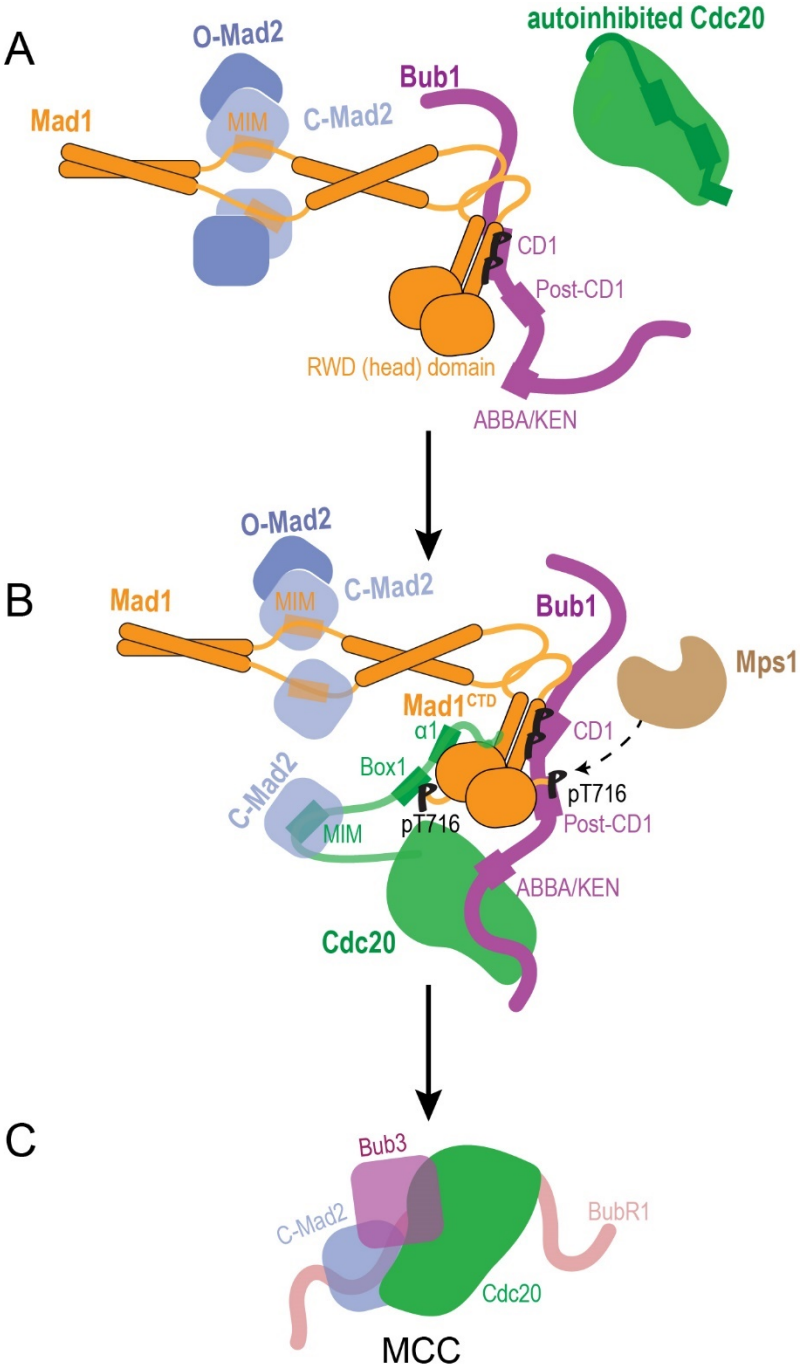

Figure 4.23: Updated model of assembly of the MCC onto phosphorylated Bub1:Mad1. (A) *The doubly phosphorylated Bub1 CD1 domain targets the Mad1:C-Mad2 complex to kinetochores which then acts as a platform for O-Mad2 binding and O-to-C conversion. Cdc20, on its own, exists in an autoinhibited state which likely impairs the Cdc20:C-Mad2 interaction and MCC formation.* ***(B)*** *Phosphorylation of the C-terminus of Mad1 at Thr716 promotes its interaction with both the N-terminus of Cdc20 and the post-CD1 domain of Bub1. Interaction between the WD40 domain of Cdc20 and the ABBA/KEN1 motif of Bub1 also occurs which likely promotes Cdc20 kinetochore targeting and positions Cdc20 close to Mad1:C-Mad2. Cdc20 autoinhibition is relieved either through its interaction with pMad1^{CTD} or by other unknown means, and this Cdc20:pMad1^{CTD} interaction then promotes Cdc20 MIM accessibility and Cdc20:C-Mad2 formation.* ***C)*** *The Cdc20:C-Mad2 complex then rapidly binds BubR1:Bub3 to form the MCC.*

Chapter 5

A mechanism of Mad1^{CTD} fold-over within the Mad1-2 complex

5.1 Chapter Abstract

The Mad1:C-Mad2 complex is the catalytic platform for MCC assembly. Mad1:C-Mad2 recruits O-Mad2, through asymmetric dimerization and Mad1 phosphorylation by Mps1 helps Mad1:C-Mad2:O-Mad2 to activate conversion of the docked O-Mad2 into C-Mad2 which then rapidly binds to Cdc20 to form the MCC. The molecular mechanisms of how Mad1 phosphorylation and the Mad1:C-Mad2 platform promotes MCC formation is not yet fully understood. Recently, it has been identified that phosphorylation of Thr716 at the very C-terminus of Mad1 promotes an interaction with the N-terminus of Cdc20 as well as the post-CD1 domain of Bub1. Here we use cryo-EM and cross-linking mass spectrometry to show that phosphorylation of Mad1 also seems to promote remodelling of the Mad1:C-Mad2 complex such that the Mad1^{CTD} head domain folds back onto the Mad1:C-Mad2 core and likely makes direct contact with Mad2. We suggest that this fold-over mechanism could directly catalyse MCC assembly by bringing the MIM motif of Cdc20, by virtue of the Cdc20^{NTD}:pMad1^{CTD} interaction, in close proximity and optimal orientation to Mad2 for entrapment by the Mad2 safety-belt.

5.2 Chapter Background & Aims

The Mad1:C-Mad2 complex is the catalytic platform for MCC assembly (overviewed in sections 1.14-1.18). Mad1:C-Mad2 recruits O-Mad2 through asymmetric dimerization, and Mad1 phosphorylation by Mps1 helps pMad1:C-Mad2:O-Mad2 to catalytically activate conversion of the docked O-Mad2 into C-Mad2, which then rapidly binds to Cdc20 to form the MCC. The structure and function of the C-terminus of Mad1 (residues 485-718) has been well studied (Fig 5.1). Residues 485-584 of Mad1 form a tight dimer through coiled-coil α-helices (Fig 5.1B, α1-2), which is disrupted by a short-disordered loop called the 'Mad2 interacting motif' (MIM), spanning residues 430-550. The MIM motif of Mad1 entraps one molecule of C-Mad2 per chain to make the Mad1:C-Mad2 tetramer (Fig 5.1B; PDB: 1GO4). This segment is then followed by another disordered loop (Fig 5.1A; residues 584-597) as predicted by PSIPRED secondary structure prediction. Interestingly, AlphaFold2 predicts that this region might actually contain a short α-helix (Fig 5.1 α3, 586-ADLEAAA-592) which

has not yet been investigated in any published study (Jumper *et al,* 2021). After this flexible loop, the coiled-coil resumes (residues 597-638; Fig 5.1B, α4) and ends in a globular head domain presenting an RWD-fold (residues 638-718; Fig 5.1B, α5-7, and β1-4) (PDB: 4DZO; Kim et al., 2012). The asymmetric C-Mad2:O-Mad2 dimer has also been crystallised (PDB: 2V64), using Mad2ΔLL which is a kinetically stabilised O-Mad2 mutant (description of Mad2ΔLL in Table 2.8; Mapelli *et al*, 2007). The expected Mad1:C-Mad2:O-Mad2 hexamer can then be visualised by docking this asymmetric dimer onto the C-Mad2 of the tetrameric Mad1:C-Mad2 (Fig 5.1B-C).

Despite all these structures, further work is still needed to gain a complete understanding of how Mad1:C-Mad2 catalyses Mad2 conversion and how Mad1 phosphorylation promotes this process. For example, several studies have hypothesized that the C-terminus of Mad1 may exist in a folded conformation where the head domain of Mad1 and the Mad1:C-Mad2 core fold onto each other (Sironi *et al*, 2002; De Antoni *et al*, 2005; Ji *et al*, 2018; Amin, 2019). Additionally, as of yet, there is no structure of full-length Mad1 (residues 1-718) or any part of the Mad1 N-terminus (residues 1-485). The Mad1 N-terminus is composed of elongated coiled-coils separated by several flexible loops which makes structure determination difficult. Several groups have reported difficulties in expressing and purifying full-length Mad1 or N-terminal truncations of Mad1 (Ji *et al*, 2017, 2018; Piano *et al*, 2021; Kim *et al*, 2012). Self-interaction of the N- and C-termini of Mad1 has also been reported (Ji *et al*, 2018). Interestingly in this study it was found that Mps1 phosphorylation of Mad1^{CTD} significantly impaired this interaction and so it was suggested that Mps1 phosphorylation of Mad1 might inhibit Mad1 self-association and open up the C-terminus of Mad1 for MCC assembly (Ji *et al*, 2018).

However, all these hypotheses are tentative suggestions and further structural work is needed to confirm if Mad1 fold-over and self-association is occurring and if it has any functional significance. The recent cryo-EM 'resolution revolution' makes it now possible to investigate the structure of small conformationally heterogenous complexes, like the Mad1:C-Mad2 complex (cryo-EM is discussed in section 2.26). Therefore, this chapter aims to investigate the structure of the non-phosphorylated and phosphorylated Mad1:C-Mad2:O-Mad2 complexes by cryo-EM, with the hopes that these studies can provide insights into how Mad1:C-Mad2 acts as a catalytic platform for Mad2 conversion and MCC formation.

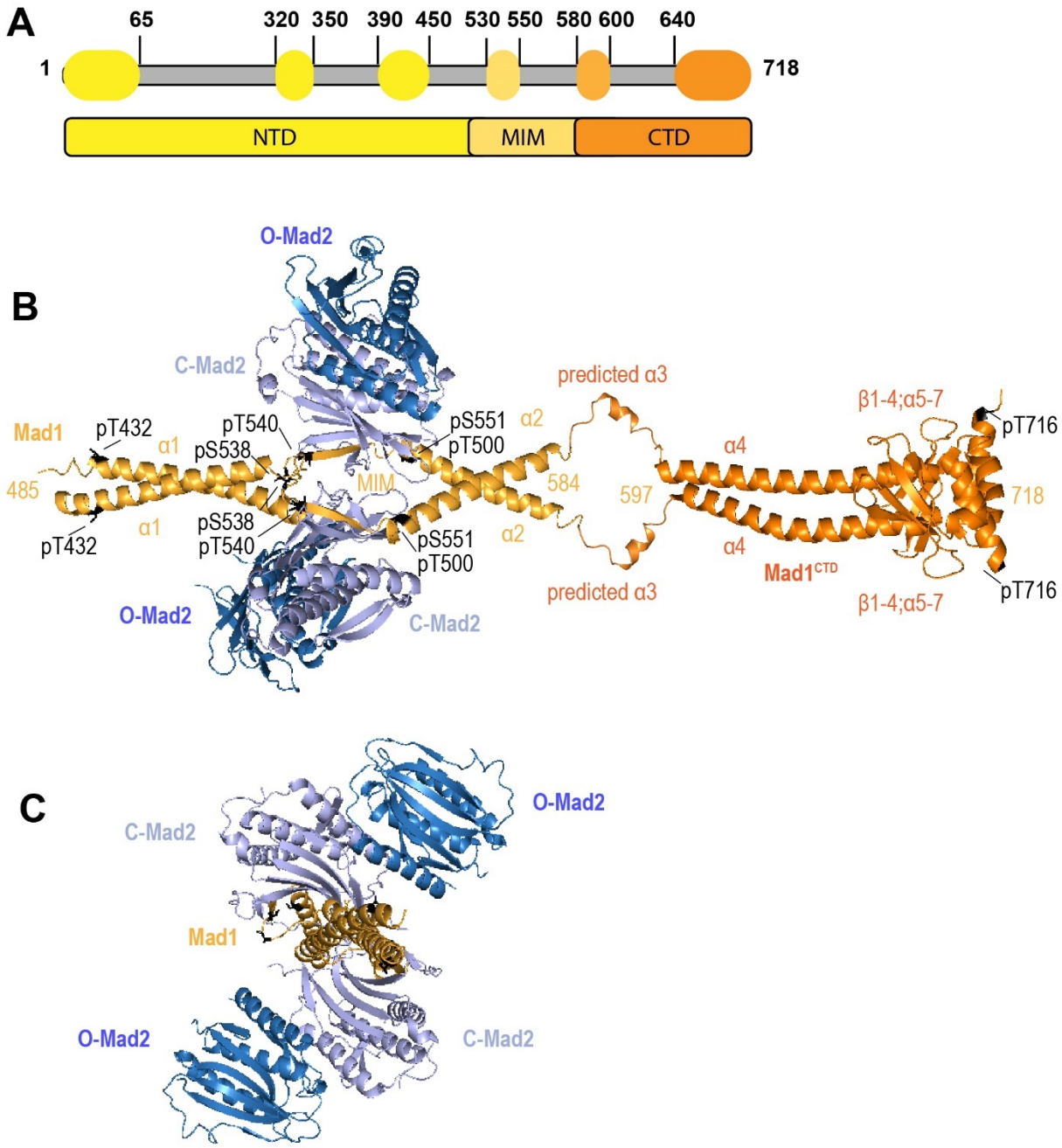

Figure 5.1: Overview of the Mad1:C-Mad2 complex structure. (A) *Schematic diagram of Mad1. Non-coiled-coil segments are depicted as ovals as predicted by the COIS program and PSIPRED (Lupas et al, 1991; Buchan & Jones, 2019). Mad1 contains three distinct regions. The NTD (yellow) of which there is no structure, composed of a long coiled-coil interrupted by several loops. The MIM (light orange) which dimerises and binds two C-Mad2 molecules, and the CTD (dark orange).* ***(B)*** *A side view of the Mad1Δ485-718:C-Mad2:O-Mad2 complex. The Mad1 dimer encompassing residues 485-584 is depicted in light orange (PDB 1GO4; Sironi et al, 2002), bound to two C-Mad2 molecules in light blue. Two O-Mad2 molecules (dark blue) dimerised to C-Mad2 are fitted using the structure of the O-C Mad2 dimer (PDB 2V64; Mapelli et al, 2007). The coiled-coil is then interrupted by a 16 amino acid segment, which is predicted by AlphaFold2 to have a short α-helix (residues 586-592). The coiled-coil then resumes and the structure of the C-terminal head domain of Mad1, residues 597-718, is depicted in dark orange (PDB 4DZO). Residues which were identified by mass spectrometry as prevalent in vitro Mps1-dependent Mad1 phosphorylation sites are coloured black within the ribbon and identified in black text.* ***(C)*** *Top view of the Mad1:C-Mad2:O-Mad2 complex, not including the flexible head domain.*

5.3 Purification of Mad1:Mad2 complexes

Our initial aim was to investigate the structure of full-length Mad1:Mad2. However, purification of full-length Mad1 failed, mostly due to poor solubility and expression levels, a phenomenon reported by several other labs (De Antoni *et al*, 2005; Ji *et al*, 2017, 2018). Successful purification of full-length His-tagged Mad1 in complex with Mad2 for use in FRET assays had recently been reported (Faesen *et al*, 2017). Despite using the same construct, expression system (baculovirus), cell line (Tna038), and buffer conditions (1000 mM NaCl), usable amounts of full-length Mad1:C-Mad2 were not obtained. As Mad1 has a high percentage of rare codons, an optimised gene for insect cell expression of full-length Mad1 from GeneArt (ThermoFisher) was also tested. However, this approach did not noticeably improve expression levels. Very recently another paper has been published which showed good expression levels of full-length Mad1 using Mad1 tagged with MBP at its N-terminus (Piano *et al*, 2021). We have not had time to test this yet. One hypothesis for why full-length Mad1 is so difficult to purify, is if indeed the N- and C-termini of Mad1 do interact with each other, it may be that a His-tag gets occluded, preventing purification, whereas an MBP-tag interferes with Mad1 self-interaction and improves stability of the complex.

Consequently, as a starting point, the previously studied Mad1 485-718 (Mad1Δ485) C-terminal truncation in complex with Mad2 was purified (Fig 2.1; schematic in Fig 5.1). Using baculovirus for expression, strep-tagged Mad1 co-expressed with Mad2 does not purify as a stoichiometric tetrameric Mad1:C-Mad2 complex due to limiting levels of Mad2 (Fig 5.2, blue). Therefore, excess Mad2 L13A (stabilised C-Mad2) was added to the complex and re-purified to form a stoichiometric tetramer, after which Mad2ΔLL (stabilised O-Mad2; Table 2.8) was added in excess to form the Mad1:C-Mad2:O-Mad2 hexamer as confirmed by SEC-MALS (Fig 5.2, red and black).

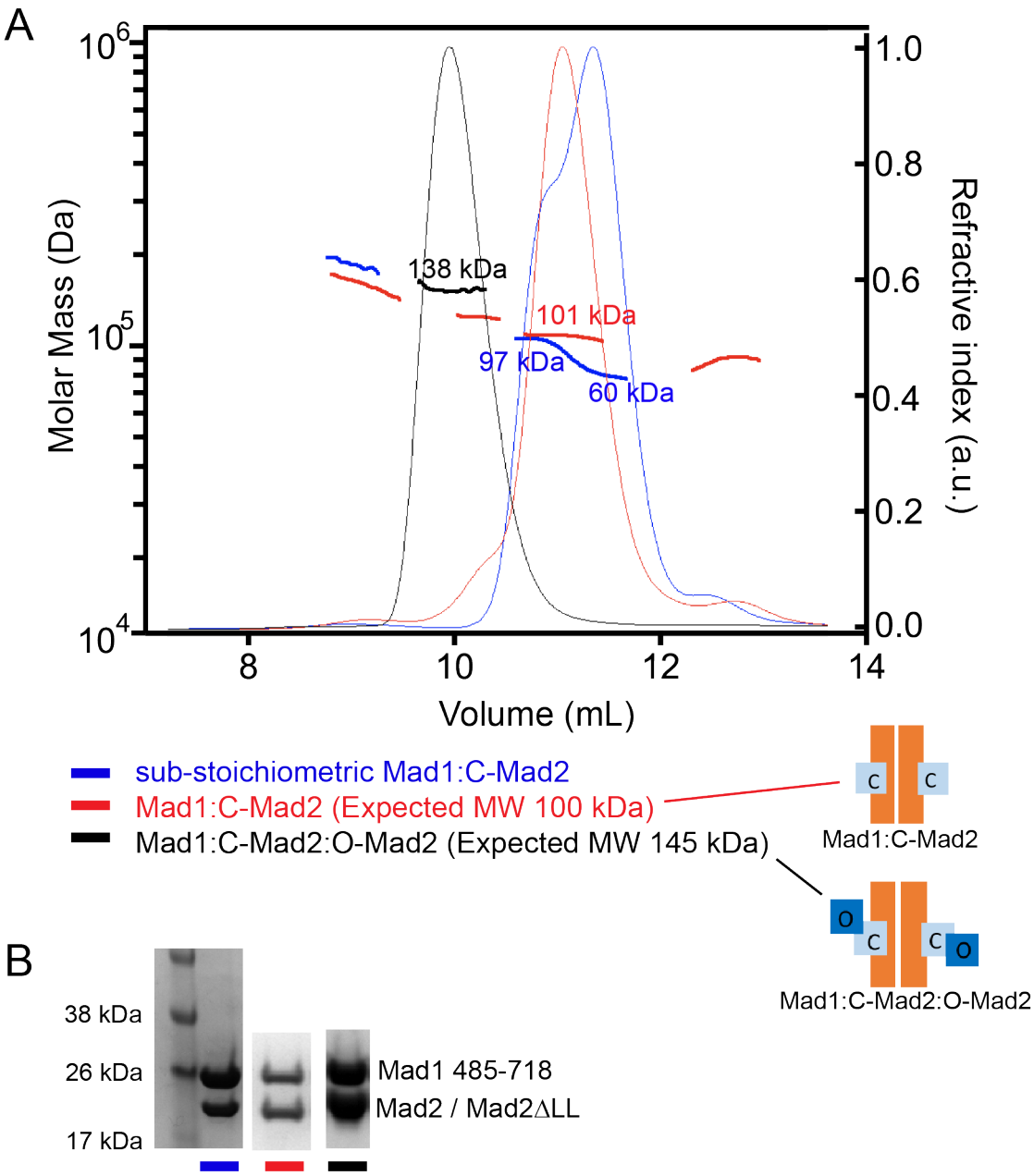

Figure 5.2: SEC-MALS of purified Mad1:Mad2 complexes. (A) *SEC-MALS of purified Mad1:Mad2 complexes. In blue: Mad1Δ485:C-Mad2 complex purified from insect cells which is a sub-stoichiometric mixture of Mad1 dimer (53 kDa), Mad1 dimer with one Mad2 molecule (77 kDa), and Mad1:C-Mad2 tetramer (100 kDa). In red: homogenous Mad1Δ485:C-Mad2 tetramer after incubating the complex with excess Mad2 L13A and then re-performing SEC. In black: homogenous Mad1Δ485:C-Mad2:O-Mad2 hexamer after incubating homogenous tetramer with excess Mad2ΔLL and re-performing SEC.* ***(B)*** *The complexes outlined in (A) analysed by SDS-PAGE using the same colour scheme.*

5.4 Cryo-EM of non-phosphorylated Mad1Δ485:C-Mad2:O-Mad2

We first investigated the structure of the unphosphorylated Mad1Δ485:C-Mad2:O-Mad2 hexamer by cryo-EM (Fig 5.3). A total of 972 movies were collected on the Titan Krios 300 kV (ThermoFisher), using a K2 detector (Gatan) in counting mode (Fig 5.3A). Despite the small size of this complex, and only 3,543 particles being used, well-resolved 2D averages

with several different orientations can be obtained for the central Mad2 core, including the N-terminal coiled-coil and C-terminal α-helices of Mad1 (Fig 5.3B). Even in pure ice (no carbon layer), this complex shows preferred orientation as no top or bottom views are seen. Several classes for the head domain alone can also be seen (Fig 5.3C). By expanding the particle box size from 150 Å to 260 Å, alignments on the core become poor, but the flexible head domain attached to the core can be captured (Fig 5.3D). Overall, these 2D classes match closely with the expected architecture of the Mad1Δ485:C-Mad2:O-Mad2 (Fig 5.3E) and indicates that the head domain is only flexibly tethered to the Mad1:C-Mad2:O-Mad2 core.

We obtained a reconstruction of the non-phosphorylated Mad1Δ485:C-Mad2:O-Mad2 complex at a resolution of 9.1 Å, according to the gold standard FSC at 0.5 (5.9 Å at 0.143 FSC) (Fig 5.4A) using only 2,714 total particles. Our reconstruction closely resembles the core of the expected hexameric complex assembled from the previously determined crystal structures which we have placed into the EM density (Fig 5.4B-C). It is likely that collecting more data and using detergent to combat preferential orientation of the complex would significantly increase the resolution of this complex, however as there are already high-resolution structures of individual components of the core, we did not prioritize this.

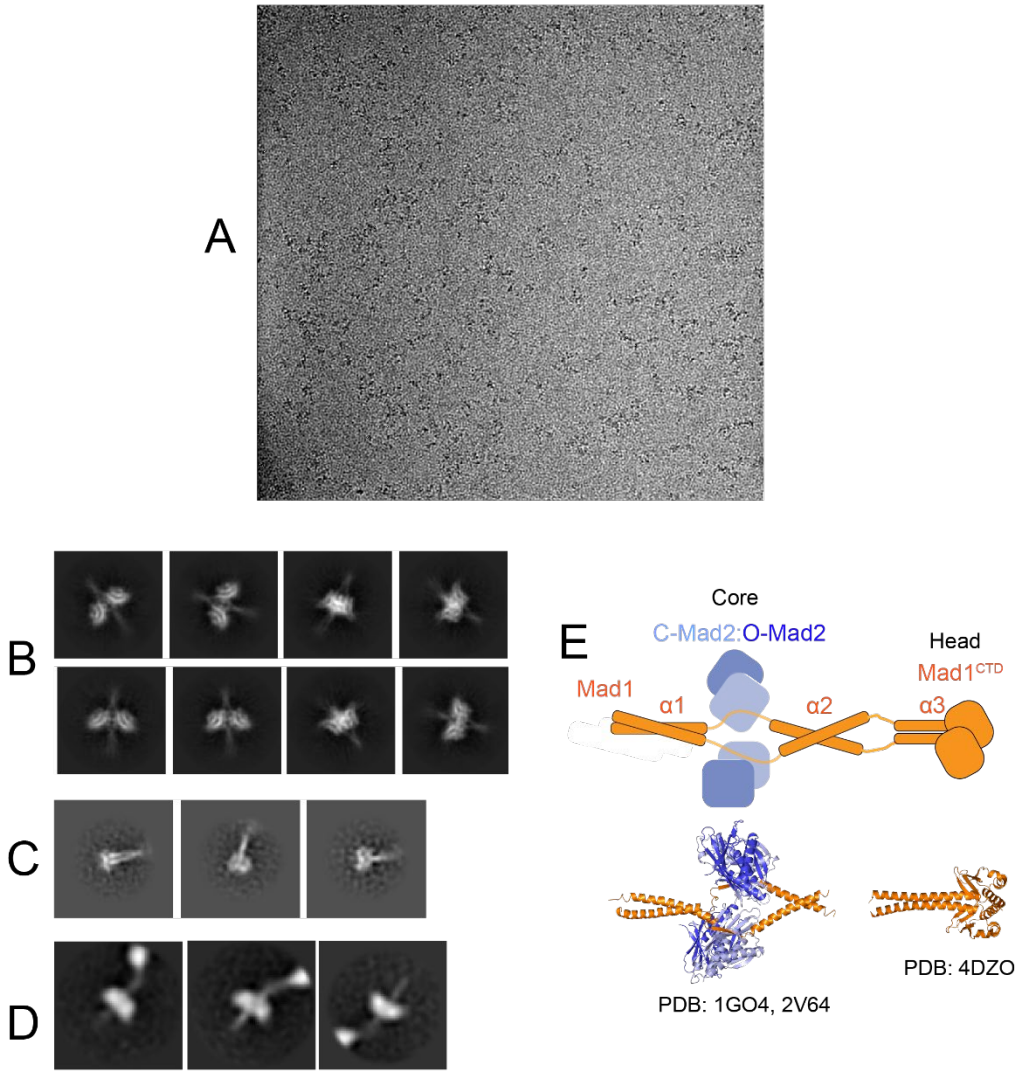

Figure 5.3: Cryo-EM of non-phosphorylated Mad1Δ485:C-Mad2:O-Mad2. (A) *A typical cryo-EM micrograph of this complex collected on a Titan Krios (ThermoFisher) 300 kV microscope equipped with a K2 detector (Gatan) in counting mode.* ***(B)*** *A sample of 2D averages of Mad1Δ485:C-Mad2:O-Mad2 which captures the rigid Mad2 core and the N-terminal coiled-coil and C-terminal α-helices.* ***(C)*** *2D averages which capture the head domain of Mad1 (Mad1^{CTD}).* ***(D)*** *Increasing the box size from 150 Å to 260 Å produces 2D averages which show Mad1^{CTD} flexibility tethered to the Mad1:C-Mad2Δ485:O-Mad2 core. E) Model diagram of Mad1Δ485:C-Mad2:O-Mad2 and the equivalent crystal structures.*

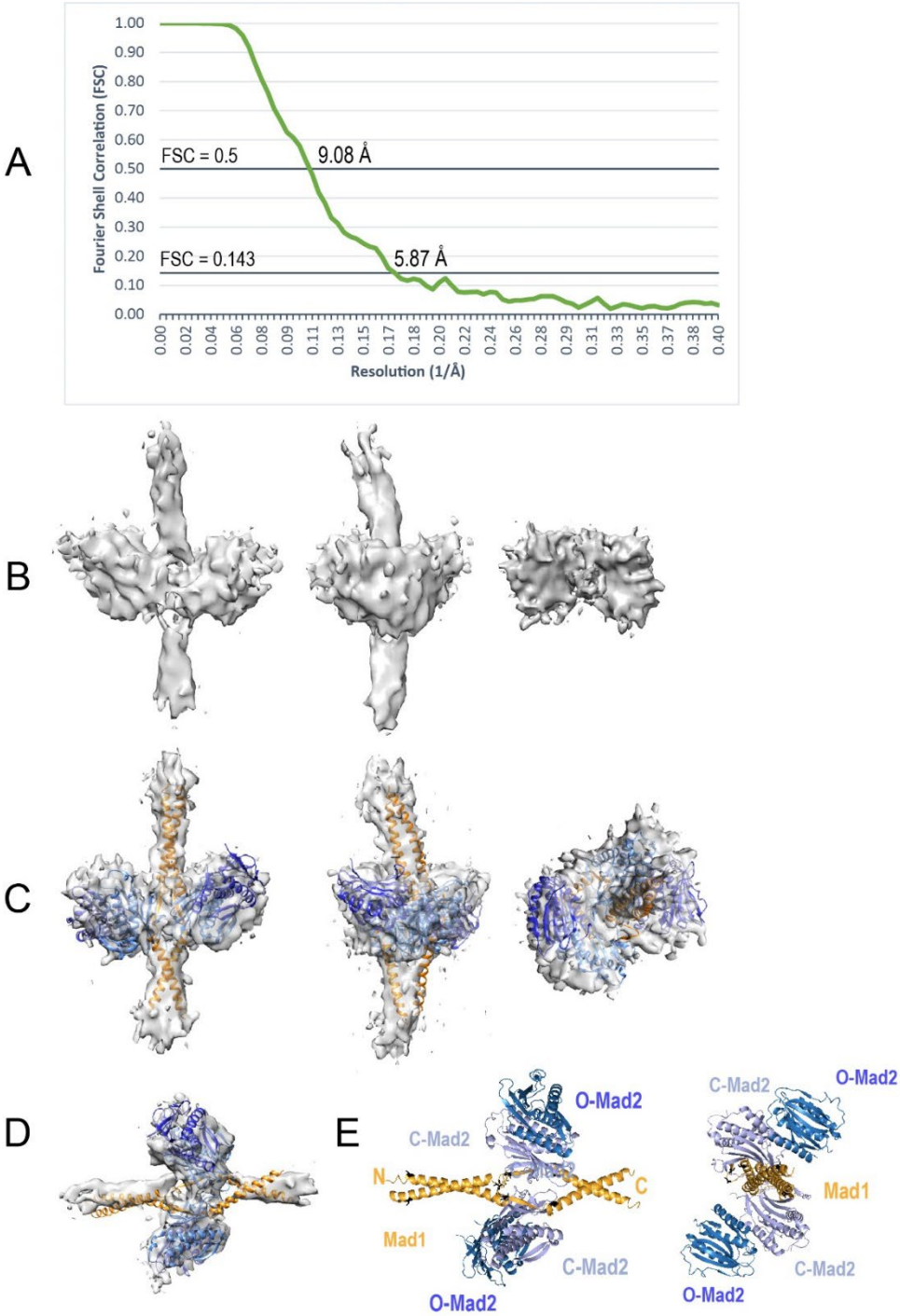

Figure 5.4: Three-dimensional reconstruction of Mad1Δ485:C-Mad2:O-Mad2. ***(A)*** *Gold-standard Fourier Shell Correlation (FSC) of the Mad1Δ485:C-Mad2:O-Mad2 reconstruction.* ***(B)*** *Several views of the 3D cryo-EM reconstruction of Mad1Δ485:C-Mad2:O-Mad2.* ***(C)*** *Comparison of our 3D reconstruction and the crystal structures by placing the crystal structures (PDB ID: 1GO4 and 2V64) into the cryo-EM reconstruction.* ***(D)*** *Placing the crystal structures into 3D reconstruction such that they are fitted best to the Mad2 core rather than the entire complex shows how the coiled-coil of the crystal structure is significantly more asymmetric that the cryo-EM reconstruction.* ***(E)*** *Side and bottom view of the Mad1Δ485:C-Mad2:O-Mad2 hexamer assembled from the crystal structures PDB 1GO4 and 2V64 for reference.*

The only clear difference in our reconstruction as compared to the previously determined crystal structure of the tetrameric Mad1Δ485-584:C-Mad2ΔR133A (PDB ID: 1GO4; Sironi *et al*, 2002), is the relative straightening of the α-helices extending from the MIM motif with respect to each other (Fig 5.4D). This is likely because, the crystal structure contained an anti-parallel dimer of tetramers with the N-terminal coiled-coil of each tetramer contacting each other and the C-terminal α-helices packing in an anti-parallel orientation with equivalent segments in an adjacent tetramer (Fig 5.5). This causes the extending α-helices to be bent with respect to the Mad2 core. Our reconstruction therefore suggests that the Mad1Δ485:C-Mad2:O-Mad2 complex is less asymmetric than the tetrameric crystal structure suggests. However, similar to the crystal structure our reconstruction indicates that as the C-terminal α-helices emerge from their cognate Mad2 ligands, they do not form a parallel coiled-coil but rather extend at an angle and cross each other.

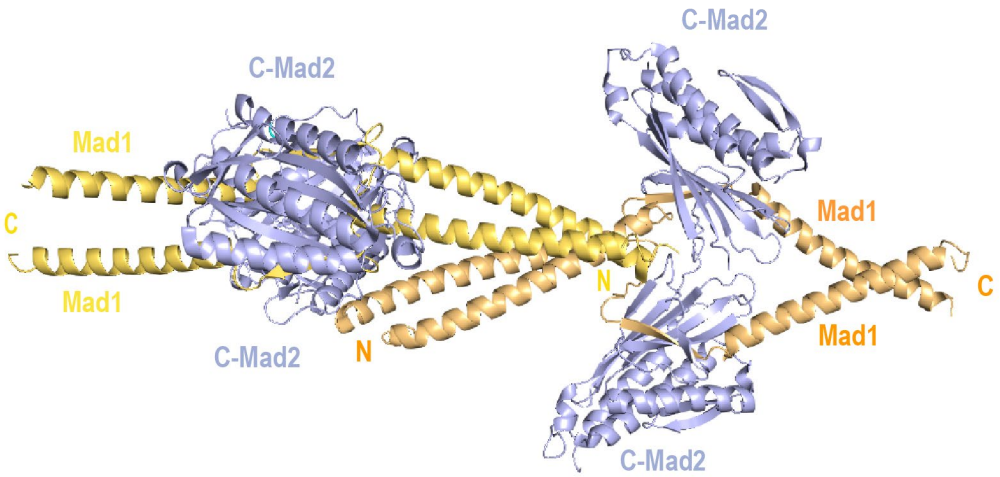

Figure 5.5: Crystal structure of the asymmetric Mad1Δ485-584:C-Mad2 tetramer crystallised as an anti-parallel dimer of tetramers *(PDB: 1GO4; Sironi et al., 2002). One Mad1 dimer is coloured in yellow (left) and the other is coloured in light orange (right).*

5.5 Cryo-EM of Phosphorylated Mad1Δ485:C-Mad2:O-Mad2

We next collected data on the Mad1Δ485:C-Mad2:O-Mad2 complex after *in vitro* Mad1 phosphorylation by Mps1. A total of 6896 movies were collected using a 300 kV FEI Titan Krios (ThermoFisher) equipped with a K2 detector (Gatan), in counting mode, and a total of 777,723 particles were picked using referenced based picking in Gautomatch v0.56 (Kai Zhang, http://www.mrc-lmb.cam.ac.uk/kzhang/Gautomatch) (Fig 5.6A). The phosphorylated complex presents strikingly different 2D classes, with only 9.2 % of particles resembling the 'open-state' non-phosphorylated complex (Fig 5.6B, boxed in blue). Instead, many different classes, generally containing three-distinct bodies, in various different orientations are seen (Fig 5.6B). Several classes display a body which resembles the Mad1:C-Mad2 core and

another body which strongly resembles the Mad1 head domain positioned close to the core and possibly contacting the core (Fig 5.6B, boxed in orange). We will refer to these classes as the 'folded-state'.

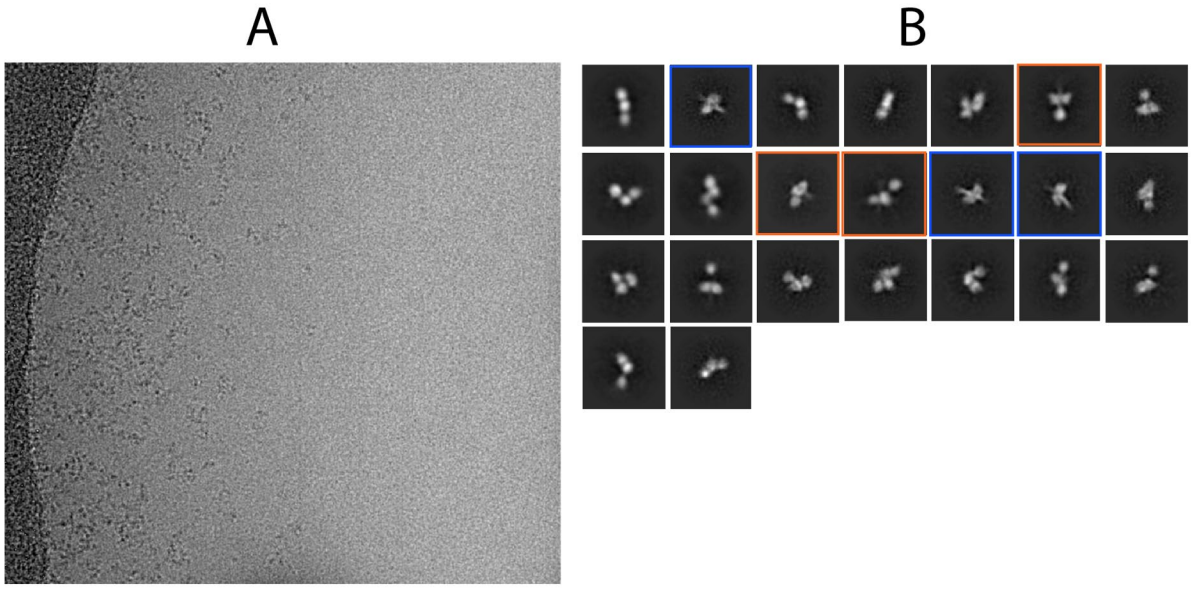

Figure 5.6: Cryo-EM of pMad1Δ485:C-Mad2:O-Mad2. (A) *A typical micrograph of the complex taken on a FEI Titan Krios (ThermoFisher) 300 kV microscope equipped with a K2 detector (Gatan).* ***(B)*** *2D averages of pMad1Δ485:C-Mad2:O-Mad2 showing different views; representative of 100 2D averages. The particles boxed in blue resemble the non-phosphorylated complex while the particles boxed in orange highlight classes which strongly resemble the Mad1Δ485:C-Mad2:O-Mad2 core with the head domain of Mad1 folded-over.*

As compared to the non-phosphorylated complex, the amount of detail present in the 2D classes of the phosphorylated complex is poor, despite averaging particles from 8-times as many micrographs. Several strategies were used to try to improve the quality of the data. Despite using similar conditions for grid preparation, the distribution of the phosphorylated particles within the ice and holes was worse than the non-phosphorylated particles, leading to particle aggregation and fewer particle numbers. We trialled various detergents and found that the addition of 0.05 % NP-40 provided the best ice quality and particle distribution (Fig 5.6A vs Fig 5.7A). We also performed cross-linking of the complex with BS3 which helped to increase the percentage of particles captured in the folded-state (Fig 5.7B). Additionally, we used a volta phase plate (VPP) during data collection to improve particle contrast, which we found increased the percentage of classes in which the coiled-coil could be seen connecting the folded head domain to the core. Lastly, we obtained significantly improved particle picking using Warp with a model specifically trained for the pMad1Δ485:C-Mad2:O-Mad2 complex (Fig 5.7C-D; Tegunov and Cramer, 2019).

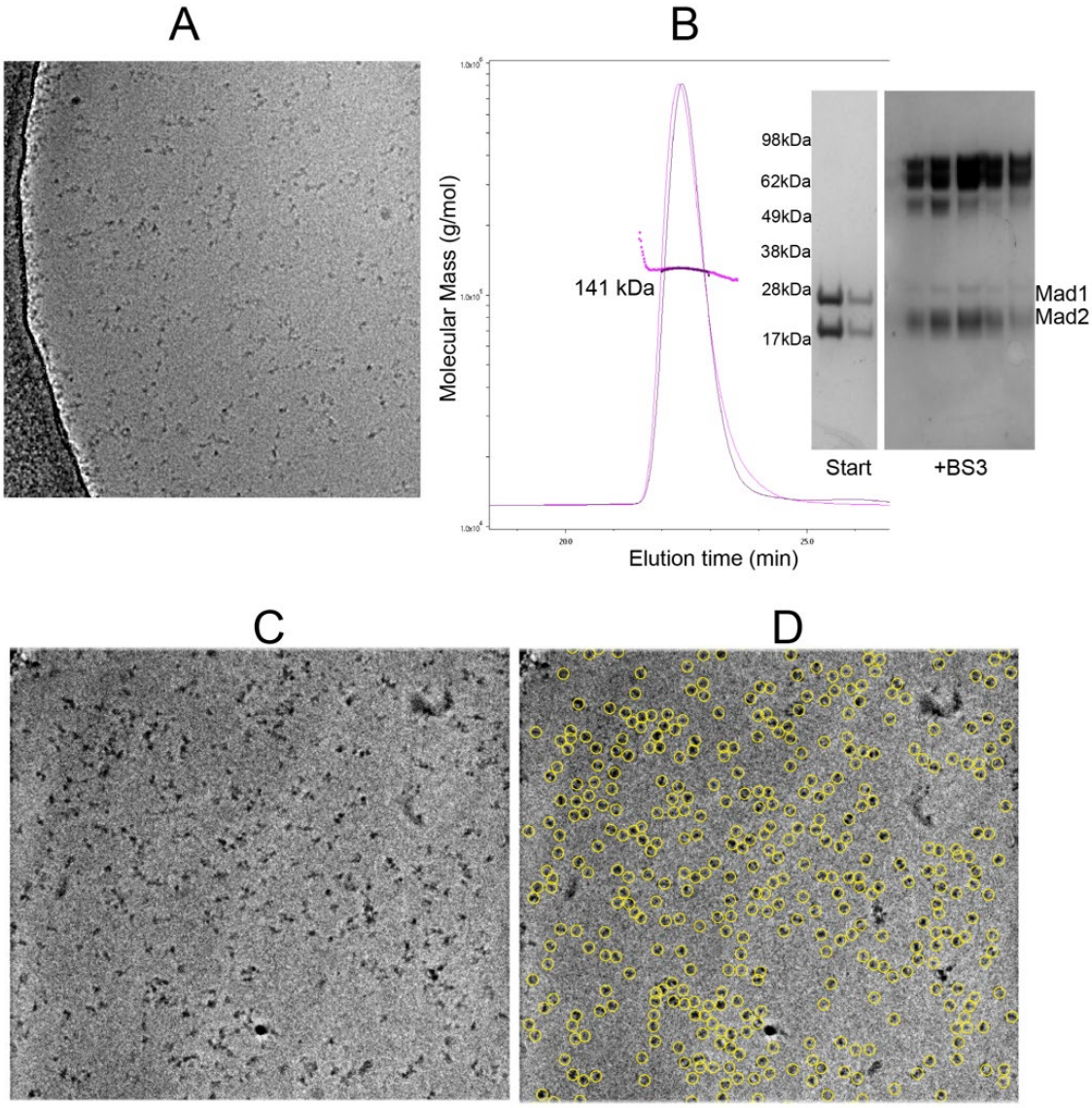

Figure 5.7: Optimising the cryo-EM of pMad1Δ485:C-Mad2:O-Mad2. (A) *Micrograph of pMad1Δ485:C-Mad2:O-Mad2 with 0.05 % NP-40, collected on a FEI Titan Krios (ThermoFisher) 300 kV microscope equipped with a K3 detector (Gatan) and a volta phase plate (VPP).* ***(B)*** *SEC-MALS of homogenous pMad1Δ485:C-Mad2:O-Mad2 before and after cross-linking with BS3. Two rounds of gel-filtration were performed after cross-linking to remove aggregates. SDS-page for each sample is shown on the right.* ***(C)*** *A typical micrograph of the BS3 cross-linked phosphorylated pMad1Δ485:C-Mad2:O-Mad2 supplemented with 0.05 % NP-40 collected on the FEI Titan Krios (ThermoFisher) 300 kV microscope equipped with a K3 detector (Gatan) and a volta phase plate (VPP).* ***(D)*** *The same micrograph showing the picking of particles using a manually trained model in Warp (Tegunov and Cramer, 2019).*

With the optimised sample and data collection parameters we were able to obtain better 2D classes, although still not as good of quality as the non-phosphorylated sample (Fig 5.8A). One issue is that despite the large number of data collected (11,980 movies and 809,135 particles), the sample is very heterogenous during 2D classification. Even after several rounds of 2D classification with 150 classes in each round, further classification occurs and

the number of particles per class becomes small and the signal-to-noise ratio becomes poorer. This is partly because many more orientations are seen for this sample, as compared to the non-phosphorylated complex which preferred to lie flat on its side. However, the phosphorylated complex is also far more conformationally heterogenous, as the classes show various degrees of folding, with some classes showing the head domain being partially-folded (boxed blue), and others being mostly-folded (boxed orange). Interestingly, in the mostly-folded averages, it appears that the head domain might be directly contacting the Mad2 core. Although BS3 cross-linking did increase the percentage of particles which are folded, the vast majority of particles are still in a flexibly folded intermediate state with only 7.15 % of particles presenting what looks to be a mostly-folded state (boxed orange). It is therefore likely that alignments on the core are no longer as good because of the mobile head domain, additionally it may be that the folding of the head domain is causing the otherwise rigid core to become remodelled and more flexible.

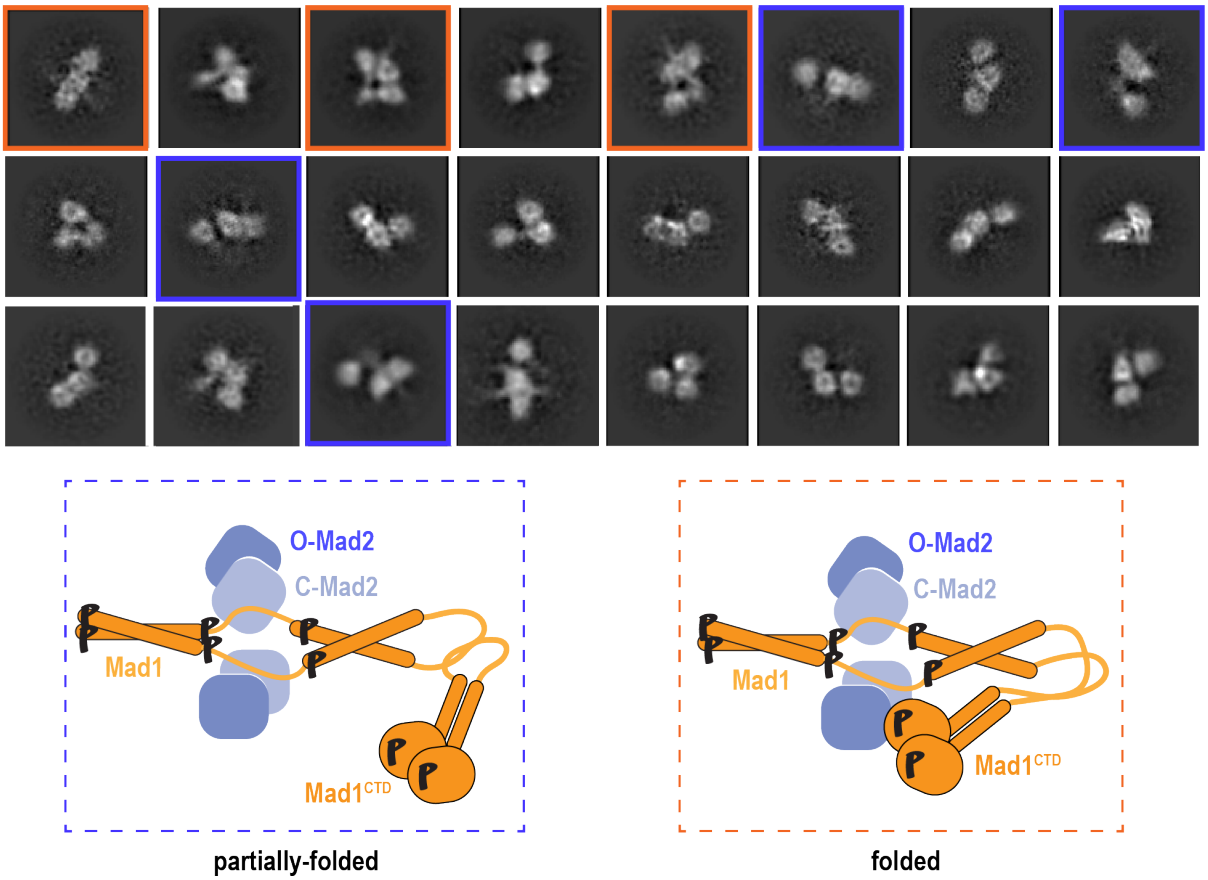

Figure 5.8: Gallery of 2D averages of the BS3 cross-linked pMad1Δ485:C-Mad2:O-Mad2 complex. *Representative from 150 classes. Classes which seem to be only partially-folded are boxed in blue, and classes which seem to be fully-folded, with the head domain touching the core are boxed in orange. A schematic of the suggested partially-folded and folded states seen in the 2D averages is shown below.*

We employed many different processing strategies in an attempt to obtain a high-resolution structure of the folded phosphorylated Mad1Δ485:C-Mad2:O-Mad2 complex. We were able to obtain may different reconstructions in which the head domain is in slightly different positions with respect to the Mad2 core as well as in various degrees of folding, which further confirms the highly dynamic nature of Mad1^{CTD} fold-over. So far, our best reconstruction has a resolution of 12.8 Å at 0.5 FSC, and 7.5 Å at 0.143 FSC, using a total of 17,812 particles (Fig 5.9A-B). We placed the crystal structure of the Mad1:C-Mad2:O-Mad2 core and the Mad1^{CTD} head domain into the electron density map which provides a reasonably good fit (Fig 5.9C). The resolution of our reconstruction is not high enough to see clear secondary structure and thus we cannot position the crystal structures with high accuracy, but we can still evaluate the general architecture of the folded-state. This includes seeing that the head domain is folding over to one side and is positioned close to the asymmetric Mad2 dimer, as well as that the coiled-coil of Mad1^{CTD} (α4) and the C-terminal α-helices (α2) of the core seem to be interacting. Additionally, our reconstruction suggests that fold-over causes the α-helices C-terminal to the core to get bent at angle, as compared to the unfolded-state, which would very likely influence the geometry of the Mad2 core and may have implications for MCC formation.

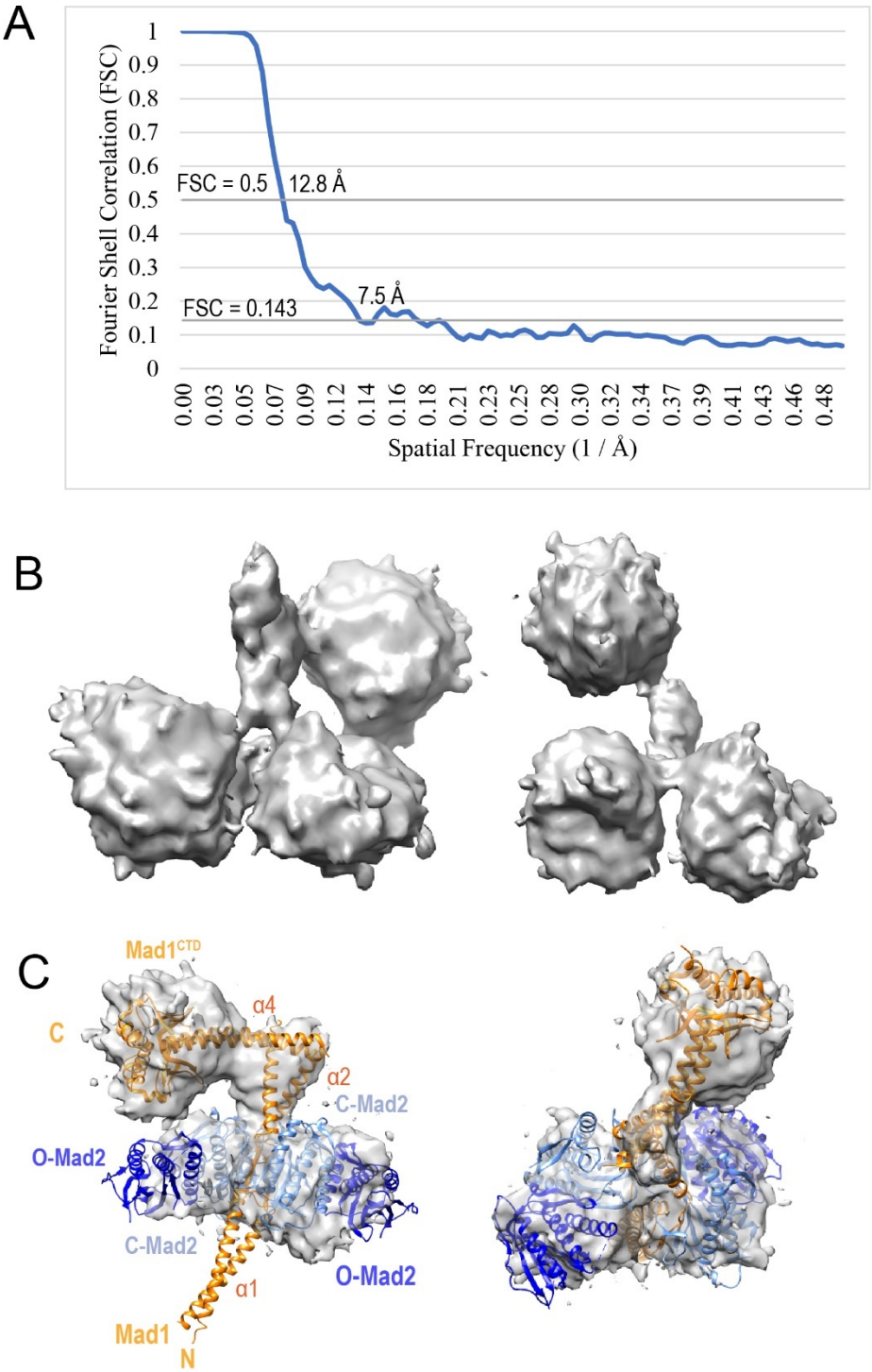

Figure 5.9: Three-dimensional reconstruction of the folded phosphorylated Mad1Δ485:C-Mad2:O-Mad2 complex by cryo-EM. (A) *The gold-standard FSC for the best phosphorylated Mad1Δ485:C-Mad2:O-Mad2 reconstruction presented in this thesis.* ***(B)*** *Two views of the 3D reconstruction of phosphorylated Mad1Δ485:C-Mad2:O-Mad2.* ***(C)*** *The Mad1^{CTD} and Mad1Δ485-584:C-Mad2:O-Mad2 crystal structures placed into the electron density (PDB IDs: 4DZO, 1GO4, 2V64).*

We used the recently released AlphaFold2 protein structure prediction program to predict the structure of the full-length Mad1 homodimer (Jumper *et al*, 2021). Mad1 residues 485-718 of this prediction are shown in Fig 5.10. The AlphaFold2 prediction closely resembles the previously crystallised segments (PDB: 1GO4, 4DZO). AlphaFold2 also predicts a short α-helix within the loop (residues 585-596) which disrupts the coiled-coil of α2 and α4 (Fig 5.10A-B, grey), despite other secondary structure programs (PSIPRED and Phyre2) not predicting any secondary structure in this loop (Jumper *et al*, 2021; Buchan *et al*, 2019, Kelley *et al*, 2015). Interestingly, AlphaFold2 predicts Mad1 to have a structure where the head domain of Mad1 ($Mad1^{CTD}$ in dark orange), is either in an open-state (Fig 5.10A) or in a folded-state (Fig 5.10B), with the folded-state having a slightly higher Local Distance Difference Test (lDDT) score in this region. The lDDT is a tool for the automated assessment of structure prediction by evaluating local distance differences of all atoms in a model and giving a per-residue measure of local confidence (Mariani *et al*, 2013). Closer examination of the positioning of the side-chains in the predicted folded-state, reveals that fold-over would be promoted by formation of a hydrophobic pocket between the hydrophobic residues within α3 of the loop and the end of the α2 coiled-coil (Fig 5.10B, zoomed box).

As previously mentioned, fold-over of $Mad1^{CTD}$ was first suggested when the Mad1:C-Mad2 core was crystallized as a dimer of tetramers, with intermolecular contacts between the C-terminal α-helices of two adjacent tetramers (PDB: 1GO4; Sironi *et* al, 2002). They suggested that although these intermolecular contacts are likely an artefact of crystal packing, that they are actually evidence for intramolecular contacts, which would allow formation of an anti-parallel coiled-coil between the C-terminal α-helices of the core (Fig 5.10B, α2), and the predicted α-helices in $Mad1^{CTD}$ (at the time there was no crystal structure of $Mad1^{CTD}$) (Fig 5.1B, α4). They showed that Mad2 binding and Mad1 stability and function was disrupted by introducing hydrophilic mutations into the solvent exposed residues of Mad1 α2 of the Mad1Δ485-718:C-Mad2 complex (L564, C568, L571, L575), while these mutations were silent in the Mad1Δ485-584:C-Mad2 complex. They conclude that destabilisation of Mad1 would only occur if those residues were buried in a folded Mad1:C-Mad2 complex and therefore proposed a model by which the $Mad1^{CTD}$ head splits apart and folds back onto the Mad1:C-Mad2 core to form an anti-parallel coiled-coil.

Although our data strongly suggest fold-over is occurring, it does not suggest that the $Mad1^{CTD}$ head domain splits apart to form an anti-parallel coiled-coil or that the folded-state

is the primary state. Rather the head domain folds over to one side and phosphorylation seems to help promote stability of the folded state. We do however find the drastic effect of these hydrophilic mutations within α2 interesting in light of the hydrophobic pocket formed in the folded AlphaFold2 structure, as this may suggest that the folded-state in our EM reconstruction is promoted by the formation of this hydrophobic pocket. We therefore plan to design similar mutations to investigate how hydrophobic residues within α3 of this loop affect fold-over.

We additionally, aligned the folded Mad1 AlphaFold2 prediction onto the hexameric Mad1$^{485-718}$:C-Mad2:O-Mad2 model (Fig 5.10C-D). Because the crystal structure is significantly asymmetric, we aligned the AlphaFold2 structure onto either Mad1 chain (Fig 5.10C versus 5.10D). This shows that the Mad1$^{485-718}$:C-Mad2:O-Mad2 folded-state suggested by AlphaFold2 closely resembles our folded cryo-EM reconstruction (Fig 5.9), with the folded Mad1^{CTD} being positioned close to O-Mad2.

Altogether, the AlphaFold2 model may hint at a mechanism by which the hydrophobic residues within the predicted α3 helix promote formation of a hydrophobic pocket which allows entrapment of a folded Mad1 state. Unfortunately, the AlphaFold2 model does not provide any insights into how phosphorylation is stabilising fold-over, unless it is simply through a pMad1^{CTD}-Mad2 interaction previously discussed. However, if this AlphaFold2 model is physiological, it seems likely that the hydrophobic interactions between α2 and α3 may allow dynamic fold-over in non-phosphorylated Mad1 which is then stabilised upon phosphorylation of Mad1 by Mps1. This model aligns with our observations that we see the head domain partially folding in the non-phosphorylated complex, while the folded-state is more prevalent in the phosphorylated complex.

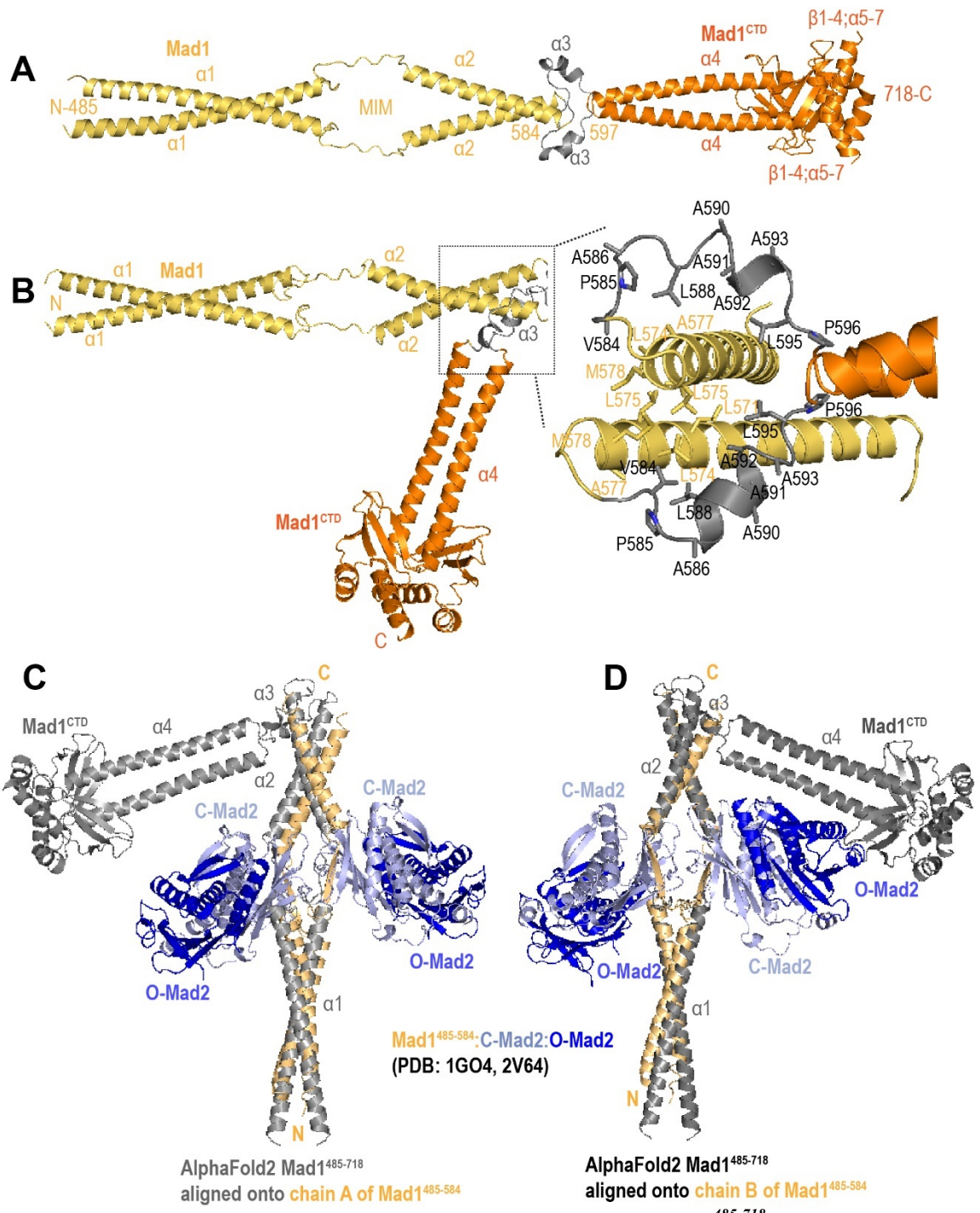

Figure 5.10: AlphaFold2 protein structure prediction for the Mad1$^{485-718}$ dimer. *AlphaFold2 predicts that the Mad1$^{485-718}$ dimer exists in either an open-state* ***(A)*** *or a folded-state* ***(B).*** *Mad1 residues 485-584 are coloured yellow, which includes the MIM motif, while the Mad1^{CTD} head domain is coloured dark orange. An additional short helix is predicted in the loop which disrupts the coiled-coil of α2 and α4 and is coloured grey. In (B) the dashed box highlights the hydrophobic α2-α3 interface with the hydrophobic side chains shown as sticks.* ***(C-D)*** *Alignment of the folded Mad1$^{485-718}$ structure predicted by AlphaFold2 onto the model of the hexameric Mad1$^{485-584}$:C-Mad2:O-Mad2 structure (PDB: 1GO4; 2V64). As the crystallised Mad1$^{485-584}$:C-Mad2 tetramer is significantly asymmetric (PDB: 1GO4), the AlphaFold2 prediction was aligned onto either chain A (C) or chain B (D) of Mad1$^{485-584}$ (PDB: 1GO4), which alters the position of the folded head domain with respect to the O-Mad2:C-Mad2 dimer.*

5.6 Investigating the mechanisms behind the folded-state

As previously mentioned, we identified five sites (S538, T540, T550, T551, and T716) within Mad1Δ485, which had a significant amount of phosphorylation in our Mad1Δ485 samples phosphorylated *in vitro* by GST-Mps1 (Fig 5.1; Appendix Table 3). We expressed and purified a Mad1Δ485 mutant in which all five sites were mutated to alanine (Mad1Δ485-5A) and confirmed by SEC-MALS that this mutant formed the hexameric complex similar to wild-type Mad1Δ485 (Fig 5.11A). We then used cryo-EM to investigate the structure of the phosphorylated Mad1Δ485-5A:C-Mad2:O-Mad2 complex. A total of 350 micrographs were collected on a FEI Titan Krios (ThermoFisher) 300 kV microscope equipped with a K3 detector, and 5,721 particles were picked using Warp (Tegunov and Cramer, 2019) (Fig 5.11B). The two-dimensional averages indicate that this complex no longer contains any fully folded-state particles (Fig 5.10C). This further suggests that it is the phosphorylation of Mad1 by GST-Mps1 at one or several of these sites which is helping to stabilise the folded-state of the Mad1Δ485:C-Mad2:O-Mad2 hexamer.

We have not yet systematically tested various phosphorylation mutants of Mad1 to determine specifically which sites are involved in promoting Mad1 fold-over. It would not be very practical to accomplish this using cryo-EM as it would be laborious to setup grids, screen grids, and collect and process the data for each sample. One idea for how to further test fold-over and measure if fold-over is occurring in a particular mutant is to use FRET. This could be accomplished by adding a flexible CFP-tag to the C-terminal head of Mad1 and conjugating a TAMRA-fluorophore to either C-Mad2 or O-Mad2 of the complex. However, many controls would have to be identified to ensure we are actually measuring fold-over, and not abrogating fold-over with the FRET tags.

Although it seems unlikely, it could be that phosphorylation of the complex is promoting stabilisation of the folded state by an indirect or artificial mechanism, such as by changing how the particle is captured on the grid. For example, it has been shown that during cryo-EM grid preparation, phosphorylation or the lack thereof, can dramatically alter preferred orientation (Velazhahan *et al*, 2021). Future studies will require further confirming both if and then how phosphorylation directly promotes the folded state of $Mad1^{CTD}$, including which specific sites are involved.

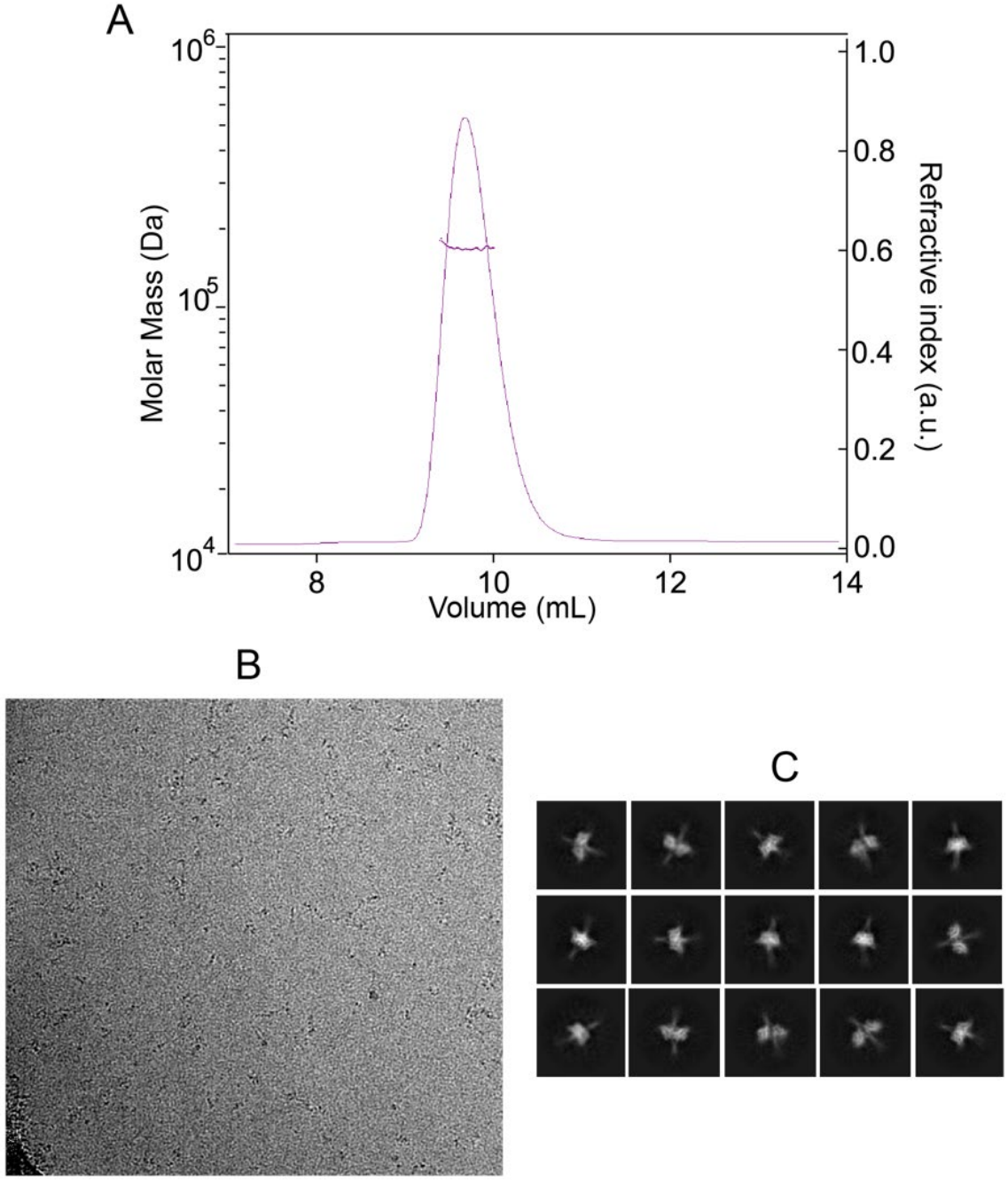

Figure 5.11: Cryo-EM analysis of Mad1Δ485-5A:C-Mad2:O-Mad2 phosphorylation mutant complex. (A) *SEC-MALS of the phosphorylated Mad1Δ485-5A:C-Mad2:O-Mad2 complex confirming homogenous hexamer is present (135 kDa).* ***(B)*** *Representative micrograph of the phosphorylated Mad1Δ485-5A:C-Mad2:O-Mad2 complex collected on a Titan Krios with a K2 detector in counting mode.* ***(C)*** *Gallery of selected 2D classes from 50 total classes.*

We also wondered whether or not O-Mad2 was required for fold-over as our 3D reconstruction tentatively suggests that the head domain is folding back to contact the outside of the core where O-Mad2 is located (Fig 5.9C). This is particularly interesting as it has been suggested that phosphorylated Mad1^{CTD} has preferential affinity for O-Mad2 over C-Mad2 (Ji et al., 2018). We attempted to analyse the structure of the Mad1Δ485:C-Mad2 tetramer by

cryo-EM, utilising a Mad2 R133A mutant which is dimerization deficient and thus ensures formation of a homogenous tetramer with no super-stoichiometric or wild-type O-Mad2 present (Fig 5.12). SEC-MALS was used to confirm that Mad1Δ485:C-Mad2ΔR133A formed a homogenous tetramer (Fig 5.12A). However, analysing this complex in both the phosphorylated and non-phosphorylated states, and with and without BS3 cross-linking, did not provide meaningful 2D classes (Fig 5.12 C-D). We were unable to visualise any of the α-helices extending from the core, but only what looks to be the two Mad2 molecules of the core. We suspect this is because in the tetramer the core is less than 50 kDa and therefore may not be providing good alignments for 2D classification. It also may be that the core is less rigid in the tetrameric state as we noticed that across various 2D averages the two Mad2 molecules seem to be quite mobile with respect to each other (Fig 5.12 C-D). However, it is tempting to suggest that the head domain is not folding over, because there is no third density for the head domain near the core in our 2D averages. Ultimately, our results remain inconclusive as to whether O-Mad2 is required for fold-over using this strategy.

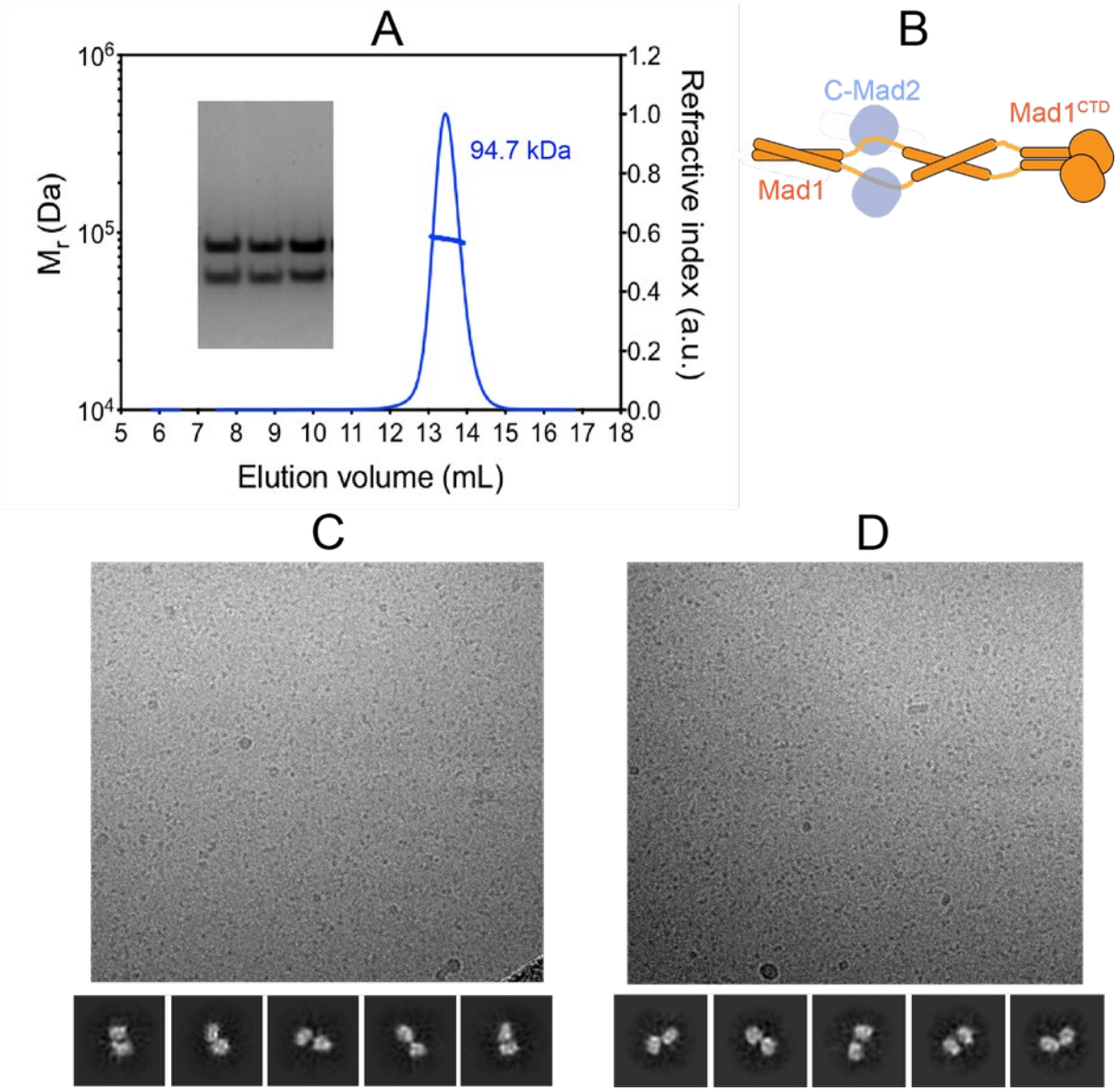

Figure 5.12: The Mad1Δ485:C-Mad2ΔR133A tetramer. *(**A**) SEC-MALS and SDS-PAGE of purified Mad1Δ485:C-Mad2ΔR133A confirms it forms a homogenous tetramer. The expected molecular mass of tetrameric Mad1:C-Mad2 is 99 kDa. (**B**) A model diagram of the Mad1:C-Mad2 tetramer. (**C**) Representative micrograph and 2D averages of non-phosphorylated Mad1Δ485:C-Mad2ΔR133A. (**D**) Representative micrograph and 2D averages of phosphorylated Mad1Δ485:C-Mad2ΔR133A.*

5.7 Cross-linking Mass Spectrometry of Mad1:Mad2

In collaboration with Johannes Hevler of the Heck group, at the Biomolecular Mass Spectrometry & Proteomics Division at Utrecht University, Netherlands, we performed cross-linking mass spectrometry on the Mad1:Mad2 complexes. To generate assembly specific cross-links for the tetrameric Mad1Δ485:C-Mad2ΔR133A complex, as well as the non-phosphorylated and phosphorylated hexameric Mad1Δ485:C-Mad2:O-Mad2 complexes were run on a blue native-PAGE gel and in-gel cross-linking mass spectrometry (IGX-MS) was performed (Hevler *et al*, 2021) (Fig 5.13A). Briefly, bands corresponding to the fully

assembled complex (tetrameric or hexameric) were excised and subsequently cross-linked with either DSS (disuccinimidyl suberate) or DMTMM (4-(4,6-Dimethoxy-1,3,5-triazin-2-yl)-4-methylmorpholinium tetrafluoroborate). While DSS predominantly forms a covalent bond between proximal lysine residues, DMTMM facilitates an aspartate or a glutamate residue to form an amide bond with a nearby lysine residue (Leitner *et al*, 2014, 2010). The detected cross-links from both cross-linkers (inter = green; intra = purple), are mapped to the sequence of Mad1Δ485-718 and Mad2 (Fig 5.13B-D). It is important to note that in these experiments it is not possible to distinguish if a Mad2 cross-link comes from O-Mad2 or C-Mad2 and thus all Mad2 cross-links are pooled together.

Surprisingly, our cross-linking mass spectrometry does not show a significant difference between the three complexes. It does however suggest that in all samples a significant number of cross-links occur between Mad1^{CTD} and Mad2, including some cross-links to the RWD-fold head domain of Mad1^{CTD}. These cross-links most prominently occur to the flexible N-terminus of Mad2, including what would be the first β-sheet and α-helix in O-Mad2, or the extended α-helix in C-Mad2, as well as the central safety-belt of Mad2. Cross-links between Mad1^{CTD} and the flexible C-terminus of Mad2 are present but seem less predominant. Additionally, in all samples, a significant number of cross-links occur between both the N- and C-terminal α-helices of the Mad1 core and Mad1^{CTD}. Interestingly, these cross-links are prevalent between the N-terminal coiled-coil (residues 490-520) of the Mad1 core and the start of the Mad1^{CTD} coiled-coil (residues 600-620). If Mad1^{CTD} was in an extended conformation, these two segments would be over 150 Å apart, which hypothetically should be too far for cross-linking by either DSS or DMTMM. In agreement with the folded-state of Mad1$^{485-718}$ predicted by AlphaFold2 (discussed in section 5.5 and Fig 5.10), cross-links are prevalent between the C-terminal segment of Mad1$^{485-718}$ α2 (residues 550-580) and the predicted α3 (585-597).

Ultimately, our cross-linking results provide further evidence for a folded-state of the Mad1^{CTD} head domain with respect to the Mad1Δ485:C-Mad2 core. We note that unpublished cross-linking mass spectrometry data from the Hardwick lab has found further evidence for fold-over of the Mad1^{CTD} head domain in *S. pombe* (mentioned in the PhD thesis of Amin, 2019). We suspect that despite our cryo-EM reconstructions showing that fold-over is only stabilised in the phosphorylated hexameric Mad1Δ485:C-Mad2:O-Mad2 complex, that the cross-linking process used in these experiments is promoting the capture of

the folded-state in all complexes. This may not be so surprising considering that even in our 2D classes of non-phosphorylated Mad1Δ485:C-Mad2:O-Mad2, we were able to visualise the head domain already folding towards the core (Fig 5.3D). Additionally, AlphaFold2 predicted that a folded-state of Mad1$^{485-718}$ is likely to exist, even when Mad1 phosphorylation and Mad2 binding is not accounted for (Fig 5.10). One way to test this hypothesis, which we have yet to try, would be to collect cryo-EM data on a cross-linked (DSS and DMTMM) non-phosphorylated hexameric sample to see if this captures the folded-state. However, as these cross-linking experiments were performed in-gel, the experiments would need to be repeated using in-solution cross-linking as a direct comparison (Klykov *et al*, 2018; Mendes *et al*, 2019; Götze *et al*, 2019).

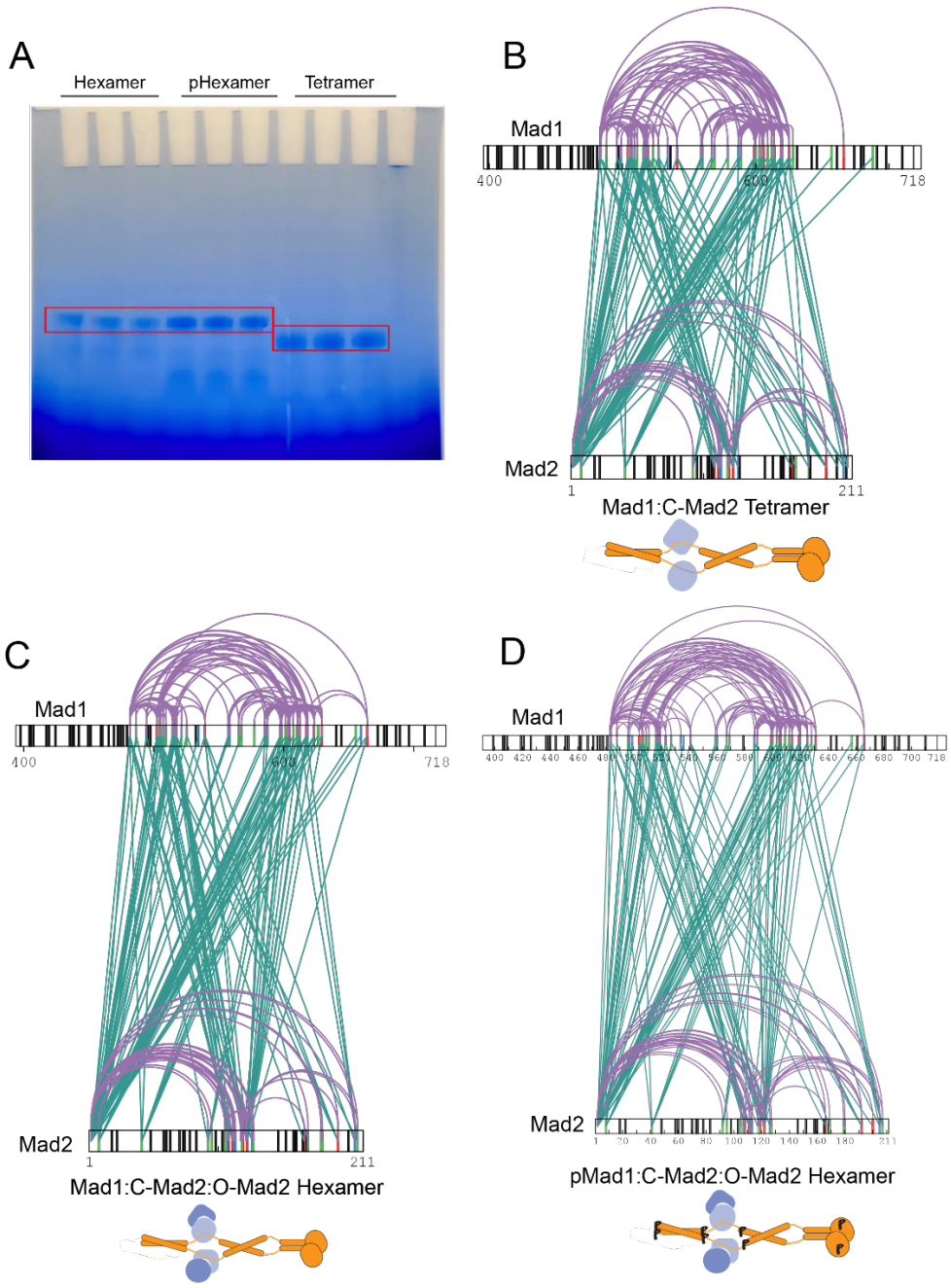

Figure 5.13: In-gel cross-linking mass spectrometry of Mad1:Mad2 complexes. (A) *Blue-native page of the three Mad1:Mad2 complexes used for cross-linking mass spectrometry.* ***(B)*** *Cross-links detected within the non-phosphorylated tetrameric Mad1Δ485:C-Mad2ΔR133A sample.* ***(C)*** *Cross-links detected within the non-phosphorylated hexameric Mad1Δ485:C-Mad2:O-Mad2 sample.* ***(D)*** *Cross-links detected within the phosphorylated hexameric pMad1Δ485:C-Mad2:O-Mad2 sample. In (B-D), green lines highlight intermolecular cross-links, while purple lines highlight intramolecular cross-links. A schematic model of the complex present in each sample is shown below. It is important to note that there is no way to distinguish between C-Mad2 or O-Mad2 cross-links and thus all Mad2 cross-links are pooled together.*

5.8 Discussion

The data presented in this chapter propose a model by which the C-terminal head domain of Mad1 folds back towards the Mad1:C-Mad2 core, a mechanism which seems to be stabilised

by Mps1 phosphorylation of Mad1 (Fig 5.14A-B). This fold-over is allowed by the 13-residue loop (residues 584-597) between the C-terminal coiled-coil of the Mad1:C-Mad2 core (Mad1 residues 485-584; α2) and Mad1^{CTD} (residues 597-718; α4). Additionally, AlphaFold2 predicts the presence of a short α-helix within this loop (α3) which may promote fold-over by forming a hydrophobic pocket with the end of the α2 coiled-coil (Fig 5.10).

Our cryo-EM and cross-linking data suggest that folded Mad1^{CTD} either directly contacts or is at least positioned very close to Mad2 of the Mad1:C-Mad2 core. We correlate this finding with the phosphorylation-specific interaction of Mad1^{CTD} and Cdc20, such that fold-over of Mad1^{CTD} might be important for positioning the MIM motif of Cdc20 close to the converting O-Mad2 bound to Mad1:C-Mad2 for optimal entrapment (Fig 5.14A-B). This seems particularly relevant considering that Mad1 phosphorylation and the Cdc20:Mad1^{CTD} interaction have both been shown to be required for catalytic MCC formation (Ji *et al*, 2017; Piano *et al*, 2021).

Our NMR work on the Cdc20^{NTD}:pMad1^{CTD} interaction (presented in chapter 4), suggests that the N-terminus of Cdc20 binds in a parallel orientation with respect to Mad1. The N-terminus of Cdc20, including the first α-helix (α1) binds to the Mad1^{CTD} coiled-coil, while C-terminal to the α1-helix the Box1 motif binds to the top of the C-terminal head domain (Fig 5.14A-B). Without a structure of pMad1^{CTD}:Cdc20 we cannot be certain they bind in a parallel orientation but if this is the case, another important aspect of Mad1^{CTD} fold-over may be to correctly orient the MIM motif of Cdc20 with respect to O-Mad2. Mad2 dimerises to itself in an anti-parallel orientation and the Cdc20 MIM motif is entrapped by the safety-belt in a parallel orientation (Fig 5.14C; PDB: 2V64). This means that O-Mad2 bound to Mad1:C-Mad2 lies in an anti-parallel orientation with respect to Mad1 and therefore Cdc20 (Fig 5.14D). Consequently, it seems likely that Cdc20 needs to be positioned in a parallel orientation with respect to O-Mad2 for optimal MIM entrapment, and the fold-over would re-orient Cdc20 in the proper parallel orientation with respect to O-Mad2 and this could be required for efficient MIM entrapment (Fig 5.14D).

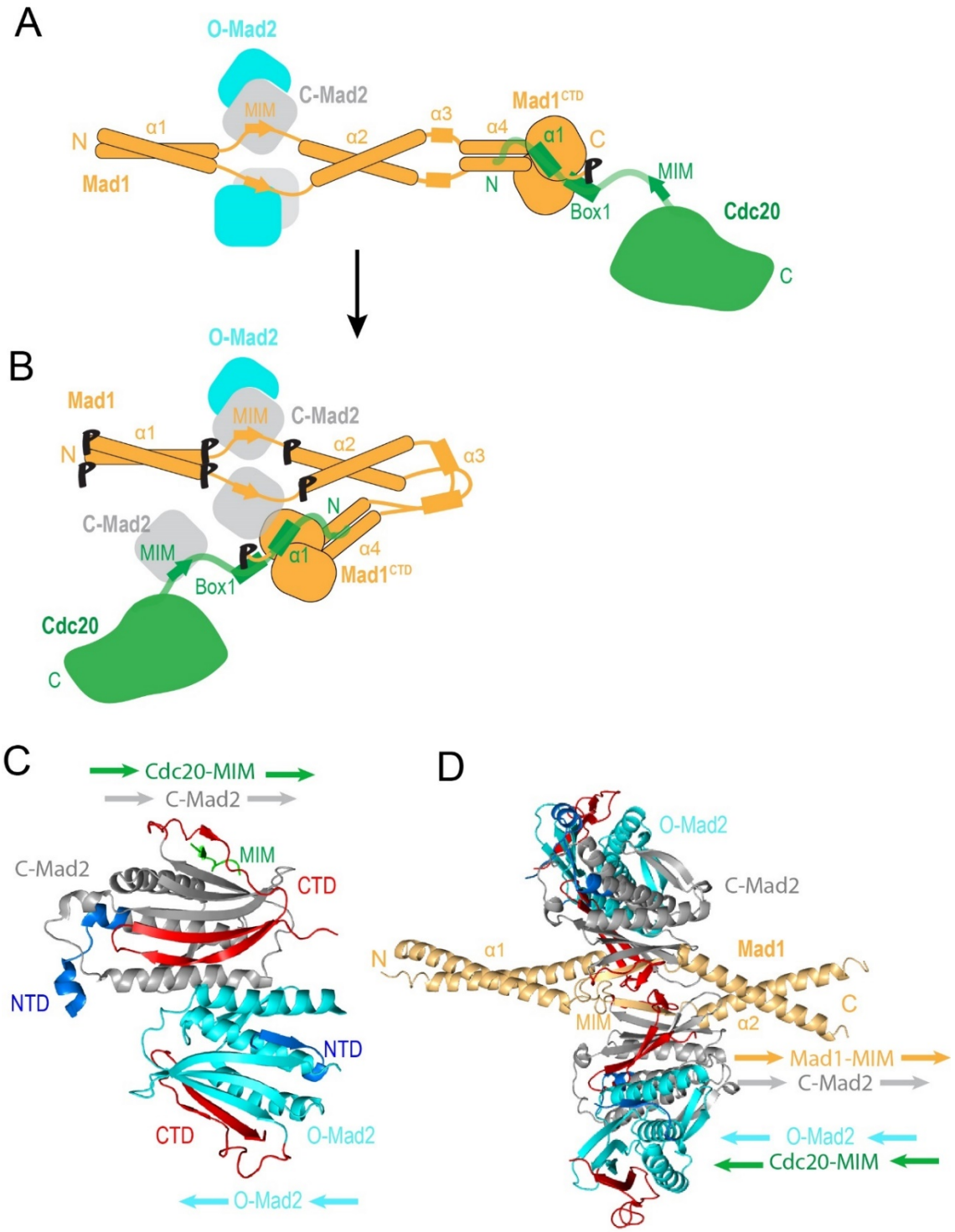

Fig 5.14: Model for how Mad1^{CTD} fold-over promotes MCC assembly. A) *The unfolded state of the pMad1:C-Mad2:O-Mad2 complex with the N-terminus of Cdc20 bound in a parallel orientation to the phosphorylated Mad1 C-terminus. In the unfolded state, The MIM motif of Cdc20 is positioned far away from Mad2.* ***B)*** *The folded state of the pMad1:C-Mad2:O-Mad2 complex with the N-terminus of Cdc20 bound in a parallel orientation to pMad1^{CTD}. Folding back of Mad1^{CTD} likely functions to bring Cdc20 in close proximity to O-Mad2 which then converts to C-Mad2 and binds Cdc20.* ***C)*** *The O-Mad2:C-Mad2 dimer (PDB 2V64). O-Mad2 is coloured in cyan, while C-Mad2 is coloured in grey while both their N- and C-termini are coloured blue and red, respectively. O-Mad2 and C-Mad2 bind each other in an anti-parallel manner as depicted by the coloured arrows, which also highlights that the MIM motif is entrapped in the safety-belt of C-Mad2 in a parallel manner.* ***D)*** *The Mad1:C-Mad2:O-Mad2 hexamer coloured using the same scheme in (C), with Mad1 coloured in pale orange.*

O-Mad2 binds anti-parallel the Mad1:C-Mad2 complex. Because Cdc20 likely binds Mad1^{CTD} in a parallel orientation, it is likely that Mad1^{CTD} not only helps to reposition Cdc20 close to Mad2, but also to re-orient it in a parallel orientation with respect to O-Mad2 as depicted by the orientation of the O-Mad2 and Cdc20-MIM errors with respect to the C-Mad2 and Mad1-MIM errors.

Recently, the Musacchio lab identified that catalytic MCC formation was impaired by decreasing the distance between the Box1 and MIM motifs of Cdc20, whereas replacing that region with GGGS linkers did not affect catalysis (Piano *et al*, 2021). This suggests that a minimal distance between Box1 and MIM and not a specific sequence or conformation is required for catalysis. The distance from the Box1 to the MIM motif of Cdc20 is approximately 100 Å, while the distance from pThr716 at the top of the Mad1^{CTD} head domain (where Box1 of Cdc20 binds) to Mad2 of the Mad1:C-Mad2 core is approximately twice that long (200 Å). This does not account for several predicted helical segments as well as possible self-interaction within the N-terminus of Cdc20 which would significantly shorten the distance between the Cdc20 N-terminus and its MIM motif. This further supports our model as fold-over would seem to be required to shorten this distance and allow Mad2 to entrap the MIM motif.

Further support for the model by which Mad1 fold-over acts to bring Cdc20 close to Mad2 during O-to-C Mad2 conversion, has been recently published by the Song-Tao Liu lab (Ji *et al*, 2018). They used both *in vitro* and endogenous pull-downs to identify that both the C-terminus (residues 585-718) and N-terminus (residues 1-485) of Mad1 interact with both the open (Mad2ΔLL mutant) and closed (Mad2 L13A mutant) conformations of Mad2. These interactions were further confirmed in live cells using GFP-tagged Mad2. Truncations of Mad1^{CTD} additionally suggested that Mad2 bound to the head of Mad1^{CTD}, not to the coiled-coil region. Additionally, a dimerization deficient construct of Mad2 (C-Mad2 L13A R133E Q134A) also bound to both the NTD and CTD domains of Mad1, suggesting that the binding mode does not use the Mad2 dimerization domain. Therefore, these results suggest a novel interaction interface on Mad2 which binds Mad1, and which is possibly shared by Mad2 conformers. Ultimately, it seems likely that this interaction may play a role in promoting the folded-state of Mad1^{CTD} and bringing Cdc20 MIM in close proximity to Mad2.

We also find it interesting that our cryo-EM analyses show that fold-over is stabilised when Mad1Δ485:C-Mad2:O-Mad2 is phosphorylated, as the Song-Tao Liu lab study also found that when Mad1 was phosphorylated by Mps1, it bound to both O-Mad2 and C-Mad2 with

higher affinity, as compared to non-phosphorylated Mad1 or when phosphorylated Mad1 with a T716A mutant was tested. This might suggest that Mps1 phosphorylation stimulates Mad2 O-C conversion through promoting a novel Mad1:Mad2 interaction which might also be the mechanism behind Mad1^{CTD} fold-over.

5.9 Future Directions

Altogether, our cryo-EM and cross-linking analyses provide compelling evidence that the C-terminal head domain of Mad1 folds back onto the Mad1:C-Mad2 core. A process which seems to be stabilised by Mps1-dependent Mad1 phosphorylation. These data combined with our current understanding of catalytic MCC formation, strongly suggests several important factors by which this fold-over may contribute to MCC formation, including bringing the MIM motif of Cdc20 not only in close proximity to Mad2 but also positioning the MIM motif in the correct orientation with respect to Mad2 for safety-belt entrapment. However, many more experiments need to be completed to understand the molecular mechanisms behind this fold-over, including which Mps1 phosphorylation sites are involved, and how specifically fold-over contributes to catalytic MCC formation.

Increasing the resolution of our folded pMad1Δ485:C-Mad2:O-Mad2 cryo-EM reconstruction seems the most promising and straight-forward way to answer these questions. Collecting more data would likely be very beneficial as the final number of particles used for the folded-state reconstruction was 17 k which is a relatively small number and only 3.7 % of the total picked particles. All other particles were either in the open-state (1.8 %), a partially-folded intermediate (67.2 %), or simply excluded due to poor quality (27.3 %). A different cross-linking scheme, such as a two-step cross-linking process to improve capture of transient intermediate states, or site-specific cross-linking to stabilise the folded-conformation could be designed to increase conformational homogeneity of the complex for cryo-EM analysis. The folded-state of Mad1 predicted by AlphaFold2 likely provides us with useful hints for how to stabilise the folded conformation. Ultimately, solving the structure of the entire pre-MCC complex (Cdc20:pMad1:C-Mad2:O-Mad2:Bub1:Bub3) would provide the most insights and may promote a more homogenous conformation, but as explained in the initial aims of this thesis, we have not yet been able to assemble a stable form of this complex.

Chapter 6
Concluding Remarks and Future Directions

This thesis, along with several other recently published studies, provides an updated view on the molecular mechanisms of MCC assembly at kinetochores. In particular, we have identified how a sequential Mps1-dependent phosphorylation cascade of key SAC components, activates checkpoint formation in response to unattached kinetochores, a process that largely serves to create a catalytic scaffold centred around the C-terminal head domain of Mad1 (model diagram in Fig 6.1).

MCC assembly starts on the outer kinetochore protein Knl1, which by means of its phosphorylated MELT motifs, recruits Bub3 bound to Bub1. Sequential phosphorylation of the Bub1 CD1 domain by Cdk1 and Mps1 phosphorylation then promotes Mad1:C-Mad2 kinetochore targeting through a direct interaction between Bub1 pThr461 and the RLK motif of Mad1^{CTD} (chapter 3). Phosphorylation of Mad1 by Mps1 then activates the Mad1:C-Mad2 complex to be a catalytic platform for MCC assembly, through juxtaposition of Bub1 and Cdc20 on pMad1^{CTD} (chapter 4). This includes phosphorylation of Thr716 at the very C-terminus of Mad1^{CTD}, which promotes Mad1^{CTD} binding to both the N-terminus of Cdc20, as well as a region within Bub1 which is just C-terminal to the Bub1 CD1 domain and just N-terminal to the Bub1 KEN1/ABBA motifs. We have additionally identified a mechanism of Mad1 remodelling by which Mad1^{CTD} can fold-back positioning the head domain (where Cdc20 and Bub1 are bound) close to O-Mad2, and this fold-over seems to be promoted or at least stabilised by Mps1 phosphorylation of Mad1 (chapter 5).

These findings have many interesting implications for MCC formation and there seem to be several plausible theories for how these interactions may act as catalysts. In particular it seems likely that this tripartite assembly of Bub1 and Cdc20 on pMad1^{CTD}, functions not only to target Bub1 and Cdc20 to the Mad1:C-Mad2 complex, but also to reposition them with respect to each other, and in close-proximity to Mad2. This seems particularly plausible in light of Mad1 fold-over, as fold-over would seem to be an ideal way to properly position the MIM motif of Cdc20 for Mad2 safety-belt entrapment. However, it is also possible that their interaction primarily functions to target Cdc20 to kinetochores, or to relieve Cdc20

autoinhibition caused by self-association of its N- and C-termini. Therefore, we can only make educated guesses for how these interactions promote MCC assembly and further insights are required to obtain a complete picture.

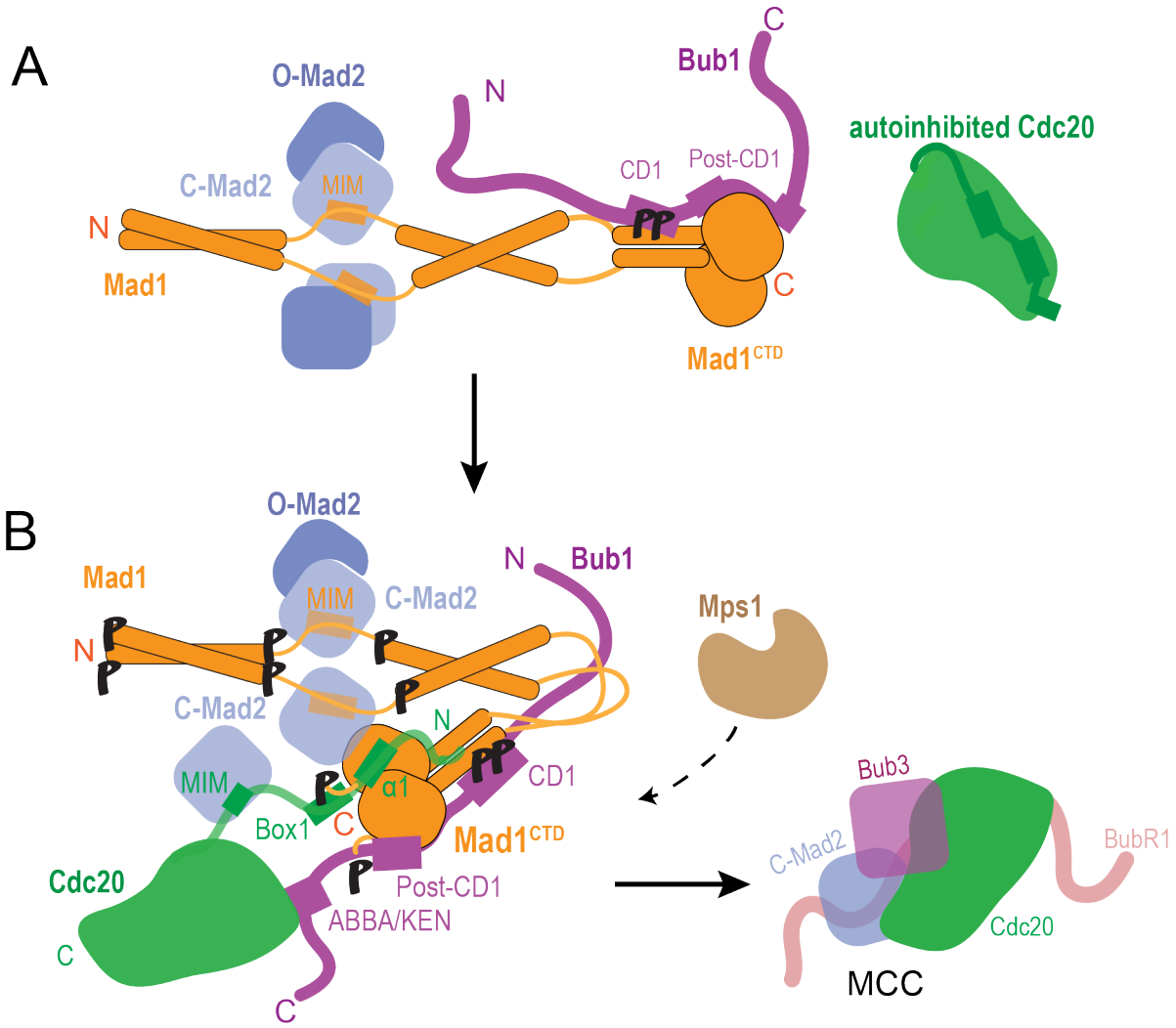

Figure 6.1: Updated model of catalytic MCC assembly onto Bub1:Mad1. ***(A)*** *The doubly phosphorylated Bub1 CD1 domain targets the Mad1:C-Mad2 complex to kinetochores which then acts as a platform for O-Mad2 binding and Mad2 O-to-C conversion. Cdc20, on its own, exists in an autoinhibited state which likely impairs the Cdc20:C-Mad2 interaction and MCC formation.* ***(B)*** *Phosphorylation of the C-terminus of Mad1 at Thr716 promotes its interaction with both the N-terminus of Cdc20 and the post-CD1 domain of Bub1. Interaction between the WD40 domain of Cdc20 and the ABBA/KEN1 motif of Bub1 also occurs which likely promotes Cdc20 kinetochore targeting and positions Cdc20 close to Mad1:C-Mad2. Cdc20 autoinhibition is relieved either through its interaction with pMad1^{CTD} or by other unknown means, and this Cdc20:pMad1^{CTD} interaction then promotes Cdc20 MIM accessibility. Phosphorylation of Mad1 by Mps1 then also promotes Mad1^{CTD} fold-over which positions the MIM motif of Cdc20 in close proximity to O-Mad2 bound to the Mad1:C-Mad2 core. In the last step, O-Mad2 undergoes conversion to C-Mad2, and the safety-belt can readily entrap the Cdc20 MIM motif positioned nearby. Formation of the C-Mad2:Cdc20 complex then promotes binding to BubR1:Bub3 to complete the MCC.*

Ultimately, our understanding of MCC assembly would be greatly improved from an atomic structure of the entire pre-MCC complex (pBub1:pMad1:Cdc20:O-Mad2:C-Mad2). As

previously mentioned, this was the original goal of this thesis, but we were unable to produce a stable complex for cryo-EM analyses. Not only is the complex relatively transient and conformationally heterogenous, but more importantly several mechanisms of autoinhibition seem to be at play that we don't yet fully understand. The interaction of both pBub1^{CD1}:Mad1^{CTD} and Cdc20^{NTD}:pMad1^{CTD} are in the low µM range, which should be suitable for creating a stable complex to study by cryo-EM. However, the binding of both full-length Bub1 as well as full-length Cdc20 to Mad1 seems to be inhibited, as neither interaction can be captured on a size-exclusion column. In the case of Cdc20 it seems quite likely that this is due to the previously reported self-association of the N- and C- termini of Cdc20 which would block access to Box1 for pMad1^{CTD} binding. Why full-length Bub1 does not bind strongly to Mad1 remains more elusive, and we have struggled to investigate this further due to Bub1 truncations centred around the CD1 and ABBA/KEN motifs being insoluble. Therefore, in order to assemble a stable form of the pre-MCC scaffold to study by cryo-EM, we likely need to first understand these possible mechanisms of autoinhibition. Additionally, because we now have a greater understanding of the molecular interactions required to assemble the pre-MCC complex, including the high-resolution crystal structure of Bub1^{CD1}:Mad1^{CTD}, it may be possible to stabilise a complex by designing site-specific crosslinking.

Mad2 metamorphosis: How is it catalysed?

Although many of the finer details of MCC assembly have been and are slowly being teased out, it still remains largely unclear how remodelling of Mad2 from the open-to-closed state, which historically, was believed to be the rate-limiting step of MCC formation, is triggered. Understanding the factors which directly promote Mad2 remodelling remains difficult because of the lack of any stable intermediate states.

In the early 2000s, NMR was fundamental to identifying the open and closed conformers of Mad2 and the dramatic conformational rearrangement which occurs between them (Luo *et al*, 2000, 2002, 2004). High-resolution X-ray structures of various Mad2 complexes, as well as careful biochemical analyses, were then fundamental to identifying the structural rearrangements which occur during conversion (Sironi *et al*, 2002; De Antoni *et al*, 2005; Mapelli *et al*, 2007; Yang *et* al, 2008; Hara *et* al, 2015).

Mad2 contains a central core (Fig 6.1, coloured cyan), which includes a three-stranded anti-parallel β-sheet, and three α-helices, with a central β-hairpin between the first two of these α-helices. The core of Mad2 remains conserved during conversion, while both the N- and C-termini undergo metamorphosis. The N-terminal β-strand (Fig 6.1, O-Mad2 β1 coloured dark blue) is displaced during conversion and refolds into a short α-helix and an extended α-helix in C-Mad2 (Fig 6.1, C-Mad2 αN and αA* coloured dark blue), while the C-terminus of O-Mad2 (Fig 6.1, coloured red), including two adjacent β-strands (β7/8) which form a C-terminal β-hairpin, swing across the central face of Mad2. This rearrangement of the C-terminal β-hairpin and its adjacent loop (the 'safety-belt'), ultimately enables the safety-belt of Mad2 to entrap the MIM motif of Cdc20 (coloured green) to form the MCC.

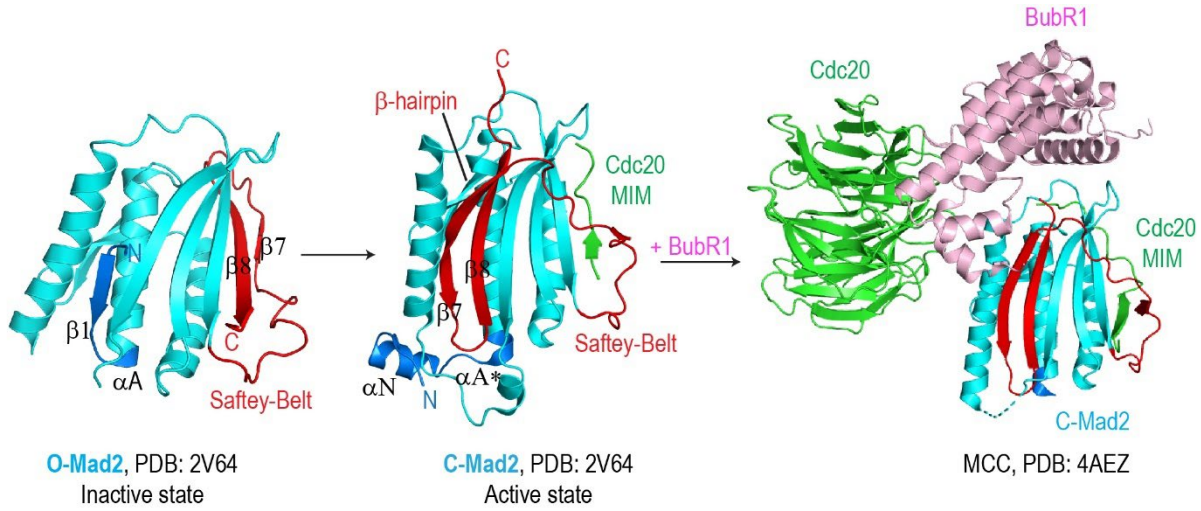

Figure 6.2: Mad2 conversion and incorporation into the MCC. *Mad2 contains a central core which is conserved during Mad2 metamorphosis (coloured cyan), while the N- and C-termini undergo dramatic remodelling (coloured dark blue and red, respectively). In O-Mad2, the N-terminus forms a β-sheet (β1), which gets ejected outwards during conversion and refolds as a short α-helix (α1) and an extended α-helix (αA*) in C-Mad2. In O-Mad2 the C-terminus contains a β-hairpin (β7/8) which pivots across the entire face of Mad2 during conversion and lies where the N-terminal β1 sheet was previously located. The rearrangement of the C-terminal β-hairpin along with its adjacent safety-belt allows entrapment of the MIM motif of Cdc20 (green). Cdc20:C-Mad2 then binds to BubR1 (pink) to form the MCC.*

The previously mentioned FRET assay, developed by the Musacchio lab (Faesen *et al,* 2017, Piano *et al*, 2021), has systematically characterised which components contribute to catalysing MCC formation. This assay specifically measures the rate of C-Mad2 conversion because it measures the FRET-pair formed when Mad2 and Cdc20 bind, which happens instantaneously *in vitro* upon C-Mad2 formation. Consequently, we understand both the metamorphosis which occurs during Mad2 conversion, as well as the catalysts which promote Cdc20:C-Mad2 formation, but we don't yet understand if any catalysts act to directly affect

Mad2 conformational change, or only indirectly. For example, it may be that catalysts promote displacement of the N-terminal β-sheet or the C-terminal β-hairpin in order to directly stimulate conversion, or catalysts may only act indirectly, such as by simply positioning the MIM motif of Cdc20 in close proximity to C-Mad2. Key to understanding this question, is whether or not Mad2 conversion happens prior to Cdc20 binding or simultaneously with MIM entrapment.

The original theory for Mad2 conversion (De Antoni *et al*, 2005), suggested a template-based model by which O-Mad2 dimerization to C-Mad2 bound to Mad1, triggering C-Mad2 formation, and this 'empty' C-Mad2 was then released and could then rapidly bind Cdc20 to form the MCC. However, with our current understanding of MCC assembly, it seems much more likely that O-Mad2:C-Mad2 dimerization primarily functions to target O-Mad2 to kinetochores, while Mad2 conversion is triggered by other means. In support of this, *in vitro* Mad2 dimerization only accelerates Mad2 conversion four-fold as compared to the over 35-fold acceleration seen when the full catalytic platform is present (Piano *et al*, 2021).

One idea is that in the open-state of Mad2, the C-terminal β-hairpin is 'breathing' in and out, and placement of the MIM motif of Cdc20 in close-proximity, enables the MIM motif to slide underneath the β-hairpin and become entrapped by the Mad2 safety-belt which then promotes the β-hairpin to swivel across the face of Mad2 triggering spontaneous C-Mad2 formation. O-Mad2 monomer alone has never been crystallised, which suggests that it is likely more dynamic than the structure of the stabilised O-Mad2 mutant in the O-Mad2:C-Mad2 complex suggests. This seems particularly likely as in the O-Mad2:C-Mad2 crystal structure (PDB: 2V64), the crystallographic packing promotes tight packing of the Mad2 dimers such that the β-hairpin which makes crystallographic contacts may be artificially stabilised in the O-Mad2 position. However, it could be that the β-hairpin is in a rigid position within O-Mad2, and that some process triggers release of the β-hairpin, such as interaction with one of the SAC proteins or allosteric changes within Mad2. If this 'breathing' model of the β-hairpin were true, it would suggest that the MIM motif of Cdc20 is actually what promotes conversion and therefore the 'true' catalyst. This model seems particularly plausible considering that when the MIM motif of Cdc20 is presented to Mad2 as a peptide, conversion of O-Mad2 into C-Mad2 is essentially spontaneous (Piano *et al*, 2021).

The Musacchio lab recently proposed a model by which the process of Mad2 conversion, not just the formation of C-Mad2, is required to entrap the MIM motif of full-length Cdc20, by allowing closure onto the MIM motif during the conversion process (Piano *et al*, 2021). The rational for this model is that full-length Cdc20 does not bind at an appreciable rate to 'empty' C-Mad2, even in the presence of catalysts, suggesting that the Cdc20 MIM motif is entrapped during the conversion process and not after (Piano *et al*, 2021). They additionally showed that truncating Cdc20 to just before the MIM motif (111-C), allows spontaneous Mad2 binding, similar to when the MIM motif is presented as a peptide.

However, the MIM motif of the Mad1 dimer, which is located centrally within the C-terminus of Mad1, such that it has a long stretch of coiled-coil on either side, binds rapidly to both O-Mad2 and C-Mad2 *in vitro* without the presence of catalysts (Appendix Fig 6), and no such mechanism in cells seems to be required for catalysing or promoting the Mad1:Mad2 interaction as is required for Cdc20. Additionally, the MIM of Mad1 and the MIM of Cdc20 have a similar K_D (3 μM) for O-Mad2, suggesting this difference is not due to binding affinity. This suggests that Mad2 conversion and MIM entrapment does not require the process of Mad2 conversion to entrap the MIM, because otherwise, the Mad1 MIM motif would not bind rapidly. What seems more likely, is that for Mad1, the MIM motif is solvent exposed and readily accessible for Mad2 entrapment allowing spontaneous Mad2 conversion, while for Cdc20, self-association autoinhibits access of Mad2 to the MIM motif of Cdc20, and spontaneous formation of C-Mad2 only occurs when the MIM motif of Cdc20 is made accessible. This would suggest that the rate-limiting step of MCC assembly is not actually conversion of Mad2, but the accessibility of the Cdc20 MIM motif and further supports our previously mentioned hypothesis for 'breathing' of the C-terminal β-hairpin of Mad2. We suspect the reason why binding of 'empty' C-Mad2 to full-length Cdc20 is not accelerated by catalysts, is because the catalytic platform requires O-Mad2 binding to C-Mad2:Mad1 to properly position Cdc20 with respect to Mad2, and 'empty' C-Mad2 cannot bind to the catalytic platform because a Mad1:C-Mad2:C-Mad2 complex cannot exist (De Antoni *et al,* 2005).

Therefore, although using a slightly different model of understanding, it does seem likely that "Cdc20 catalyses its own incorporation into the MCC" as was suggested in Piano *et al*, 2021. This model fits well with the fact that nearly every mechanism of MCC catalysis

identified seems to be centred around bringing the MIM motif of Cdc20 in close-proximity to Mad2.

Ongoing Mad2 conversion work

As discussed above (Fig 6.1), we know the conformational rearrangements which occur between open and closed Mad2, but not the specific steps or their chronological sequence, and if any true intermediate states exist. Figuring out these mechanisms is key to understanding how the MCC is catalysed and whether Mad2 remodelling is directly catalysed. This includes, exploring, how the N-terminus of Mad2, including β1, is ejected to allow the C-terminal β-hairpin to swivel around and bind where the N-terminus was previously positioned. Additionally, is the N-terminus first displaced which then promotes the C-terminal β-hairpin to remodel, or does the remodelling of the β-hairpin eject the N-terminus? Further analysing the structure of monomeric O-Mad2 as compared to dimerized O-Mad2 would also be interesting. Dimerization of O-Mad2 with C-Mad2 of the $Mad1^{485-584}$ tetramer (lacking the $Mad1^{CTD}$ head domain) accelerates Mad2 conversion four-fold, albeit minimally compared to the whole catalytic platform (Piano et al, 2021). Additionally, O-Mad2 undergoes an unknown conformational rearrangement upon dimerising with C-Mad2 as seen by NMR spectroscopy (Mapelli *et al,* 2007). This would suggest that binding of O-Mad2 to C-Mad2, somehow promotes a more favourable conformation of Mad2 for conversion. Important insights could also be gained by further investigating the structure of 'empty' C-Mad2, especially in light of the recent work which showed the 'empty' C-Mad2 does not bind appreciably to full-length Cdc20 while O-Mad2 does (Piano *et al*, 2021; Mapelli *et al*, 2007).

The best way to explore these questions is likely through NMR, particularly as all previous crystal structures required either locking Mad2 in a particular state or truncating the flexible N- or C-termini, and the possibility that crystallographic packing promotes an artificially stabilised state. Nearly all Mad2 conversion studies using NMR were completed in the early 2000s, when the sensitivity of measurements was limited by sample concentration and buffer conditions. Since then significant improvements in NMR spectroscopy have been made (Barrett *et al*, 2013). This includes the introduction of stronger magnets, cryoprobes, improved pulse sequences (e.g. BEST-TROSY), and non-uniform sampling (NUS) data collection. Altogether these advancements have dramatically increased the sensitivity of NMR, which allows much faster data collection and the ability to study proteins at lower

concentrations, and more physiological conditions. Additionally, our understanding of the cellular mechanisms which promote Mad2 conversion and MCC assembly has significantly improved since the 2000s, allowing a better interpretation of the NMR data.

We have therefore been re-investigating the conversion of O-Mad2 into C-Mad2 using NMR to gain new insights into some of the questions posed above. Utilising several forms of O-Mad2, we now have the first complete backbone assignment of full-length O-Mad2 and will soon have this for both 'empty' and 'bound' C-Mad2. Interestingly, O-Mad2, 'empty' C-Mad2 and 'bound' C-Mad2 all give strikingly different NMR spectra (Appendix Fig 5). This suggests 'empty' C-Mad2 has a significantly different structural arrangement than C-Mad2 bound to $Cdc20^{MIM}$, which may explain why full-length Cdc20 does not bind to 'empty' C-Mad2 at an appreciable rate (Piano *et al*, 2021). We are also working to get a complete backbone assignment of labelled O-Mad2 bound to unlabelled C-Mad2 so that we can analyse how Mad2 dimerization enhances conversion. Additionally, current advancements in NMR spectroscopy, makes it possible to obtain near real-time structural information of Mad2 as it undergoes the conversion process, allowing us to investigate the specific sequence of conformational rearrangements which occur during Mad2 conversion.

Appendix

	Mad1^{CTD}-Bub1^{CD1} ($P2_12_12_1$)	**Mad1^{CTD}-Bub1^{CD1} ($P2_1$)**	**Mad1^{CTD}-Bub1^{CD1} ($P2_12_12$)**
PDB ID	7B1F	7B1H	7B1J
Data Collection	DLS i04	DLS i04	DLS i04
Wavelength (Å)	0.9795	0.9795	0.9795
Resolution range (Å)	40.25 - 1.75 (1.81 - 1.75)	39.43 - 2.4 (2.49 - 2.4)	34.76 - 2.90 (3.00 - 2.90)
Space group	$P2_12_12_1$	$P2_1$	$P2_12_12$
Unit cell (Å)	34.2 80.5 134.0 90.0° 90.0° 90.0°	34.63 132.34 82.75 90.0° 93.34° 90.0°	87.68 133.98 34.75 90.0° 90.0° 90.0°
Dimers per asymmetric unit	1	2	1
Total reflections	191826 (2738)	100346 (4893)	62788 (2992)
Unique reflections	33937 (1863)	28972 (2901)	9638 (454)
Multiplicity	5.6 (3.2)	3.5 (3.4)	3.6 (3.6)
Completeness (%)	88.7 (44.5)	99.6 (99.0)	100 (99.6)
Mean I/sigma(I)	16 (0.25)	14.5 (1.7)	25.9 (3.9)
Wilson B-factor (Å^2)	30	43	89.9
R-merge	0.05(1.97)	0.06 (0.78)	0.03 (0.47)
R-meas	0.06 (2.3)	0.07 (0.93)	0.04 (0.51)
R-pim	0.02 (1.2)	0.04 (0.50)	0.01 (0.20)
CC1/2	1.0 (0.30)	1.0 (0.68)	1.0 (.98)
Refinement			
Reflections used in refinement (N)	32886 (1294)	28946 (2898)	9541 (892)
Reflections used for R-free (N)	1569 (68)	1376 (110)	480 (47)
R-work	0.2558	0.2314	0.2618
R-free	0.2873	0.2806	0.2972
Non-hydrogen atoms (N)	2408	4542	2262
Protein residues (N)	282	565	282
RMS (bonds) (Å)	0.013	0.014	0.024
RMS (angles) (°)	1.52	1.90	2.33
Ramachandran favoured (%)	98.85	96.49	92.88
Ramachandran allowed (%)	1.15	3.33	6.37
Ramachandran outliers (%)	0.00	0.18	0.75
Rotamer outliers (%)	0.81	0.80	1.59
Molprobity Score	1.81	2.07	2.70
Average B-factor (Å^2)	56.95	61.78	104.52
Subunits (N)	4	8	4

Appendix Table 1. Data collection and refinement statistics for Mad1^{CTD}:Bub1^{CD1} complexes.
Statistics for the highest-resolution shell are shown in parentheses.

	i23 Data
Data Collection	DLS i23
Wavelength (Å)	2.7552
Resolution range (Å)	131 - 2.4 (2.49 - 2.40)
Space group	$P2_12_12_1$
Unit cell (Å)	34.58 84.56 131.89 90.0° 90.0° 90.0°
Dimers per asymmetric unit	1
Total reflections (N)	585078 (50188)
Unique reflections (N)	15780 (1601)
Multiplicity	37.1 (31.3)
Completeness (%)	99.4 (97.6)
Mean I/sigma(I)	29.5 (2.6)
Wilson B-factor ($Å^2$)	61
R-merge	0.078 (1.545)
R-meas	0.080 (1.595)
R-pim	0.013 (0.282)
CC1/2	1.0 (0.899)
Anomalous completeness (%)	99.1 (96.6)
Anomalous multiplicity	19.9 (16.6)
Mid slope	1.258

Appendix Table 2: Anomalous Data Statistics. *Statistics for the highest-resolution shell are shown in parentheses.*

Phospho-sites	Mad1Δ420-718	Mad1Δ420-718	Mad1Δ420-718	Mad1Δ597-718 (Mad1^{CTD})	Mad1Δ597-718 (Mad1^{CTD}	Comparison with published studies
Kinase	GST-Mps1	Mps1ΔKD	Okadaic Acid **	GST-Mps1	Mps1ΔKD	
T432	31/78	50/124				
S457			7/208			
S482			2/82			
S484		2/27	10/72			1
S485		1/389	5/80			1
S486		2/290	7/91			
S490		4/170	2/30			1
S494						1
T500	1/5	2/7				1
Y535						1
S538	17/121	8/46	1/5			1
T540	51/56	30/0				1
S546		2/104				1
T550	7/345	11/431				1
S551	5/11	4/17	1/4			1
S562			2/321			
S594		3/109				
S597		2/79				
S583		12/201				1
S598						1, 2
S610						2
T624						2
T644	1/200	1/212		2/300	1/103	1
T645		1/190	1/121			
S699	2/561	1/141				
S705		2/461				
T716	121/0	33/1		45/2	71/3	1, 2

Appendix Table 3: Phosphorylation sites within Mad1 constructs when phosphorylated by full-length GST-Mps1 or Mps1ΔKD in vitro. *The data obtained were compared with two prior studies from two different labs (1) Ji et al, 2017; (2) Ji et al, 2018. The orange shading shows the presence of phosphorylation and white indicates its absence. The fraction inside the orange shade is phosphorylated versus non-phosphorylated peptides found. No phosphorylation was found in any of the samples prior to treatment.*

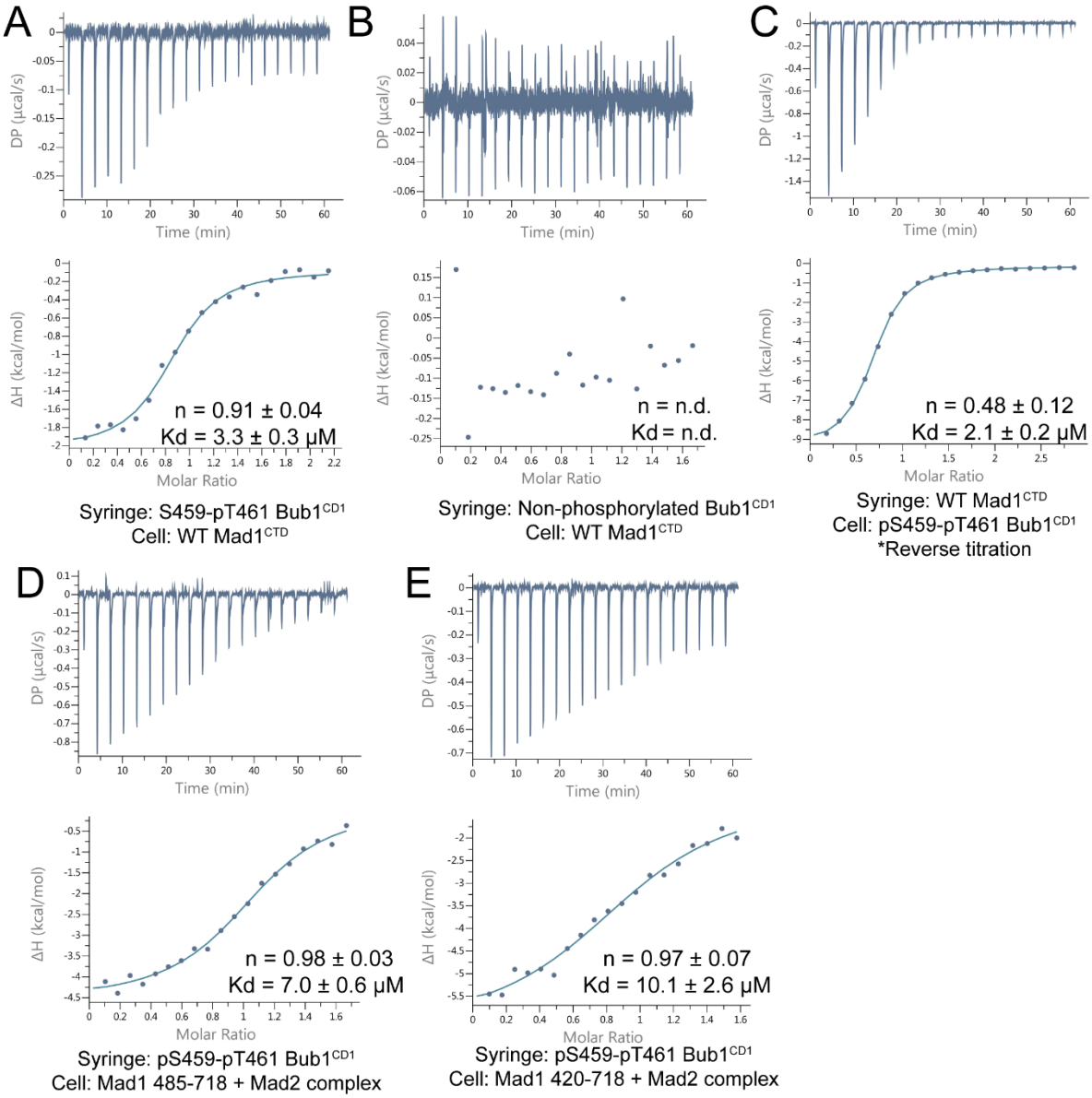

Appendix Figure 1: Isothermal calorimetry of Mad1^{CTD} and Bub1^{CD1}. *The K_D and stoichiometry (n) values were obtained by averaging at least three experiments. The reported error values are calculated standard deviations. Mad1^{CTD} was in the cell and Bub1^{CD1} peptide was in the syringe, unless otherwise noted.*

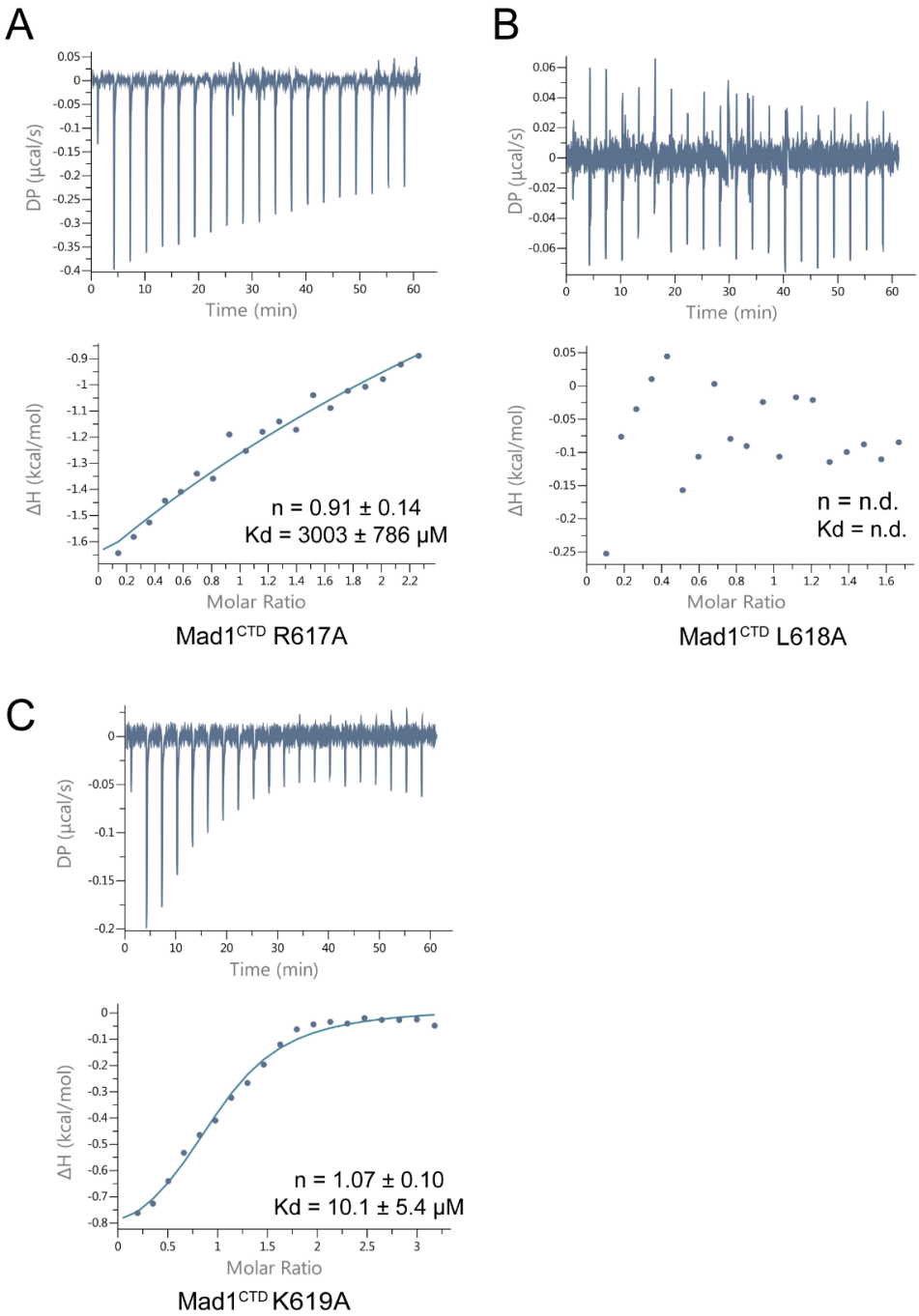

Appendix Figure 2: Isothermal calorimetry of Mad1^{CTD} RLK mutants. *The K_D and stoichiometry (n) values were obtained by averaging at least three experiments. The reported error values are calculated standard deviations. Mad1^{CTD} was in the cell and Bub1^{CD1} peptide was in the syringe, unless otherwise noted.*

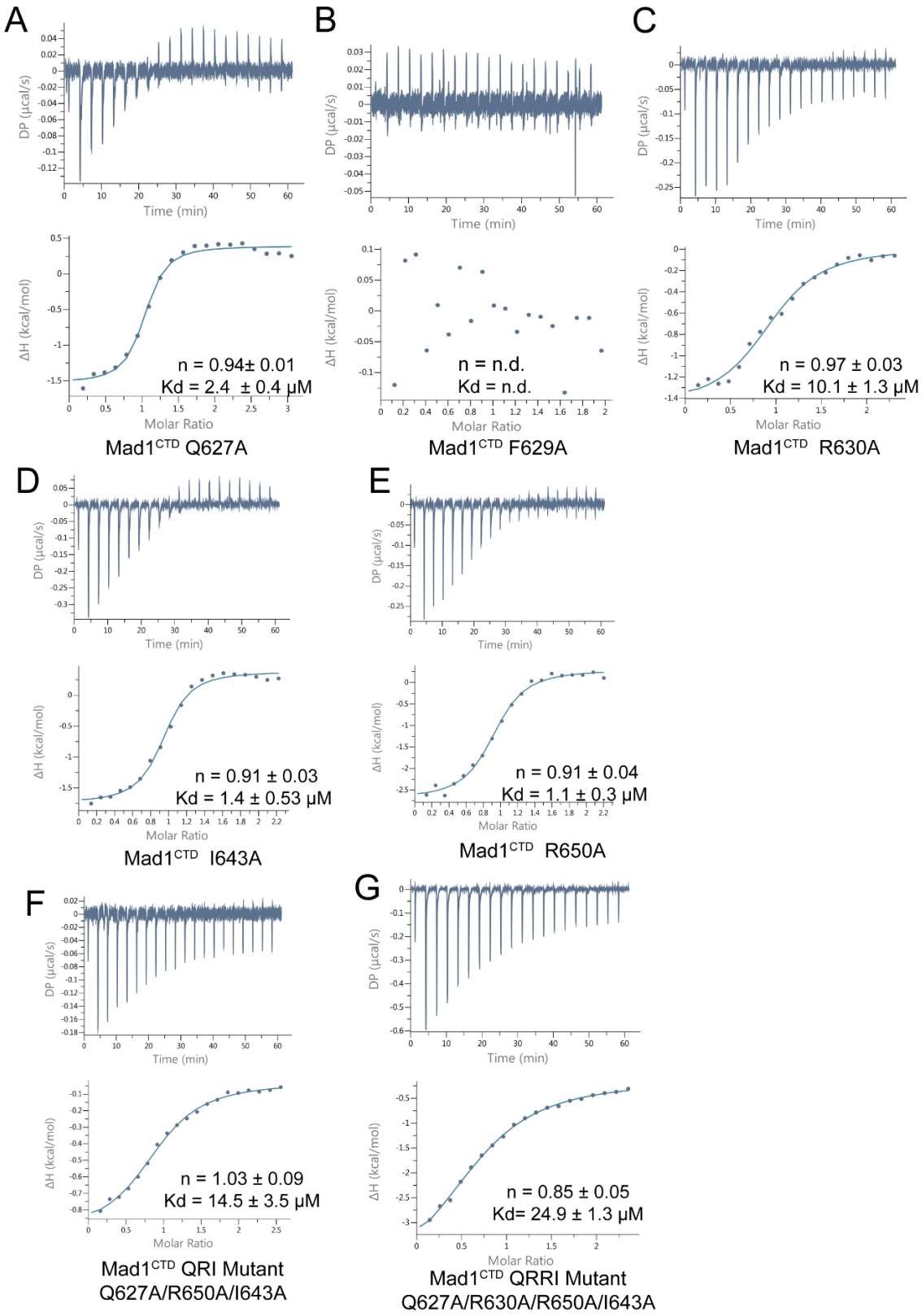

Appendix Figure 3: Isothermal calorimetry of Mad1^{CTD} head domain mutants. *The K_D and stoichiometry (n) values were obtained by averaging at least three experiments. The reported error values are calculated standard deviations. In each case, the Mad1^{CTD} mutant was in the cell and a doubly phosphorylated pThr461-pSer459 Bub1^{CD1} peptide was in the syringe.*

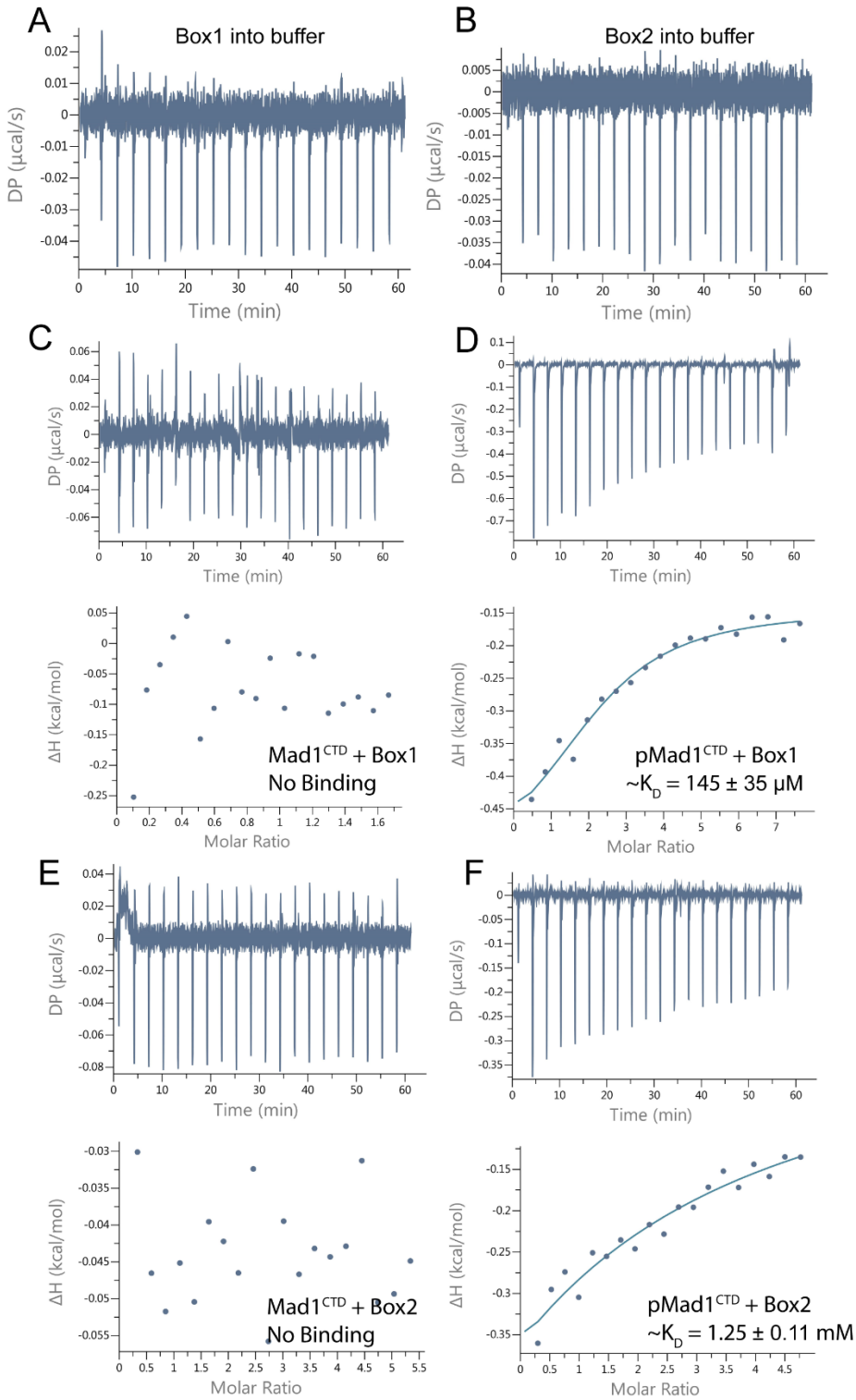

Appendix Figure 4: Isothermal calorimetry Box1 and Box2 binding to Mad1^{CTD}. *The K_D and stoichiometry (n) values were obtained by averaging at least three experiments. The reported error values are calculated standard deviations. In each case, Mad1^{CTD} was in the cell and the Box1 and Box2 peptides were titrated.*

	pT716 Mad1^{CTD}
Data Collection	
Wavelength (Å)	0.9795
Resolution range (Å)	22.19 - 1.87 (1.937 – 1.87)
Space group	$P6_5$
Unit cell (Å)	44.4 44.4 209.4 90.0° 90.0° 120.0°
Total reflections	190975
Unique reflections	19150 (1935)
Multiplicity	9.9 (7.0)
Completeness (%)	99.2 (88.30)
Mean I/sigma(I)	39.5 (8.8)
Wilson B-factor (Å^2)	17.34
R-merge	0.103
R-meas	0.109
R-pim	0.035
CC1/2	0.998 (0.869)
Refinement	
Reflections used in refinement (N)	18937 (1726)
Reflections used for R-free (N)	927 (97)
R-work	0.2300 (0.2767)
R-free	0.2702 (0.3778)
Non-hydrogen atoms (N)	1918
Protein residues (N)	237
RMS (bonds) (Å)	0.01
RMS (angles) (°)	1.11
Ramachandran favoured (%)	97.36
Ramachandran allowed (%)	2.64
Ramachandran outliers (%)	0.00
Rotamer outliers (%)	0.47
Molprobity Score	1.64
Average B-factor (Å^2)	25.9
Subunits (N)	4

Appendix Table 4: Data collection and refinement statistics for the phosphorylated Mad1^{CTD} crystal structure. *Statistics for the highest-resolution shell are shown in parentheses.*

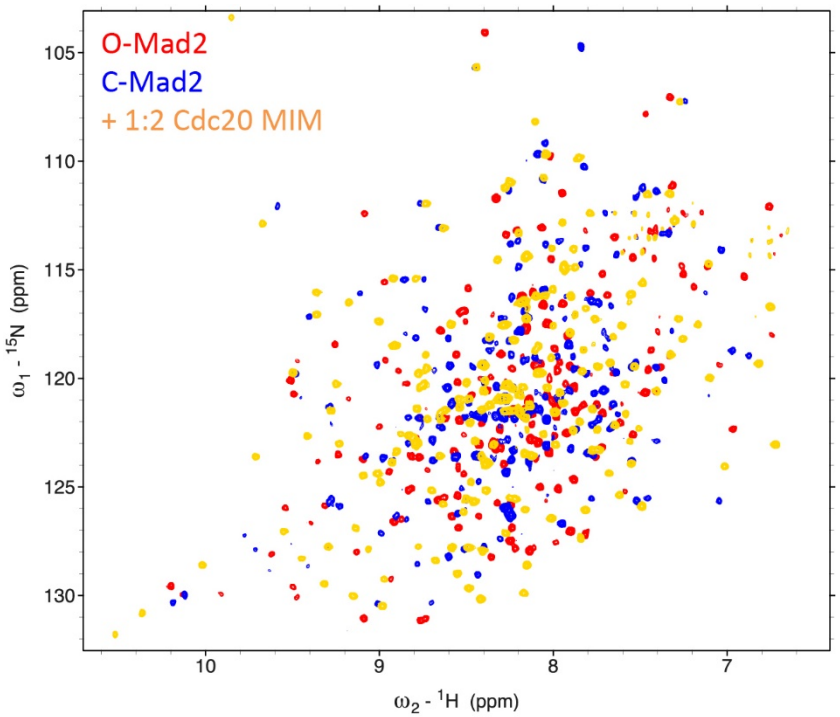

Appendix Figure 5: ^{1}H, ^{15}N-2D HSQC spectrum showing ^{15}N-labelled O-Mad2 (red), 'empty' C-Mad2 L13A (blue), and C-Mad2 bound to MIM peptide (yellow).

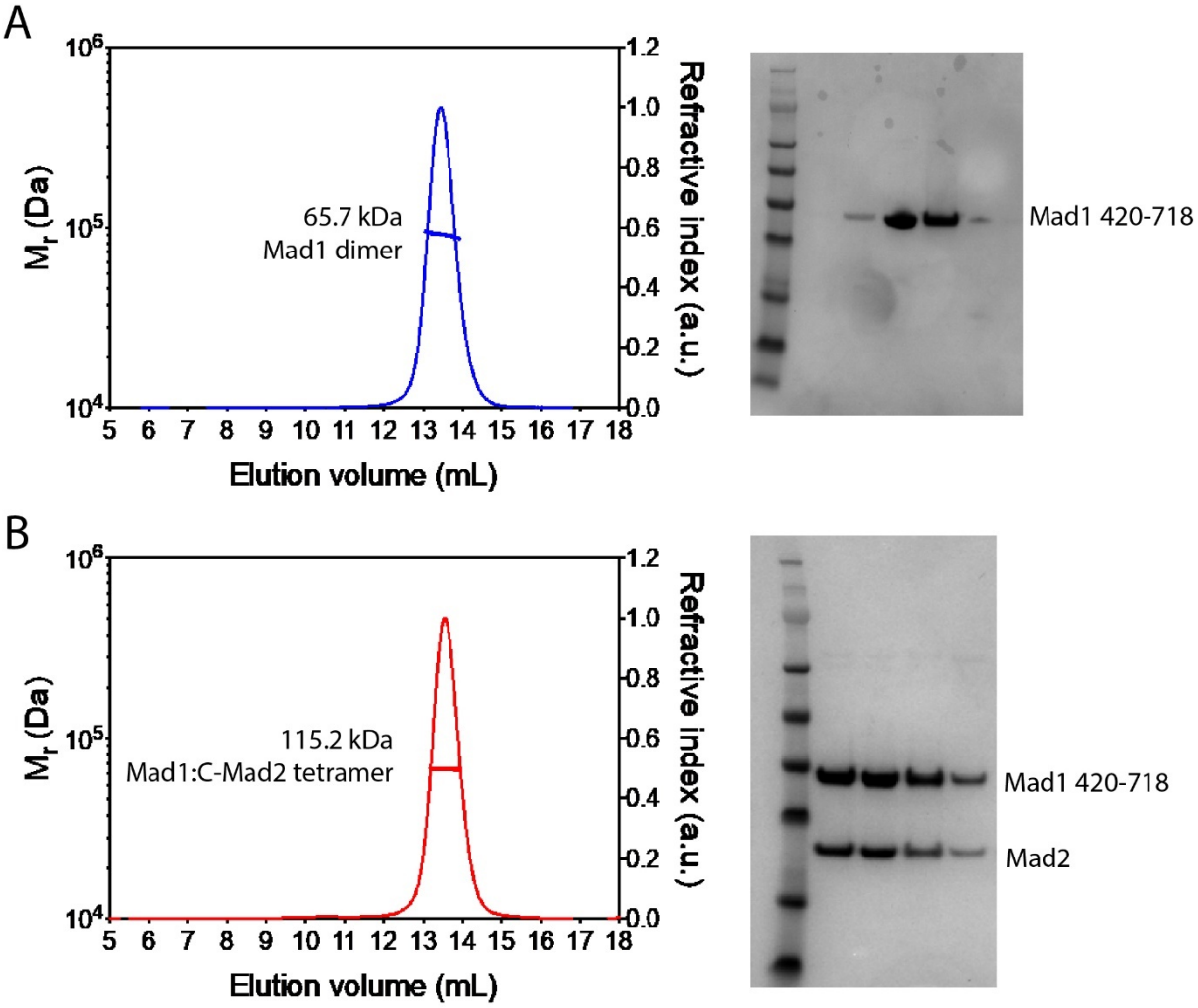

Appendix Fig 6: The MIM motif of dimeric Mad1 420-718 truncation readily entraps O-Mad2 to form Mad1:C-Mad2 tetramer. A) *SEC-MALS of Mad1 420-718 dimer purified using baculovirus expression.* ***B)*** *SEC-MALS of Mad1 420-718 dimer after incubation with O-Mad2 R133A on ice for 20 minutes.*

References

Abrieu A, Magnaghi-Jaulin L, Kahana JA, Peter M, Castro A, Vigneron S, Lorca T, Cleveland DW & Labbé JC (2001) Mps1 is a kinetochore-associated kinase essential for the vertebrate mitotic checkpoint. *Cell* 106: 83–93

Adrian M, Dubochet J, Lepault J & McDowall AW (1984) Cryo-electron microscopy of viruses. *Nature* 308: 32–36

Akera T, Goto Y, Sato M, Yamamoto M & Watanabe Y (2015) Mad1 promotes chromosome congression by anchoring a kinesin motor to the kinetochore. *Nat Cell Biol* 17: 1124–1133

Alfieri C, Chang L & Barford D (2018) Mechanism for remodelling of the cell cycle checkpoint protein MAD2 by the ATPase TRIP13. *Nature* 559: 274–278

Alfieri C, Chang L, Zhang Z, Yang J, Maslen S, Skehel M & Barford D (2016) Molecular basis of APC/C regulation by the spindle assembly checkpoint. *Nature* 536: 431–436

Alfieri C, Zhang S & Barford D (2017) Visualizing the complex functions and mechanisms of the anaphase promoting complex/cyclosome (APC/C). *Open Biol* 7

Alfonso-Pérez T, Hayward D, Holder J, Gruneberg U & Barr FA (2019) MAD1-dependent recruitment of CDK1-CCNB1 to kinetochores promotes spindle checkpoint signaling. *J Cell Biol* 218: 1108–1117

Allan LA, Camacho Reis M, Ciossani G, Huis in ‘t Veld PJ, Wohlgemuth S, Kops GJ, Musacchio A & Saurin AT (2020) Cyclin B1 scaffolds MAD 1 at the kinetochore corona to activate the mitotic checkpoint . *EMBO J* 39

Altschul SF, Gish W, Miller W, Myers EW & Lipman DJ (1990) Basic local alignment search tool. *J Mol Biol* 215: 403–410

Amin P (2019) Reconstituting the Spindle Assembly Checkpoint and the Signalling Roles of Mad1. *PhD Thesis*: https://era.ed.ac.uk/handle/1842/36115

Amor DJ, Kalitsis P, Sumer H & Choo KHA (2004) Building the centromere: From foundation proteins to 3D organization. *Trends Cell Biol* 14: 359–368

De Antoni A, Pearson CG, Cimini D, Canman JC, Sala V, Nezi L, Mapelli M, Sironi L, Faretta M, Salmon ED, *et al* (2005) The Mad1/Mad2 complex as a template for Mad2 activation in the spindle assembly checkpoint. *Curr Biol* 15: 214–225

Aravamudhan P, Goldfarb AA & Joglekar AP (2015) The kinetochore encodes a mechanical switch to disrupt spindle assembly checkpoint signalling. *Nat Cell Biol* 17: 868–879

Asghar A, Lajeunesse A, Dulla K, Combes G, Thebault P, Nigg EA & Elowe S (2015) Bub1 autophosphorylation feeds back to regulate kinetochore docking and promote localized substrate phosphorylation. *Nat Commun* 6: 1–14

Atherton-Fessler S, Parker LL, Geahlen RL & Piwnica-Worms H (1993) Mechanisms of p34cdc2 regulation. *Mol Cell Biol* 13: 1675–1685

Bai XC, Fernandez IS, McMullan G & Scheres SHW (2013) Ribosome structures to near-atomic resolution from thirty thousand cryo-EM particles. *Elife* 2013

Bajaj R, Bollen M, Peti W & Page R (2018) KNL1 Binding to PP1 and Microtubules Is Mutually Exclusive. *Structure* 26: 1327–1336.e4

Barisic M & Geley S (2011) Spindly switch controls anaphase: Spindly and RZZ functions in chromosome attachment and mitotic checkpoint control. *Cell Cycle* 10: 449–456

Barrett PJ, Chen J, Cho MK, Kim JH, Lu Z, Mathew S, Peng D, Song Y, Van Horn WD, Zhuang T, *et al* (2013) The quiet renaissance of protein nuclear magnetic resonance. *Biochemistry* 52: 1303–1320

Benzi G & Piatti S (2020) Silencing the spindle assembly checkpoint: Let’s play polo! *J Cell Biol* 219

Bi E, Maddox P, Lew DJ, Salmon ED, McMillan JN, Yeh E & Pringle JR (1998) Involvement of an actomyosin contractile ring in Saccharomyces cerevisiae cytokinesis. *J Cell Biol* 142: 1301–1312

Biggins S (2013) The composition, functions, and regulation of the budding yeast kinetochore. *Genetics* 194: 817–846

Biggins S & Murray AW (2001) The budding yeast protein kinase Ipl1/Aurora allows the absence of tension to activate the spindle checkpoint. *Genes Dev* 15: 3118–3129

Bokros M & Wang Y (2016) Spindle assembly checkpoint silencing and beyond. *Cell Cycle* 15: 1661–1662

Bolanos-Garcia VM & Blundell TL (2011) BUB1 and BUBR1: Multifaceted kinases of the cell cycle. *Trends Biochem Sci* 36: 141–150

Bollen M (2014) Kinetochore signalling: The KIss that MELTs Knl1. *Curr Biol* 24: R68–R70

Brady DM & Hardwick KG (2000) Complex formation between Mad1p, Bub1p and Bub3p is crucial for spindle checkpoint function

Brautigam CA (2015) Calculations and Publication-Quality Illustrations for Analytical Ultracentrifugation Data. In *Methods in Enzymology* pp 109–133. Academic Press Inc.

Buchan DWA & Jones DT (2019) The PSIPRED Protein Analysis Workbench: 20 years on. *Nucleic Acids Res* 47: W402–W407

Buffin E, Lefebvre C, Huang J, Gagou ME & Karess RE (2005) Recruitment of Mad2 to the kinetochore requires the Rod/Zw10 complex. *Curr Biol* 15: 856–861

Burton JL & Solomon MJ (2007) Mad3p, a pseudosubstrate inhibitor of APCCdc20 in the spindle assembly checkpoint. *Genes Dev* 21: 655–667

Calda G V., Lynch TR, Anderson R, Afreen S, Varma D & De Luca JG (2015) The RZZ complex requires the N-terminus of KNL1 to mediate optimal Mad1 kinetochore localization in human cells. *Open Biol* 5

Caldas G V. & DeLuca JG (2014) KNL1: Bringing order to the kinetochore. *Chromosoma* 123: 169–181

Chakrabartty A, Doig AJ & Baldwin RL (1993) Helix capping propensities in peptides parallel those in proteins. *Proc Natl Acad Sci U S A* 90: 11332–11336

Chang B, Partha S, Hofmann K, Lei M, Goebl M, Harper JW & Elledge SJ (1996) SKP1 connects cell cycle regulators to the ubiquitin proteolysis machinery through a novel motif, the F-box. *Cell* 86: 263–274

Chang L & Barford D (2014) Insights into the anaphase-promoting complex: A molecular machine that regulates mitosis. *Curr Opin Struct Biol* 29: 1–9

Chang L, Zhang Z, Yang J, McLaughlin SH & Barford D (2015) Atomic structure of the APC/C and its mechanism of protein ubiquitination. *Nature* 522: 450–454

Chao WCH, Kulkarni K, Zhang Z, Kong EH & Barford D (2012) Structure of the mitotic checkpoint complex. *Nature* 484: 208–213

Cheeseman IM, Anderson S, Jwa M, Green EM, Kang J seog, Yates JR, Chan CSM, Drubin DG & Barnes G (2002) Phospho-regulation of kinetochore-microtubule attachments by the Aurora kinase Ipl1p. *Cell* 111: 163–172

Cheeseman IM, Chappie JS, Wilson-Kubalek EM & Desai A (2006) The Conserved KMN Network Constitutes the Core Microtubule-Binding Site of the Kinetochore. *Cell* 127: 983–997

Chen RH, Shevchenko A, Mann M & Murray AW (1998) Spindle checkpoint protein Xmad1 recruits Xmad2 to unattached kinetochores. *J Cell Biol* 143: 283–295

Chen S, McMullan G, Faruqi AR, Murshudov GN, Short JM, Scheres SHW & Henderson R (2013) High-resolution noise substitution to measure overfitting and validate resolution in 3D structure determination by single particle electron cryomicroscopy.

Ultramicroscopy 135: 24–35
Chen ZL, Meng JM, Cao Y, Yin JL, Fang RQ, Fan SB, Liu C, Zeng WF, Ding YH, Tan D, *et al* (2019) A high-speed search engine pLink 2 with systematic evaluation for proteome-scale identification of cross-linked peptides. *Nat Commun* 10: 1–12
Chi YH, Haller K, Ward MD, Semmes OJ, Li Y & Jeang KT (2008) Requirements for protein phosphorylation and the kinase activity of polo-like kinase 1 (Plk1) for the kinetochore function of mitotic arrest deficiency protein 1 (Mad1). *J Biol Chem* 283: 35834–35844
Chung E & Chen RH (2002) Spindle checkpoint requires Mad1-bound and Mad1-free Mad2. *Mol Biol Cell* 13: 1501–1511
Ciferri C, Musacchio A & Petrovic A (2007) The Ndc80 complex: Hub of kinetochore activity. *FEBS Lett* 581: 2862–2869
Ciferri C, Pasqualato S, Screpanti E, Varetti G, Santaguida S, Dos Reis G, Maiolica A, Polka J, De Luca JG, De Wulf P, *et al* (2008) Implications for Kinetochore-Microtubule Attachment from the Structure of an Engineered Ndc80 Complex. *Cell* 133: 427–439
Clute P & Pines J (1999) Temporal and spatial control of cyclin B1 destruction in metaphase. *Nat Cell Biol* 1: 82–87
Cohen-Fix O, Peters JM, Kirschner MW & Koshland D (1996) Anaphase initiation in saccharomyces cerevisiae is controlled by the APC-dependent degradation of the anaphase inhibitor Pds1p. *Genes Dev* 10: 3081–3093
Cohen P (2002) The origins of protein phosphorylation. *Nat Cell Biol* 4
Cole JL, Lary JW, P. Moody T & Laue TM (2008) Analytical Ultracentrifugation: Sedimentation Velocity and Sedimentation Equilibrium. *Methods Cell Biol* 84: 143–179
Collin P, Nashchekina O, Walker R & Pines J (2013) The spindle assembly checkpoint works like a rheostat rather than a toggle switch. *Nat Cell Biol* 15: 1378–1385
Collins BM, Cubeddu L, Naidoo N, Harrop SJ, Kornfeld GD, Dawes IW, Curmi PMG & Mabbutt BC (2003) Homomeric ring assemblies of eukaryotic Sm proteins have affinity for both RNA and DNA: Crystal structure of an oligomeric complex of yeast SmF. *J Biol Chem* 278: 17291–17298
Combe CW, Fischer L & Rappsilber J (2015) xiNET: Cross-link network maps with residue resolution. *Mol Cell Proteomics* 14: 1137–1147
Combes G, Barysz H, Garand C, Gama Braga L, Alharbi I, Thebault P, Murakami L, Bryne DP, Stankovic S, Eyers PA, *et al* (2018) Mps1 Phosphorylates Its N-Terminal Extension to Relieve Autoinhibition and Activate the Spindle Assembly Checkpoint. *Curr Biol* 28: 872–883.e5
Cunha-Silva S, Osswald M, Goemann J, Barbosa J, Santos LM, Resende P, Bange T, Ferrás C, Sunkel CE & Conde C (2020) Mps1-mediated release of Mad1 from nuclear pores ensures the fidelity of chromosome segregation. *J Cell Biol* 219
Daub H, Olsen J V., Bairlein M, Gnad F, Oppermann FS, Körner R, Greff Z, Kéri G, Stemmann O & Mann M (2008) Kinase-Selective Enrichment Enables Quantitative Phosphoproteomics of the Kinome across the Cell Cycle. *Mol Cell* 31: 438–448
Davenport J, Harris LD & Goorha R (2006) Spindle checkpoint function requires Mad2-dependent Cdc20 binding to the Mad3 homology domain of BubR1. *Exp Cell Res* 312: 1831–1842
Défachelles L, Hainline SG, Menant A, Lee LA & Karess RE (2015a) A maternal effect rough deal mutation suggests that multiple pathways regulate Drosophila RZZ kinetochore recruitment. *J Cell Sci* 128: 1204–1216
Défachelles L, Raich N, Terracol R, Baudin X, Williams B, Goldberg M & Karess RE (2015b) RZZ and Mad1 dynamics in Drosophila mitosis. *Chromosom Res* 23: 333–342
Deibler RW & Kirschner MW (2010) Quantitative Reconstitution of Mitotic CDK1

Activation in Somatic Cell Extracts. *Mol Cell* 37: 753–767
DeLuca JG, Gall WE, Ciferri C, Cimini D, Musacchio A & Salmon ED (2006) Kinetochore Microtubule Dynamics and Attachment Stability Are Regulated by Hec1. *Cell* 127: 969–982
Diaz-Martinez LA, Tian W, Li B, Warrington R, Jia L, Brautigam CA, Luo X & Yu H (2015) The Cdc20-binding Phe box of the spindle checkpoint protein BubR1 maintains the mitotic checkpoint complex during mitosis. *J Biol Chem* 290: 2431–2443
Dick AE & Gerlich DW (2013) Kinetic framework of spindle assembly checkpoint signalling. *Nat Cell Biol* 15: 1370–1377
DiFiore B, Davey NE, Hagting A, Izawa D, Mansfeld J, Gibson TJ & Pines J (2015) The ABBA Motif binds APC/C activators and is shared by APC/C substrates and regulators. *Dev Cell* 32: 358–372
Dimitrova YN, Jenni S, Valverde R, Khin Y & Harrison SC (2016) Structure of the MIND Complex Defines a Regulatory Focus for Yeast Kinetochore Assembly. *Cell* 167: 1014–1027.e12
Ditchfield C, Johnson VL, Tighe A, Ellston R, Haworth C, Johnson T, Mortlock A, Keen N & Taylor SS (2003) Aurora B couples chromosome alignment with anaphase by targeting BubR1, Mad2, and Cenp-E to kinetochores. *J Cell Biol* 161: 267–280
Dobro MJ, Melanson LA, Jensen GJ & McDowall AW (2010) Plunge freezing for electron cryomicroscopy. *Methods Enzymol* 481: 63–82
Doerks T, Copley RR, Schultz J, Ponting CP & Bork P (2002) Systematic identification of novel protein domain families associated with nuclear functions. *Genome Res* 12: 47–56
Domingo-Sananes MR, Kapuy O, Hunt T & Novak B (2011) Switches and latches: A biochemical tug-of-war between the kinases and phosphatases that control mitosis. *Philos Trans R Soc B Biol Sci* 366: 3584–3594
Dou Z, Prifti D, Gui P, Liu X, Elowe S & Yao X (2019) Recent Progress on the Localization of the Spindle Assembly Checkpoint Machinery to Kinetochores. *Cells* 8: 278
Dou Z, von Schubert C, Körner R, Santamaria A, Elowe S & Nigg EA (2011) Quantitative mass spectrometry analysis reveals similar substrate consensus motif for human Mps1 kinase and Plk1. *PLoS One* 6: e18793
Dubochet J, Adrian M, Lepault J & McDowall AW (1985) Emerging techniques: Cryo-electron microscopy of vitrified biological specimens. *Trends Biochem Sci* 10: 143–146
Elledge SJ (1996) Cell cycle checkpoints: Preventing an identity crisis. *Science (80-)* 274: 1664–1672
Emsley P, Lohkamp B, Scott WG & Cowtan K (2010) Features and development of Coot. *Acta Crystallogr Sect D Biol Crystallogr* 66: 486–501
Erzberger JP & Berger JM (2006) Evolutionary relationships and structural mechanisms of AAA+ proteins. *Annu Rev Biophys Biomol Struct* 35: 93–114
Espeut J, Cheerambathur DK, Krenning L, Oegema K & Desai A (2012) Microtubule binding by KNL-1 contributes to spindle checkpoint silencing at the kinetochore. *J Cell Biol* 196: 469–482
Espeut J, Lara-Gonzalez P, Sassine M, Shiau AK, Desai A & Abrieu A (2015) Natural Loss of Mps1 Kinase in Nematodes Uncovers a Role for Polo-like Kinase 1 in Spindle Checkpoint Initiation. *Cell Rep* 12: 58–65
Evans P (2006) Scaling and assessment of data quality. *Acta Crystallogr Sect D Biol Crystallogr* 62: 72–82
Eytan E, Wang K, Miniowitz-Shemtov S, Sitry-Shevah D, Kaisari S, Yen TJ, Liu ST & Hershko A (2014) Disassembly of mitotic checkpoint complexes by the joint action of the AAA-ATPase TRIP13 and p31comet. *Proc Natl Acad Sci U S A* 111: 12019–12024
Faesen AC, Thanasoula M, Maffini S, Breit C, Müller F, Van Gerwen S, Bange T &

Musacchio A (2017) Basis of catalytic assembly of the mitotic checkpoint complex. *Nature* 542: 498–502

Fang G, Yu H & Kirschner MW (1998) The checkpoint protein MAD2 and the mitotic regulator CDC20 form a ternary complex with the anaphase-promoting complex to control anaphase initiation. *Genes Dev* 12: 1871–1883

Di Fiore B, Wurzenberger C, Davey NE & Pines J (2016) The Mitotic Checkpoint Complex Requires an Evolutionary Conserved Cassette to Bind and Inhibit Active APC/C. *Mol Cell* 64: 1144–1153

Fischer ES, Yu CWH, Bellini D, McLaughlin SH, Orr CM, Wagner A, Freund SM V & Barford D (2021) Molecular mechanism of Mad1 kinetochore targeting by phosphorylated Bub1. *EMBO Rep* 22

Foe IT, Foster SA, Cheung SK, Deluca SZ, Morgan DO & Toczyski DP (2011) Ubiquitination of Cdc20 by the APC occurs through an intramolecular mechanism. *Curr Biol* 21: 1870–1877

Foley EA & Kapoor TM (2013) Microtubule attachment and spindle assembly checkpoint signalling at the kinetochore. *Nat Rev Mol Cell Biol* 14: 25–37

Fujimitsu K, Grimaldi M & Yamano H (2016) Cyclin-dependent kinase 1-dependent activation of APC/C ubiquitin ligase. *Science (80-)* 352: 1121–1124

Fukagawa T & Earnshaw WC (2014) The centromere: Chromatin foundation for the kinetochore machinery. *Dev Cell* 30: 496–508

Gascoigne KE & Cheeseman IM (2013) CDK-dependent phosphorylation and nuclear exclusion coordinately control kinetochore assembly state. *J Cell Biol* 201: 23–32

Gassmann R, Carvalho A, Henzing AJ, Ruchaud S, Hudson DF, Honda R, Nigg EA, Gerloff DL & Earnshaw WC (2004) Borealin: A novel chromosomal passenger required for stability of the bipolar mitotic spindle. *J Cell Biol* 166: 179–191

Gassmann R, Holland AJ, Varma D, Wan X, Çivril F, Cleveland DW, Oegema K, Salmon ED & Desai A (2010) Removal of Spindly from microtubule-attached kinetochores controls spindle checkpoint silencing in human cells. *Genes Dev* 24: 957–971

Ghongane P, Kapanidou M, Asghar A, Elowe S & Bolanos-Garcia VM (2014) The dynamic protein Knl1 - a kinetochore rendezvous. *J Cell Sci* 127: 3415–3423

Gimona M, Djinovic-Carugo K, Kranewitter WJ & Winder SJ (2002) Functional plasticity of CH domains. *FEBS Lett* 513: 98–106

Glaeser RM (2016) Specimen Behavior in the Electron Beam. *Methods Enzymol* 579: 19–50

Gorrec F & Löwe J (2018) Automated protocols for macromolecular crystallization at the MRC laboratory of molecular biology. *J Vis Exp* 2018: 55790

Götze M, Iacobucci C, Ihling CH & Sinz A (2019) A Simple Cross-Linking/Mass Spectrometry Workflow for Studying System-wide Protein Interactions. *Anal Chem* 91: 10236–10244

Grieco D & Serpico AF (2020) Recent advances in understanding the role of Cdk1 in the Spindle Assembly Checkpoint. *F1000Research* 9

Griffis ER, Stuurman N & Vale RD (2007) Spindly, a novel protein essential for silencing the spindle assembly checkpoint, recruits dynein to the kinetochore. *J Cell Biol* 177: 1005–1015

Guimaraes GJ, Dong Y, McEwen BF & DeLuca JG (2008) Kinetochore-Microtubule Attachment Relies on the Disordered N-Terminal Tail Domain of Hec1. *Curr Biol* 18: 1778–1784

H. P. Erickson and Aaron Klug (1971) Measurement and compensation of defocusing and aberrations by Fourier processing of electron micrographs. *Philos Trans R Soc London B, Biol Sci* 261: 105–118

Hagting A, Den Elzen N, Vodermaier HC, Waizenegger IC, Peters JM & Pines J (2002)

Human securin proteolysis is controlled by the spindle checkpoint and reveals when the APC/C switches from activation by Cdc20 to Cdh1. *J Cell Biol* 157: 1125–1137

Han JS, Holland AJ, Fachinetti D, Kulukian A, Cetin B & Cleveland DW (2013) Catalytic assembly of the mitotic checkpoint inhibitor BubR1-Cdc20 by a Mad2-induced functional Switch in Cdc20. *Mol Cell* 51: 92–104

Hara M, Özkan E, Sun H, Yu H & Luo X (2015) Structure of an intermediate conformer of the spindle checkpoint protein Mad2. *Proc Natl Acad Sci U S A* 112: 11252–11257

Harashima H, Dissmeyer N & Schnittger A (2013) Cell cycle control across the eukaryotic kingdom. *Trends Cell Biol* 23: 345–356

Hardwick KG, Johnston RC, Smith DL & Murray AW (2000) MAD3 encodes a novel component of the spindle checkpoint which interacts with Bub3p, Cdc20p, and Mad2p. *J Cell Biol* 148: 871–882

Hardwick KG & Murray AW (1995) Mad1p, a phosphoprotein component of the spindle assembly checkpoint in budding yeast. *J Cell Biol* 131: 709–20

Hardwick KG, Weiss E, Luca FC, Winey M & Murray AW (1996) Activation of the budding yeast spindle assembly checkpoint without mitotic spindle disruption. *Science (80-)* 273: 953–956

Hartwell LH & Weinert TA (1989) Checkpoints: Controls that ensure the order of cell cycle events. *Science (80-)* 246: 629–634

Hauf S, Cole RW, LaTerra S, Zimmer C, Schnapp G, Walter R, Heckel A, Van Meel J, Rieder CL & Peters JM (2003) The small molecule Hesperadin reveals a role for Aurora B in correcting kinetochore-microtubule attachment and in maintaining the spindle assembly checkpoint. *J Cell Biol* 161: 281–294

He X, Patterson TE & Sazer S (1997) The Schizosaccharomyces pombe spindle checkpoint protein mad2p blocks anaphase and genetically interacts with the anaphase-promoting complex. *Proc Natl Acad Sci U S A* 94: 7965–7970

Van Heel M & Frank J (1981) Use of multivariate statistics in analysing the images of biological macromolecules. *Ultramicroscopy* 6: 187–194

Van Heel M, Gowen B, Matadeen R, Orlova E V., Finn R, Pape T, Cohen D, Stark H, Schmidt R, Schatz M, *et al* (2000) Single-particle electron cryo-microscopy: Towards atomic resolution. *Q Rev Biophys* 33: 307–369

Heinrich S, Sewart K, Windecker H, Langegger M, Schmidt N, Hustedt N & Hauf S (2014) Mad1 contribution to spindle assembly checkpoint signalling goes beyond presenting Mad2 at kinetochores. *EMBO Rep* 15: 291–298

Hershko A (1999) Mechanisms and regulation of the degradation of cyclin B. *Philos Trans R Soc B Biol Sci* 354: 1571–1576

Herzog F, Primorac I, Dube P, Lenart P, Sander B, Mechtler K, Stark H & Peters JM (2009) Structure of the anaphase-promoting complex/cyclosome interacting with a mitotic checkpoint complex. *Science (80-)* 323: 1477–1481

Hevler JF, Lukassen M V, Cabrera-Orefice A, Arnold S, Pronker MF, Franc V & Heck AJR (2021) Selective cross-linking of coinciding protein assemblies by in-gel cross-linking mass spectrometry. *EMBO J* 40: e106174

Hewitt L, Tighe A, Santaguida S, White AM, Jones CD, Musacchio A, Green S & Taylor SS (2010) Sustained Mps1 activity is required in mitosis to recruit O-Mad2 to the Mad1-C-Mad2 core complex. *J Cell Biol* 190: 25–34

Hiruma Y, Sacristan C, Pachis ST, Adamopoulos A, Kuijt T, Ubbink M, Von Castelmur E, Perrakis A & Kops GJPL (2015) Competition between MPS1 and microtubules at kinetochores regulates spindle checkpoint signaling. *Science (80-)* 348: 1264–1267

Hochegger H, Takeda S & Hunt T (2008) Cyclin-dependent kinases and cell-cycle transitions: Does one fit all? *Nat Rev Mol Cell Biol* 9: 910–916

Hol W, Duijnen P Van & Berendsen H (1978) The alpha-helix dipole and the properties of proteins. Cited by me. *Nature* 273: 443–446

Holland AJ & Cleveland DW (2012) Losing balance: The origin and impact of aneuploidy in cancer. *EMBO Rep* 13: 501–514

Honda R, Körner R & Nigg EA (2003) Exploring the functional interactions between Aurora B, INCENP, and survivin in mitosis. *Mol Biol Cell* 14: 3325–3341

Hornung P, Maier M, Alushin GM, Lander GC, Nogales E & Westermann S (2011) Molecular architecture and connectivity of the budding yeast Mtw1 kinetochore complex. *J Mol Biol* 405: 548–559

Huisin'T Veld PJ, Jeganathan S, Petrovic A, Singh P, John J, Krenn V, Weissmann F, Bange T & Musacchio A (2016) Molecular basis of outer kinetochore assembly on CENP-T. *Elife* 5

Hwang LH, Lau LF, Smith DL, Mistrot CA, Hardwick KG, Hwang ES, Amon A & Murray AW (1998) Budding yeast Cdc20: A target of the spindle checkpoint. *Science (80-)* 279: 1041–1044

Ito D, Saito Y & Matsumoto T (2012) Centromere-tethered Mps1 pombe homolog (Mph1) kinase is a sufficient marker for recruitment of the spindle checkpoint protein Bub1, but not Mad1. *Proc Natl Acad Sci U S A* 109: 209–214

Izawa D & Pines J (2012) Mad2 and the APC/C compete for the same site on Cdc20 to ensure proper chromosome segregation. *J Cell Biol* 199: 27–37

Izawa D & Pines J (2015) The mitotic checkpoint complex binds a second CDC20 to inhibit active APC/C. *Nature* 517: 631–634

Jancarik J & Kim SH (1991) Sparse matrix sampling. A screening method for crystallization of proteins. *J Appl Crystallogr* 24: 409–411

Jang JK, Messina L, Erdman MB, Arbel T & Hawley RS (1995) Induction of metaphase arrest in Drosophila oocytes by chiasma-based kinetochore tension. *Science (80-)* 268: 1917–1919

Jelluma N, Dansen TB, Sliedrecht T, Kwiatkowski NP & Kops GJPL (2010) Release of Mps1 from kinetochores is crucial for timely anaphase onset. *J Cell Biol* 191: 281–290

Ji W, Luo Y, Ahmad E & Liu ST (2018) Direct interactions of mitotic arrest deficient 1 (MAD1) domains with each other and MAD2 conformers are required for mitotic checkpoint signaling. *J Biol Chem* 293: 484–496

Ji Z, Gao H, Jia L, Li B & Yu H (2017) A sequential multi-target Mps1 phosphorylation cascade promotes spindle checkpoint signaling. *Elife* 6: e22513

Ji Z, Gao H & Yu H (2015) Kinetochore attachment sensed by competitive Mps1 and microtubule binding to Ndc80C. *Science (80-)* 348: 1260–1264

Jia L, Li B & Yu H (2016) The Bub1-Plk1 kinase complex promotes spindle checkpoint signalling through Cdc20 phosphorylation. *Nat Commun* 7

Jones DT (1999) Protein secondary structure prediction based on position-specific scoring matrices. *J Mol Biol* 292: 195–202

Jumper J, Evans R, Pritzel A, Green T, Figurnov M, Ronneberger O, Tunyasuvunakool K, Bates R, Žídek A, Potapenko A, *et al* (2021) Highly accurate protein structure prediction with AlphaFold. *Nat 2021 5967873* 596: 583–589

Jung YS & Zweckstetter M (2004) Backbone assignment of proteins with known structure using residual dipolar couplings. *J Biomol NMR* 30: 25–35

Kabsch W (2010) XDS. *Acta Crystallogr D Biol Crystallogr* 66: 125–32

Kallio MJ, McCleland ML, Todd Stukenberg P & Gorbsky GJ (2002) Inhibition of Aurora B kinase blocks chromosome segregation, overrides the spindle checkpoint, and perturbs microtubule dynamics in mitosis. *Curr Biol* 12: 900–905

Kang J, Yang M, Li B, Qi W, Zhang C, Shokat KM, Tomchick DR, Machius M & Yu H

(2008) Structure and Substrate Recruitment of the Human Spindle Checkpoint Kinase Bub1. *Mol Cell* 32: 394–405

Karess R (2005) Rod-Zw10-Zwilch: A key player in the spindle checkpoint. *Trends Cell Biol* 15: 386–392

Keeler J (2010) Understanding NMR Spectroscopy, 2nd Edition | Wiley. *Wiley*: 190–200

Keller A, Nesvizhskii AI, Kolker E & Aebersold R (2002) Empirical statistical model to estimate the accuracy of peptide identifications made by MS/MS and database search. *Anal Chem* 74: 5383–5392

Kelley LA, Mezulis S, Yates CM, Wass MN & Sternberg MJE (2015) The Phyre2 web portal for protein modeling, prediction and analysis. *Nat Protoc* 10: 845–858

Khodjakov A & Pines J (2010) Centromere tension: A divisive issue. *Nat Cell Biol* 12: 919–923

Khodjakov A & Rieder CL (2006) Imaging the division process in living tissue culture cells. *Methods* 38: 2–16

Kilmartin J V. (2014) Lessons from yeast: the spindle pole body and the centrosome. *Philos Trans R Soc B Biol Sci* 369

Kim S, Sun H, Tomchick DR, Yu H & Luo X (2012) Structure of human Mad1 C-terminal domain reveals its involvement in kinetochore targeting. *Proc Natl Acad Sci U S A* 109: 6549–6554

Kim S & Yu H (2015) Multiple assembly mechanisms anchor the KMN spindle checkpoint platform at human mitotic kinetochores. *J Cell Biol* 208: 181–196

King RW, Peters JM, Tugendreich S, Rolfe M, Hieter P & Kirschner MW (1995) A 20s complex containing CDC27 and CDC16 catalyzes the mitosis-specific conjugation of ubiquitin to cyclin B. *Cell* 81: 279–288

Kiyomitsu T, Obuse C & Yanagida M (2007) Human Blinkin/AF15q14 Is Required for Chromosome Alignment and the Mitotic Checkpoint through Direct Interaction with Bub1 and BubR1. *Dev Cell* 13: 663–676

Kjaergaard M & Poulsen FM (2011) Sequence correction of random coil chemical shifts: Correlation between neighbor correction factors and changes in the Ramachandran distribution. *J Biomol NMR* 50: 157–165

Kline SL, Cheeseman IM, Hori T, Fukagawa T & Desai A (2006) The human Mis12 complex is required for kinetochore assembly and proper chromosome segregation. *J Cell Biol* 173: 9–17

Klykov O, Steigenberger B, Pektaş S, Fasci D, Heck AJR & Scheltema RA (2018) Efficient and robust proteome-wide approaches for cross-linking mass spectrometry. *Nat Protoc* 13: 2964–2990

Koch LB, Opoku KN, Deng Y, Barber A, Littleton AJ, London N, Biggins S & Asbury CL (2019) Autophosphorylation is sufficient to release Mps1 kinase from native kinetochores. *Proc Natl Acad Sci U S A* 116: 17355–17360

Kops GJPL, Kim Y, Weaver BAA, Mao Y, McLeod I, Yates JR, Tagaya M & Cleveland DW (2005) ZW10 links mitotic checkpoint signaling to the structural kinetochore. *J Cell Biol* 169: 49–60

Kops GJPL & Shah J V. (2012) Connecting up and clearing out: How kinetochore attachment silences the spindle assembly checkpoint. *Chromosoma* 121: 509–525

Kragelund BB & Skriver K (2020) Intrinsically Disordered Proteins: Methods and Protocols, Chapter 27 1st ed. Springer

Krenn V & Musacchio A (2015) The Aurora B kinase in chromosome bi-orientation and spindle checkpoint signaling. *Front Oncol* 5

Krenn V, Overlack K, Primorac I, Van Gerwen S & Musacchio A (2014) KI motifs of human Knl1 enhance assembly of comprehensive spindle checkpoint complexes around MELT

repeats. *Curr Biol* 24: 29–39
Krenn V, Wehenkel A, Li X, Santaguida S & Musacchio A (2012) Structural analysis reveals features of the spindle checkpoint kinase Bub1-kinetochore subunit Knl1 interaction. *J Cell Biol* 196: 451–467
Kruse T, Larsen MSY, Sedgwick GG, Sigurdsson JO, Streicher W, Olsen J V. & Nilsson J (2014) A direct role of Mad1 in the spindle assembly checkpoint beyond Mad2 kinetochore recruitment. *EMBO Rep* 15: 282–290
Kuijt TEF, Omerzu M, Saurin AT & Kops GJPL (2014) Conditional targeting of MAD1 to kinetochores is sufficient to reactivate the spindle assembly checkpoint in metaphase. *Chromosoma* 123: 471–480
Kulukian A, Han JS & Cleveland DW (2009) Unattached Kinetochores Catalyze Production of an Anaphase Inhibitor that Requires a Mad2 Template to Prime Cdc20 for BubR1 Binding. *Dev Cell* 16: 105–117
Lara-Gonzalez P, Kim T, Oegema K, Corbett K & Desai A (2021a) A tripartite mechanism catalyzes Mad2-Cdc20 assembly at unattached kinetochores. *Science (80-)* 371: 64–67
Lara-Gonzalez P, Pines J & Desai A (2021b) Spindle assembly checkpoint activation and silencing at kinetochores. *Semin Cell Dev Biol* 117: 86–98
Lara-Gonzalez P, Scott MIF, Diez M, Sen O & Taylor SS (2011) Bubr1 blocks substrate recruitment to the APC/C in a KEN-box-dependent manner. *J Cell Sci* 124: 4332–4345
Larkin MA, Blackshields G, Brown NP, Chenna R, Mcgettigan PA, McWilliam H, Valentin F, Wallace IM, Wilm A, Lopez R, *et al* (2007) Clustal W and Clustal X version 2.0. *Bioinformatics* 23: 2947–2948
Larsen NA, Al-Bassam J, Wei RR & Harrison SC (2007) Structural analysis of Bub3 interactions in the mitotic spindle checkpoint. *Proc Natl Acad Sci U S A* 104: 1201–1206
Larsen NA & Harrison SC (2004) Crystal structure of the spindle assembly checkpoint protein Bub3. *J Mol Biol* 344: 885–892
Lee S, Thebault P, Freschi L, Beaufils S, Blundell TL, Landry CR, Bolanos-Garcia VM & Elowe S (2012) Characterization of spindle checkpoint kinase mps1 reveals domain with functional and structural similarities to tetratricopeptide repeat motifs of Bub1 and BubR1 checkpoint kinases. *J Biol Chem* 287: 5988–6001
Lee W, Tonelli M & Markley JL (2015) NMRFAM-SPARKY: Enhanced software for biomolecular NMR spectroscopy. *Bioinformatics* 31: 1325–1327
Leitner A, Joachimiak LA, Unverdorben P, Walzthoeni T, Frydman J, Förster F & Aebersold R (2014) Chemical cross-linking/mass spectrometry targeting acidic residues in proteins and protein complexes. *Proc Natl Acad Sci U S A* 111: 9455–9460
Leitner A, Walzthoeni T, Kahraman A, Herzog F, Rinner O, Beck M & Aebersold R (2010) Probing native protein structures by chemical cross-linking, mass spectrometry, and bioinformatics. *Mol Cell Proteomics* 9: 1634–1649
Leontiou I, London N, May KM, Ma Y, Grzesiak L, Medina-Pritchard B, Amin P, Jeyaprakash AA, Biggins S & Hardwick KG (2019) The Bub1-TPR Domain Interacts Directly with Mad3 to Generate Robust Spindle Checkpoint Arrest. *Curr Biol* 29: 2407–2414.e7
Lepault J, Booy FP & Dubochet J (1983) Electron microscopy of frozen biological suspensions. *J Microsc* 129: 89–102
Lesage B, Qian J & Bollen M (2011) Spindle checkpoint silencing: PP1 tips the balance. *Curr Biol* 21
Li R & Murray AW (1991) Feedback control of mitosis in budding yeast. *Cell* 66: 519–531
Li X & Nicklas RB (1995) Mitotic forces control a cell-cycle checkpoint. *Nature* 373: 630–632
Li Y, Gorbea C, Mahaffey D, Rechsteiner M & Benezra R (1997) MAD2 associates with the

cyclosome/anaphase-promoting complex and inhibits its activity. *Proc Natl Acad Sci U S A* 94: 12431–12436

Liebschner D, Afonine P V., Baker ML, Bunkoczi G, Chen VB, Croll TI, Hintze B, Hung LW, Jain S, McCoy AJ, *et al* (2019) Macromolecular structure determination using X-rays, neutrons and electrons: Recent developments in Phenix. *Acta Crystallogr Sect D Struct Biol* 75: 861–877

Lim S & Kaldis P (2013) Cdks, cyclins and CKIs: Roles beyond cell cycle regulation. *Dev* 140: 3079–3093

Lince-Faria M, Maffini S, Orr B, Ding Y, Florindo C, Sunkel CE, Tavares Á, Johansen J, Johansen KM & Maiato H (2009) Spatiotemporal control of mitosis by the conserved spindle matrix protein megator. *J Cell Biol* 184: 647–657

Lindqvist A, Rodríguez-Bravo V & Medema RH (2009) The decision to enter mitosis: feedback and redundancy in the mitotic entry network. *J Cell Biol* 185: 193–202

Lischetti T & Nilsson J (2015) Regulation of mitotic progression by the spindle assembly checkpoint. *Mol Cell Oncol* 2: e970484.

Lischetti T, Zhang G, Sedgwick GG, Bolanos-Garcia VM & Nilsson J (2014) The internal Cdc20 binding site in BubR1 facilitates both spindle assembly checkpoint signalling and silencing. *Nat Commun* 5: 1–12

Liu D, Vleugel M, Backer CB, Hori T, Fukagawa T, Cheeseman IM & Lampson MA (2010) Regulated targeting of protein phosphatase 1 to the outer kinetochore by KNL1 opposes Aurora B kinase. *J Cell Biol* 188: 809–820

Liu S-T & Zhang H (2016) The mitotic checkpoint complex (MCC): looking back and forth after 15 years. *AIMS Mol Sci* 3: 597–634

Liu ST, Hittle JC, Jablonski SA, Campbell MS, Yoda K & Yen TJ (2003) Human CENP-I specifies localization of CENP-F, MAD1 and MAD2 to kinetochores and is essential for mitosis. *Nat Cell Biol* 5: 341–345

London N & Biggins S (2014a) Signalling dynamics in the spindle checkpoint response. *Nat Rev Mol Cell Biol* 15: 735–747

London N & Biggins S (2014b) Mad1 kinetochore recruitment by Mps1-mediated phosphorylation of Bub1 signals the spindle checkpoint. *Genes Dev* 28: 140–152

London N, Ceto S, Ranish JA & Biggins S (2012) Phosphoregulation of Spc105 by Mps1 and PP1 regulates Bub1 localization to kinetochores. *Curr Biol* 22: 900–906

Lou X, Fang G, Coldiron M, Lin Y, Yu H, Kirschner MW & Wagner G (2000) Structure of the Mad2 spindle assembly checkpoint protein and its interaction with Cdc20. *Nat Struct Biol* 7: 224–229

Lou Y, Yao J, Zereshki A, Dou Z, Ahmed K, Wang H, Hu J, Wang Y & Yao X (2004) NEK2A Interacts with MAD1 and Possibly Functions as a Novel Integrator of the Spindle Checkpoint Signaling. *J Biol Chem* 279: 20049–20057

Luo X, Tang Z, Rizo J & Yu H (2002) The Mad2 spindle checkpoint protein undergoes similar major conformational changes upon binding to either Mad1 or Cdc20. *Mol Cell* 9: 59–71

Luo X, Tang Z, Xia G, Wassmann K, Matsumoto T, Rizo J & Yu H (2004) The Mad2 spindle checkpoint protein has two distinct natively folded states. *Nat Struct Mol Biol* 11: 338–345

Luo X & Yu H (2008) Protein Metamorphosis: The Two-State Behavior of Mad2. *Structure* 16: 1616–1625

Lupas A, Van Dyke M & Stock J (1991) Predicting coiled coils from protein sequences. *Science (80-)* 252: 1162–1164

Maciejowski J, George KA, Terret ME, Zhang C, Shokat KM & Jallepalli P V. (2010) Mps1 directs the assembly of Cdc20 inhibitory complexes during interphase and mitosis to

control M phase timing and spindle checkpoint signaling. *J Cell Biol* 190: 89–100
Maiato H, DeLuca J, Salmon ED & Earnshaw WC (2004) The dynamic kinetochore-microtubule interface. *J Cell Sci* 117: 5461–5477
Maldonado M & Kapoor TM (2011) Constitutive Mad1 targeting to kinetochores uncouples checkpoint signalling from chromosome biorientation. *Nat Cell Biol* 13: 475–483
Mandt S, Hof Fman MD & Blei DM (2017) Stochastic gradient descent as approximate Bayesian inference. *J Mach Learn Res* 18: 1–35
Mapelli M, Massimiliano L, Santaguida S & Musacchio A (2007) The Mad2 Conformational Dimer: Structure and Implications for the Spindle Assembly Checkpoint. *Cell* 131: 730–743
Maresca TJ & Salmon ED (2010) Welcome to a new kind of tension: Translating kinetochore mechanics into a wait-anaphase signal. *J Cell Sci* 123: 825–835
Mariani V, Biasini M, Barbato A & Schwede T (2013) IDDT: A local superposition-free score for comparing protein structures and models using distance difference tests. *Bioinformatics* 29: 2722–2728
Marion D (2013) An introduction to biological NMR spectroscopy. *Mol Cell Proteomics* 12: 3006–3025
Martin-Lluesma S, Stucke VM & Nigg EA (2002) Role of Hec1 in spindle checkpoint signaling and kinetochore recruitment of Mad1/Mad2. *Science (80-)* 297: 2267–2270
Maskell DP, Hu XW & Singleton MR (2010) Molecular architecture and assembly of the yeast kinetochore MIND complex. *J Cell Biol* 190: 823–834
Matson DR & Stukenberg PT (2014) CENP-I and Aurora B act as a molecular switch that ties RZZ/Mad1 recruitment to kinetochore attachment status. *J Cell Biol* 205: 541–554
Mayzel M, Rosenlöw J, Isaksson L & Orekhov VY (2014) Time-resolved multidimensional NMR with non-uniform sampling. *J Biomol NMR* 58: 129–139
McCully EK & Robinow CF (1971) Mitosis in the fission yeast Schizosaccharomyces pombe: a comparative study with light and electron microscopy. *J Cell Sci* 9: 475–507
McKinley KL & Cheeseman IM (2016) The molecular basis for centromere identity and function. *Nat Rev Mol Cell Biol* 17: 16–29
McPherson A & Gavira JA (2014) Introduction to protein crystallization. *Acta Crystallogr Sect FStructural Biol Commun* 70: 2–20
Mendes ML, Fischer L, Chen ZA, Barbon M, O'Reilly FJ, Giese SH, Bohlke-Schneider M, Belsom A, Dau T, Combe CW, *et al* (2019) An integrated workflow for crosslinking mass spectrometry. *Mol Syst Biol* 15: e8994
Mielke SP & Krishnan V V. (2009) Characterization of protein secondary structure from NMR chemical shifts. *Prog Nucl Magn Reson Spectrosc* 54: 141–165
Mirdita M, Ovchinnikov S & Steinegger M (2021) ColabFold - Making protein folding accessible to all. *bioRxiv*: 2021.08.15.456425
Moyle MW, Kim T, Hattersley N, Espeut J, Cheerambathur DK, Oegema K & Desai A (2014) A Bub1-Mad1 interaction targets the Mad1-Mad2 complex to unattached kinetochores to initiate the spindle checkpoint. *J Cell Biol* 204: 647–657
Murray AW (1992) Creative blocks: Cell-cycle checkpoints and feedback controls. *Nature* 359: 599–604
Musacchio A (2015) The Molecular Biology of Spindle Assembly Checkpoint Signaling Dynamics. *Curr Biol* 25: R1002–R1018
Musacchio A & Desai A (2017) A molecular view of kinetochore assembly and function. *Biology (Basel)* 6: 5
Musacchio A & Salmon ED (2007) The spindle-assembly checkpoint in space and time. *Nat Rev Mol Cell Biol* 8: 379–393
Nameki N, Yoneyama M, Koshiba S, Tochio N, Inoue M, Seki E, Matsuda T, Tomo Y,

Harada T, Saito K, *et al* (2004) Solution structure of the RWD domain of the mouse GCN2 protein. *Protein Sci* 13: 2089–2100

Neumann P, Dickmanns A & Ficner R (2018) Validating Resolution Revolution. *Structure* 26: 785–795.e4

Nezi L & Musacchio A (2009) Sister chromatid tension and the spindle assembly checkpoint. *Curr Opin Cell Biol* 21: 785–795

Nezi L, Rancati G, De Antoni A, Pasqualato S, Piatti S & Musacchio A (2006) Accumulation of Mad2-Cdc20 complex during spindle checkpoint activation requires binding of open and closed conformers of Mad2 in Saccharomyces cerevisiae. *J Cell Biol* 174: 39–51

Nicklas RB & Koch CA (1969) Chromosome micromanipulation. 3. Spindle fiber tension and the reorientation of mal-oriented chromosomes. *J Cell Biol* 43: 40–50

Nijenhuis W, Von Castelmur E, Littler D, De Marco V, Tromer E, Vleugel M, Van Osch MHJ, Snel B, Perrakis A & Kops GJPL (2013) A TPR domain-containing N-terminal module of MPS1 is required for its kinetochore localization by Aurora B. *J Cell Biol* 201: 217–231

Nishino T, Rago F, Hori T, Tomii K, Cheeseman IM & Fukagawa T (2013) CENP-T provides a structural platform for outer kinetochore assembly. *EMBO J* 32: 424–436

Overlack K, Primorac I, Vleugel M, Krenn V, Maffini S, Hoffmann I, Kops GJPL & Musacchio A (2015) A molecular basis for the differential roles of Bubl and BubR1 in the spindle assembly checkpoint. *Elife* 2015

Páez-Pereda M & Arzt E (2015) Function and structure of the RWD domain. *J Biol Chem* 290: 20627

Palmer DK, O'Day K, Wener MH, Andrews BS & Margolis RL (1987) A 17-kD centromere protein (CENP-A) copurifies with nucleosome core particles and with histones. *J Cell Biol* 104: 805–815

Passmore LA & Russo CJ (2016) Specimen Preparation for High-Resolution Cryo-EM. *Methods Enzymol* 579: 51–86

Patton EE, Willems AR, Sa D, Kuras L, Thomas D, Craig KL & Tyers M (1998) Cdc53 is a scaffold protein for multiple Cdc34/Skp1/F-box protein complexes that regulate cell division and methionine biosynthesis in yeast. *Genes Dev* 12: 692–705

Penczek PA, Grassucci RA & Frank J (1994) The ribosome at improved resolution: New techniques for merging and orientation refinement in 3D cryo-electron microscopy of biological particles. *Ultramicroscopy* 53: 251–270

Perkins DN, Pappin DJC, Creasy DM & Cottrell JS (1999) Probability-based protein identification by searching sequence databases using mass spectrometry data. *Electrophoresis* 20: 3551–3567

Perpelescu M & Fukagawa T (2011) The ABCs of CENPs. *Chromosoma* 120: 425–446

Perry JA & Kornbluth S (2007) Cdc25 and Wee1: Analogous opposites? *Cell Div* 2: 1–12

Pervushin K (2000) Impact of transverse relaxation optimized spectroscopy (TROSY) on NMR as a technique in structural biology. *Q Rev Biophys* 33: 161–197

Pesin JA & Orr-Weaver TL (2008) Regulation of APC/C activators in mitosis and meiosis. *Annu Rev Cell Dev Biol* 24: 475–499

Petrovic A, Keller J, Liu Y, Overlack K, John J, Dimitrova YN, Jenni S, van Gerwen S, Stege P, Wohlgemuth S, *et al* (2016) Structure of the MIS12 Complex and Molecular Basis of Its Interaction with CENP-C at Human Kinetochores. *Cell* 167: 1028–1040.e15

Petrovic A, Mosalaganti S, Keller J, Mattiuzzo M, Overlack K, Krenn V, DeAntoni A, Wohlgemuth S, Cecatiello V, Pasqualato S, *et al* (2014a) Modular Assembly of RWD Domains on the Mis12 Complex Underlies Outer Kinetochore Organization. *Mol Cell* 53: 591–605

Petrovic A, Mosalaganti S, Keller J, Mattiuzzo M, Overlack K, Krenn V, DeAntoni A,

Wohlgemuth S, Cecatiello V, Pasqualato S, *et al* (2014b) Modular Assembly of RWD Domains on the Mis12 Complex Underlies Outer Kinetochore Organization. *Mol Cell* 53: 591–605

Petrovic A, Pasqualato S, Dube P, Krenn V, Santaguida S, Cittaro D, Monzani S, Massimiliano L, Keller J, Tarricone A, *et al* (2010) The MIS12 complex is a protein interaction hub for outer kinetochore assembly. *J Cell Biol* 190: 835–852

Pettersen EF, Goddard TD, Huang CC, Couch GS, Greenblatt DM, Meng EC & Ferrin TE (2004) UCSF Chimera - A visualization system for exploratory research and analysis. *J Comput Chem* 25: 1605–1612

Pfleger CM, Lee E & Kirschner MW (2001) Substrate recognition by the Cdc20 and Cdh1 components of the anaphase-promoting complex. *Genes Dev* 15: 2396–2407

Piano V, Alex A, Stege P, Maffini S, Stoppiello GA, Huis In'T Veld PJ, Vetter IR & Musacchio A (2021) CDC20 assists its catalytic incorporation in the mitotic checkpoint complex. *Science (80-)* 371: 67–71

Pidoux AL & Allshire RC (2004) Kinetochore and heterochromatin domains of the fission yeast centromere. *Chromosom Res* 12: 521–534

Pines J (2011) Cubism and the cell cycle: The many faces of the APC/C. *Nat Rev Mol Cell Biol* 12: 427–438

Pinsky BA & Biggins S (2005) The spindle checkpoint: Tension versus attachment. *Trends Cell Biol* 15: 486–493

Pinsky BA, Kung C, Shokat KM & Biggins S (2006) The Ipl1-Aurora protein kinase activates the spindle checkpoint by creating unattached kinetochores. *Nat Cell Biol* 8: 78–83

Primorac I, Weir JR, Chiroli E, Gross F, Hoffmann I, van Gerwen S, Ciliberto A & Musacchio A (2013) Bub3 reads phosphorylated MELT repeats to promote spindle assembly checkpoint signaling. *Elife* 2013

Proudfoot KG, Anderson SJ, Dave S, Bunning AR, Sinha Roy P, Bera A & Gupta ML (2019) Checkpoint Proteins Bub1 and Bub3 Delay Anaphase Onset in Response to Low Tension Independent of Microtubule-Kinetochore Detachment. *Cell Rep* 27: 416–428.e4

Przewloka MR, Venkei Z, Bolanos-Garcia VM, Debski J, Dadlez M & Glover DM (2011) CENP-C is a structural platform for kinetochore assembly. *Curr Biol* 21: 399–405

Puchades C, Sandate CR & Lander GC (2020) The molecular principles governing the activity and functional diversity of AAA+ proteins. *Nat Rev Mol Cell Biol* 21: 43–58

Pullen K, Rajagopal P, Klevit RE, Branchini BR, Reizer J, Saier MH, Scholtz JM & Huffine ME (1995) Phosphorylation of serine-46 in HPr, a key regulatory protein in bacteria, results in stabilization of its solution structure. *Protein Sci* 4: 2478–2486

Punjani A, Rubinstein JL, Fleet DJ & Brubaker MA (2017) CryoSPARC: Algorithms for rapid unsupervised cryo-EM structure determination. *Nat Methods* 14: 290–296

Punjani A, Zhang H & Fleet DJ (2020) Non-uniform refinement: adaptive regularization improves single-particle cryo-EM reconstruction. *Nat Methods* 17: 1214–1221

Purslow JA, Khatiwada B, Bayro MJ & Venditti V (2020) NMR Methods for Structural Characterization of Protein-Protein Complexes. *Front Mol Biosci* 7

Qi W & Yu H (2007) KEN-box-dependent degradation of the Bub1 spindle checkpoint kinase by the anaphase-promoting complex/cyclosome. *J Biol Chem* 282: 3672–3679

Qian J, García-Gimeno MA, Beullens M, Manzione MG, Van der Hoeven G, Igual JC, Heredia M, Sanz P, Gelens L & Bollen M (2017) An Attachment-Independent Biochemical Timer of the Spindle Assembly Checkpoint. *Mol Cell* 68: 715–730.e5

Qiao R, Weissmann F, Yamaguchi M, Brown NG, VanderLinden R, Imre R, Jarvis MA, Brunner MR, Davidson IF, Litos G, *et al* (2016) Mechanism of APC/CCDC20 activation by mitotic phosphorylation. *Proc Natl Acad Sci U S A* 113: E2570–E2578

Radermacher M, Wagenknecht T, Verschoor A & Frank J (1986) a New 3-D Reconstruction Scheme Applied To the 50S Ribosomal Subunit of E. Coli. *J Microsc* 141: RP1-RP2

Rago F, Gascoigne KE & Cheeseman IM (2015) Distinct organization and regulation of the outer kinetochore KMN network downstream of CENP-C and CENP-T. *Curr Biol* 25: 671–677

Ramírez-Aportela E, Maluenda D, Fonseca YC, Conesa P, Marabini R, Heymann JB, Carazo JM & Sorzano COS (2021) FSC-Q: a CryoEM map-to-atomic model quality validation based on the local Fourier shell correlation. *Nat Commun* 12: 1–7

Reddy SK, Rape M, Margansky WA & Kirschner MW (2007) Ubiquitination by the anaphase-promoting complex drives spindle checkpoint inactivation. *Nature* 446: 921–925

Reis A, Levasseur M, Chang HY, Elliott DJ & Jones KT (2006) The CRY box: A second APCcdh1-dependent degron in mammalian cdc20. *EMBO Rep* 7: 1040–1045

Rieder CL, Cole RW, Khodjakov A & Sluder G (1995) The checkpoint delaying anaphase in response to chromosome monoorientation is mediated by an inhibitory signal produced by unattached kinetochores. *J Cell Biol* 130: 941–948

Rieder CL, Schultz A, Cole R & Sluder G (1994) Anaphase onset in vertebrate somatic cells is controlled by a checkpoint that monitors sister kinetochore attachment to the spindle. *J Cell Biol* 127: 1301–1310

Rodriguez-Bravo V, Maciejowski J, Corona J, Buch HK, Collin P, Kanemaki MT, Shah J V. & Jallepalli P V. (2014) Nuclear pores protect genome integrity by assembling a premitotic and mad1-dependent anaphase inhibitor. *Cell* 156: 1017–1031

Rosenberg JS, Cross FR & Funabiki H (2011) KNL1/Spc105 recruits PP1 to silence the spindle assembly checkpoint. *Curr Biol* 21: 942–947

Russo CJ & Passmore LA (2016) Progress towards an optimal specimen support for electron cryomicroscopy. *Curr Opin Struct Biol* 37: 81–89

Sacristan C & Kops GJPL (2015) Joined at the hip: Kinetochores, microtubules, and spindle assembly checkpoint signaling. *Trends Cell Biol* 25: 21–28

Samejima I, Spanos C, De Lima Alves F, Hori T, Perpelescu M, Zou J, Rappsilber J, Fukagawa T & Earnshaw WC (2015) Whole-proteome genetic analysis of dependencies in assembly of a vertebrate kinetochore. *J Cell Biol* 211: 1141–1156

Sang HL, Sterling H, Burlingame A & McCormick F (2008) Tpr directly binds to Mad1 and Mad2 and is important for the Mad1-Mad2-mediated mitotic spindle checkpoint. *Genes Dev* 22: 2926–2931

Santaguida S & Amon A (2015) Short- and long-term effects of chromosome mis-segregation and aneuploidy. *Nat Rev Mol Cell Biol* 16: 473–485

Sarangapani KK, Koch LB, Nelson CR, Asbury CL & Biggins S (2021) Kinetochore-bound Mps1 regulates kinetochore-microtubule attachments via Ndc80 phosphorylation. *J Cell Biol* 220

Satyanarayana A & Kaldis P (2009) Mammalian cell-cycle regulation: Several cdks, numerous cyclins and diverse compensatory mechanisms. *Oncogene* 28: 2925–2939

Saurin AT (2018) Kinase and phosphatase cross-talk at the kinetochore. *Front Cell Dev Biol* 6: 62

Saurin AT, Van Der Waal MS, Medema RH, Lens SMA & Kops GJPL (2011) Aurora B potentiates Mps1 activation to ensure rapid checkpoint establishment at the onset of mitosis. *Nat Commun* 2: 1–9

Schafer KA (1998) The Cell Cycle: A Review. *Vet Pathol* 35: 461–478

Scheres SHW & Chen S (2012) Prevention of overfitting in cryo-EM structure determination. *Nat Methods* 9: 853–854

Schmitzberger F & Harrison SC (2012) RWD domain: A recurring module in kinetochore

architecture shown by a Ctf19-Mcm21 complex structure. *EMBO Rep* 13: 216–222
Schuck P (2003) On the analysis of protein self-association by sedimentation velocity analytical ultracentrifugation. *Anal Biochem* 320: 104–124
Schultz P (1988) Cryo-electron microscopy of vitrified specimens. *Q Rev Biophys* 21: 129–228
Schweizer N, Ferrás C, Kern DM, Logarinho E, Cheeseman IM & Maiato H (2013) Spindle assembly checkpoint robustness requires Tpr-mediated regulation of Mad1/Mad2 proteostasis. *J Cell Biol* 203: 883–893
Screpanti E, De Antoni A, Alushin GM, Petrovic A, Melis T, Nogales E & Musacchio A (2011) Direct binding of Cenp-C to the Mis12 complex joins the inner and outer kinetochore. *Curr Biol* 21: 391–398
Sczaniecka M, Feoktistova A, May KM, Chen JS, Blyth J, Gould KL & Hardwick KG (2008) The spindle checkpoint functions of Mad3 and Mad2 depend on a Mad3 KEN box-mediated interaction with Cdc20-anaphase-promoting complex (APC/C). *J Biol Chem* 283: 23039–23047
Shah J V., Botvinick E, Bonday Z, Furnari F, Berns M & Cleveland DW (2004) Dynamics of centromere and kinetochore proteins: Implications for checkpoint signaling and silencing. *Curr Biol* 14: 942–952
Shepperd LA, Meadows JC, Sochaj AM, Lancaster TC, Zou J, Buttrick GJ, Rappsilber J, Hardwick KG & Millar JBA (2012) Phosphodependent recruitment of Bub1 and Bub3 to Spc7/KNL1 by Mph1 kinase maintains the spindle checkpoint. *Curr Biol* 22: 891–899
Shevchenko A, Tomas H, Havliš J, Olsen J V. & Mann M (2007) In-gel digestion for mass spectrometric characterization of proteins and proteomes. *Nat Protoc* 1: 2856–2860
Shteinberg M, Protopopov Y, Listovsky T, Brandeis M & Hershko A (1999) Phosphorylation of the cyclosome is required for its stimulation by Fizzy/cdc20. *Biochem Biophys Res Commun* 260: 193–198
Sigworth FJ (1998) A maximum-likelihood approach to single-particle image refinement. *J Struct Biol* 122: 328–339
Silió V, McAinsh AD & Millar JB (2015) KNL1-Bubs and RZZ Provide Two Separable Pathways for Checkpoint Activation at Human Kinetochores. *Dev Cell* 35: 600–613
Silva PMA, Reis RM, Bolanos-Garcia VM, Florindo C, Tavares ÁA & Bousbaa H (2014) Dynein-dependent transport of spindle assembly checkpoint proteins off kinetochores toward spindle poles. *FEBS Lett* 588: 3265–3273
Simonetta M, Manzoni R, Mosca R, Mapelli M, Massimiliano L, Vink M, Novak B, Musacchio A & Ciliberto A (2009) The influence of catalysis on Mad2 activation dynamics. *PLoS Biol* 7: e1000010
Sironi L, Mapelli M, Knapp S, De Antoni A, Jeang KT & Musacchio A (2002) Crystal structure of the tetrameric Mad1-Mad2 core complex: Implications of a 'safety belt' binding mechanism for the spindle checkpoint. *EMBO J* 21: 2496–2506
Sivakumar S & Gorbsky GJ (2015) Spatiotemporal regulation of the anaphase-promoting complex in mitosis. *Nat Rev Mol Cell Biol* 16: 82–94
Slep KC & Vale RD (2007) Structural Basis of Microtubule Plus End Tracking by XMAP215, CLIP-170, and EB1. *Mol Cell* 27: 976–991
Sliedrecht T, Zhang C, Shokat KM & Kops GJPL (2010) Chemical Genetic Inhibition of Mps1 in Stable Human Cell Lines Reveals Novel Aspects of Mps1 Function in Mitosis. *PLoS One* 5
Snider J, Thibault G & Houry WA (2008) The AAA+ superfamily of functionally diverse proteins. *Genome Biol* 9: 216
Sorger PK, Dobles M, Tournebize R & Hyman AA (1997) Coupling cell division and cell death to microtubule dynamics. *Curr Opin Cell Biol* 9: 807–814

Spera S & Bax A (1991) Empirical Correlation between Protein Backbone Conformation and Cα and Cβ 13C Nuclear Magnetic Resonance Chemical Shifts. *J Am Chem Soc* 113: 5490–5492

Starr DA, Williams BC, Hays TS & Goldberg ML (1998) ZW10 helps recruit dynactin and dynein to the kinetochore. *J Cell Biol* 142: 763–774

Stern BM & Murray AW (2001) Lack of tension at kinetochores activates the spindle checkpoint in budding yeast. *Curr Biol* 11: 1462–1467

Stucke VM, Baumann C & Nigg EA (2004) Kinetochore localization and microtubule interaction of the human spindle checkpoint kinase Mps1. *Chromosoma* 113: 1–15

Sudakin V, Chan GKT & Yen TJ (2001) Checkpoint inhibition of the APC/C in HeLa cells is mediated by a complex of BUBR1, BUB3, CDC20, and MAD2. *J Cell Biol* 154: 925–936

Suijkerbuijk SJE, Vleugel M, Teixeira A & Kops GJPL (2012) Integration of Kinase and Phosphatase Activities by BUBR1 Ensures Formation of Stable Kinetochore-Microtubule Attachments. *Dev Cell* 23: 745–755

Takai A, Bialojan C, Troschka M & Caspar Rüegg J (1987) Smooth muscle myosin phosphatase inhibition and force enhancement by black sponge toxin. *FEBS Lett* 217: 81–84

Tanaka TU, Rachidi N, Janke C, Pereira G, Galova M, Schiebel E, Stark MJR & Nasmyth K (2002) Evidence that the Ipl1-Sli15 (Aurora Kinase-INCENP) complex promotes chromosome bi-orientation by altering kinetochore-spindle pole connections. *Cell* 108: 317–329

Tang Z, Bharadwaj R, Li B & Yu H (2001) Mad2-Independent Inhibition of APCCdc20 by the Mitotic Checkpoint Protein BubR1. *Dev Cell* 1: 227–237

Tegunov D & Cramer P (2019) Real-time cryo-electron microscopy data preprocessing with Warp. *Nat Methods* 16: 1146–1152

Teichner A, Eytan E, Sitry-Shevah D, Miniowitz-Shemtov S, Dumin E, Gromis J & Hershko A (2011) p31comet promotes disassembly of the mitotic checkpoint complex in an ATP-dependent process. *Proc Natl Acad Sci U S A* 108: 3187–3192

Teng Q (2013) Structural biology: Practical NMR applications 2nd ed. Springer US

Thapar R, Nicholson EM, Rajagopal P, Bruce Waygood E, Martin Scholtz J & Klevit RE (1996) Influence of N-cap mutations on the structure and stability of Escherichia coli HPr. *Biochemistry* 35: 11268–11277

Thorn A & Sheldrick GM (2011) ANODE: Anomalous and heavy-atom density calculation. *J Appl Crystallogr* 44: 1285–1287

Tian W, Li B, Warrington R, Tomchick DR, Yu H & Luo X (2012) Structural analysis of human Cdc20 supports multisite degron recognition by APC/C. *Proc Natl Acad Sci U S A* 109: 18419–18424

Tighe A, Staples O & Taylor S (2008) Mps1 kinase activity restrains anaphase during an unperturbed mitosis and targets Mad2 to kinetochores. *J Cell Biol* 181: 893–901

Tipton AR, Ji W, Sturt-Gillespie B, Bekier ME, Wang K, Taylor WR & Liu ST (2013) Monopolar Spindle 1 (MPS1) kinase promotes production of closed MAD2 (C-MAD2) conformer and assembly of the mitotic checkpoint complex. *J Biol Chem* 288: 35396–35405

Tipton AR, Tipton M, Yen T & Liu ST (2011) Closed MAD2 (C-MAD2) is selectively incorporated into the mitotic checkpoint complex (MCC). *Cell Cycle* 10: 3740–3750

Tromer E, Snel B & Kops GJPL (2015) Widespread recurrent patterns of rapid repeat evolution in the kinetochore scaffold KNL1. *Genome Biol Evol* 7: 2383–2393

Ubersax JA & Ferrell JE (2007) Mechanisms of specificity in protein phosphorylation. *Nat Rev Mol Cell Biol* 8: 530–541

Uhlmann F & Nasmyth K (1998) Cohesion between sister chromatids must be established during DNA replication. *Curr Biol* 8: 1095–1102

Uzunova K, Dye BT, Schutz H, Ladurner R, Petzold G, Toyoda Y, Jarvis MA, Brown NG, Poser I, Novatchkova M, *et al* (2012) APC15 mediates CDC20 autoubiquitylation by APC/C MCC and disassembly of the mitotic checkpoint complex. *Nat Struct Mol Biol* 19: 1116–1123

Vader G, Medema RH & Lens SMA (2006) The chromosomal passenger complex: Guiding Aurora-B through mitosis. *J Cell Biol* 173: 833–837

Valverde R, Ingram J & Harrison SC (2016) Conserved Tetramer Junction in the Kinetochore Ndc80 Complex. *Cell Rep* 17: 1915–1922

Vanoosthuyse V & Hardwick KG (2009a) A Novel Protein Phosphatase 1-Dependent Spindle Checkpoint Silencing Mechanism. *Curr Biol* 19: 1176–1181

Vanoosthuyse V & Hardwick KG (2009b) Overcoming inhibition in the spindle checkpoint. *Genes Dev* 23: 2799–805

Varma D, Wan X, Cheerambathur D, Gassmann R, Suzuki A, Lawrimore J, Desai A & Salmon ED (2013) Spindle assembly checkpoint proteins are positioned close to core microtubule attachment sites at kinetochores. *J Cell Biol* 202: 735–746

Velazhahan V, Ma N, Pándy-Szekeres G, Kooistra AJ, Lee Y, Gloriam DE, Vaidehi N & Tate CG (2021) Structure of the class D GPCR Ste2 dimer coupled to two G proteins. *Nature* 589: 148–153

Vigneron S, Prieto S, Bernis C, Labbé JC, Castro A & Lorca T (2004) Kinetochore localization of spindle checkpoint proteins: Who controls whom? *Mol Biol Cell* 15: 4584–4596

Vleugel M, Hoogendoorn E, Snel B & Kops GJPL (2012) Evolution and Function of the Mitotic Checkpoint. *Dev Cell* 23: 239–250

Vleugel M, Omerzu M, Groenewold V, Hadders MA, Lens SMA & Kops GJPL (2015) Sequential Multisite Phospho-Regulation of KNL1-BUB3 Interfaces at Mitotic Kinetochores. *Mol Cell* 57: 824–835

Vleugel M, Tromer E, Omerzu M, Groenewold V, Nijenhuis W, Snel B & Kops GJPL (2013) Arrayed BUB recruitment modules in the kinetochore scaffold KNL1 promote accurate chromosome segregation. *J Cell Biol* 203: 943–955

Wada A (1976) The alpha-helix as an electric macro-dipole. *Adv Biophys*: 1–63

Wagner A, Duman R, Henderson K & Mykhaylyk V (2016) In-vacuum long-wavelength macromolecular crystallography. *Acta Crystallogr Sect D Struct Biol* 72: 430–439

Wagner G (1993) P. R. Buseck, J. M. Cowley, L. Eyring. High-Resolution Transmission Electron Microscopy and Associated Techniques. Oxford University Press, Inc. 1992. Price £ 27.50. ISBN 0-19-507262-6 (pbk.) and ISBN 0-19-504275-1. *Cryst Res Technol* 28: 628–628

Wagner T, Merino F, Stabrin M, Moriya T, Antoni C, Apelbaum A, Hagel P, Sitsel O, Raisch T, Prumbaum D, *et al* (2019) SPHIRE-crYOLO is a fast and accurate fully automated particle picker for cryo-EM. *Commun Biol* 2: 1–13

Waizenegger IC, Giménez-Abián JF, Wernic D & Peters JM (2002) Regulation of human separase by securin binding and autocleavage. *Curr Biol* 12: 1368–1378

Wan X, O'Quinn RP, Pierce HL, Joglekar AP, Gall WE, DeLuca JG, Carroll CW, Liu ST, Yen TJ, McEwen BF, *et al* (2009) Protein Architecture of the Human Kinetochore Microtubule Attachment Site. *Cell* 137: 672–684

Wang H, Hu X, Ding X, Dou Z, Yang Z, Shaw AW, Teng M, Cleveland DW, Goldberg ML, Niu L, *et al* (2004) Human Zwint-1 specifies localization of Zeste White 10 to kinetochores and is essential for mitotic checkpoint signaling. *J Biol Chem* 279: 54590–54598

Wang X, Babu JR, Harden JM, Jablonski SA, Gazi MH, Lingle WL, De Groen PC, Yen TJ & Van Deursen JMA (2001) The Mitotic Checkpoint Protein hBUB3 and the mRNA Export Factor hRAE1 Interact with GLE2p-binding Sequence (GLEBS)-containing Proteins. *J Biol Chem* 276: 26559–26567

Watson ER, Brown NG, Peters JM, Stark H & Schulman BA (2019) Posing the APC/C E3 Ubiquitin Ligase to Orchestrate Cell Division. *Trends Cell Biol* 29: 117–134

Waudby CA, Ouvry M, Davis B & Christodoulou J (2020) Two-dimensional NMR lineshape analysis of single, multiple, zero and double quantum correlation experiments. *J Biomol NMR* 74: 95–109

Wei RR, Al-Bassam J & Harrison SC (2007) The Ndc80/HEC1 complex is a contact point for kinetochore-microtubule attachment. *Nat Struct Mol Biol* 14: 54–59

Weiss E & Winey M (1996) The Saccharomyces cerevisiae spindle pole body duplication gene MPS1 is part of a mitotic checkpoint. *J Cell Biol* 132: 111–123

Welburn JPI, Vleugel M, Liu D, Yates JR, Lampson MA, Fukagawa T & Cheeseman IM (2010) Aurora B Phosphorylates Spatially Distinct Targets to Differentially Regulate the Kinetochore-Microtubule Interface. *Mol Cell* 38: 383–392

Willems AR, Schwab M & Tyers M (2004) A hitchhiker's guide to the cullin ubiquitin ligases: SCF and its kin. *Biochim Biophys Acta - Mol Cell Res* 1695: 133–170

Williams CJ, Headd JJ, Moriarty NW, Prisant MG, Videau LL, Deis LN, Verma V, Keedy DA, Hintze BJ, Chen VB, *et al* (2018) MolProbity: More and better reference data for improved all-atom structure validation. *Protein Sci* 27: 293–315

Williams DB & Carter CB (2009) The Transmission Electron Microscope. *Transm Electron Microsc*: 3–22

Winn MD, Ballard CC, Cowtan KD, Dodson EJ, Emsley P, Evans PR, Keegan RM, Krissinel EB, Leslie AGW, McCoy A, *et al* (2011) Overview of the CCP4 suite and current developments. *Acta Crystallogr Sect D Biol Crystallogr* 67: 235–242

Winter G (2010) Xia2: An expert system for macromolecular crystallography data reduction. *J Appl Crystallogr* 43: 186–190

Wlodawer A, Minor W, Dauter Z & Jaskolski M (2013) Protein crystallography for aspiring crystallographers or how to avoid pitfalls and traps in macromolecular structure determination. *FEBS J* 280: 5705–5736

Xia G, Luo X, Habu T, Rizo J, Matsumoto T & Yu H (2004) Conformation-specific binding of p31comet antagonizes the function of Mad2 in the spindle checkpoint. *EMBO J* 23: 3133–3143

Xia Y & Xun L (2017) Revised mechanism and improved efficiency of the quikchange site-directed mutagenesis method. *Methods Mol Biol* 1498: 367–374

Yamagishi Y, Yang CH, Tanno Y & Watanabe Y (2012) MPS1/Mph1 phosphorylates the kinetochore protein KNL1/Spc7 to recruit SAC components. *Nat Cell Biol* 14: 746–752

Yamaguchi M, VanderLinden R, Weissmann F, Qiao R, Dube P, Brown NG, Haselbach D, Zhang W, Sidhu SS, Peters JM, *et al* (2016) Cryo-EM of Mitotic Checkpoint Complex-Bound APC/C Reveals Reciprocal and Conformational Regulation of Ubiquitin Ligation. *Mol Cell* 63: 593–607

Yamamoto TG, Watanabe S, Essex A & Kitagawa R (2008) Spdl-1 functions as a kinetochore receptor for MDF-1 in Caenorhabditis elegans. *J Cell Biol* 183: 187–194

Yan K, Yang J, Zhang Z, McLaughlin SH, Chang L, Fasci D, Ehrenhofer-Murray AE, Heck AJR & Barford D (2019) Structure of the inner kinetochore CCAN complex assembled onto a centromeric nucleosome. *Nature* 574: 278–282

Yang M, Li B, Liu CJ, Tomchick DR, Machius M, Rizo J, Yu H & Luo X (2008) Insights into Mad2 regulation in the spindle checkpoint revealed by the crystal structure of the symmetric Mad2 dimer. *PLoS Biol* 6: 0643–0655

Yang M, Li B, Tomchick DR, Machius M, Rizo J, Yu H & Luo X (2007) p31comet Blocks Mad2 Activation through Structural Mimicry. *Cell* 131: 744–755

Ye Q, Rosenberg SC, Moeller A, Speir JA, Su TY & Corbett KD (2015) TRIP13 is a protein-remodeling AAA+ ATPase that catalyzes MAD2 conformation switching. *Elife* 2015: 1–44

Yu H (2007) Cdc20: A WD40 Activator for a Cell Cycle Degradation Machine. *Mol Cell* 27: 3–16

Zhang G, Kruse T, Guasch Boldú C, Garvanska DH, Coscia F, Mann M, Barisic M & Nilsson J (2019) Efficient mitotic checkpoint signaling depends on integrated activities of Bub1 and the RZZ complex . *EMBO J* 38: e100977

Zhang G, Kruse T, López-Méndez B, Sylvestersen KB, Garvanska DH, Schopper S, Nielsen ML & Nilsson J (2017) Bub1 positions Mad1 close to KNL1 MELT repeats to promote checkpoint signalling. *Nat Commun* 8: 15822

Zhang G, Lischetti T, Hayward DG & Nilsson J (2015) Distinct domains in Bub1 localize RZZ and BubR1 to kinetochores to regulate the checkpoint. *Nat Commun* 6: 7162

Zhang G, Lischetti T & Nilsson J (2014) A minimal number of MELT repeats supports all the functions of KNL1 in chromosome segregation. *J Cell Sci* 127: 871–884

Zhang G, Mendez BL, Sedgwick GG & Nilsson J (2016a) Two functionally distinct kinetochore pools of BubR1 ensure accurate chromosome segregation. *Nat Commun* 7: 1–12

Zhang K (2016) Gctf: Real-time CTF determination and correction. *J Struct Biol* 193: 1–12

Zhang S, Chang L, Alfieri C, Zhang Z, Yang J, Maslen S, Skehel M & Barford D (2016b) Molecular mechanism of APC/C activation by mitotic phosphorylation. *Nature* 533: 260–264

Zhang Y & Lees E (2001) Identification of an Overlapping Binding Domain on Cdc20 for Mad2 and Anaphase-Promoting Complex: Model for Spindle Checkpoint Regulation. *Mol Cell Biol* 21: 5190–5199

Zhang Z, Yang J & Barford D (2016c) Recombinant expression and reconstitution of multiprotein complexes by the USER cloning method in the insect cell-baculovirus expression system. *Methods* 95: 13–25

Zhao H, Brautigam CA, Ghirlando R & Schuck P (2013) Overview of current methods in sedimentation velocity and sedimentation equilibrium analytical ultracentrifugation. *Curr Protoc Protein Sci* 71: 20.12.1-20.12.49

Zheng N & Shabek N (2017) Ubiquitin ligases: Structure, function, and regulation. *Annu Rev Biochem* 86: 129–157

Zheng SQ, Palovcak E, Armache JP, Verba KA, Cheng Y & Agard DA (2017) MotionCor2: Anisotropic correction of beam-induced motion for improved cryo-electron microscopy. *Nat Methods* 14: 331–332

Zhou Z, He M, Shah AA & Wan Y (2016) Insights into APC/C: From cellular function to diseases and therapeutics. *Cell Div* 11

Zhu T, Dou Z, Qin B, Jin C, Wang X, Xu L, Wang Z, Zhu L, Liu F, Gao X, *et al* (2013) Phosphorylation of microtubule-binding protein hec1 by mitotic kinase aurora b specifies spindle checkpoint kinase mps1 signaling at the kinetochore. *J Biol Chem* 288: 36149–36159

Zich J, Sochaj AM, Syred HM, Milne L, Cook AG, Ohkura H, Rappsilber J & Hardwick KG (2012) Kinase Activity of Fission Yeast Mph1 Is Required for Mad2 and Mad3 to Stably Bind the Anaphase Promoting Complex. *Curr Biol* 22: 296–301

Zivanov J, Nakane T, Forsberg BO, Kimanius D, Hagen WJH, Lindahl E & Scheres SHW (2018) New tools for automated high-resolution cryo-EM structure determination in RELION-3. *Elife* 7: e42166

Zivanov J, Nakane T & Scheres SHW (2019) A Bayesian approach to beam-induced motion correction in cryo-EM single-particle analysis. *IUCrJ* 6: 5–17